The Dissertation Committee for Paul Michael Betka Certifies that this is the approved version of the following dissertation:

Structure of the Patagonian fold-thrust belt in the Magallanes region of Chile, 53° - 55° S Lat.

Committee:

Sharon Mosher, Supervisor

Keith Klepeis, Co-Supervisor

Ian Dalziel

Brian Horton

Randall Marrett

Constantino Mpodozis

Structure of the Patagonian fold-thrust belt in the Magallanes region of Chile, 53° - 55° S Lat.

by

Paul Michael Betka, B.S., M.S.

Dissertation

Presented to the Faculty of the Graduate School of

The University of Texas at Austin

in Partial Fulfillment

of the Requirements

for the Degree of

Doctor of Philosophy

The University of Texas at Austin

December 2013

Acknowledgements

I am grateful to my advisors, Sharon Mosher and Keith Klepeis, who have always supported and encouraged this project. Sharon has been a particularly exceptional supervisor and academic mentor as well as an excellent editor. She has greatly improved my geologic skills and ability to reason and communicate as a scientist. Keith inspired this research project and has always encouraged my interests in field-based geology. He has consistently challenged me to become a better 'all-around' geologist and to support my interpretations in writing as clearly and objectively as possible. I am also grateful to my dissertation committee members, Ian Dalziel, Randy Marrett, Brain Horton, and Constantino Mpodozis. Ian has provided me with several incredible opportunities to see the geology of Tierra del Fuego, South Georgia Island, the Antarctic Peninsula, and the Scottish Highlands. These invaluable experiences have fueled my interests in understanding tectonics and cultivated new research ideas for the future. I have especially enjoyed numerous field-camp experiences and unique conversations with Randy about all things structural geology and otherwise that have broadened my knowledge. I have benefited significantly from Brian's experience in foreland basin and thrust belt tectonics, and I have enjoyed many classroom and field discussions with him. I was especially honored to have Constantino travel to Texas from Santiago, Chile to attend my dissertation defense (11/21/13). He provided an excellent dissertation review and I enjoyed several interesting discussions with him about the geology of Southern Patagonia.

I am also grateful to the Jackson School of Geosciences. The geology program was an incredible source of intellectual, analytical, and financial support. Several

financial awards for field and analytical expenses that I received from the Jackson School have fully supported much of this project and made it possible to pursue my research questions through to the end. Additionally, the expansive scientific community within the Jackson School of Geosciences provided an exciting environment for discussing geology and cultivating ideas. I am especially grateful to my fellow Mosher group graduate students John, Jamie, Ephraim, Brittney and Miriam from whom I learned a lot about surviving graduate school, being a good teaching assistant, and finishing a PhD. I also want to thank Mark Helper for providing me with several opportunities to teach field-camp, something that I would like to do again in the future. Most importantly, I want to thank my family and friends for their constant friendship and support.

Structure of the Patagonian fold-thrust belt in the Magallanes region of Chile, 53° - 55° S Lat.

Paul Michael Betka, Ph.D.

The University of Texas at Austin, 2013

Supervisor: Sharon Mosher

Co-Supervisor: Keith Klepeis

The southern Patagonian Andes record the Late Cretaceous closure and inversion of the Late Jurassic – Early Cretaceous Rocas Verdes marginal basin, subsequent development of the Patagonian retroarc fold-thrust belt and the Neogene to present tectonic superposition of a left-lateral strike-slip plate margin defined by the Magallanes-Fagnano fault zone. In this dissertation, I present new geologic maps, cross sections and detailed macro- and microscopic structural analyses that describe the geometry and kinematic evolution of the fold-thrust belt and superposed strike-slip deformation over ~200 km along-strike between 53° and 55° S latitude. Results are discussed in the context of the regional tectonic development of the southernmost Andes and are relevant to the understanding of important tectonic processes including the development of a retroarc fold-thrust belt, the formation of a basal décollement below and toward the hinterland of a fold-thrust belt and the spatial distribution of deformation along a strike-slip plate margin.

New maps and balanced cross-sections of the Patagonian fold-thrust belt show that it developed during two main phases of Late Cretaceous to Paleogene shortening that were partly controlled by the antecedent geology and mechanical stratigraphy of the Rocas Verdes basin. During the Late Cretaceous, a thin-skinned thrust belt developed above a décollement that formed first in relatively weak shale deposits of the Rocas Verdes basin and later deepened to <1 km below the basement-cover contact. Ramps that

cut mechanically rigid volcanic rocks of the marginal basin link the two décollements. Basement-involved reverse faults that cut the early décollements and probably reactivate Jurassic normal faults reflect Paleogene shortening. Shortening estimates increase northwest to southeast from 26 to 37% over 100 km along-strike and are consistent with regional models of the fold-thrust belt.

Structural data, kinematic analyses, and microstructural observations from the lower décollement show that it is defined by transposition of several generations of northeast-vergent noncylindrical folds, shear bands, and a quartz stretching lineation that are kinematically compatible with first-generation structures of the fold-thrust belt. Quartz microstructural data from the décollement are consistent with deformation temperatures that decrease from ~500-650° C to ~400-550° C over ~75 km in the transport direction, indicating that the décollement dipped shallowly (~6°) toward the hinterland. The décollement decoupled the underthrust continental margin from the fold-thrust belt and exemplifies the kinematic relationship between shortening that occurs coevally in a retroarc fold thrust-belt and its polydeformed metamorphic 'basement'.

Fault kinematic data and crosscutting relationships show kinematic and temporal relationships between populations of thrust, strike-slip and normal faults that occur in the study area. Thrust faults form an internally compatible population that shows subhorizontal northeast-trending shortening of the fold-thrust belt and is kinematically distinct from populations of normal and strike-slip faults. Both strike-slip and normal faults crosscut the fold-thrust belt, are localized near segments of the Magallanes-Fagnano fault zone, have mutually compatible kinematic axes and are interpreted to be coeval. Strike-slip faults form Riedel and P-shear geometries that are compatible with left-lateral slip on the Magallanes-Fagnano fault-zone. Strike-slip and normal faults occur in a releasing step-over between two overlapping left-lateral, left-stepping segments of the Magallanes fault zone and record a tectonic event defined by sinistral transtension that probably reflects changing plate dynamics associated with the opening of the Drake Passage during the Early Miocene.

Table of Contents

List of Plates

List of Tables

List of Figures

INTRODUCTION

The southern Patagonian Andes extend for ~1000 km along-strike between 50° S lat. around the bend of the Patagonian orocline to Isla de los Estados, east of Isla Grande de Tierra del Fuego. The mountain-belt preserves at least 150 m.y. of geologic history that includes formation of a marginal basin during the Jurassic rifting of Gondwana, the inversion of that basin during a Cretaceous-Paleogene orogeny, and the development of a strike-slip plate margin since the Neogene. In southern Chile, mafic rocks that comprise the Jurassic to Early Cretaceous Rocas Verdes marginal basin are tectonically imbricated with pre-Jurassic schist of the Cordillera Darwin Metamorphic Complex and Cretaceous to Neogene sedimentary rocks of the Magallanes foreland basin that altogether form the Patagonian fold-thrust belt. In this dissertation, I describe the geometry and structural evolution of the Patagonian fold-thrust belt where it is exposed for ~200 km along-strike between 53° and 55° S latitude and use it as a proxy for understanding the regional tectonic history, the kinematic evolution of a retroarc fold-thrust belt, the relationship between tectonic shortening in both basement and cover rocks during orogenesis, and the distribution of deformation along a strike-slip plate margin. Conducting this study in the Patagonian fold-thrust belt is important because it preserves one of the largest exposures of the lower levels of the orogen in the Andes (*i.e.* near and below the brittle-ductile transition) that has been exhumed and can be observed.

The study area is a ~120 km^2 area of the Patagonian fold-thrust belt between 53° and 55° S that is located within the bend of the Patagonian orocline, south of the Ultima Esperanza region of Chile and west of Argentine Tierra del Fuego. Here, rocks of the Rocas Verdes basin and Cordillera Darwin Metamorphic Complex are imbricated with those of the Magallanes foreland basin. The trend of the thrust belt follows along the bend of the Patagonian orocline from Ultima Esperanza to Tierra del Fuego. I participated in four ship-based and one land-based mapping campaigns for a total of ~6

months of fieldwork between 2008-2012 to produce new 1:50,000 and 1:25,000 scale geological maps of Seno Otway, Peninsula Brunswick and Seno Martínez. Inflatable boats were used to map transects along all of the fiords in the map area where wave-washed shoreline outcrops provide the best bedrock exposure. The geologic maps presented herein build upon the existing 1:1,000,000 scale Mapa Geológico del Chile (SERNAGEOMIN, 2002). I used the local stratigraphic nomenclature of Mpodozis *et al*. (2007) and stratigraphic thicknesses and ages of McAtamney *et al*. (2011). Surface geological data was collected at each data station and integrated to construct the geologic map. Where the surface geology was not telling, I used publically available satellite imagery (SRTM DEMs, Google Earth) to correlate geologic contacts between fiords. No subsurface data was available for this study.

This dissertation is divided into three chapters that are each intended to be submitted as stand-alone manuscripts for peer-reviewed journals. Chapter one discusses the geometry and structure of the Patagonian fold-thrust belt for ~100 km along-strike in a previously poorly known region near Peninsula Brunswick and Seno Otway. Data presented in this chapter include a new geologic map and eight strike-perpendicular cross-sections of the (1:100,000 scale, Plate 1), structural analyses of geologic data, and three line-length balanced reconstructions of the fold-thrust belt. This study documents the geometry and structural evolution of the fold-thrust belt and discusses the influence of the antecedent geology of the Rocas Verdes basin on its development.

Chapter two considers the kinematic evolution of the basal décollement of the Patagonian fold-thrust belt. In this chapter, I present new geologic mapping as well as detailed macro- and microscopic structural analyses including quartz textural descriptions and deformation mechanisms, quartz crystallographic fabrics, shear zone kinematic indicators, and superposed fold patterns from the décollement where it crops out near Seno Martínez and Bahía Fortesque. Results from the two locations are compared and indicate that the décollement is a regional structure. I present a new model that describes

the kinematic evolution of the décollement and how shortening in the overlying fold-thrust belt is related to shortening in the polydeformed metamorphic basement.

In chapter three, I present kinematic analyses of populations of thrust, strike-slip and normal faults that occur within the Patagonian fold-thrust belt near Seno Otway and Peninsula Brusnwick. Data include the attitudes of faults and striae, as well as observations of fault-slip indicators such as Riedel, P- and T-shears, fault surface asperities and/or the orientations of tensile and sigmoidal veins. This study demonstrates that thrust faults form a population that is kinematically distinct from mutually compatible sets of strike-slip and normal faults. I conclude that strike-slip and normal faults in the study are part of a Neogene to present phase of transtensinoal deformation that is superimposed on the Patagonian fold-thrust belt. I document the extent of this deformation where it was previously not recognized.

CHAPTER 1: ALONG-STRIKE VARIATION IN CRUSTAL SHORTENING AND KINEMATIC EVOLUTION OF THE MAGALLANES FOLD-THRUST BELT, MAGALLANES, CHILE 53°-54°

Abstract

The Late Cretaceous closure and inversion of the Late Jurassic – Early Cretaceous Rocas Verdes marginal basin defines the onset of the Andean orogeny and the development of the Patagonian retroarc fold-thrust belt and Magallanes foreland basin between 50°-54.5° S. New geologic maps, structural data, and three retrodeformed, line-balanced cross-sections of the fold-thrust belt over 100 km^2 in the Magallanes region of Chile between 53°-54° S constrain the kinematic evolution and along-strike structural correlations of the fold-thrust belt. Results show the stratigraphic architecture of the antecedent Rocas Verdes basin was a primary control on position of décollement levels that formed in the subsequent fold-thrust belt. During the initial stage of closure (Albian-Campanian), the basaltic floor of the Rocas Verdes basin was imbricated and thrust onto the continental margin to form a regional décollement within Jurassic-Lower Cretaceous shale deposits. Continued shortening resulted in the deepening of the décollement to a ductile shear zone that formed <1 km below the basement-cover contact. Below the lower décollement and toward the hinterland, ductile polyphase folding accommodated basement shortening and was detached from the overlying fold-thrust belt. Ramps cut Jurassic volcanic deposits to link the lower and upper décollements and transfer displacement into the nascent Magallanes foreland basin. A second stage of shortening is characterized by thick-skinned basement-involved reverse faults that cut the early décollements and reflect complete closure of the Rocas Verdes basin by the Maastrichtian-Eocene. Shortening estimates show a systematic northwest-southeast increase from 26-37%, respectively, over 100 km along-strike and is consistent with regional models of the Patagonian fold-thrust belt. The results provide an important

example of the kinematic evolution of the base of a retroarc fold-thrust belt in an 'Andean-style' orogen.

1. Introduction

The Cretaceous-Paleogene Patagonian retroarc fold-thrust belt formed by the closure and inversion of a Jurassic-Early Cretaceous marginal basin. The basin, known as the Rocas Verdes basin, formed during the Jurassic rifting of Gondwana and was floored by new oceanic crust (Dalziel *et al.,* 1974; Bruhn *et al.,* 1978; Saunders, 1979; Dalziel, 1981; Stern and De Wit, 2003; Fildani and Hessler, 2005; Calderón *et al.,* 2007). By the Cretaceous, the Rocas Verdes basin began to close in a compressional setting defining the onset of the Andean orogeny in the southern Andes (Dalziel and Palmer, 1979; Nelson, 1980; Klepeis *et al.,* 2010). Rocks of the Rocas Verdes basin were thrust onto the continental margin and formed a retroarc fold-thrust belt and foreland basin, known as the Patagonian fold-thrust belt and Magallanes Foreland Basin by the Late Cretaceous (Katz, 1963; Biddle, 1986; Wilson, 1991; Klepeis, 1994a; Fildani *et al.,* 2003; Fosdick *et al.,* 2011). Here, I report on the structural evolution of the base of this fold-thrust belt where it is exposed in a previously understudied ~100 km^2 location in southern Chile near Seno Otway and Peninsula Brunswick in the Magallanes region of Chile (Figure 1.1). This location allowed me to evaluate the influence of the structure and stratigraphy of an antecedent marginal basin on the kinematic evolution of a retroarc fold-thrust belt, to understand the structural evolution of the base of a fold-thrust belt near the basement-cover contact, and to determine along-strike spatial variation in the structure of the fold-thrust belt by comparing it with previous work toward the northwest and southeast of the study area (Figure 1.1).

The study area (Figure 1.1) is an important locality for understanding the structure of the Patagonian fold-thrust belt because it is situated in the bend of the Patagonian orocline, a ~90° counterclockwise bend in the trend of the orogen between 51° and 54° S

latitude located between the Ultima Esperanza region of Chile toward the northwest and Tierra del Fuego to the southeast (Figure 1.1). The structure of the Patagonian fold-thrust belt is well known in both Ultima Esperanza (*e.g.* Fosdick *et al.,* 2011) and Tierra del Fuego (*e.g.*, Klepeis *et al.,* 1994a; 2010; Rojas and Mpodozis, 2006), and regional tectonic models associate the development of the Patagonian orocline with a systematic northwest to southeast increase in tectonic shortening during the closure of the Rocas Verdes basin and development of the fold-thrust belt (Cunningham *et al.,* 1995; Diraison *et al.,* 2000; Kraemer *et al.,* 2003; Ghiglione and Cristallini, 2007). However, little is known about the geology and structure of the Magallanes region of Chile for >250 km along-strike between Ultima Esperanza and Tierra del Fuego, casting some doubt on regional structural correlations. New mapping results from a ~100 km^2 in the Magallanes region of Chile, eight new structural cross sections, and three new balanced and restored cross sections of the Magallanes segment of the Patagonian fold-thrust belt presented in this paper allow more robust structural correlations and test for systematic along-strike increase in tectonic shortening between Ultima Esperanza and Tierra del Fuego. The results match well with regional tectonic interpretations and help to correlate the kinematic evolution of the fold-thrust belt for over 400 km along-strike of the orogen.

Finally, the present structural depth-of-exposure in the study area preserves outcrops at the base of the fold-thrust belt where Jurassic and Cretaceous volcanic and sedimentary cover rocks of the Rocas Verdes basin and Magallanes foreland basin are in tectonic contact with the pre-Jurassic metamorphic 'basement' (Figure 1.1). In Patagonia, the 'basement' comprises a belt of Paleozoic lower-greenschist to upper-amphibolite facies metamorphic rocks that are capped by a regional unconformity and were deformed and metamorphosed during the Late Cretaceous contemporaneous with the development of the Patagonian fold-thrust belt (Nelson *et al.,* 1980; Klepeis *et al.,* 2010). I test two hypotheses regarding the kinematic development of a retroarc fold-thrust belt: 1) the structure of the fold-thrust belt is strongly influenced by the antecedent stratigraphic architecture of the predecessor marginal basin; 2) shortening in the basement may be detached from the overlying thrust belt. These questions are important to address because

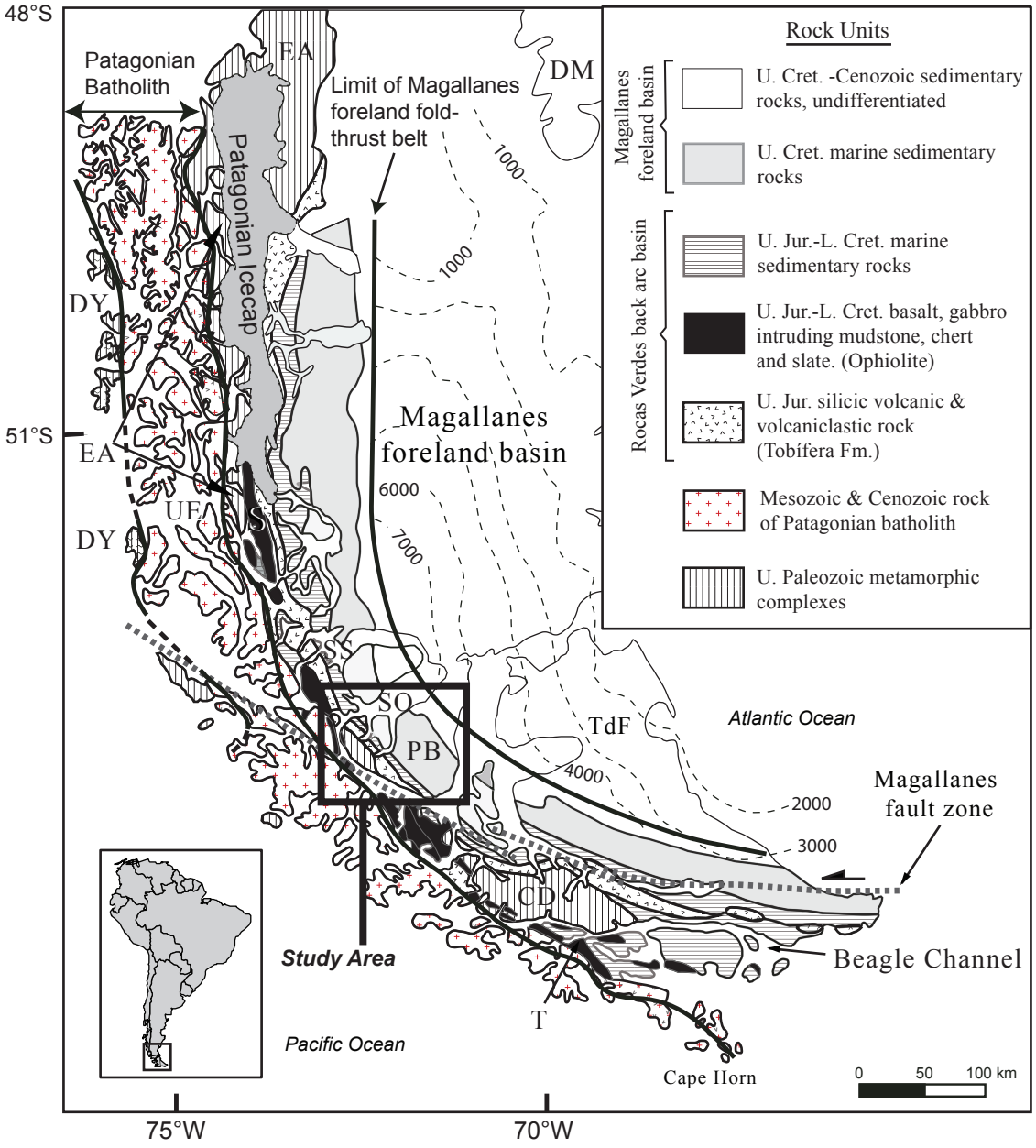

Figure 1.1 Simplified geologic map of the southernmost Andes showing tectonostratigraphic provinces, modified from McAtamney *et al*. (2011); Fildani & Hessler (2005). Contours (thin dashed lines) show sediment isopach overlying Jurassic volcanic rocks after Biddle *et al*. (1986). Metamorphic complexes include Cordillera Darwin (CD), Eastern Andes (EA), Duque de York, (DY), the Deseado Massif (DM). Ophiolitic suites include the Sarmiento (S) and Tortuga (T) complexes. UE, Ultima Esperanza; SS, Seno Skyring; SO, Seno Otway; PB, Peninsula Brunswick; TdF, Tierra del Fuego. Extent of the study area is shown in figure 1.3.

many orogens are the result of compressional inversions of extensional basins (*e.g.* the Central Andes: Allmendinger, 1997; Mpodozis *et al.,* 2005; the Alpine-Apennine orogen: Butler *et al.,* 2006; Taiwan: Mouthereau and Lacombe, 2006; *see review by* Lowell, 1995), and many orogens have high topographic relief that cannot be entirely explained by shortening in a fold-thrust belt and therefore require mid-lower crustal thickening (*e.g.* Eastern Cordillera of the Central Andes, McQuarrie *et al.,* 2005; Himalayan-Tibet orogen, Clark and Royden, 2000). Our results describe the formation of two décollement levels that formed 1) in the Jurassic-Lower Cretaceous shale deposits, and 2) near the basement-cover contact on the continental margin. Décollement levels control the kinematic development of the Patagonian fold-thrust belt and effectively decouple shortening that occurs in the metamorphic basement from the overlying fold-thrust belt.

2. Geologic setting and tectonostratigraphy

2.1 Cordillera Darwin Metamorphic Complex

The Cordillera Darwin Metamorphic Complex comprises a ~5000 km^2 exhumed massif of lower-greenschist to upper-amphibolite schist and orthogneiss of mixed origin that forms a topographic high in the southernmost Andes (Figure 1.1; Darwin, 1846; Kranck, 1932; Nelson *et al.,* 1980; Kohn *et al.,* 1995; Cunningham *et al.,* 1995; Hervé *et al.,* 2003, 2010; Klepeis *et al.,* 2010). Detrital zircon ages from schistose rocks within the Cordillera Darwin yielded both Ordovician-Devonian (Hervé *et al.,* 2010) and Carboniferous-Permian (Barbeau *et al.,* 2009) populations. Schistose rocks of the Cordillera Darwin Metamorphic Complex are interpreted to be similar to the Eastern Andes Metamorphic Complex (Hervé and Mpodozis, 2005) that was deposited on the Gondwanan passive margin during the Paleozoic (Hervé *et al.,* 2010). Upper Jurassic and Lower Cretaceous volcanic and sedimentary cover rocks unconformably overlie the Cordillera Darwin Metamorphic Complex, which defines the local 'basement.'

Late Cretaceous upper amphibolite metamorphic mineral assemblages include garnet, kyanite, staurolite and sillimanite and occur in both Paleozoic basement and

Jurassic-Early Cretaceous cover rocks (Nelson, 1980). Peak metamorphic conditions of P = 9-12 kbar and T = 620°C are reported from the high-grade core of the metamorphic complex near the Beagle Channel (Kohn *et al.,* 1993; Maloney *et al.,* 2011). Metamorphic isograds within the Cordillera Darwin Metamorphic Complex form an antiformal dome, and thus outcrops along the margins of the Cordillera Darwin Metamorphic Complex preserve chlorite- and biotite-bearing lower-greenschist facies assemblages that were not as deeply buried as the upper-amphibolite facies rocks that are exposed in the core (Nelson *et al.,* 1980; Kohn *et al.,* 1993; Klepeis *et al.,* 2010). Low-grade rocks around the margins of the Cordillera Darwin are commonly tectonically interleaved with weakly metamorphosed Jurassic-Lower Cretaceous cover rocks (Nelson *et al.,* 1980; Kohn *et al.,* 1993; Klepeis *et al.,* 2010). In the study area, pervasively deformed lower greenschist facies, quartz-chlorite schist that form the local basement are hereafter referred to as part of the Cordillera Darwin Metamorphic Complex after the Paleozoic detrital zircon ages, map, and definition of the Cordillera Darwin Metamorphic Complex presented by Hervé *et al.,* (2010).

Granitic plutons and dikes of the Upper Jurassic Darwin suite and intruding basaltic dikes of the Rocas Verdes basin floor intrude the Cordillera Darwin schist and its cover rocks (Nelson *et al.,* 1980; Mukasa & Dalziel, 1996; Calderon *et al.,* 2007; Klepeis *et al.,* 2010). Upper Cretaceous granitic plutons and post-tectonic pegmatite dikes of the Beagle Granite suite crosscut rocks of the Cordillera Darwin, its cover, and all Jurassic intrusive suites (Nelson, *et al.,* 1980; Hervé *et al.,* 1981; 2010; Klepeis *et al.,* 2010).

2.2 ROCAS VERDES BASIN

Middle to Late Jurassic continental extension and crustal thinning of the pre-Jurassic continental crust of southern South America, the Antarctic Peninsula and Africa (Bruhn *et al.,* 1978; Dalziel, 1981; Pankhurst *et al.,* 2000) ultimately resulted in the rifting of Gondwana. Widespread silicic volcanic rocks of the Chon Aike Province (Pankhurst *et al.,* 1998) were deposited from the Middle Jurassic to Late Jurassic and largely reflect magmas resulting from anatexis of continental crust (Pankhurst *et al.,* 2000). Middle-Late Jurassic subaqueous ignimbrite deposits known as the Tobífera

Formation, record volcanism associated with continental rifting and unconformably overlie Paleozoic schist of the Cordillera Darwin and Eastern Andes metamorphic complexes (Figure 1.1; Dalziel and Cortés, 1972; Natland, 1974; Gust *et al.,* 1985; Hanson and Wilson, 1991; Pankhurst *et al.,* 2003).

In southern Patagonia, Late Jurassic mafic metaigneous complexes, known as the Sarmiento and Tortuga complexes (Figure 1.1), include pillow lava, chert and breccia, sheeted dikes, and gabbro. Rocks of the Sarmiento and Tortuga complexes are interpreted as the upper part of an ophiolite sequence that formed at a mid-ocean-ridge-type spreading center along the continental margin of South America and floor the Late Jurassic-Early Cretaceous Rocas Verdes basin (Dalziel, *et al.,* 1974; Dalziel, 1981; Stern & De Wit, 2003; Calderón *et al.,* 2007). Mafic submarine volcanism in the Sarmiento complex began prior to 150 Ma (Calderón *et al.,* 2007). Zircon U/Pb ages from crystal lapilli tuffs in the Tobífera Formation as young as 148 and 142 Ma are reported from outcrops near the Sarmiento complex and indicate silicic ignimbrite volcanism continued into the Berriasian (Early Cretaceous) and was coeval with sea-floor spreading in the Rocas Verdes basin (Calderón *et al.,* 2007). The southern part of the Rocas Verdes basin became a back-arc basin after the onset of magmatism in the southern Patagonian Batholith during Late Cretaceous (see below, Mpodozis and Rojas, 2006).

Late Jurassic and Early Cretaceous sedimentation into the Rocas Verdes basin is recorded by successions of 1000-1200 m-thick deep marine hemipelagic mudstones and shallow water interbedded shale and siltstone known as the Zapata Formation that were deposited conformably on top of the Tobífera Formation and Sarmiento complex (Figure 1.2; Fildani & Hessler, 2005; McAtamney *et al.,* 2011). A 3000 m-thick succession of Jurassic – Upper Cretaceous volcanoclastic turbidites known as the Yaghan Formation filled the Rocas Verdes basin to the south, overlie the Tortuga complex (Suárez *et al.,* 1976) and correlate with the Zapata Formation. In the study area near Seno Otway, Mpodozis *et al.* (2007) and McAtamney *et al.* (2011) report successions of sandy, distal turbidite deposits that overlie the Zapata Formation. They refer to these deposits as the Canal Bertrand Formation (Figure 1.2). Mpodozis *et al.* (2007) report detrital zircon U/Pb

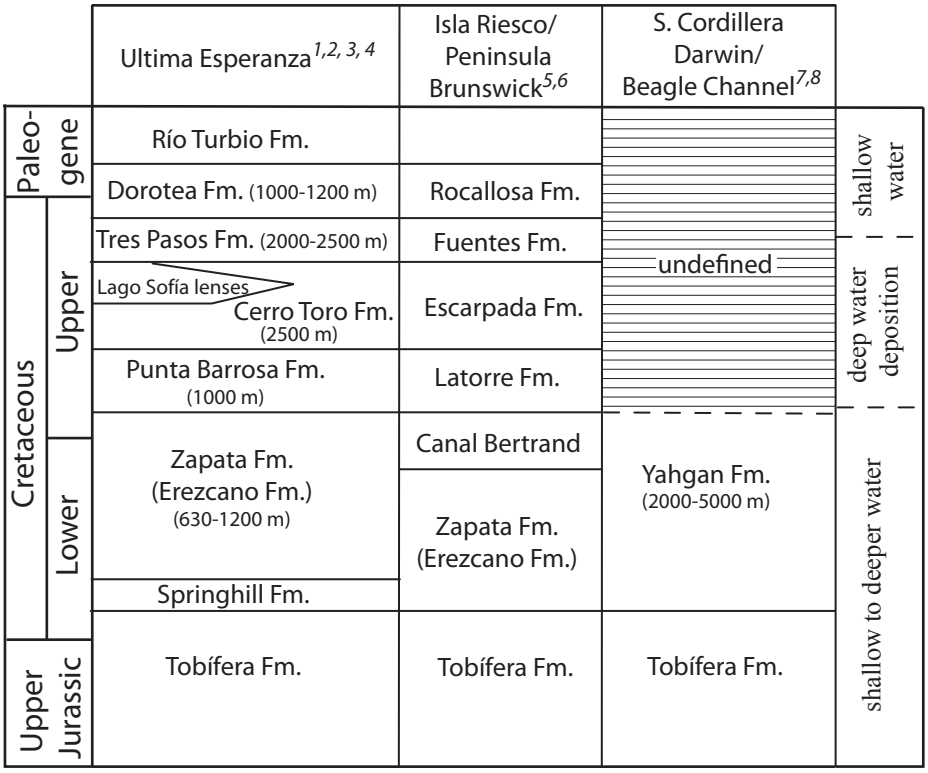

Figure 1.2. Simplified stratigraphic correlations for Upper Jurassic-Lower Paleogene rocks units of the Rocas Verdes and Magallanes basin in Chile modified after McAtameny *et al.* (2011). Data sources: 1, Cortés (1964); 2, Wilson (1991); 3, Fildani and Hessler (2005); 4, Hubbard *et al.* (2008); 5, Castelli *et al.* (1993); 6 Mpodozis *et al.* (2007), 7, Winn (1978); 8, Suárez *et al.* (1985).

ages of ~106-98 Ma from the top of the Canal Bertrand Formation near Seno Skyring that are consistent with 104 Ma U/Pb detrital zircon ages reported by McAtamney *et al*. (2011) from the similar deposits at Seno Otway (Figure 1.1). In the study area, thinly bedded volcanoclastic turbidites of both the Zapata and Canal Bertrand Formations are pervasively deformed and the distinction between the two units is difficult to make in the field, for this reason the units are grouped and hereafter referred to as the Zapata-Canal Bertrand Formation (*c.f*. McAtameny *et al*., 2011). McAtamney *et al*. (2011) demonstrate that the Zapata-Canal Bertrand Formation is between 1000-1500m thick at Seno Otway.

2.3 PATAGONIAN BATHOLITH

The Patagonian Batholith (Figure 1.1) resulted from subduction related magmatism that occurred along the western margin of South America from the Late Jurassic to the Neogene (Hervé *et al*., 1984; Bruce *et al*., 1991; Hervé *et al*., 2007). The oldest pulses of magmatism formed a biomodal suite composed of leucogranite and gabbro between 157 and 145 Ma., contemporaneous with silicic ignimbrite deposits of the Tobífera Formation, the Darwin Granite intrusive suite (Mukasa and Dalziel, 1996) and the mafic igneous complexes that form the floor of the Rocas Verdes basin (Hervé *et al*., 2007; Calderón *et al*., 2007). The batholith is interpreted as the root of a volcanic arc that developed along the western rim of the Rocas Verdes basin in the Late Jurassic (Hervé *et al*., 2007; Fildani and Hessler, 2005) north of the Magallanes Straits, however Mpodozis and Rojas (2006) point out that no evidence exists for a magmatic arc south of Tierra del Fuego until the Late Cretaceous. North of Magallanes Straits near Ultima Esperanza, provenance analyses from sandstones within Upper Jurassic-Lower Cretaceous turbidite deposits of the Zapata Formation contain a volcanic arc signature derived from the Patagonian Batholith and its corresponding volcanic arc, indicating that the turbidites were deposited in a back-arc setting in the northern part of the Rocas Verdes basin (Fildani and Hessler, 2005). By the Early Cretaceous the locus of magmatism shifted to the west, outboard of the Late Jurassic belt, and magmatism

initiated in the southern Patagonian Batholith near Tierra del Fuego (Suárez and Pettigrew, 1976; Fildani & Hessler, 2005; McAtamney *et al.,* 2011). The timing of this shift coincides with the opening of the south Atlantic and the beginning of the closure of the Rocas Verdes basin (Herve *et al.,* 2007). Sedimentation in the Rocas Verdes basin ultimately occurred in a back-arc setting everywhere after the onset of Late Cretaceous magmatism within the southern Patagonian Batholith.

2.4 MAGALLANES FORELAND BASIN

Cretaceous-Neogene crustal shortening was accompanied by the formation of the Magallanes foreland basin (Figure 1.1). In Ultima Esperanza distal turbidite deposits known as the Punta Barrosa Formation conformably overlie the Zapata Formation and were first recognized by Katz (1963) as 'flysch-type' sedimentation related to Late Cretaceous tectonism (Figure 1.2). Subsequent work on the Punta Barrosa Formation confirmed that it marks the onset of thrusting and sedimentation into the Magallanes foreland basin (Biddle *et al.,* 1986; Wilson, 1991) and that this transition occurred at ~92 Ma in Ultima Esperanza (Fildani *et al.,* 2003; Fildani & Hessler, 2005).

In central southern Patagonia near Seno Otway (Figure 1.1), the transition from back-arc to foreland basin sedimentation occurred during the Turonian-Coniacian. Recent detrital zircon studies from medium-bedded turbidite deposits that overlie the Zapata-Canal Bertrand Formation near Seno Otway identify early Coniacian (~89 Ma.) turbidite deposits of the Latorre Formation as the earliest foreland basin sediments in this region (Mpodozis *et al.,* 2007). Sedimentological, provenance, and U/Pb detrital zircon studies by McAtamney *et al.* (2011) confirm that the Latorre Formation represents the first flux of sediments into the Magallanes foreland basin, spanned the time interval from ~106-84 Ma, and is ~1200 m thick near Seno Otway. A thick succession of submarine fan channel-fill conglomerates and turbidite deposits, known as the Escarpada Formation, are interbedded with and conformably overly the top of the Latorre Formation (Figure 1.2; Mpodozis *et al.,* 2007; McAtamney *et al.,* 2011). The top of the Escarpada Formation is not observed in the study area but map patterns presented in this paper indicate that it must be ~1800 m thick. U/Pb detrital zircon populations of ~86 Ma (Mpodozis *et al.,*

2007) and ~81 Ma (McAtamney *et al*., 2011) from the Escarpada Formation indicate that it was deposited from the late Coniacian to the Campanian. The Escarpada Formation correlates along-strike with well documented submarine fan deposits of the Lago Sofía member of the Cerro Toro Formation found in Ultima Esperanza (*e.g*. Scott, 1966; Natland *et al*., 1974; Winn and Dott, 1979; Hubbard *et al*., 2008; Fildani *et al*., 2009; Romans *et al*., 2011; Bernhardt *et al*., 2011).

Slope and shelf-edge deposits (Fuentes Formation) and nearshore estuarine deposits (Rocallosa Formation) overlie the Escarpada Formation near Seno Otway and Seno Skyring in central southern Patagonia (Figure 1.1) and were deposited over the time interval from 84-66 Ma (Mpodozis *et al*., 2007). The Fuentes and Rocallosa Formations are interpreted by Mpodozis *et al*. (2007) as along-strike equivalents of the shallower water slope systems of the Campanian-early Maastrichtian Tres Pasos Formation (Figure 1.2; Biddle *et al*., 1986; Romans *et al*., 2010) and shallow marine and deltaic facies of the Maastrichtian-Danian Dorotea Formation that crop out in Ultima Esperanza (Covault *et al*., 2009). In this study no distinction is made between the Fuentes and Rocallosa Formations due to lack of quality field exposures; instead they are grouped and referred to as the Fuentes/Rocallosa Formation. The Tertiary stratigraphic evolution of the Magallanes foreland basin is poorly known and not exposed in the study area near Seno Otway. However, work to the north in Ultima Esperanza (*e.g*. Fosdick *et al*., 2011) and to the east on Argentine Tierra del Fuego (*e.g*. Olivero & Martinioni, 2001) document continuous syntectonic shallow marine and deltaic sedimentation until the early Miocene (Katz, 1963; Natland *et al*., 1974; Wilson, 1991; Fildani and Hessler, 2005; Hubbard *et al*., 2008; Covault *et al*., 2009; Romans *et al*., 2010, 2011).

2.5 PATAGONIAN FOLD-THRUST BELT

Late Cretaceous crustal shortening closed and inverted the Rocas Verdes basin, leading to the formation of the Patagonian fold-thrust belt and Magallanes foreland basin. The development of the Patagonian thrust belt occurred in two main stages separated by several million years (Klepeis *et al*., 2010). Near the Beagle Channel, the earliest thrusts emplaced the oceanic floor of the Rocas Verdes basin onto the adjacent continental

margin (Dalziel *et al*., 1974; Nelson *et al*., 1980; Klepeis *et al*., 2010; Fosdick, 2011; Calderón *et al*., 2012) and resulted in the underthrusting, thickening and metamorphism of the continental margin to depths ~35 km (Kohn *et al*., 1993; Klepeis *et al*., 2010; Maloney *et al*., 2011). These early thrusts formed prior to ~86 Ma based on U/Pb zircon crystallization ages from cross cutting granitic dikes of the Beagle Suite (Klepeis *et al*., 2010; *c.f*. Mukasa and Dalziel, 1996). In Ultima Esperanza, *in situ* $^{40}Ar/^{39}Ar$ laserprobe chronology from syntectonic phengite in a shear zone at the base of the Sarmiento complex yields an age ca. 85 Ma (Calderón *et al*., 2012).

Near the Beagle Channel, a second stage of thrusting marked by bivergent thick-skinned thrusts cut the early thrusts, uplifting and juxtaposing the high-grade core of the Cordillera Darwin against the nascent fold-thrust belt (Klepeis, 1994a; Mpodozis & Rojas, 2006; Klepeis *et al*., 2010). Exhumation began by the Campanian-Maastrichtian as shown by ~80-60 Ma $^{40}Ar/^{39}Ar$ cooling ages reported by Kohn *et al*. (1995) and pseudosection modeling of aluminosilicate-bearing assemblages that yielded 76.2 ± 1.1 Ma U-Th-Pb ages from synkinematic monazite associated with second generation thrusts in the Cordillera Darwin (Maloney *et al*., 2011). Sandstone provenance and detrital zircon studies of the Upper Cretaceous strata in the Magallanes basin indicate that Jurassic rocks of the Rocas Verdes basin were a significant component of detritus by ~70 Ma (Romans *et al*., 2010) and were the dominant source of detritus by the Eocene (Barbeau *et al*., 2009; Gambosi *et al*., 2009). Klepeis *et al*. (2010) and Maloney *et al*. (2011) argue that the onset of uplift and exhumation of the Cordillera Darwin Metamorphic Complex began in the Maastrichtian (76.2 ± 1.1 Ma after Maloney *et al*., 2011) and culminated in the Paleogene. The Paleogene phase of deformation is coincident in time with an expansion of the Patagonian fold-thrust belt into the foreland basin (Alvarez-Marrón *et al*., 1993; Ghiglione and Ramos, 2005; Ghiglione *et al*., 2010; Fosdick *et al*., 2011).

2.6 NEOGENE STRIKE-SLIP FAULTING

The tectonic setting of the southernmost Andes changed in the Neogene as contraction subsided and left-lateral strike-slip faulting dominated (Cunningham, 1993; Klepeis, 1994b; Klepeis and Austin, 1997; Lodolo *et al.,* 2003; Menichetti *et al.,* 2008). The left-lateral Magallanes-Fagnano fault zone strikes sub-parallel to the trend of the Patagonian fold-thrust belt and defines the current plate boundary between the South American and Scotia Sea plates (Klepeis, 1994b; Klepeis and Austin, 1997; Lodolo *et al.,* 2003). Motion along this fault zone is slow (~0.5 cm/yr, Del Cogliano *et al.,* 2000; 6.6 ± 1.3 mm/yr, Smalley *et al.*, 2007) and accounts for ~40 km displacement (Klepeis, 1994b; Lodolo *et al.,* 2003) near Lago Fagnano. Several left-lateral fault segments are linked by en echelon arrays that form either pull-apart basins or restraining bends, depending on the geometry of the fault segments (see Lodolo *et al.,* 2003; Menichetti *et al.,* 2008 for a review).

3. Methodology

Geologic maps and eight strike-perpendicular cross sections were constructed from surface geological data and are presented in this paper (Plate 1; locations in Figure 1.2). From these eight sections, three serial, strike-perpendicular, line-balanced and incrementally restored cross-sections were constructed using line and area balancing techniques to provide a quasi-three-dimensional reconstruction of the fold-thrust belt (Dalstrom, 1969; Marshak & Mitra. 1998). Structural analyses of deformed rocks in the field and in thin sections were conducted to confirm the sense of shear of faults and related folds in the thrust belt. The structural modeling software *LithoTect*™ was used to model the depth and dip of décollement for second-generation thrusts where surface geologic data did not provide adequate control. Otherwise, all décollement levels, dips and structures drawn in cross section are projections of surface geological data coupled with stratigraphic constraints.

4. Results

The field area is divided into four geological domains (Figure 1.3): 1) The Patagonian Batholith and Rocas Verdes basin terrane are best preserved in the northwestern part of the study area where the mafic floor of the Rocas Verdes basin is thrust on top of rocks of the Tobífera Formation and Zapata-Canal Bertrand Formation. 2) Structurally below the Rocas Verdes basin rocks and trending southeast along-strike, the pre-Jurassic schist of Cordillera Darwin Metamorphic Complex is exposed in the hanging wall of a reverse fault that cuts earlier structures in the fold-thrust belt and is continuous along-strike for ~80 km. 3) In the footwall of this fault, Jurassic rocks of the Tobífera and Zapata-Canal Bertrand Formations are imbricated with Cretaceous synorogenic sediments of the Magallanes foreland basin. A major décollement (defined below) is contained within the Zapata-Canal Bertrand Formation and is exposed along-strike for >100 km. 4) Cretaceous-Paleogene Magallanes foreland basin sedimentary rocks are exposed in the northeast of the study area (Figure 1.3). Mapping results, structural analyses, and cross-section are presented below from northwest to southeast along-strike across the study area. Plate 1 shows the geologic map and cross sections at 1:100,000 scale.

4.1 Patagonian Batholith and Rocas Verdes Terrane

Seno Condor (Figure 1.4), in the western most part of the study area, preserves exposures of the contact between the Patagonian Batholith and mafic rocks of the Rocas Verdes basin floor (Figure 1.3, 1.4). Felsic intrusive rocks, including granodiorite, tonalite and diorite that lack any foliation, crop out on the southern shore of Seno Condor and are interpreted to form part of the Southern Patagonian Batholith (Figure 1.4, 1.5a). The northern shore exposes gabbro and porphyritic basalt comprised of plagioclase, hornblende, clinopyroxene and olivine that is commonly altered to chlorite and actinolite. Along the northeast shore of Seno Condor and the southeast shore of Canal Jeronimo

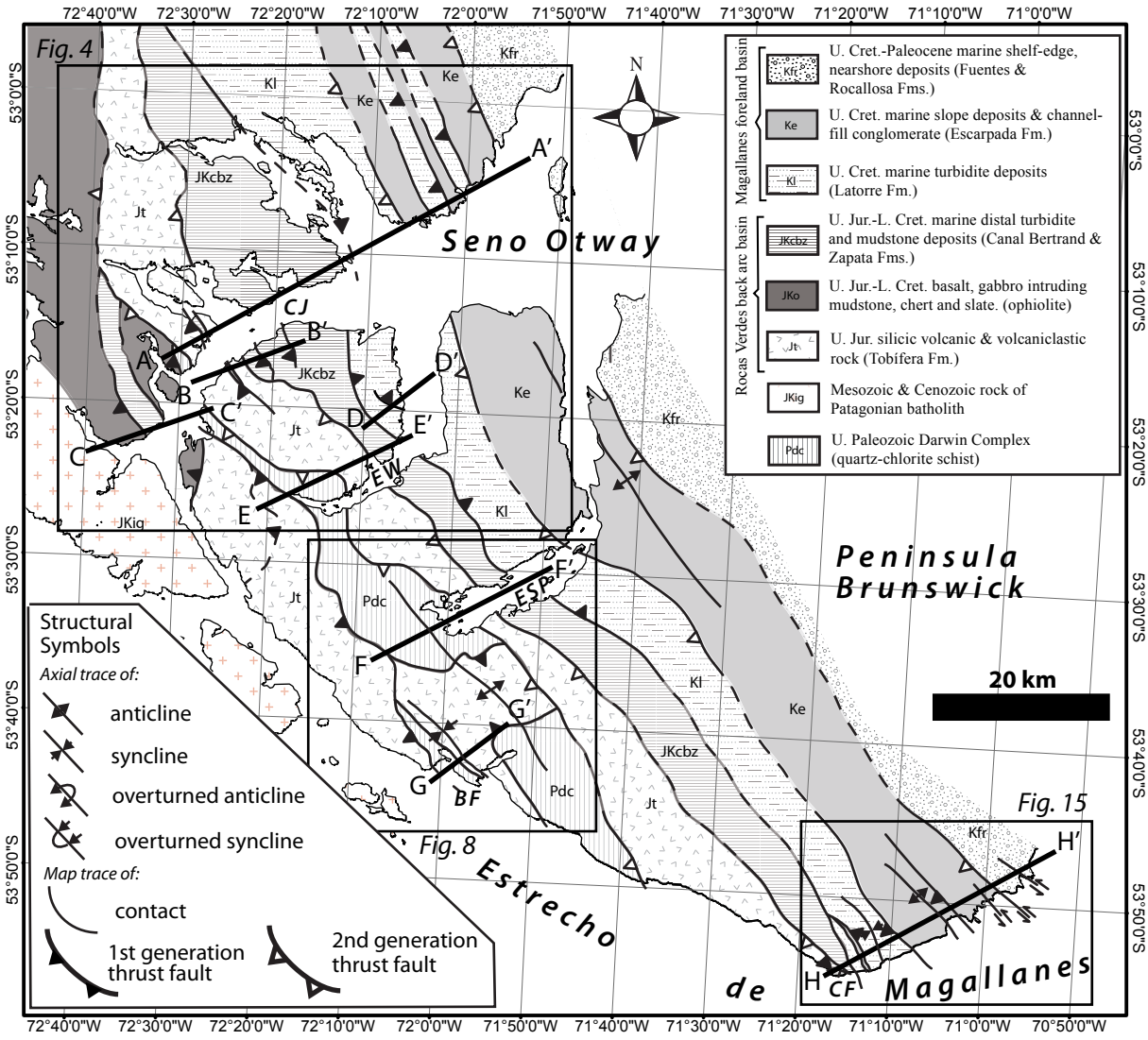

Figure 1.3. Geologic map of Seno Otway and Peninsula Brunswick constructed from data collected in this study. Unit names for Cretaceous sedimentary strata are from Castielli *et al.* (1993) and Mpodozis *et al.* (2007). The locations of figures 3, 7 and 14 are shown as well as the locations of cross section lines A-H. CJ, Canal Jeronimo; EW, Estuario Wickham; ESP, Estuario Silva Palma; BF, Bahía Fortesque; CF, Cabo Froward.

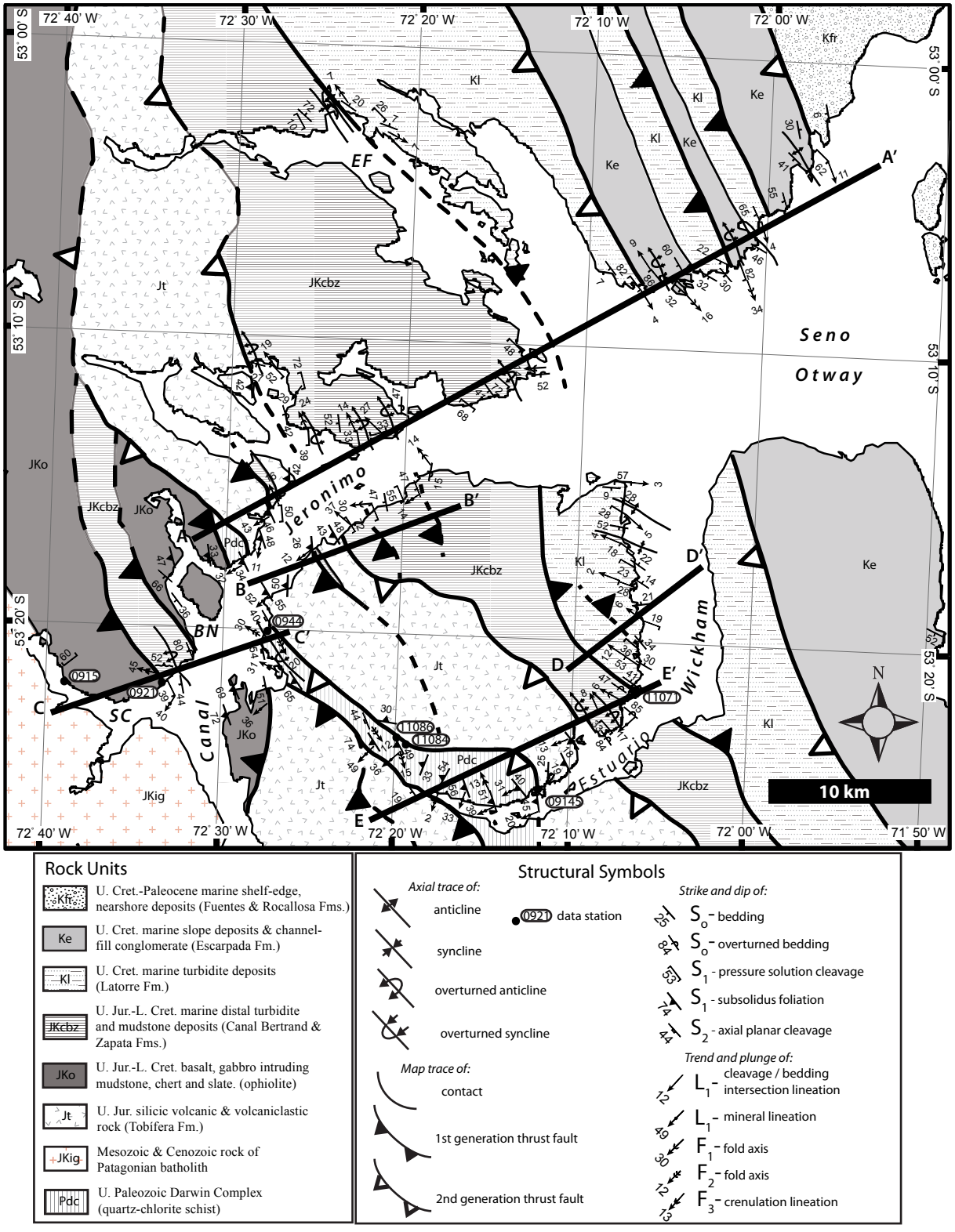

Rock Units

- Kfr — U. Cret.-Paleocene marine shelf-edge, nearshore deposits (Fuentes & Rocallosa Fms.)
- Ke — U. Cret. marine slope deposits & channel-fill conglomerate (Escarpada Fm.)
- Kl — U. Cret. marine turbidite deposits (Latorre Fm.)
- JKcbz — U. Jur.-L. Cret. marine distal turbidite and mudstone deposits (Canal Bertrand & Zapata Fms.)
- JKo — U. Jur.-L. Cret. basalt, gabbro intruding mudstone, chert and slate. (ophiolite)
- Jt — U. Jur. silicic volcanic & volcaniclastic rock (Tobífera Fm.)
- JKig — Mesozoic & Cenozoic rock of Patagonian batholith
- Pdc — U. Paleozoic Darwin Complex (quartz-chlorite schist)

Structural Symbols

Axial trace of:
- anticline
- syncline
- overturned anticline
- overturned syncline

Map trace of:
- contact
- 1st generation thrust fault
- 2nd generation thrust fault

0921 data station

Strike and dip of:
- S_o - bedding
- S_o - overturned bedding
- S_1 - pressure solution cleavage
- S_1 - subsolidus foliation
- S_2 - axial planar cleavage

Trend and plunge of:
- L_1 - cleavage / bedding intersection lineation
- L_1 - mineral lineation
- F_1 - fold axis
- F_2 - fold axis
- F_3 - crenulation lineation

Figure 1.4. Geologic map of Canal Jeronimo, Seno Otway and Estuario Wickham showing data collected during this study. Black dots and corresponding numbers refer to data stations mentioned in text. Data collected at 1:50,000 scale. SC, Seno Condor; BN, Brazo Nuñez; EF, Estuario Fanny.

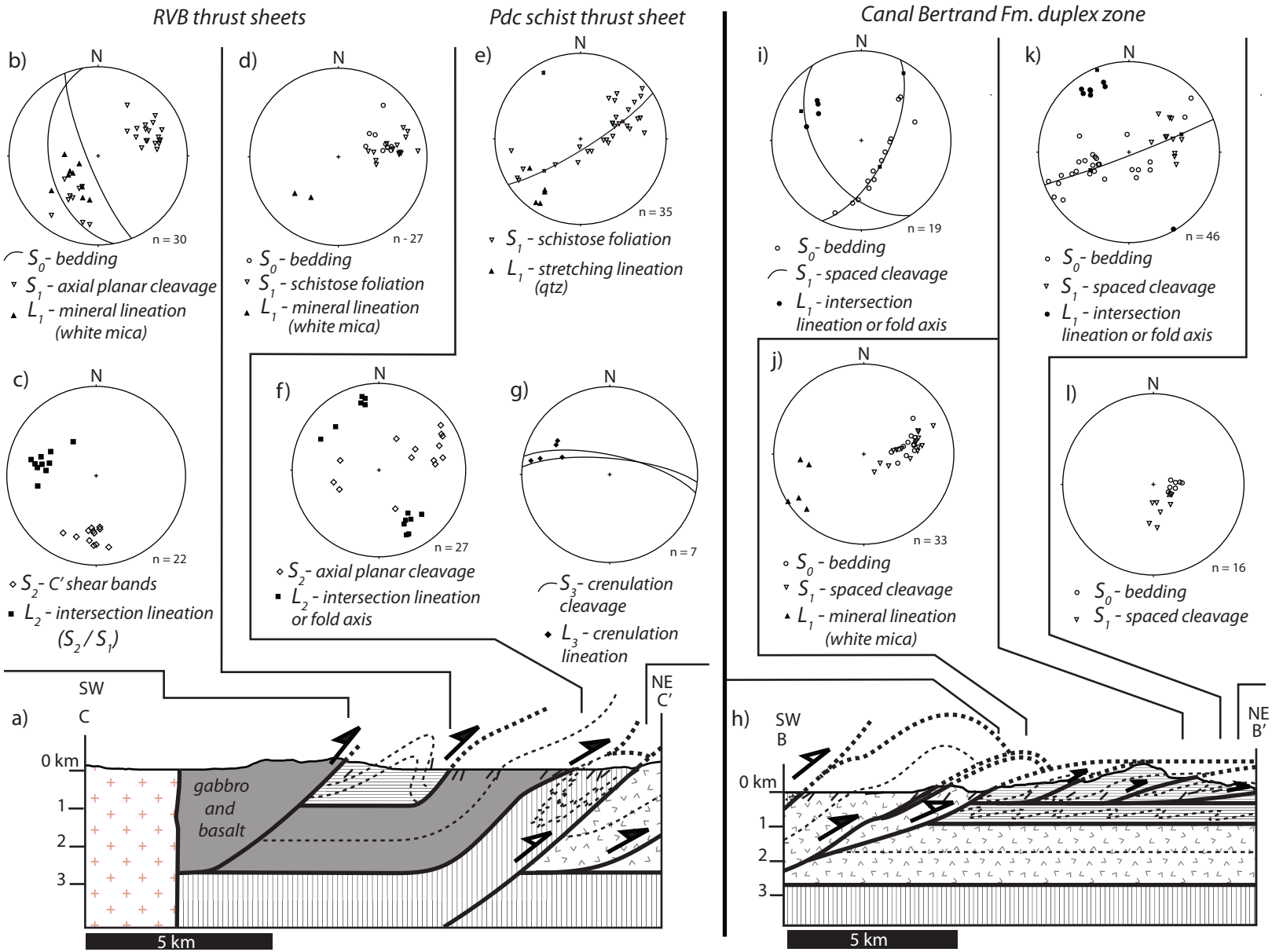
RVB thrust sheets
Pdc schist thrust sheet
Canal Bertrand Fm. duplex zone
b)
N
n = 30
S_0 - bedding
S_1 - axial planar cleavage
L_1 - mineral lineation (white mica)
d)
N
n - 27
S_0 - bedding
S_1 - schistose foliation
L_1 - mineral lineation (white mica)
e)
N
n = 35
S_1 - schistose foliation
L_1 - stretching lineation (qtz)
i)
N
n = 19
S_0 - bedding
S_1 - spaced cleavage
L_1 - intersection lineation or fold axis
k)
N
n = 46
S_0 - bedding
S_1 - spaced cleavage
L_1 - intersection lineation or fold axis
c)
N
n = 22
S_2 - C' shear bands
L_2 - intersection lineation (S_2 / S_1)
f)
N
n = 27
S_2 - axial planar cleavage
L_2 - intersection lineation or fold axis
g)
N
n = 7
S_3 - crenulation cleavage
L_3 - crenulation lineation
j)
N
n = 33
S_0 - bedding
S_1 - spaced cleavage
L_1 - mineral lineation (white mica)
l)
N
n = 16
S_0 - bedding
S_1 - spaced cleavage
a)
SW
C
NE
C'
0 km
1
2
3
gabbro and basalt
5 km
h)
SW
B
NE
B'
0 km
1
2
3
5 km

Figure 1.5

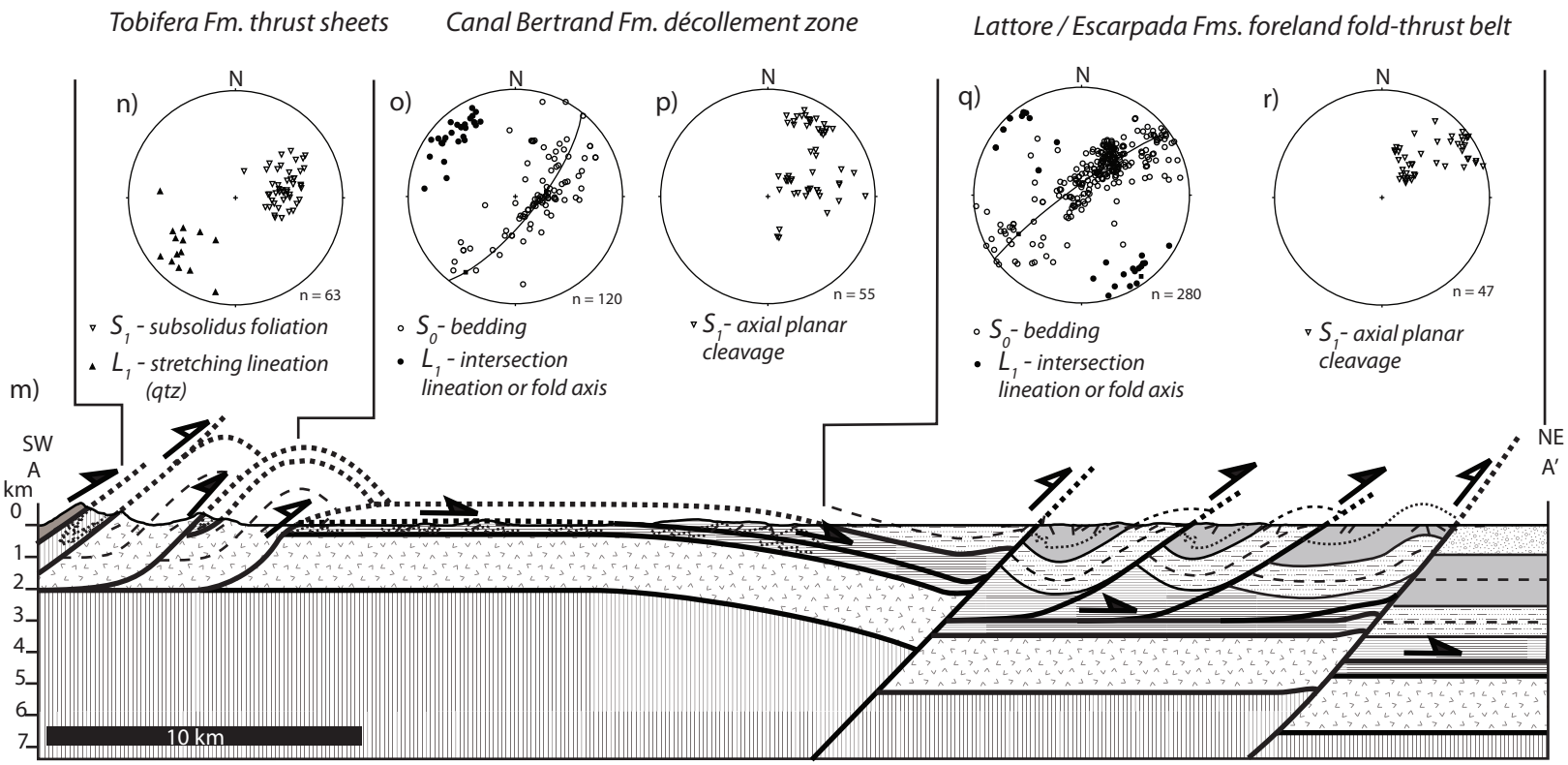
Tobifera Fm. thrust sheets
Canal Bertrand Fm. décollement zone
Lattore / Escarpada Fms. foreland fold-thrust belt
n)
o)
p)
q)
r)
N
n = 63
n = 120
n = 55
n = 280
n = 47
S1 - subsolidus foliation
L1 - stretching lineation (qtz)
S0 - bedding
L1 - intersection lineation or fold axis
S1 - axial planar cleavage
S0 - bedding
L1 - intersection lineation or fold axis
S1 - axial planar cleavage
m)
SW
A
NE
A'
km
0
1
2
3
4
5
6
7
10 km

Figure 1.5

Figure 1.5. Cross sections and structural data from Canal Jeronimo and Seno Otway. See figure 1.4 for cross section locations. (a) Cross section from C-C'. (b) Stereograms showing structural data from the Rocas Verdes basin terrane (b-d) and Cordillera Darwin Metamorphic Complex (e-g). (h) Cross section from B-B'. (i-l) Stereograms showing structural data from the Zapata-Canal Bertrand duplex. (m) Cross section from A-A'. Stereograms showing structural data from three structural domains: (n) the Tobífera Fm., (o-p) the Zapata-Canal Bertrand décollement, and (q-r) the foreland fold-thrust belt. All stereograms hereafter are equal-area stereographic projections. Planar data are represented as poles (white symbols) unless otherwise plotted as great circles. Linear data are represented with black symbols. Great circles through girdles are cylindrical best fits to data.

interlayered massive gabbro and porphyritic basalt crop out. These units generally either lack or display a poorly developed subsolidus foliation that dips steeply toward the southwest. The contact between the felsic rocks of the Patagonian Batholith and gabbro and porphyritic basalt is exposed at site 0915 (Figure 1.4) where it is an igneous contact characterized by co-magmatic textures between a crosscutting plagiogranite dike and olivine-bearing gabbro (Figure 1.6a). Zircon U/Pb dating reported by McAtamney *et al.* (2011) yield a crystallization age of 154.3 ± 1.6 Ma. for the plagiogranite dike, indicating a Late Jurassic emplacement age for the dike and probably a similar age for the gabbroic host based on the textural relationship. On the basis of their age and field context, I interpret the mafic intrusive suites as the gabbro and sheeted dike part of the mafic floor of the Rocas Verdes basin, similar to the ophiolitic sequence described near the Beagle Channel by Cunningham (1994).

Site 0921 (Figure 1.4) exposes a tectonic contact where massive gabbro and basalt of the Rocas Verdes basin rocks are thrust on top of thinly bedded turbidite deposits interpreted to be the Zapata-Canal Bertrand Formation. In the footwall, turbiditic rocks are deformed and folded into a top-northeast overturned anticline (Figure 1.5a). Near the contact, the turbidite deposits are sheared and contain a moderately southwest-dipping spaced cleavage (S_1) that is subparallel to bedding (S_0) on the right-side-up limb of the fold. North-dipping C' shear bands, northwest- to west-northwest-trending intersection lineations between shear bands and spaced cleavages, and a southwest-trending white mica mineral lineation (L_1) that occurs on cleavage surfaces, all show a top-northeast thrust sense of shear (Figure 1.5b, c). Approximately 2 km toward the northeast near the mouth of Brazo Nuñez (location on Figure 1.4), bedding in the turbidite deposits is overturned-to-the-northeast and dips more steeply than the spaced cleavage (S_1) indicating the overturned limb of the regional anticline.

Brazo Nuñez exposes serpentinized and chloritized gabbro and basalt similar to those discussed above. Along the southwest shore of Brazo Nuñez, quartzite, slate containing chert nodules and basaltic sills are interbedded and overlie serpentinized gabbro. Here, bedding dips moderately to the southwest and is right way up

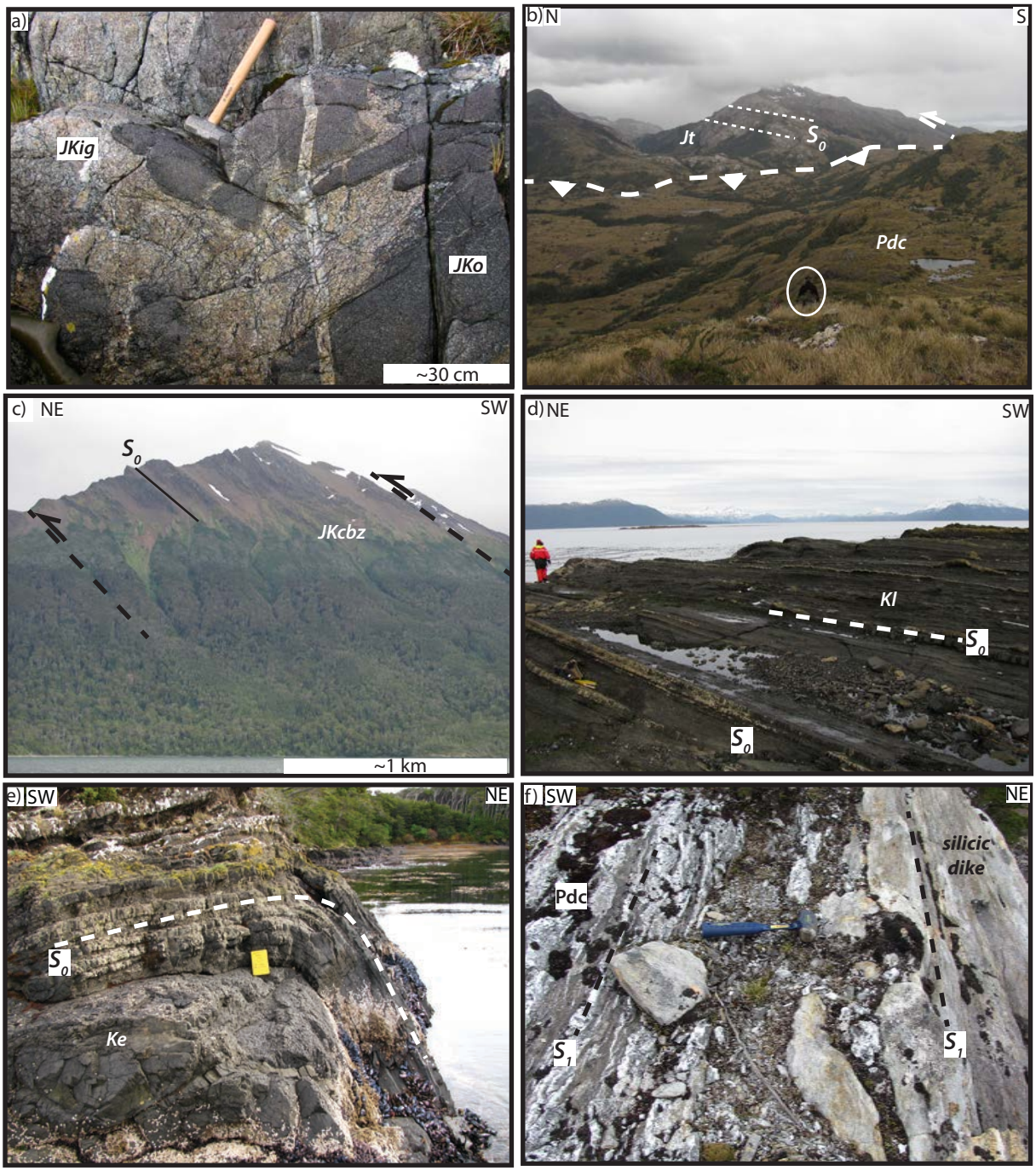

Figure 1.6. Photographs of (a) plagiogranite dike intruding olivine-bearing gabbro at Seno Condor, (b) view looking northeast from site 11086 at a second-generation basement-involved fault, person for scale, (c) view looking southeast from Canal Jeronimo at the Zapata-Canal Bertrand duplex, (d) strata of the Latorre Fm. dipping homoclinally southwest on the long limb of a regional fold near Seno Otway, person for scale, (e) strata of the Escarpada Fm. forming northeast-vergent closed folds on the short limb of a regional fold near Seno Otway, and (f) silicic dike that intrudes the Cordillera Darwin Metamorphic Complex near site 11086 and displays a schistose foliation that is coplanar with S_1 in the Cordillera Darwin Metamorphic Complex, sledge hammer for scale.

(Figure 1.5d), in contrast to the overturned beds of the Zapata-Canal Bertrand Formation on the southwest side of the contact. Near the contact on the southwest shore of Brazo Nuñez, metepelitic layers display a southwest-dipping schistose foliation that contains a southwest-plunging white-mica lineation (Figure 1.5d). Here, the contact is not exposed but I interpret the interbedded quartzites, chert bearing slate, and basaltic sills as the upper part of the Rocas Verdes basin oceanic floor that was overlain by deep marine turbidite deposits of the Zapata-Canal Bertrand Formation. The depositional contact is sheared and forms a thrust-flat, the turbidite deposits are deformed above the contact.

Near the northeastern entry to Brazo Nuñez, rocks of the Rocas Verdes basin ocean floor are thrust above quartz-chlorite schist of the Cordillera Darwin Metamorphic Complex. In the footwall, the schist is pervasively deformed by several generations of structures that are discussed below. These rocks are juxtaposed against the Jurassic ignimbrite deposits of the Tobífera Formation along a southwest-dipping, second generation reverse fault. This fault is best observed in the valley between Canal Jeronimo and the southern end of Estuario Wickham near site 11086 (Figure 1.4, 1.5a, 1.6b). Cross-section C-C' (Figure 1.4, 1.5a) displays the structure of the Rocas Verdes basin terrane exposed in the study area and overlaps slightly with the southwestern ends of sections B-B' and A-A'.

4.2 Structure of Canal Jeronimo and Seno Otway: Duplexes and Décollements

Along Canal Jeronimo to the north of the second-generation basement-involved fault, the Tobífera Formation crops-out on both shores and is imbricated, forming a hinterland-dipping duplex (Figure 1.5h, m). Here, the Tobífera Formation dips moderately toward the southwest and displays a poorly developed schistose foliation defined by the alignment of white mica and quartz (S_1). A southwest-plunging recrystallized quartz stretching lineation occurs on S_1 surfaces (Figure 1.5n). Rigid feldspar porphyroclasts have asymmetric recrystallized quartz and mica tails that indicate top-northeast sense of shear. The top of the formation is exposed on the north side of Canal Jeronimo where ignimbrite deposits and ash beds of the Tobífera Formation are

interbedded with deep marine shale of the Zapata-Canal Bertrand Formation. The base of the Tobífera Formation is sheared and displays a well-defined schistose foliation where it is thrust on top of the Zapata-Canal Bertrand Formation. Map patterns indicate the Tobífera Formation must be at least 1800 m thick. Hanging-wall cutoffs are eroded and not exposed in the study area.

Toward the northeast, the Zapata-Canal Bertrand Formation crops out along the southeast shore of Canal Jeronimo (Figure 1.4, section B-B'). Here strata of the Zapata-Canal Bertrand Formation are imbricated by two thrust faults to form a hinterland-dipping duplex (Figure 1.5h, 1.6c). Strata dip homoclinally toward the west to west-southwest (Figure 1.5j, l), except in the footwall of the faults where they are folded into northeast-vergent overturned tight folds (F_1) that plunge gently toward the northwest (Figure 1.5h-i, k). The formation displays a well-developed spaced cleavage (S_1) that is axial-planar to F_1 folds. A southwest-plunging white-mica lineation occurs on S_1 surfaces (Figures 1.5j). Microscopically, well-developed pressure solution seams are subparallel to bedding and form calcite and white-mica pressure shadows around quartz and feldspar clasts. The southern contact with the Tobífera Formation is defined by a second-generation thrust that cuts the earlier structures that form duplex in the Zapata-Canal Bertrand Formation (Figure 1.4, 1.5h).

On the north shore of Canal Jeronimo, the Zapata-Canal Bertrand Formation crops out for 15 km to the northeast of the Tobífera Formation along transect A-A' (Figure 1.4, 1.5m). Here it is pervasively deformed by a series of tight to isoclinal northeast vergent, inclined to recumbent overturned folds (F_1) that fold bedding (S_0) and have ~1 m wavelengths (Figure 1.5o, 1.7a-d). A well-developed spaced cleavage (S_1) is axial-planar to the folds (Figure 1.7a-f). Subhorizontal fold axes trend northeast-southwest and are parallel to cleavage-bedding intersection lineations (Figure 1.5o). Spaced cleavages that are axial planar to F_1 folds occupy two dominant orientations, either moderately-dipping southwest where F_1 folds are inclined (Figures 5p, 1.7a-d) or shallowly-dipping west-southwest where F_1 folds are recumbent (Figures 1.5p, 1.7e-f).

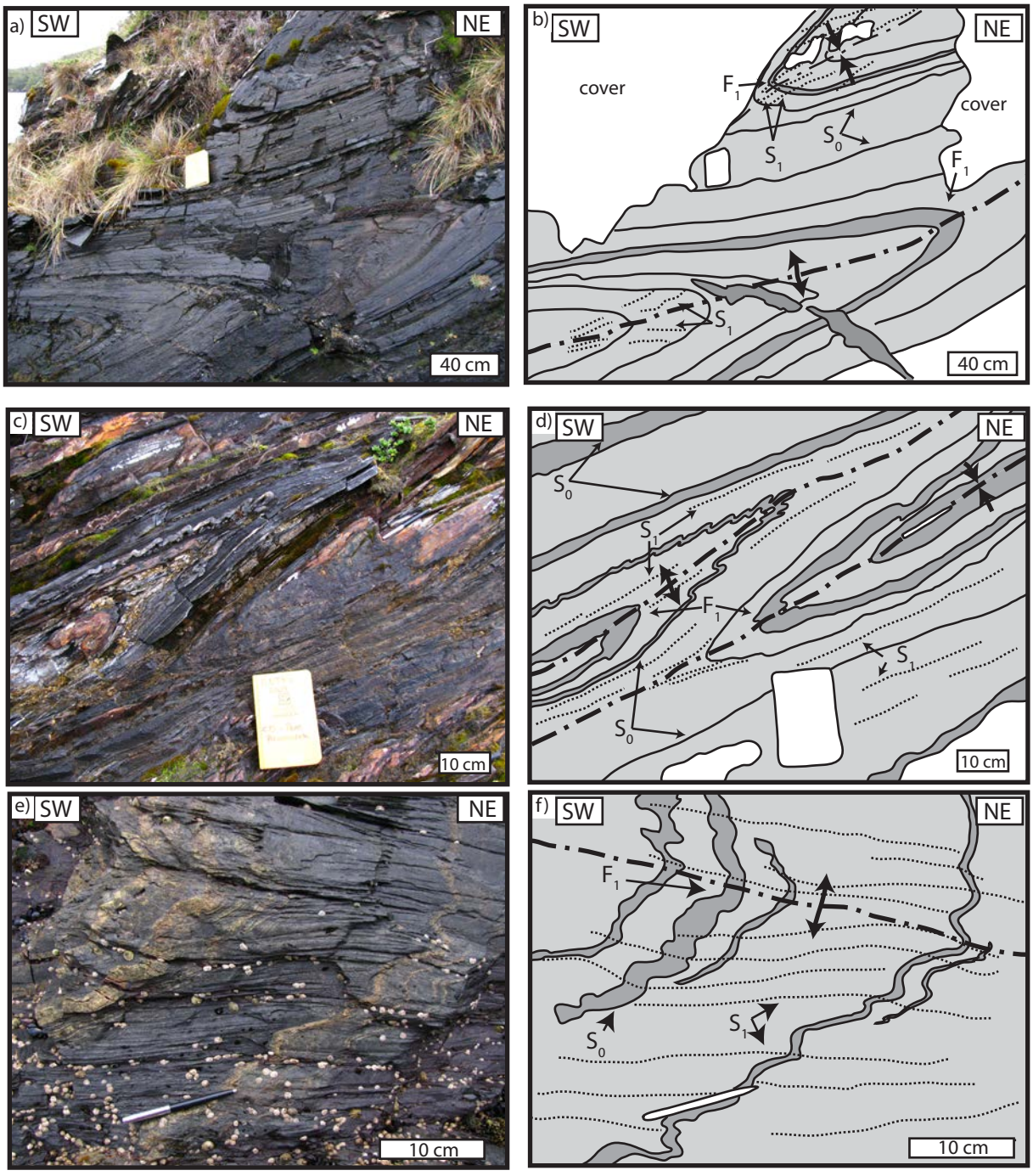

Figure 1.7. (a-f) Photographs and corresponding outcrop sketches of structures that define the Zapata-Canal Bertrand décollement zone along section A-A' near Canal Jeronimo and Seno Otway. Bedding is folded forming northeast-vergent, overturned, steeply inclined to recumbent tight folds. A prominent spaced cleavage forms axial planar to folds. Dark-grey shading indicates silt-sandstone. Light-grey shading indicates mudstone. Pencil or field book for scale.

This change in orientation indicates that S_1 is gently refolded by open folds (F_2). These F_2 folds are coaxial with F_1 and have long (~2 km) wavelengths based on the map pattern. Along transect A-A' northeast of the thrust uplifting the Tobífera Formation, the train of tight to isoclinal folds is continuous for ~15 km to the mouth of Estuario Fanny (Figure 1.4). There, F_1 folds open and their wavelengths increase to ~2-5 m, indicating qualitatively lower strain than toward the southwest and down-section. Thus the train of tight to isoclinal folds defines a shear zone at the base of the Zapata-Canal Bertrand Formation (Figure 1.5m). This shear zone is important because it is the basal décollement of the Magallanes fold-thrust belt (discussed below).

4.3 Structure of the Magallanes fold-thrust belt near Seno Otway

The basal member of the Latorre Formation is exposed on the north shore of Estuario Fanny where it dips shallowly toward the north and is gently folded into open folds with wavelengths >100 m (Figure 1.4, 1.5m). The contact between the Zapata-Canal Bertrand Formation and overlying Latorre Formation is not well exposed in Estuario Fanny, however, to the south of the contact in Estuario Fanny, inclined, overturned folds deform the Zapata-Canal Bertrand Formation indicating that the contact is either an angular unconformity or a fault. I map the contact here as a north-dipping top-southwest thrust fault on the basis of field relationships exposed on Estuario Wickham that are discussed below.

Along transect A-A' toward the north, the Latorre Formation is folded into an open syncline that is truncated by a southwest-dipping reverse fault. The fault juxtaposes the Latorre Formation in the hanging wall against strata of the Escarpada Formation in the footwall. This fault is inferred to be basement involved because of a change in stratigraphic level across the fault; northeast of this structure, sea-level exposures do not return to the level of the Zapata-Canal Bertrand Formation (Figure 1.4, 1.5m). In the footwall, strata of the Escarpada Formation conformably overlie the Latorre Formation, and both formations are imbricated by two first generation thrust faults that dip southwest and sole into a décollement at the level of the Zapata-Canal Bertrand Formation (Figure 1.4, 1.5m). The Latorre Formation is exposed along long limbs of regional folds that dip

homoclinally toward the southwest and probably reflect hanging-wall thrust flats over footwall ramps (Figure 1.5m, 1.6d). On short northeast-dipping limbs of regional folds, strata of the Escarpada Formation (S_0) are folded by tight, northeast-vergent folds (F_1) with horizontal northwest-southeast-trending fold axes and moderately inclined southwest-dipping axial planar cleavages (S_1) (Figure 1.5q, r; 1.6e). Hanging wall cutoffs are eroded and not exposed in the study area.

At the northeastern end of transect A-A', strata of the Latorre and Escarpada Formations are juxtaposed against Maastrichtian strata of the Fuentes/Rocallosa Formation along a second-generation basement-involved reverse fault (Figure 1.4, 1.5m). In the footwall, strata of the Fuentes/Rocallosa Formation are flat lying and not deformed. Northeast of the section line the bedrock geology is covered by Quaternary glacial sediment, and no exposures are present.

4.4 Structure of Estuario Wickham and Estuario Silva Palma: Triangle Zone and Passive-Roof Thrust

Structural and stratigraphic contacts exposed along Canal Jeronimo can be traced for more than 40 km along-strike to Estuario Wickham (Figure 1.3, 1.4) and Estuario Silva Palma (Figure 1.3, 1.8). The basement-involved reverse fault mapped near site 0944 in Canal Jeronimo crops out in Estuario Wickham near site 09145 (Figure 1.4) and Estuario Silva Palma near site 11055 (Figure 1.8). In the hanging wall, the Paleozoic greenschist of the Cordillera Darwin Metamorphic Complex and overlying Tobífera Formation are thrust on top of imbricated strata of the Tobífera and Zapata-Canal Bertrand Formations in the footwall. Strata of the Tobífera Formation are exposed in a valley at the southwestern end of Estuario Wickham where they overlie the Paleozoic schist (Figure 1.4). Here the contact is sheared, characterized by a southwest-dipping schistose foliation defined by white mica and quartz alignment (Figure 1.9a, b). Although inaccessible, the Tobífera Formation was observed from a distance to overlie the Cordillera Darwin Metamorphic Complex in the ridges to the southwest of Estuario Silva Palma, where I infer that the contact is also sheared (Figure 1.8). In both Estuarios Wickham and Silva Palma, basement schist is pervasively deformed by several

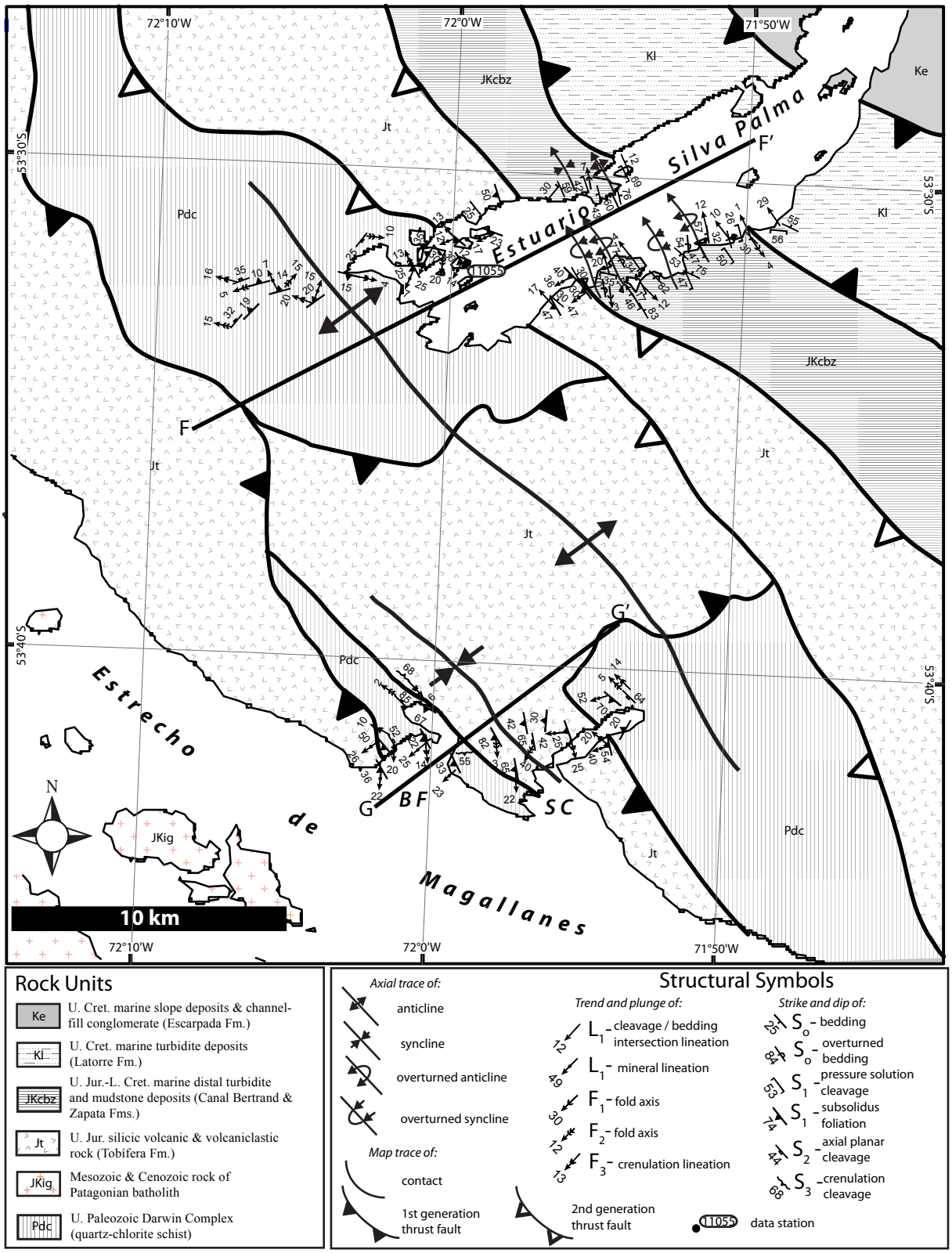

Figure 1.8. Geologic map of Estuario Silva Palma, Bahía Fortesque and Seno Cordes showing data collected during this study. Black dot and corresponding number refers to data station mentioned in text. Data collected at 1:50,000 scale. BF, Bahía Fortesque; SC, Seno Condor.

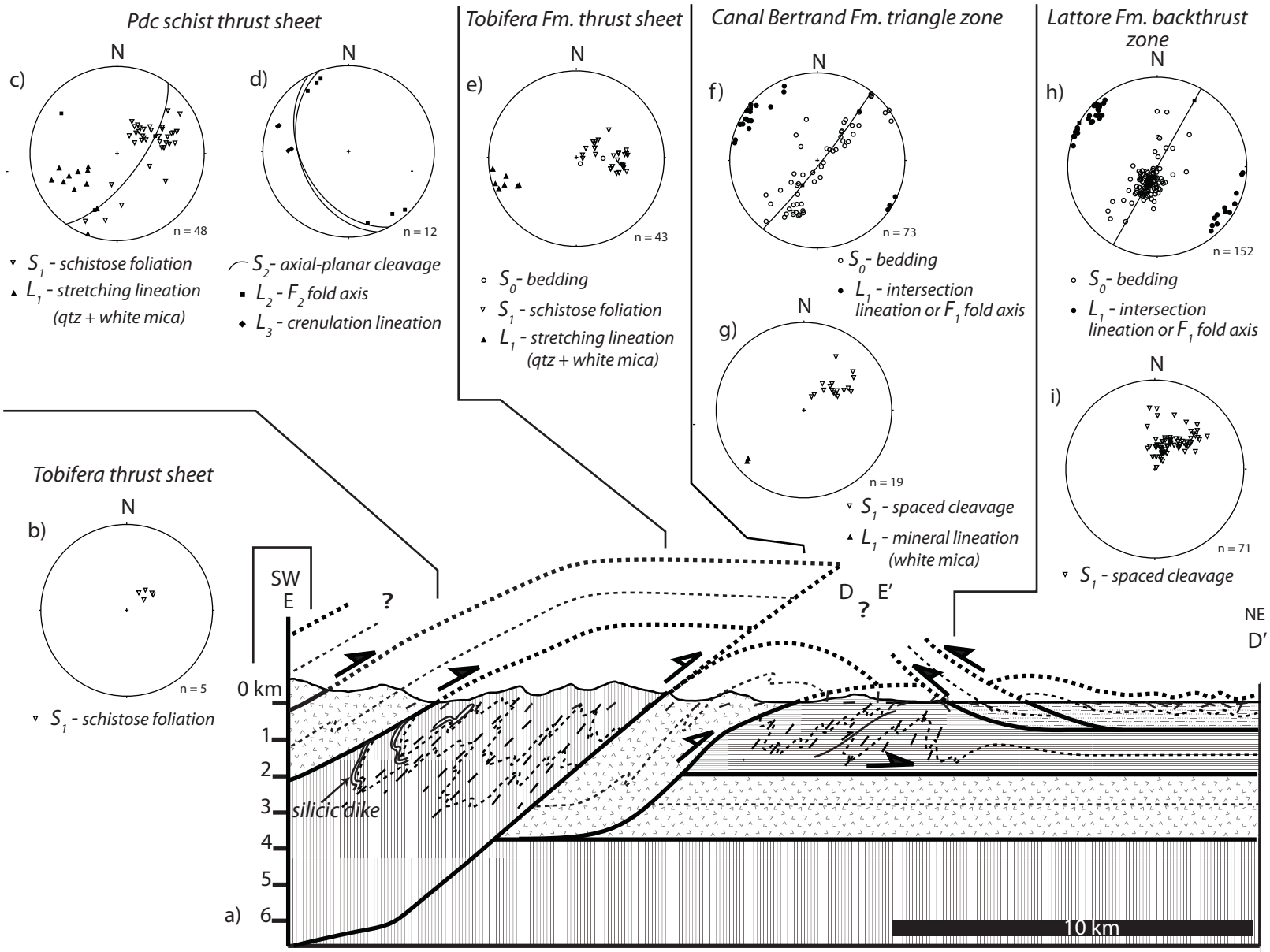
Pdc schist thrust sheet
c)
N
n = 48
S_1 - schistose foliation
L_1 - stretching lineation (qtz + white mica)
d)
N
n = 12
S_2 - axial-planar cleavage
L_2 - F_2 fold axis
L_3 - crenulation lineation
Tobifera Fm. thrust sheet
e)
N
n = 43
S_0 - bedding
S_1 - schistose foliation
L_1 - stretching lineation (qtz + white mica)
Canal Bertrand Fm. triangle zone
f)
N
n = 73
S_0 - bedding
L_1 - intersection lineation or F_1 fold axis
g)
N
n = 19
S_1 - spaced cleavage
L_1 - mineral lineation (white mica)
Lattore Fm. backthrust zone
h)
N
n = 152
S_0 - bedding
L_1 - intersection lineation or F_1 fold axis
i)
N
n = 71
S_1 - spaced cleavage
Tobifera thrust sheet
b)
N
n = 5
S_1 - schistose foliation
SW
E
?
D
E′
?
NE
D′
0 km
1
2
3
4
5
a)
6
silicic dike
10 km

Figure 1.9

Figure 1.9. Cross-section and structural data from Estuario Wickham. (a) Composite cross section from E-E' and D-D', see figure 1.4 for location. Short-dashed lines show schematic trace of bedding, long-dashed lines show trace of axial-planar cleavage. Stereograms of structural data from four structural domains: (b,e) the Tobífera Fm., (c-d) the Cordillera Darwin Metamorphic Complex, (f-g) the Zapata-Canal Bertrand triangle zone, and (h-i) the Latorre back thrust.

generations of folds that do not affect the Tobífera Formation or overlying strata (discussed below). In all locations, the basement-involved reverse fault truncates the Tobífera Formation and associated duplex structures that occur in the footwall (discussed below), indicating that it is a second-generation fault relative to the duplex structures (Figure 1.5a, m, 1.9a, 1.10a).

In the footwall of the basement-involved reverse fault, strata of the Tobífera Formation crop out everywhere in the study area. In both Estuarios Wickham and Silva Palma, the Tobífera Formation is not imbricated as near Canal Jeronimo to the north, but instead is folded. Bedding is difficult to distinguish, but in Estuario Silva Palma it is observed folded by mesoscale (~3m wavelength) tight, northeast-vergent asymmetric folds with a northwest-plunging fold axis (Figure 1.10e). A prominent schistose foliation defined by the alignment of white-mica and quartz is axial planar to these folds, dips southwest, and contains a southwest-plunging quartz and white-mica stretching lineation. In both locations the foliation is subparallel to bedding along the limbs of the folds, indicating tight folds (Figure 1.9e).

Everywhere in the study area within the footwall of the basement-involved reverse fault, the Tobífera Formation is thrust on top of the Zapata-Canal Bertrand Formation. The thrust can be traced for ~100 km along strike from Canal Jeronimo to exposures near Cabo Froward (Figure 1.3). It is best exposed in Estuario Silva Palma where it is a shallowly southwest-dipping thrust fault (Figure 1.11a). In the footwall, the Zapata-Canal Bertrand Formation is pervasively deformed. Tight northeast-vergent inclined folds (F_1) that have northwest- and southeast-trending subhorizontal fold axes fold bedding (S_0). A southwest-dipping spaced cleavage (S_1) is axial planar to F_1 folds, and its intersection with bedding forms a prominent intersection lineation that is parallel to F_1 fold axes. In some outcrops a poorly developed white mica lineation plunges southwest on S_1 surfaces (Figure 1.9f, g; 1.10f, g; 1.11b). Microscopically, well-developed pressure solution seams are subparallel to bedding and form calcite, chlorite and white-mica pressure shadows around quartz and feldspar clasts. In close proximity

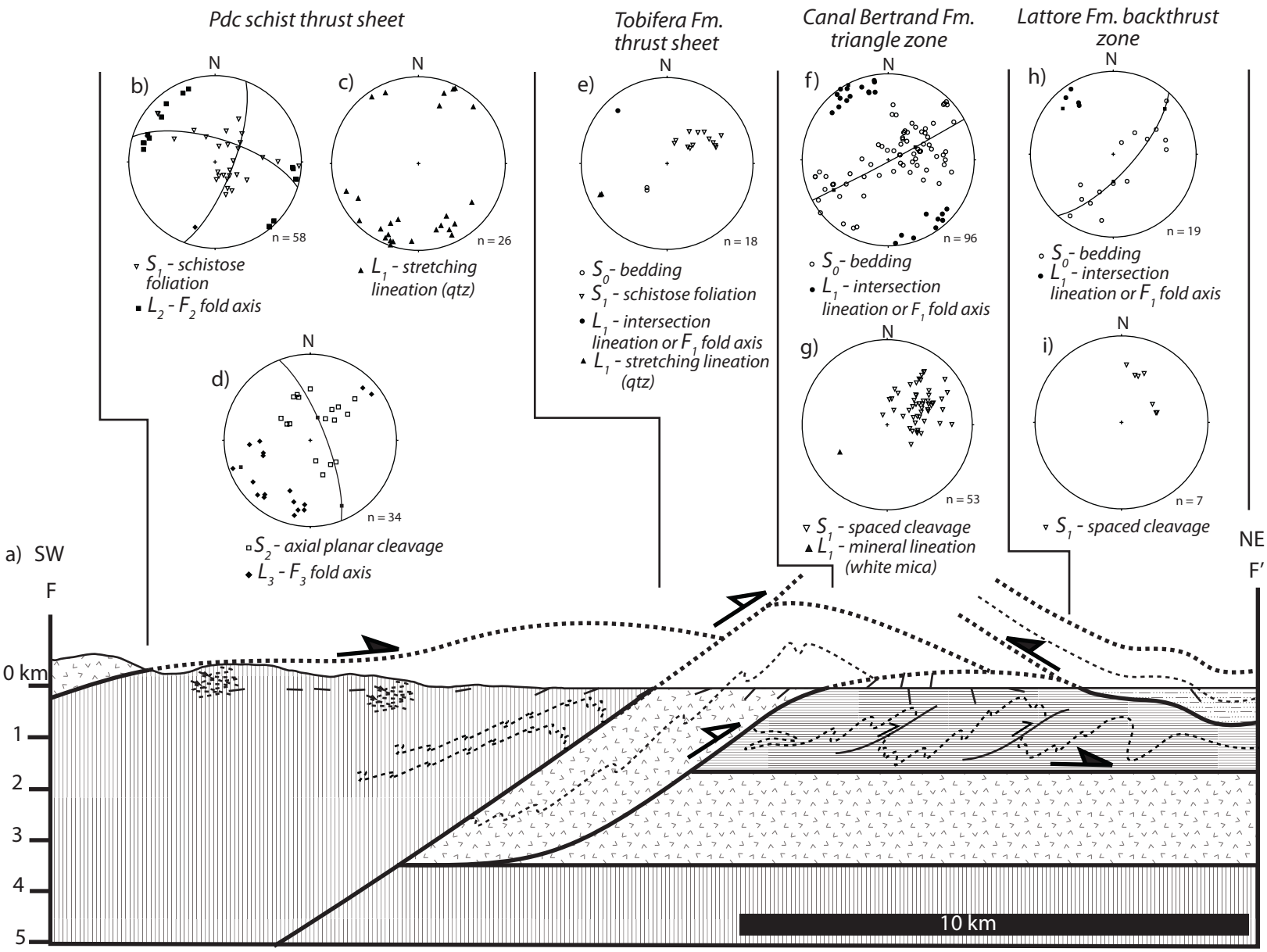
Pdc schist thrust sheet
Tobifera Fm. thrust sheet
Canal Bertrand Fm. triangle zone
Lattore Fm. backthrust zone
b)
N
n = 58
S_1 - schistose foliation
L_2 - F_2 fold axis
c)
N
n = 26
L_1 - stretching lineation (qtz)
d)
N
n = 34
S_2 - axial planar cleavage
L_3 - F_3 fold axis
e)
N
n = 18
S_0 - bedding
S_1 - schistose foliation
L_1 - intersection lineation or F_1 fold axis
L_1 - stretching lineation (qtz)
f)
N
n = 96
S_0 - bedding
L_1 - intersection lineation or F_1 fold axis
g)
N
n = 53
S_1 - spaced cleavage
L_1 - mineral lineation (white mica)
h)
N
n = 19
S_0 - bedding
L_1 - intersection lineation or F_1 fold axis
i)
N
n = 7
S_1 - spaced cleavage
a) SW
F
NE
F'
0 km
1
2
3
4
5
10 km

Figure 1.10

Figure 1.10. Cross-section and structural data from Estuario Silva Palma. (a) Cross section from F-F', see figure 1.8 for location. Short-dashed lines show schematic trace of bedding. Stereograms of structural data from four structural domains: (b-d) the Cordillera Darwin Metamorphic Complex, (e) Tobífera Fm., (f-g) the Zapata-Canal Bertrand triangle zone, and (h-i) the Latorre back thrust.

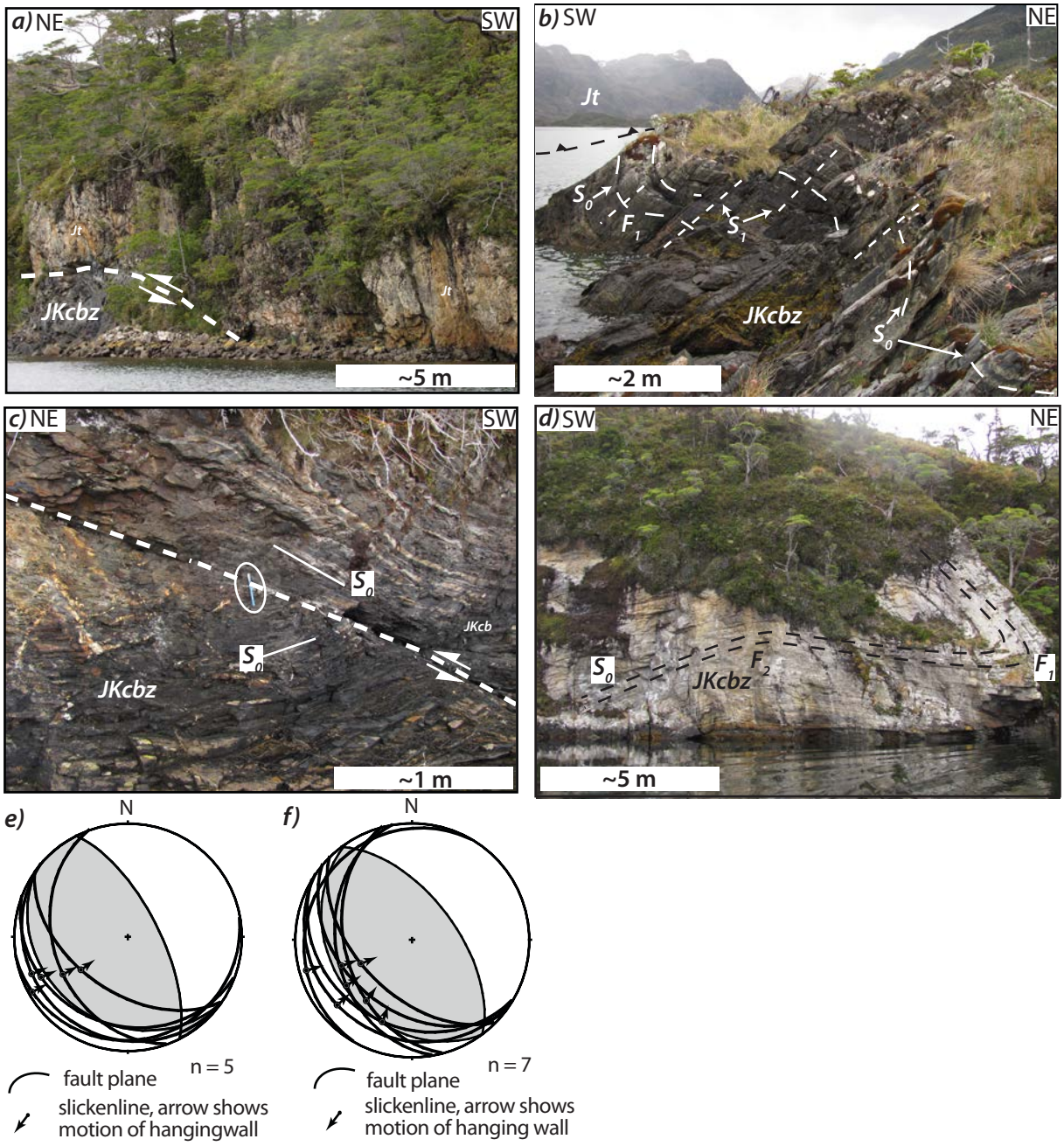

Figure 1.11. Photographs of triangle zone exposed in Estuarios Wickham and Silva Palma. (a) Tobífera over Zapata-Canal Bertrand thrust in Estuario Silva Palma. (b) Bedding (S_0) of the Zapata-Canal Bertrand Fm. folded by northeast-vergent inclined closed folds (F_1) in the footwall of the Tobífera thrust, spaced cleavage (S_1) is axial planar to the folds. (c) Intraformational thrust faults that truncate folds of the Zapata-Canal Bertrand Fm. within the core of the triangle zone, inset shows equal area stereonet projection of the fault surfaces (great circles) and slickenlines (points) with arrow showing the motion of the hanging wall, shaded area shows linked Bingham fault plane solution to data. (d) Bedding of the Zapata-Canal Bertrand Fm. folded by recumbent tight folds (F_1) that are refolded by upright open folds (F_2) within close proximity of the Tobífera thrust within the core of the triangle zone. (e) Equal area stereonet projection of fault surfaces (great circles) and slickenlines (points) from Figure 11a with arrow showing the motion of the hanging wall, shaded area shows linked Bingham fault plane solution to data. (f) Equal area stereonet projection of fault surfaces (great circles) and slickenlines (points) from Figure 11c.

to the Tobífera thrust, a second set of pressure solution seams that overprint bedding defines crenulation cleavage that is parallel to S_1.

F_1 folds are commonly truncated by top-northeast intraformational thrust faults that thicken the Zapata-Canal Bertrand Formation (Figure 1.11c). Within close proximity of the thrust that uplifts the Tobífera Formation, open upright folds that lack an axial-planar cleavage (F_2) refold tight F_1 folds (Figure 1.11d). This thrust truncates the structures observed in the Zapata-Canal Bertrand Formation and therefore, it is mapped as a second-generation fault that is probably coeval with the F_2 folds its footwall.

In all localities in the study area, the Latorre Formation overlies the Zapata-Canal Bertrand Formation and dips gently toward the north. The contact between the Latorre and Zapata-Canal Bertrand Formations is best exposed in Estuario Wickham near site 11071 (Figure 1.4). Here the contact is tectonized, defined by a north-dipping back thrust that contains a 0.5 m thick zone of cataclasite. In the footwall, overturned beds and a penetrative spaced cleavage of the Zapata-Canal Bertrand Formation dip southwest and are truncated by the back thrust. In the hanging wall, strata of the Latorre Formation dip shallowly toward the north and are gently folded, but lack evidence of pervasive strain displayed by the Zapata-Canal Bertrand Formation (Figure 1.12a). Kinematic indicators within the fault zone include a northeast-dipping fault zone cleavage, both synthetic and antithetic microfaults, and tensile veins that formed at high angles to the fault zone cleavage confirm a top-southwest sense of shear (Figure 1.12b-d).

In the hanging wall of the back thrust exposed in Estuario Wickham, the Latorre Formation dips toward the north and is imbricated by a second north-dipping thrust, forming a duplex that is detached at the base of the Latorre Formation (Figure 1.4, 1.9a). In the hanging wall of the duplex, the Latorre Formation dips dominantly toward the north except where it is gently folded by a series of upright open folds (F_1) with subhorizontal northwest- and southeast-trending fold axes. A well-developed southwest-dipping spaced cleavage is axial planar to F_1 folds, and it forms a prominent intersection lineation that is parallel to the fold axis (Figure 1.9a, h-i). In Estuario Silva Palma, the

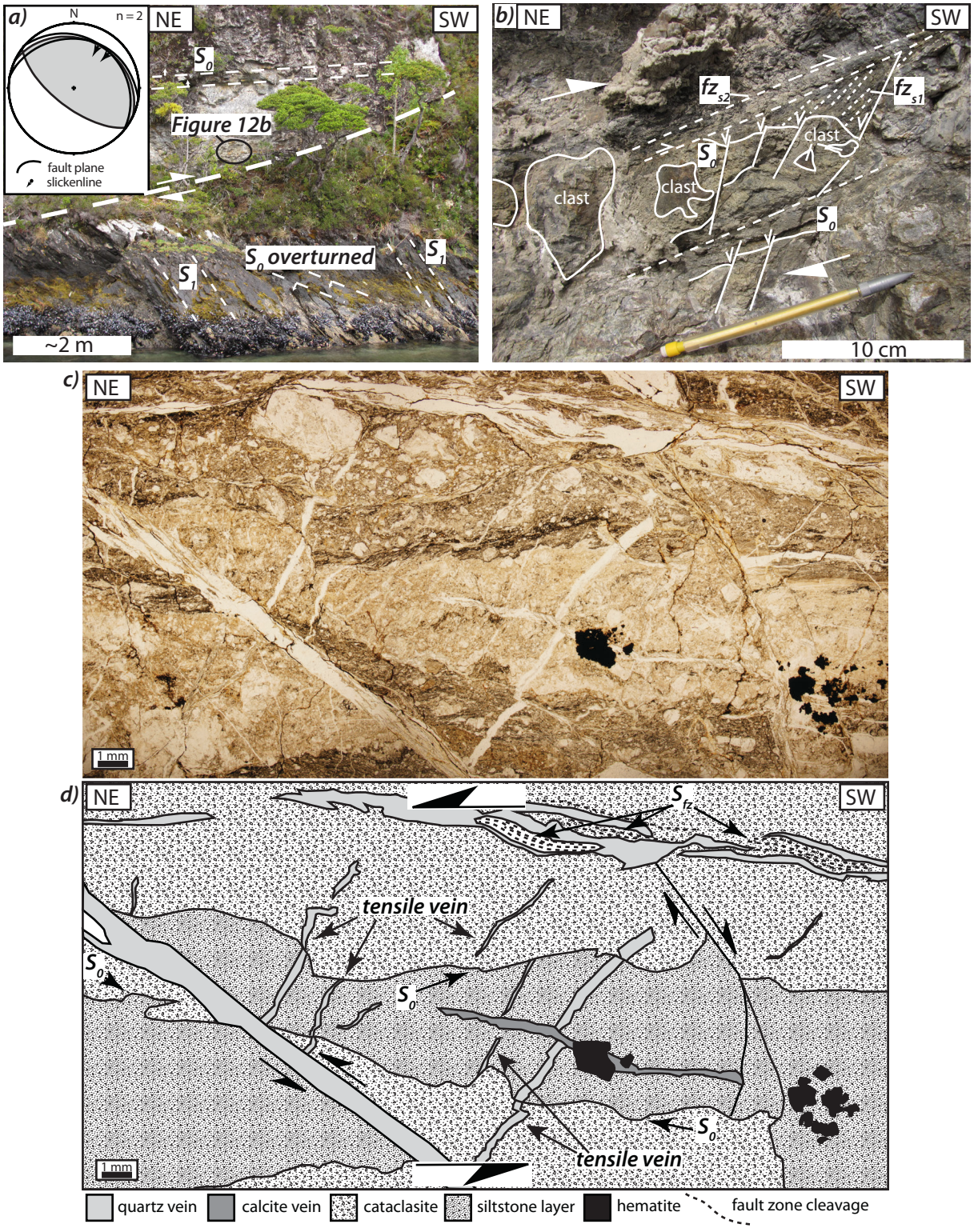
a)
N
n = 2
fault plane
slickenline
NE
SW
S_0
Figure 12b
S_0 overturned
S_1
S_1
~2 m
b)
NE
SW
fz_{s2}
fz_{s1}
clast
clast
clast
S_0
S_0
10 cm
c)
NE
SW
1 mm
d)
NE
SW
S_{fz}
tensile vein
S_0
S_0
S_0
tensile vein
1 mm
quartz vein
calcite vein
cataclasite
siltstone layer
hematite
fault zone cleavage

Figure 1.12

Figure 1.12. Photographs of (a) back thrust exposed in Estuario Wickham showing shallowly north-dipping upright strata of the Latorre Fm. thrust on top of overturned bedding and southwest-dipping cleavage in the Zapata-Canal Bertrand Fm. in the footwall of the thrust, inset shows equal area stereonet projection of the fault surfaces (great circles) and slickenlines (points) with arrow showing the motion of the hanging wall, shaded area shows linked Bingham fault plane solution to data, and (b) fault zone cataclasite exhibiting fault zone cleavage that forms a top-southwest asymmetric fabric (FZS_1, FZS_2) and antithetic microfaults consistent with top-southwest sense of shear, location shown in Figure 12a. Photomicrograph (c) and corresponding sketch (d) of fault zone cataclasite from Figure 12b that shows angular clasts within the cataclasite, fault zone cleavage (S_{fz}) tensile quartz veins and both synthetic and antithetic microfaults that are consistent with top-southwest sense of shear.

Latorre Formation crops out along the northeastern end of section F-F' where it is gently folded by open, upright folds with northwest-plunging fold axes and southwest-dipping axial planar cleavages (Figure 1.9a, h-i). Although the contact between the Latorre Formation and Zapata-Canal Bertrand Formation is not as well exposed in Estuario Fanny to the north of Estuario Wickham, nor Silva Palma to the southeast, it must be discordant in all locations because the Latorre Formation lacks evidence for penetrative strain displayed everywhere by the Zapata-Canal Bertrand Formation. On the basis of similarities in the hanging wall structure of the Latorre Formation exposed in Estuario Wickham to those observed to the northwest and southeast, I infer that the back thrust is continuous for ~70 km along strike and defines a northeastern boundary of a triangle-zone that is cored by the Zapata-Canal Bertrand Formation. Displacements on the thrust are not known, but they are inferred to be small and to decrease toward the northwest and southeast of site 11071 in Esutario Wickham (Figure 1.3). The Latorre Formation is relatively weakly deformed along a passive-roof duplex in the hanging wall of the triangle-zone (Figure 1.9a, 1.10a).

4.5 Structure of Cordillera Darwin Metamorphic Complex near Canal Jeronimo, Estuarios Wickham and Silva Palma

Nearly everywhere in the study area, exposures of the pre-Jurassic metamorphic 'basement' (Cordillera Darwin Metamorphic Complex) are juxtaposed against Jurassic and younger cover along a second-generation reverse fault (Figure 1.3). In the hanging wall of the fault, the Cordillera Darwin Metamorphic Complex is pervasively deformed by several generations of structures that do not affect the overlying volcanic and sedimentary cover. Near Canal Jeronimo (Figure 1.4), the schist displays a pervasive schistose foliation (S_1) that is defined by the alignment of chlorite, white-mica and quartz. A prominent, recrystallized, quartz stretching lineation (L_1) occurs on S_1 surfaces and trends dominantly toward the southwest (Figure 1.5e). Conjugate sets of closed, inclined, horizontal folds (F_2) have steeply southwest- and northeast-dipping axial planes and shallowly-plunging northwest and southeast-trending fold axes and fold both S_1 and L_1 in the hinge of an overturned-to-the-northeast synform (Figure 1.5e, f). S_1 and S_2 surfaces

are overprinted by a well-developed crenulation cleavage (S_3) that dips steeply toward the north and has a west-northwest-plunging crenulation lineation (L_3, Figure 1.5g).

Along-strike toward the southeast, outcrops of the Cordillera Darwin Metamorphic Complex exposed in Estuario Wickham (Figure 1.4, 1.9a) display three generations of structures. A pervasive schistose foliation (S_1) defined by chlorite and quartz dips southwest and contains a recrystallized quartz and mica stretching lineation (L_1) that plunges southwest (Figure 1.9c). Both S_1 and L_1 are refolded by isoclinal inclined folds (F_2) with an axial planar cleavage (S_2) that dips southwest and is parallel to the limbs of the folds. F_2 fold axes are subhorizontal and trend northwest-southeast. A west-northwest-trending crenulation lineation overprints F_2 folds (Figure 1.9d) and is parallel to those exposed near Canal Jeronimo. In the valley between Canal Jeronimo and Estuario Wickham near site 11084 (Figure 1.4), silicic dikes intrude the Cordillera Darwin Metamorphic Complex and are interpreted to be feeder dikes to the Jurassic Tobífera Formation (Figure 1.6f, 1.9a). The dikes are dynamically recrystallized and contain a pervasive schistose foliation that is co-planar with those of the Cordillera Darwin Metamorphic Complex. On this basis, I interpret that the S_1/L_1 and younger fabrics in the Cordillera Darwin Metamorphic Complex formed after the Jurassic.

Greenschist of the Cordillera Darwin Metamorphic Complex is well exposed at the southeastern end of Estuario Silva Palma where the depth of exposure is >1 km below the sheared contact with the overlying Tobífera Formation (Figure 1.8, 1.10a). Here, a pervasive schistose foliation (S_1) contains a prominent dynamically recrystallized quartz stretching lineation (L_1). The S_1/L_1 surface is refolded by two generations of folds with perpendicular, subhorizontal axes. Recumbent, horizontal, tight folds (F_2) that trend west-northwest and east-southeast fold S_1/L_1 (Figure 1.10b-d). Figure 1.13a-b shows the scale of F_2 folds and the L_1 recrystallized quartz lineation refolded around F_2 hinges. Open, shallowly southwest-plunging folds (F_3) gently refold the axial planes of F_2 folds (S_2) (Figure 1.10d, 1.13c). In the valley near the southwestern end of transect F-F' (Figure 1.8, 1.10a), north-dipping C' shear bands cut F_2 and F_3 folds and display top-northeast transport. I interpret these structures to reflect top-northeast motion along the

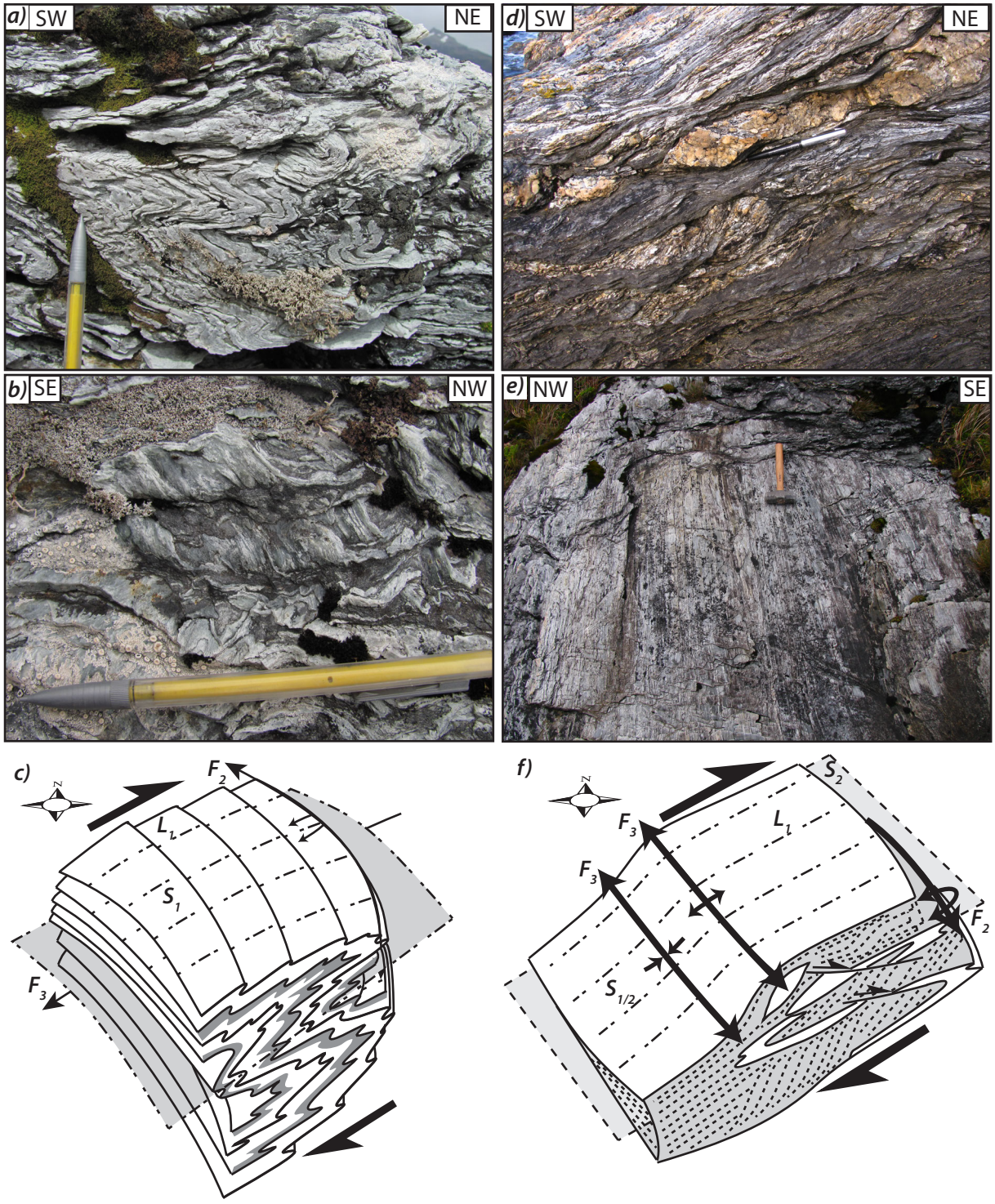

Figure 1.13

Figure 1.13. Photographs and sketches of structures in the Cordillera Darwin metamorphic complex exposed near Estuario Silva Palma (a-c) showing (a) recumbent, tight-isoclinal F_2 folds that refold the schistose foliation (S_1) viewed parallel to the fold axis, (b) the L_1 quartz stretching lineation and S_1 surface refolded around F_2 axes viewed orthogonal to the fold axes, and (c) a sketch of the three-dimensional geometry of the F_2 folds; the S_2 surface is folded by open F_3 folds with fold axes orthogonal to F_2, dark shaded layers represent chlorite-rich domains. (d-f) Photographs and sketches of the Cordillera Darwin metamorphic complex within the shear zone exposed at Bahía Fortesque showing (d) relict F_2 folds that are tightened and transposed within the shear zone fabric, C' shear bands and C-S fabrics that indicate top-northeast sense of shear, (e) a prominent southwest-plunging quartz stretching lineation on the shear zone surface ($S_{1\text{-}2}$), and (f) sketch showing structural elements of the shear zone at Bahía Fortesque including the transposition of F_2 folds, C' shear bands and C-S fabrics that indicate top-northeast sense of shear, a southwest-plunging quartz stretching lineation on the composite $S_{1\text{-}2}$ surface, and upright, north-dipping kink folds (F_3) that refold the shear zone surface, dark shaded layers represent chlorite-rich domains.

sheared contact with the overlying Tobífera Formation, an interpretation supported by the lack of these structures in deeper exposures of the Cordillera Darwin Metamorphic Complex <5 km to the northeast (Figure 1.10a). Everywhere in the Cordillera Darwin Metamorphic Complex from Canal Jeronimo to Estuario Silva Palma, the prominent L_1 quartz stretching lineation is overprinted by at least two younger generations of folds (*e.g.* Figure 1.13a-c), suggesting that continued shortening by progressive folding outlasted shearing.

4.6 Structure of the Cordillera Darwin Metamorphic Complex near Bahía Fortesque and Seno Cordes

Near the Estrecho de Magallanes (Figure 1.3), Bahía Fortesque and Seno Cordes provide important hinterland exposures of the Cordillera Darwin Metamorphic Complex where it is imbricated with the Tobífera Formation in the hanging wall of the second-generation reverse fault (Section G-G'; Figure 1.8, 1.14). The Cordillera Darwin Metamorphic Complex crops out at the northern end of transect G-G' in Seno Cordes, where it displays a schistose foliation defined by quartz, chlorite and white mica (S_1). Upright, horizontal, northwest-southeast-trending tight folds, with < 1m wavelengths fold S_1 surfaces (F_2; Figure 1.14a, f). A recrystallized quartz stretching lineation (L_1) is preserved on S_1 surfaces that is perpendicular to F_2 fold axes is also folded by F_2. Axial planes to F_2 folds (S_2) are sub-vertical (Figure 1.14g). The contact with the Tobífera Formation is moderately sheared and folded by upright to inclined F_2 folds.

Overlying the Cordillera Darwin Metamorphic Complex, the Tobífera Formation is internally deformed and folded by a steeply inclined syncline. In the core of the syncline a white-mica schistose foliation (S_1) contains a poorly developed southwest-plunging quartz stretching lineation (L_1), and both are refolded by a conjugate set of steeply inclined kink folds (F_2). The kink folds have axial planes (S_2) that dominantly dip steeply to the southwest, however a subordinate northeast-dipping conjugate set exists. F_2 fold axes trend toward the northwest and south-southeast and are subparallel to a crenulation lineation that occurs on the limbs of the kink folds (Figure 1.14a, d-e).

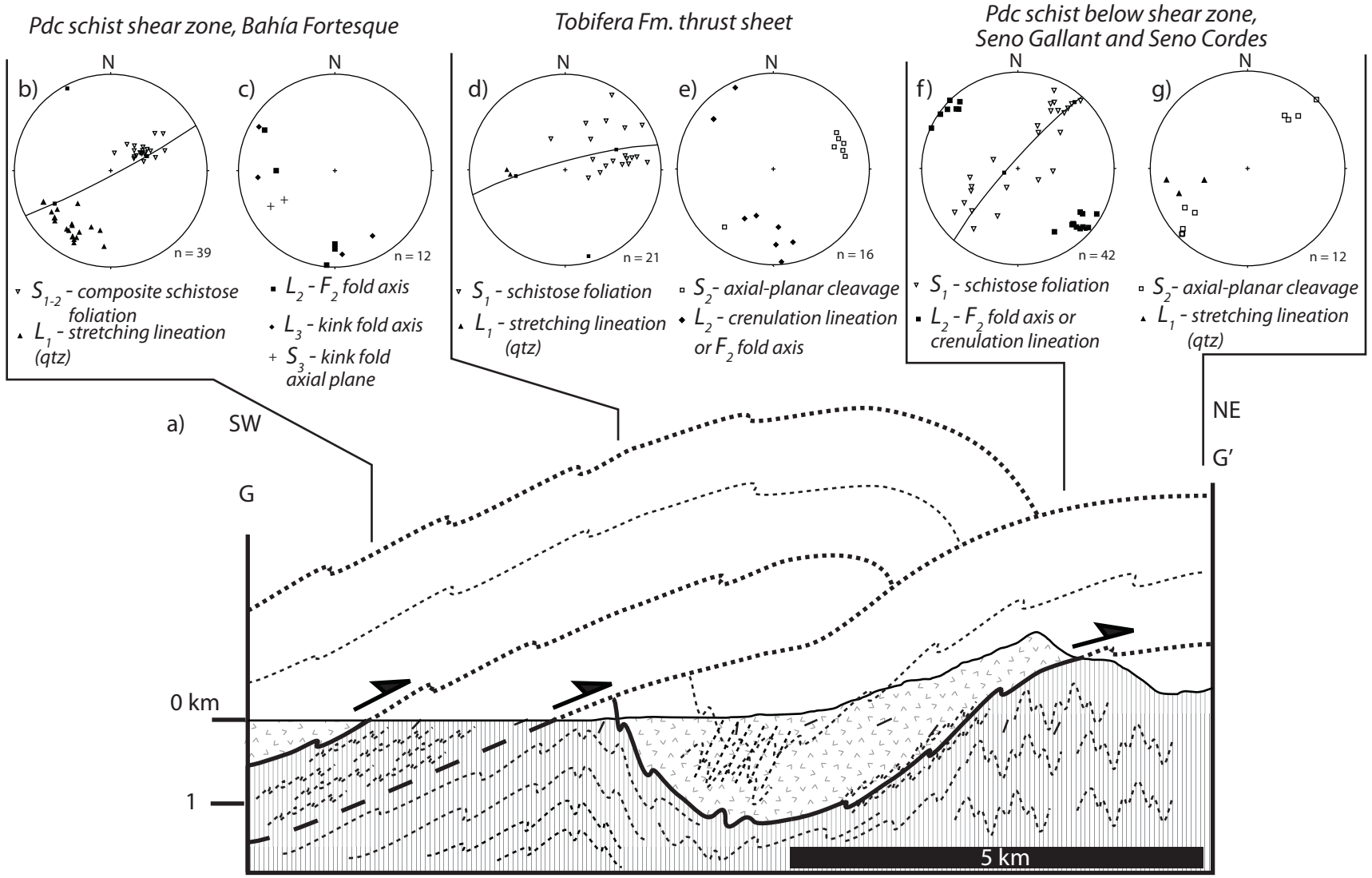

Figure 1.14. (a) Cross section from G-G', see figure 1.8 for location. Short dashed lines show trace of bedding (Tobífera Fm.) or pervasive schistose foliation (S_1, Cordillera Darwin Metamorphic Complex), long-dashed lines show trace of axial planar cleavage. Stereograms showing structural data from three structural domains: (b-c) the Bahía Fortesque high strain zone, (d-e) the Tobífera Fm., and (f-g) the Cordillera Darwin Metamorphic Complex below the high-strain zone.

In Bahía Fortesque at the southwestern end of transect G-G', the contact between the Tobífera Formation and the Cordillera Darwin Metamorphic Complex is strongly tectonized and dips moderately to the southwest. Here <1 km below the contact, the Cordillera Darwin Metamorphic Complex displays a southwest-dipping schistose foliation (S_1) and prominent, recrystallized, quartz stretching lineation (L_1) that plunges southwest (Figure 1.14a, b). Isoclinal rootless folds (F_2) that have curved west-northwest and south-southeast-trending axes (Figure 1.14c) fold the S_1/L_1 surface and are sheared to form the composite $S_{1\text{-}2}$ foliation. The limbs of F_2 folds are commonly truncated by C' shear bands that indicate top-northeast transport. In micaceous domains the composite foliation is transposed and forms well developed C-S fabrics that also indicates top-northeast shear (Figure 1.13d-f). Steeply inclined kink folds (F_3) refold the composite foliation. F_3 folds have north-dipping axial planes and trend northwest-southeast subparallel to F_2 fold axes (Figure 1.13f, 1.14c). The tightening, transposition, and shearing of F_2 folds defines a 1-km thick shear zone that cuts up-section through the basement-cover contact imbricating the Cordillera Darwin Metamorphic Complex with the Tobífera Formation (Figure 1.14a). This shear zone is interpreted as the first-generation basal décollement that developed <1 km below the basement-cover contact and is an important example of the structurally lowest and most hinterland exposures of the fold-thrust belt in the study area.

4.7 Structure of the Magallanes fold-thrust belt near Peninsula Brunswick

Shoreline exposures along a 30-km transect from Cabo Froward toward the northeast preserve the structure of the Magallanes foreland basin in the southeastern most part of the study area (Transect H-H'; Figure 1.3, 1.15, 1.16). Near Cabo Froward at the southwestern end of transect H-H', the Tobífera Formation crops out along the Estrecho de Magallanes and can be easily correlated using satellite imagery with exposures in Silva Palma (Figure 1.3). Near Cabo Froward, the top of the Tobífera Formation is exposed and sheared. A schistose white mica and quartz foliation (S_1) dips north and contains a well-defined, recrystallized, quartz lineation that plunges toward the north

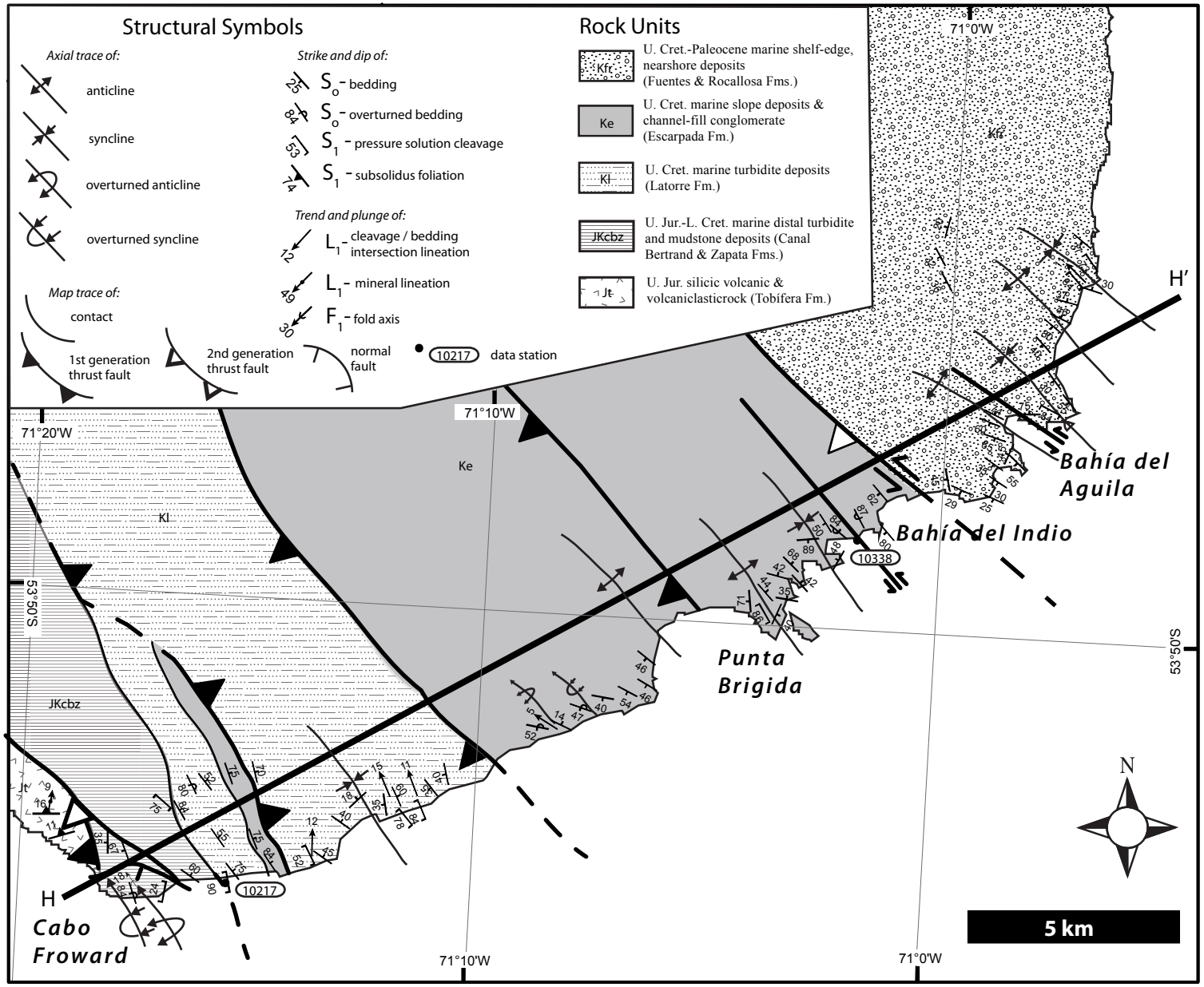
Structural Symbols
Axial trace of:
anticline
syncline
overturned anticline
overturned syncline
Map trace of:
contact
1st generation thrust fault
2nd generation thrust fault
normal fault
Strike and dip of:
S0 - bedding
S0 - overturned bedding
S1 - pressure solution cleavage
S1 - subsolidus foliation
Trend and plunge of:
L1 - cleavage / bedding intersection lineation
L1 - mineral lineation
F1 - fold axis
10217 data station
Rock Units
Kfr U. Cret.-Paleocene marine shelf-edge, nearshore deposits (Fuentes & Rocallosa Fms.)
Ke U. Cret. marine slope deposits & channel-fill conglomerate (Escarpada Fm.)
Kl U. Cret. marine turbidite deposits (Latorre Fm.)
JKcbz U. Jur.-L. Cret. marine distal turbidite and mudstone deposits (Canal Bertrand & Zapata Fms.)
Jt U. Jur. silicic volcanic & volcaniclasticrock (Tobífera Fm.)
71°0'W
71°10'W
71°20'W
53°50'S
H
H'
Cabo Froward
Punta Brigida
Bahía del Aguila
Bahía del Indio
10217
10338
N
5 km

Figure 1.15

Figure 1.15. Geologic map of Peninsula Brunswick near Cabo Froward showing data collected during this study. Black dot and corresponding number refers to data station mentioned in text. Data collected at 1:25,000 scale.

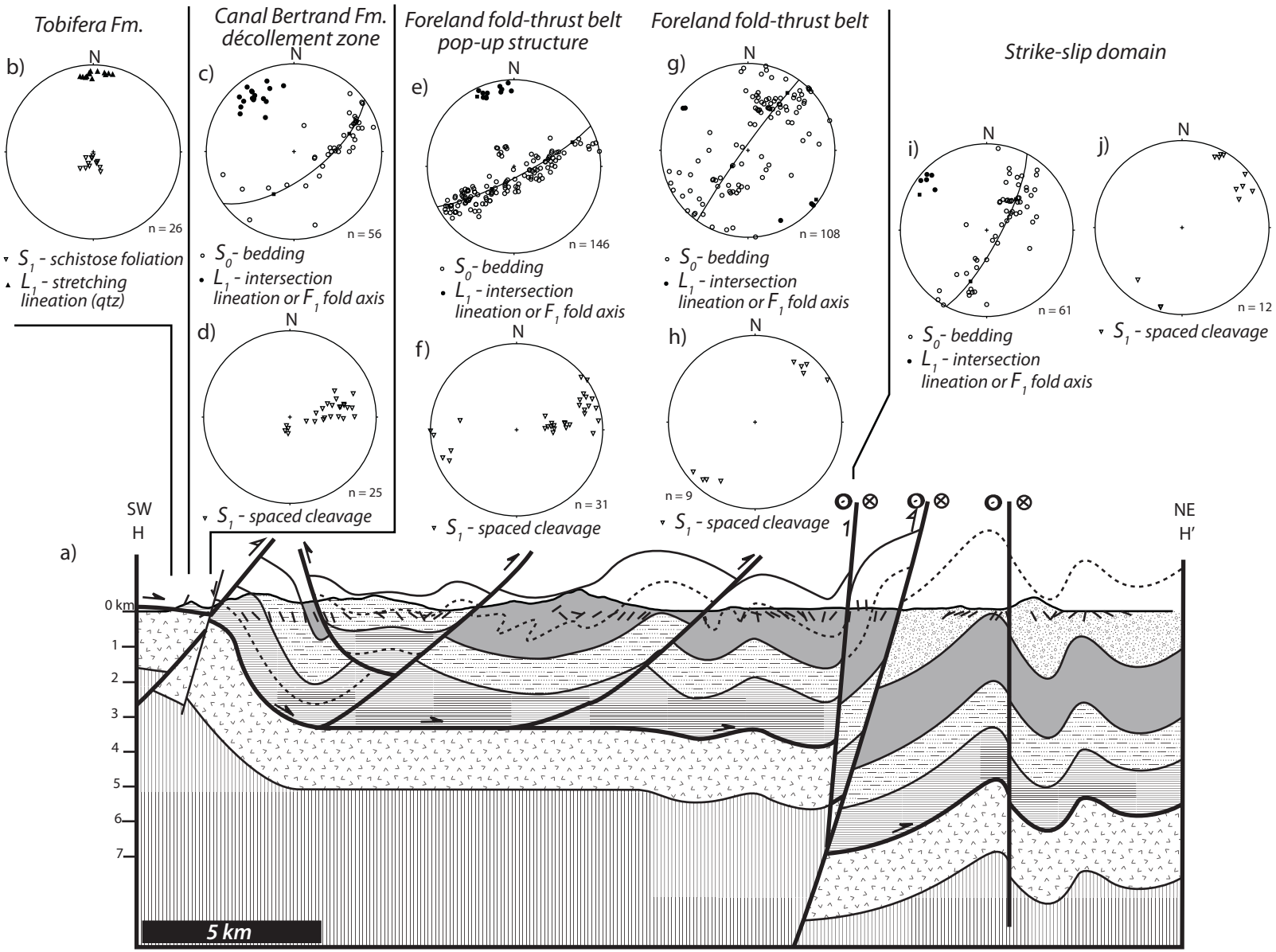
Tobifera Fm.
b)
N
n = 26
S_1 - schistose foliation
L_1 - stretching lineation (qtz)
Canal Bertrand Fm. décollement zone
c)
N
n = 56
S_0- bedding
L_1 - intersection lineation or F_1 fold axis
d)
N
n = 25
S_1 - spaced cleavage
Foreland fold-thrust belt pop-up structure
e)
N
n = 146
S_0- bedding
L_1 - intersection lineation or F_1 fold axis
f)
N
n = 31
S_1 - spaced cleavage
Foreland fold-thrust belt
g)
N
n = 108
S_0- bedding
L_1 - intersection lineation or F_1 fold axis
h)
N
n = 9
S_1 - spaced cleavage
Strike-slip domain
i)
N
n = 61
S_0- bedding
L_1 - intersection lineation or F_1 fold axis
j)
N
n = 12
S_1 - spaced cleavage
a)
SW
H
NE
H'
0 km
1
2
3
4
5
6
7
5 km

Figure 1.16

Figure 1.16. Cross-section and structural data from Cabo Froward and the Magallanes Straits. (a) Cross section from H-H', see figure 1.15 for locations. Short-dashed lines show schematic trace of bedding. Stereograms of structural data from five structural domains: (b) the Tobífera Fm. at Cabo Froward, (c-d) the Zapata-Canal Bertrand décollement at Cabo Froward, (e-f) bedding orientations and folds within the Zapata-Canal Bertrand, Latorre, and Escarpada-Fuentes Fms. near the pop-up structure, (g-h) folds within the Escarpada-Fuentes Fms. in the foreland fold-thrust belt, and (i-j) folds within the Fuentes-Rocallosa Fm. in close proximity to Neogene strike-slip faults.

(L_1, Figure 1.16a,b). On surfaces oriented perpendicular to S_1 and parallel to L_1, rigid, feldspar porphyroclasts with asymmetric recrystallized quartz tails and C' shear bands that truncate and displace S_1 indicate top-north sense of shear.

Above the contact at Cabo Froward, the Zapata-Canal Bertrand Formation crops out and is pervasively deformed. Here, bedding (S_0) of the Zapata-Canal Bertrand Formation is folded into tight, northeast-vergent overturned folds with northwest-plunging fold axes (F_1) and west-southwest-dipping axial planes (S_1). A prominent cleavage-bedding intersection lineation (S_1) is exposed on bedding surfaces and is parallel to F_1 fold axes (Figure 1.16c, d). At Cabo Froward, F_1 folds in the Zapata-Canal Bertrand Formation are detached from the underlying Tobífera Formation which is not folded. The top-north sense of shear at the contact between the two formations is sympathetic with the vergence of the overturned folds in the overlying Zapata-Canal Bertrand Formation.

A basement-involved, southwest-dipping reverse fault is inferred and mapped in the valley north of Cabo Froward to explain the juxtaposition of stratigraphic levels between exposures of the Tobífera-Zapata-Canal Bertrand contact in the hanging wall and the Zapata-Canal Bertrand-Latorre contact in the footwall (Figure 1.15, 1.16a). This fault correlates with the second-generation thrust that uplifts the Tobífera Formation where it crops out in Estuarios Silva Palma and Wickham to the northwest (Figure 1.3). A minor southeast-dipping normal fault cuts the reverse fault and strikes northeast along the valley between Cabo Froward and Peninsula Brunswick (Figure 1.15, 1.16a). To the north of these faults, the upper part of the Zapata-Canal Bertrand Formation is exposed and is not deformed. Bedding (S_0) dips steeply toward the north. The contact between the Zapata-Canal Bertrand Formation and overlying Latorre Formation is exposed near site 10217 (Figure 1.15) where it is conformable and dips north. Above the contact the full thickness of the Latorre Formation (~1200 m) is intermittently exposed. The Escarpada Formation conformably overlies the Latorre Formation and also dips to the north (Figure 1.15, 1.16).

Approximately 1 km northeast of site 10217, a back thrust juxtaposes the base of the Latorre Formation against the Escarpada Formation (Figure 1.15, 1.16). In the

hanging wall of the back thrust, bedding (S_0) is folded by a regional syncline. Mesoscale (~5 m wavelengths) second order folds have axes that trend north-northwest and steeply southwest-dipping or upright axial planar cleavages (S_1). Bedding-cleavage intersection lineations occur on bedding surfaces and trend north-northwest (Figure 1.16e, f). The northern limb of the syncline is truncated by a southwest-dipping thrust fault that uplifts the Latorre Formation in the hanging wall above the Escarpada Formation in the footwall. On the basis of the stratigraphic separation across the fault, the thrust is inferred to be detached at the base of the Zapata-Canal Bertrand Formation, and it forms a pop-up structure with the back thrust exposed to the south (Figure 1.16a).

To the north of the pop-up structure, the Escarpada Formation is imbricated by a southwest-dipping thrust fault that also is inferred to be detached at the base of the Zapata-Canal Bertrand Formation on the basis of geometric constraints from stratigraphic thicknesses (Figure 1.16a). In the hanging wall, bedding is folded into a regional syncline-anticline pair. Second order folds in the core of the syncline are overturned-to-the-northeast and have northwest-southeast-trending horizontal fold axes. In the footwall north of Punta Brigida (Figure 1.15), regional F_1 folds are upright and tighter than those in the hanging wall. Here, second-order F_1 folds display a subvertical axial planar cleavages (S_1, Figure 1.16a, g-h). Near site 10338 (Figure 1.15), bedding dips vertically and is cut by a 2 m wide sinistral strike-slip fault zone that strikes northwest subparallel to bedding (Figure 1.15, 1.16a). The amount of offset is unknown, however stratigraphic thickness constraints require at least 1 km of throw across the fault indicating a reverse-sinistral sense-of-motion (Figure 1.16a).

On the south shore of Bahía del Indio, the Escarpada Formation crops out and is subvertical. Here, clustered sets of conjugate strike-slip faults cut bedding and indicate dominantly sinistral slip. On the north shore 1.5 km toward the northeast, strata of the Fuentes/Rocallosa Formation dip shallowly to the southwest. A high-angle basement-involved reverse fault is inferred to explain the stratigraphic separation across the bay. This fault probably correlates with similar structures exposed near Seno Otway on section A-A', ~100 km to the northeast (Figure 1.3). Here, the fault also is inferred to have a left-

lateral component of motion on the basis of the clustered sets of conjugate faults on the south shore of Bahia del Indio (discussed in Chapter 3).

Toward the north in the footwall of the basement-involved fault, the Fuentes/Rocallosa Formation is folded by a series of three tight upright folds with ~2 km wavelengths (F_1). A vertical spaced cleavage is axial planar to the folds (S_1). Fold axes and cleavage-bedding intersection lineations plunge shallowly toward the northwest (Figure 1.16i-j). Several sets of conjugate strike-slip faults cluster on the limb of the fold near Bahía del Aguila and show dominantly sinistral-slip. A steeply-dipping, bedding parallel, left-lateral strike slip fault is mapped along the north shore of Bahía del Aguila where conjugate fault sets are densely clustered (Figure 1.15, 1.16a). Tight upright folds and strike-slip deformation preserved on the northern end of transect H-H' post-date the fold-thrust belt and probably reflect Neogene strike-slip tectonics.

5. Discussion

5.1 Correlation of Structures and Tectonic Interpretations

5.1.1 Second-Generation Basement-Involved Structures

New mapping results presented above reveal several faults that correlate along-strike from Seno Otway to Peninsula Brunswick. A second-generation basement-involved reverse fault crops out on each transect A-F and again along the Estrecho de Magallanes, and everywhere it juxtaposes deformed schist of the Cordillera Darwin Metamorphic Complex in its hanging wall against deformed and imbricated strata of the Tobífera and Zapata-Canal Bertrand Formations in the footwall. This fault is continuous for ~80 km along-strike from Seno Otway to the Estrecho de Magallanes (Figure 1.3), and it may be similar to an out of sequence basement-involved reverse fault mapped to the southeast along the northern boundary of the Cordillera Darwin (Figure 1.1; Klepeis, 1994; Klepeis *et al.,* 2010; McAtamney *et al.,* 2011). If correct, this suggests the fault is continuous along-strike for >300 km and everywhere defines the northern boundary of the Cordillera Darwin Metamorphic Complex on Tierra del Fuego (Figure 1.1). North of this structure

exposed near Seno Otway, two additional basement-involved reverse faults cut first-generation structures and Cretaceous strata within the Magallanes foreland basin (Figure 1.4, 1.5m). Each of these faults must be a second-generation basement-uplift because the stratigraphic level of exposure changes across the fault and they cut earlier structures including the Escarpada and Latorre duplex, as well as the Tobífera duplex along transect A-A' (Figure 1.4, 1.5). The basement involved reverse fault exposed along transect H-H' near Bahía del Indio that juxtaposes the Escarpada Formation above the Fuentes/Rocallosa Formation (Figure 1.15) probably correlates with the northernmost basement structure near Seno Otway, suggesting that it is continuous for ~100 km along-strike (Figure 1.3).

In the Ultima Esperanza region of Chile (Figure 1.1), Fosdick *et al*. (2011) documented a phase of out-of-sequence basement involved faulting that reactivated Jurassic normal faults, cut early décollement levels in the Magallanes fold-thrust belt and occurred from the Campanian to the early Oligocene. This pulse of thrusting is coeval with Late Cretaceous-Paleogene synorogenic deposition of the Tres Pasos and Dorotea Formations (Figure 1.2) that sample uplifted and eroded Jurassic volcanic and volcanoclastic rocks of the Rocas Verdes basin (Romans *et al*., 2010). Mpodozis *et al*. (2007) showed peak U-Pb detrital zircon populations from 62-66 Ma for the Fuentes and Rocallosa Formations near Seno Otway that are equivalents of the Tres Pasos and Dorotea Formations in Ultima Esperanza (Figure 1.2). On the basis of similarities in the sequence and structural-style of basement-involved faults between Seno Otway and Ultima Esperanza (*e.g*. Fosdick *et al*., 2011) and the timing of Paleogene synorogenic sedimentation that samples uplifted Rocas Verdes basin terrane, I postulate that basement-involved faulting near Seno Otway reflects the reactivation of Jurassic normal faults and was probably coeval with that to the northwest beginning in the Maastrichtian and culminating in the Paleogene (*c.f*. Winslow *et al*., 1981; Fosdick *et al*., 2011). This interpretation is consistent with a phase of basement-involved, out-of-sequence thrusting documented on Tierra del Fuego toward the southeast (Klepeis, 1994a) and a phase of rapid exhumation and erosion of basement and Upper Jurassic igneous rocks of the

Cordillera Darwin Metamorphic Complex during the Paleogene (Barbeau *et al.,* 2009; Gombosi *et al.,* 2009; Zahid & Barbeau, 2010). Data from this study indicate that basement-involved faults crop out continuously along the trend of the fold-thrust belt and suggest that out-of-sequence basement-involved faulting was an orogen-wide event probably resulting from the complete closure of the Rocas Verdes basin and collision of the Patagonian batholith (*c.f.* Klepeis *et al.,* 2010).

5.1.2 First Generation Décollement Levels, Basement Deformation, Triangle Zone and Mechanical Stratigraphy

Lower décollement. The basement-cover contact between the Cordillera Darwin Metamorphic Complex and Jurassic volcanic rocks of the Rocas Verdes basin and Tobífera Formation is exposed along transects C, E, F and G, where it is sheared and displays top-northeast sense of transport (Figure 1.3, 1.4, 1.5a, 1.6, 1.9a, 1.10a, 1.13, 1.14a). Important exposures near Bahía Fortesque (transect G-G') are the most hinterlandward and structurally lowest exposures in the study area. Here, the sheared contact ramps up-section through the Tobífera Formation and imbricates the basement schist with the cover (Figure 1.14), defining a lower décollement < 1 km below the basement-cover contact at the base of the thrust-belt. The Cordillera Darwin Metamorphic Complex displays a pervasive schistose foliation S_1 that contains a prominent, recrystallized, quartz stretching lineation (L_1) everywhere it is exposed within and below the décollement near Bahía Fortesque, Seno Cordes and the southwestern ends of Estuarios Silva Palma and Wickham (Figure 1.4, 1.8). I interpret the S_1/L_1 surface to reflect the earliest phase of shearing along the basal décollement that thrust the Rocas Verdes terrane onto the continental margin. These early structures are similar to those reported in contractional craton-vergent shear zones that formed at the base of the Rocas Verdes terrane rocks near the Beagle Channel prior to ~86 Ma (Klepeis *et al.,* 2010; Nelson, 1980) and in the Sarmiento complex to the north ~ 85 Ma (Calderon *et al.,* 2012), suggesting that obduction of the Rocas Verdes rocks was everywhere underway by the Turonian-Coniacian.

Observations from the base of the fold-thrust belt presented in this study provide an important example of crustal thickening that occurred in the metamorphic basement below and toward the hinterland of a fold-thrust belt. Below the basal décollement S_1/L_1 are refolded by two generations of folds (F_2 -3; Figure 1.13) that are not expressed in the overlying Tobífera Formation (Figures 1.9a, c-d, 1.10a-d, 1.14), indicating that basement shortening was accommodated by progressive polyphase folding and dynamic recrystallization processes that did not occur in the overlying thrust-belt. Here, basement shortening was accommodated by different deformation mechanisms and was mechanically detached from the overlying thrust belt, perhaps providing some insight to orogenic processes elsewhere that form large topographic reliefs that cannot be completely explained by balancing shortening within a retroarc fold-thrust belt and therefore require mid-lower crustal thickening (*e.g.* Altiplano Plateau, McQuarrie *et al.*, 2005).

Upper décollement. Material above the basal décollement was translated along the décollement and up-section over ramps through the Tobífera Formation. Exposures of the upper contact of the Tobífera Formation with the Zapata-Canal Bertrand Formation near Cabo Froward confirm that this is also a sheared contact with a top-north sense-of-shear and forms a thrust-flat (Figure 1.15, 1.16a-d), thus defining a higher décollement level at the base of the Zapata-Canal Bertrand Formation. The thrust ramp exposed at Bahía Fortesque links the lower and upper décollements (Figure 1.3, 1.8, 1.14a, 1.15, 1.16a). Similarly, near Canal Jeronimo (Transect A-A', B-B'; Figure 1.5h, m), the floor-thrust of the duplex within the Tobífera Formation occurs at the basement-cover contact and ramps up-section to form a roof-thrust in the Zapata-Canal Bertrand Formation <400 m stratigraphically above the contact between the Zapata-Canal Bertrand and Tobífera Formations. Structures that imbricate the Tobífera Formation are consistent with those near Bahía Fortesque and Cabo Froward and indicate that everywhere ignimbrite deposits of the Tobífera Formation are bound on both sides by thrust flats linked by ramps that cut the formation. A second-generation thrust that soles into the lower décollement uplifts the

Tobífera Formation, cuts first generation structures, and is exposed for >80 km along-strike at Canal Jeronimo, Estuario Wickham and Estuario Silva Palma (Figure 1.3).

Along transects A, B, E and F in the footwall of the second generation thrust that uplifts the Tobífera Formation (Figure 1.3), the Zapata-Canal Bertrand Formation is pervasively deformed by up to two generations of folds with top-northeast vergence and shallowly northwest-plunging fold axes that are subparallel everywhere in the study area (Figure 1.5m, o-p; 1.9a, f-g; 1.10a, f-g; 1.16c-d). Intraformational thrust faults with top-northeast slip indicators truncate folds in the Zapata-Canal Bertrand Formation (Figure 1.11c) and are synthetic with the top-northeast vergence of the folds. Along section B-B' the Zapata-Canal Bertrand Formation is imbricated by at least two southwest-dipping thrust faults that sole into a thrust-flat at the base of the formation to form a hinterland-dipping duplex (Figure 1.5h). Here, northeast-vergent folds occur in the footwalls of the thrusts (Figure 1.5i-l) and are subparallel to those observed elsewhere. Folds observed within the Zapata-Canal Bertrand Formation along transect A-A' occur at the base of the formation where they are tighter than folds exposed elsewhere near the top of the formation (*e.g.* Estuarios Wickham and Silva Palma), indicating increasing strain toward the base of the Zapata-Canal Bertrand Formation that defines a regional décollement at the base of the formation (Figure 1.5m).

The Zapata-Canal Bertrand décollement is the floor-thrust for the Zapata-Canal Bertrand duplex exposed along transect B-B' and the Escarpada-Latorre duplex exposed near Seno Otway along transect A-A'. This inference is supported by the observation that footwall folds in both duplexes are subparallel to those in the décollement (Figures 1.5m, i, k, o-p, q-r). Furthermore, the second-generation basement-involved fault exposed near the mouth of Estuario Fanny at the north shore (Figure 1.4) uplifts the Zapata-Canal Bertrand décollement in the hanging wall relative to the Escarpada-Latorre imbricate thrusts in the footwall (Figure 1.5m), indicating the décollement formed a regional structural level prior to being displaced by second-generation reverse faults. Exposed along transect H-H' ~100 km to the southeast, the Zapata-Canal Bertrand décollement crops out at Cabo Froward where tight overturned folds are parallel to those in the

décollement near Canal Jeronimo (Figures 1.5o-p, 1.16c, d). Folds associated with thrusts that imbricate foreland base strata along section H-H' trend northwest-southeast are subparallel to those exposed at Seno Otway and in the Zapata-Canal Bertrand décollement at Cabo Froward and Canal Jeronimo (Figure 1.16g, h) and indicate the same southwest-northeast shortening direction. One exception includes folds in the hanging wall of the pop-up structure along transect H-H' that trend more toward the north (Figures 1.16e-f). The misorientation of these folds probably indicates that folding in the hanging wall of the pop-up was not exactly coaxial with the rest of the thrust belt.

The orientations and shortening directions associated with folds and faults in the foreland basin strata and Canal Bertand Formation are subparallel for >100 km along-strike, suggesting that the Zapata-Canal Bertrand Formation acts as a regional basal décollement that accommodated top-northeast thrusting and folding of foreland basin strata everywhere in the study area. Structures within the Zapata-Canal Bertrand Formation in the study area probably correlate with similar structures, including top-northeast intraformational tight folds and faults reported >100 km toward the southeast near Bahía Brookes (McAtamney *et al.,* 2011; Mpodozis and Rojas, 2006), suggesting that it is a major regional décollement level below the fold-thrust belt for >200 km along-strike in southern Patagonia and Tierra del Fuego (*see also,* Klepeis, 1994a).

Triangle Zone. Everywhere in the study area, neither the underlying Tobífera Formation, nor the overlying Latorre Formation record the pervasive deformation exhibited by the Zapata-Canal Bertrand Formation, indicating that this deformation is localized within the formation. The lower contact between the Zapata-Canal Bertrand and Tobífera Formations is exposed near Canal Jeronimo and Cabo Froward where it is sheared along a lower décollement within ~400 m of the contact with the Tobífera Formation. The upper contact between the Zapata-Canal Bertrand and Latorre Formations is exposed near Estuario Wickham where strata of the Latorre Formation are back thrust above the pervasively deformed Zapata-Canal Bertrand Formation (Figure 1.3, 1.5, 1.9, 1.10, 1.12). Although the Latorre Formation is less deformed than the Zapata-Canal Bertrand Formation, the orientations of axial planar cleavages (S_1),

intersection lineations (L_1), and F_1 folds of bedding of the Latorre Formation in the hanging wall of the back thrust (Figure 1.9h-i, 1.10h-i) are subparallel to those from folds of bedding in the Zapata-Canal Bertrand Formation in the footwall (Figure 1.9f-g, 1.10f-g) suggesting that the deformation probably formed coevally. These observations suggest that pervasively deformed strata of the Zapata-Canal Bertrand Formation occupy the core of a triangle-zone that is detached at both the upper and lower contacts (*c.f.* MacKay, 1996).

Triangle zone structures are commonly reported at the leading edge of thin-skinned thrust belts (*e.g.* MacKay, 1996; Stockmal *et al.,* 2001; Banks and Warburton, 1986; Sans et la., 1996; Sobornov, 1996; Ramos, 1989), especially in settings characterized by weak shale décollements that are overlain by synorogenic sedimentary rocks (*see review by* Couzens & Wiltschko, 1996; McMechan, 1985). I postulate that the mechanical contrast between relatively weak shale with the underlying volcanoclastic rocks and overlying siliciclastic turbidites allowed a triangle-zone to form within the Zapata-Canal Bertrand Formation at the tip of the propagating thrust wedge as it advanced into the Magallanes Foreland basin (*c.f.* Couzens & Wiltschko, 1996). It is well known that mechanically layered stratigraphy can influence the kinematic development of a fold-thrust belt (*e.g.* Thomas, 2007; Davis & Engelder, 1985; Cotton & Koyi, 2000; Farzipour-Saein *et al.* 2009; Teixell & Koyi, 2003). In Patagonia, silicic ignimbrites of the Tobífera Formation form a competent layer relative to the ductile chlorite-schist below, and shale above. I attribute the occurrence of regional décollement levels along both the upper and lower contacts of the Tobífera Formation to reflect a mechanical stratigraphy inherited from the predecessor marginal basin that ultimately controlled the location of décollement levels and kinematic development of the thrust-belt.

5.1.3 Neogene Strike-Slip Deformation

Structures exposed in the foreland fold-thrust belt along the northeastern segment of transect H-H' contrast slightly with those near Seno Otway toward the northwest. Along transect H-H' northeast of Cabo Froward, F_1 folds are upright with subvertical axial planar cleavages (S_1) in contrast to southwest-dipping inclined folds that occur near

Seno Otway. I postulate that upright fold orientations along transect H-H' (Figure 1.16) reflect a Neogene strike-slip overprint on the Late Cretaceous-Paleogene thrust belt that rotated initially northeast-vergent folds into upright orientations. Near Bahía del Indio and Bahía del Aguila, at least three left-lateral strike slip faults cut the thrust-belt, strike northwest-southeast parallel to the trend of the thrust belt, and probably reactivated Cretaceous-Paleogene faults (Figure 1.15, 1.16a). These faults are likely right-stepping, left-lateral splays from the Magallanes left-lateral fault zone to the south (Figure 1.1; *c.f.* Lodolo *et al.,* 2003). I interpret that Cretaceous-Paleogene folds initially formed in the thrust-belt and subsequently were tightened and rotated into upright orientations within close proximity of the strike-slip faults. This interpretation is consistent with a well documented phase of wrench tectonics (Menichetti *et al.,* 2008; Lodolo *et al.,* 2003; Diraison *et al.,* 1998) that began after the Eocene (Barbeau *et al.,* 2009; Gombosi *et al.,* 2009; Zahid & Barbeau, 2010) and was associated with the Magallanes-Fagnano fault zone and opening of the Scotia Sea (Klepeis *et al.,* 1994; Cunningham 1993; 1995).

5.1.4 Timing of Deformation: Correlation with Synorogenic Sedimentation in the Magallanes Foreland Basin

The Latorre and Escarpada Formations record the earliest Late Cretaceous synorogenic sedimentation foreland of the advancing thrust belt in the Magallanes region of Chile (Mpodozis *et al.,* 2007; McAtamney *et al.,* 2011). U-Pb detrital zircon analyses from the Latorre Formation near Seno Otway indicate that it spanned the interval from 106 – 84 Ma (McAtamney *et al.,* 2011) with large peaks ~91 Ma (Mpodozis *et al.,* 2007). Provenance analyses and sandstone petrography by McAtamney *et al.* (2011) show a dominant volcanic arc signature for sediments of the Latorre Formation. These authors suggest that early thrusts that obducted the Rocas Verdes terrane prior to ~85 Ma (*e.g.* Calderon *et al.,* 2012; Klepeis *et al.,* 2010; Hervé *et al.,* 1984) were initially buried and coeval with deposition of the Latorre Formation which sampled the active volcanic arc (*c.f.* McAtamney *et al.,* 2011).

The overlying Escarpada Formation is reported to have a more complex rock composition; sandstone modal analysis and detrital zircon populations that indicate rocks

of the Rocas Verdes terrane were emergent and shedding sediment into the foreland basin by ~80-81 Ma (McAtamney *et al.,* 2011) or slightly earlier (~86 Ma, Mpodozis *et al.,* 2007). Exhumation and denudation of the Rocas Verdes terrane that was coeval with deposition of the Escarpada Formation indicates substantial hinterland shortening of the Rocas Verdes terrane prior to the Campanian propagation of the thrust front into the foreland basin (*c.f.* Fosdick *et al.,* 2011). During the Campanian, deformation propagated along the Zapata-Canal Bertrand décollement into the Late Cretaceous foreland basin where thrusts imbricated the Latorre and Escarpada Formations. Detrital zircon ages and provenance analyses from the overlying Fuentes and Rocallosa Formations (Ultima Esperanza: Tres Pasos and Dorotea Formations; Mpodozis *et al.,* 2007; Romans *et al.,* 2010; discussed above) indicate that Jurassic-Lower Cretaceous rocks of the Rocas Verdes basin were a substantial source of sediment into the foreland basin by the Maastrichtian (84-66 Ma, Mpodozis *et al.,* 2007; 70 Ma, Romans *et al.,* 2010) and into the Eocene (Barbeau *et al.,* 2009; Gambosi *et al.,* 2009). These data lend credence to the interpretation that out-of-sequence basement-involved thrusting began in the Maastrichtian and probably culminated in the Paleogene (*c.f.* Klepeis *et al.,* 2010).

5.2 Regional Kinematic Evolution of the Fold-Thrust Belt and Shortening Estimates

To help constrain the kinematic evolution of the fold-thrust belt and test for along-strike variability in tectonic shortening, I constructed and incrementally restored three strike-perpendicular, line-balanced cross sections. The northwestern section includes transects A-A', B-B' and C-C', the central section includes transects D-D' and E-E' and the southeastern-most section includes transects F-F' and G-G' (Figure 1.3). Transect H-H' was not restored because Neogene strike-slip deformation deems it unsuitable for cross-section balancing.

In each restored cross section, the depths to the lower décollements for basement-involved structures were modeled using the cross-section balancing software *LithoTect*™. Upper décollement levels were assumed to be horizontal where data did not provide adequate constraints. The Tobífera Formation is selected as a marker bed for estimating

shortening using line-length restoration as it is the most competent unit in the study area. The pin line in the Tobífera Formation where shortening estimates were measured is marked with a red line in each cross section (*e.g.* Figure 1.17a). In most locations hanging wall cutoffs are eroded; to be conservative and minimize shortening estimates, the hanging wall cutoffs were constructed as close to the corresponding footwall cutoffs as possible. In all of the restored cross-sections, shortening within the Cordillera Darwin Metamorphic Complex below the lower décollement is shown schematically where polyphase folding accommodates shortening that is detached from the overlying cover. No attempt was made to quantify internal strain in the thrust sheets. Therefore, shortening estimates should be considered minimums and are most useful when contrasted with shortening estimates made elsewhere in the fold-thrust belt (*e.g.* this study, Fosdick *et al.,* 2011; Klepeis *et al.,* 2010; Kramer *et al.,* 2003). The timing constraints associated with each stage of the restorations are from previously published data and are discussed in section 5.1.4. Incrementally restoring the composite cross-sections demonstrates how each of the structural elements, décollement levels and geologic terranes discussed above may have evolved during the formation of the thrust-belt.

5.2.1 Composite Section A-B-C, Restoration

Cross sections A-A', B-B' and C-C' each overlap at the basement-involved second generation thrust that crops out in Canal Jeronimo (Figure 1.3). Transect C-C' mostly represents the hanging wall of the fault whereas transects A-A' and B-B' are in the footwall. The southwest-dipping duplex in the Zapata-Canal Bertrand Formation along transect B-B' is floored by the Zapata-Canal Bertrand décollement (Figure 1.5h) and is projected above the Zapata-Canal Bertrand décollement on transect A-A' to form composite section ABC (Figure 1.17a). Starting in the Paleogene and working back in time, removal of slip along basement-involved structures restores 6.9 km of shortening and accounts for ~11.5% of the total shortening. The restored geometry (Figure 1.17b) retains the foreland fold-thrust belt that is detached along the Zapata-Canal Bertrand décollement and the Tobífera duplex that is detached at the basement-cover contact. At this time (Campanian-Maastrichtian) the second-generation Tobífera thrust was the active

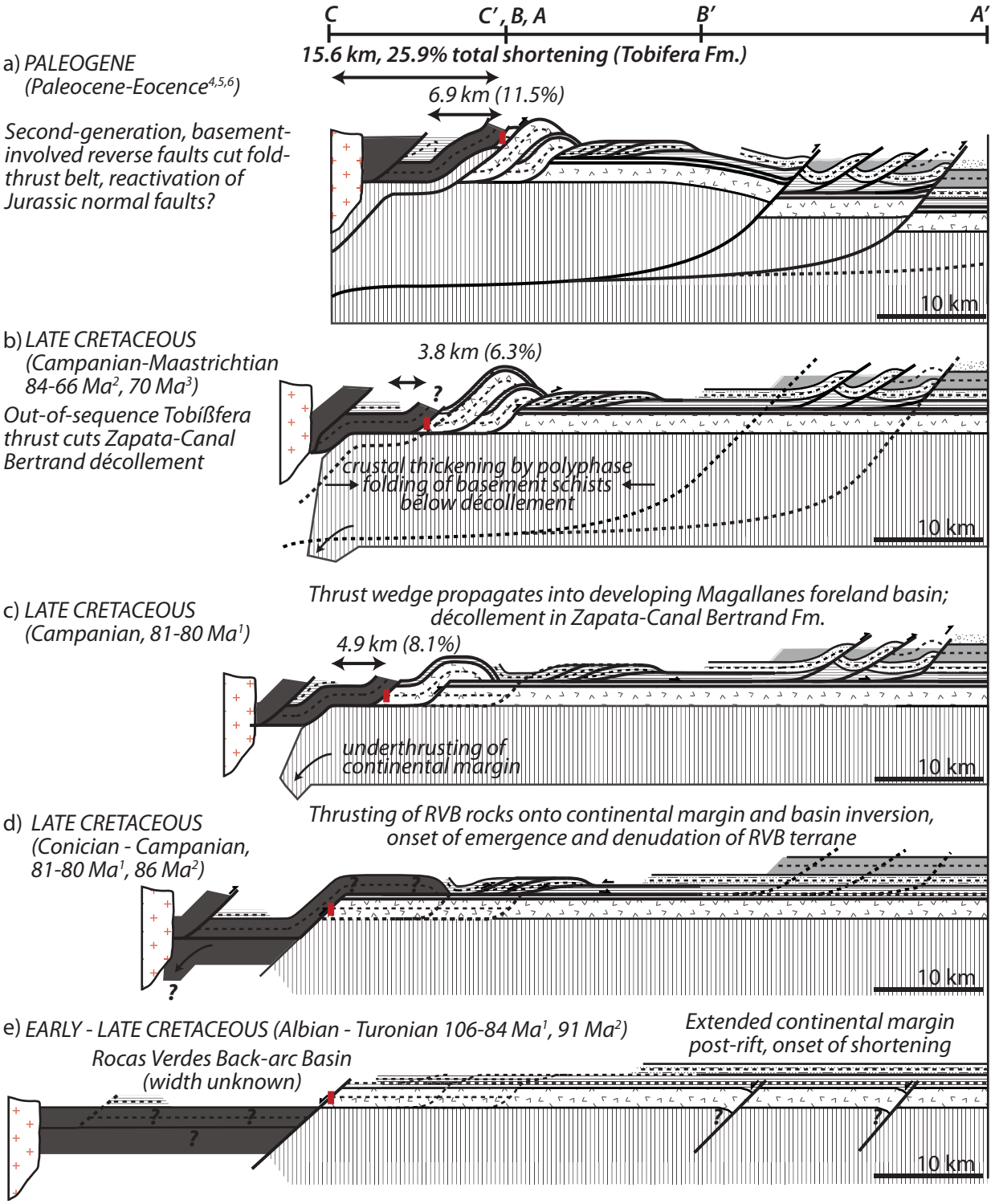
C
C′, B, A
B′
A′
15.6 km, 25.9% total shortening (Tobifera Fm.)
a) PALEOGENE
(Paleocene-Eocence[4,5,6])
6.9 km (11.5%)
Second-generation, basement-involved reverse faults cut fold-thrust belt, reactivation of Jurassic normal faults?
10 km
b) LATE CRETACEOUS
(Campanian-Maastrichtian
84-66 Ma[2], 70 Ma[3])
3.8 km (6.3%)
Out-of-sequence Tobífera thrust cuts Zapata-Canal Bertrand décollement
crustal thickening by polyphase folding of basement schists below décollement
10 km
Thrust wedge propagates into developing Magallanes foreland basin; décollement in Zapata-Canal Bertrand Fm.
c) LATE CRETACEOUS
(Campanian, 81-80 Ma[1])
4.9 km (8.1%)
underthrusting of continental margin
10 km
Thrusting of RVB rocks onto continental margin and basin inversion, onset of emergence and denudation of RVB terrane
d) LATE CRETACEOUS
(Conician - Campanian,
81-80 Ma[1], 86 Ma[2])
10 km
e) EARLY - LATE CRETACEOUS (Albian - Turonian 106-84 Ma[1], 91 Ma[2])
Extended continental margin post-rift, onset of shortening
Rocas Verdes Back-arc Basin
(width unknown)
10 km

Figure 1.17

Figure 1.17. (a) Composite profile A-B-C constructed from profiles A-A', B-B' and C-C' near Canal Jeronimo and Seno Otway presented in this study see text for details. (b-e) incrementally restored cross sections showing the kinematic evolution of the thrust belt and positions of major décollements discussed in text. The red line marks the position of the footwall cutoff in the Tobífera Fm. to which shortening estimates are measured. Incremental shortening estimates are labeled. Basement shortening and thickening is shown schematically in each step to reflect pervasive strain. Restoration of the Rocas Verdes Terrane in (d-e) is schematic due to paucity of data. Data sources: 1, McAtamney *et al*. (2011); 2, Mpodozis *et al*. (2007); 3, Romans *et al*. (2010); 4, Barbeau *et al*. (2009); 5, Gombosi *et al*. (2009); 6, Fosdick *et al*. (2011).

fault and cuts the Zapata-Canal Bertrand duplex. Restoring the second-generation Tobífera thrust accounts for an additional 3.8 km (6.3%) of shortening (Figure 1.17c). During the Campanian, the first thrust in the Tobífera duplex was active and transfers slip from the décollement at the base of the Tobífera Formation over a ramp into the Zapata-Canal Bertrand décollement allowing deformation to propagate into the foreland basin. Restoring the first-generation Tobífera thrust accounts for an additional 4.9 km (8.1%) of shortening and balances the total shortening in the foreland fold-thrust belt above the Zapata-Canal Bertrand décollement. A kinematic restoration to this stage (Conician-Campanian, Figure 1.17d) yields a total of 15.6 km (~26%) shortening of the Tobífera Formation.

Although the paucity of data from the Rocas Verdes Terrane in the study area does not warrant shortening estimates, field relations indicate that the first thrusts to form partially obducted the Rocas Verdes Terrane onto the continental margin and formed a décollement in the shale and turbidites of the Zapata and Zapata-Canal Bertrand Formations (schematically drawn in Figure 1.17d-e). Restoring shortening in the Zapata-Canal Bertrand duplex extends the original length of the Zapata-Canal Bertrand Formation entirely over the top of the Tobífera Formation (Figure 1.17e), a constraint that requires the Zapata-Canal Bertrand duplex to have formed before any motion along the Tobífera thrust sheets. This constraint suggests that the Zapata-Canal Bertrand décollement was the first active décollement and is supported by structural observations from transect C-C' (Figure 1.5a) that indicate the Tobífera duplex is structurally below the Rocas Verdes basin terrane. Our interpretation is consistent with structural studies elsewhere in Patagonia that conclude the first thrusts to form partially obducted the oceanic floor of the Rocas Verdes basin basin (Nelson *et al*., 1980; Klepeis *et al*., 2010; Fosdick *et al*., 2011; Calderon *et al*. 2012).

5.2.2 Composite Section D-E, Restoration

Along-strike ~20 km toward the southeast, Estuario Wickham (section D-E; Figure 1.3, 1.9, 1.18a) preserves important exposures of the second-generation basement fault, the Zapata-Canal Bertrand Triangle zone, and the passive-roof thrust in the Latorre

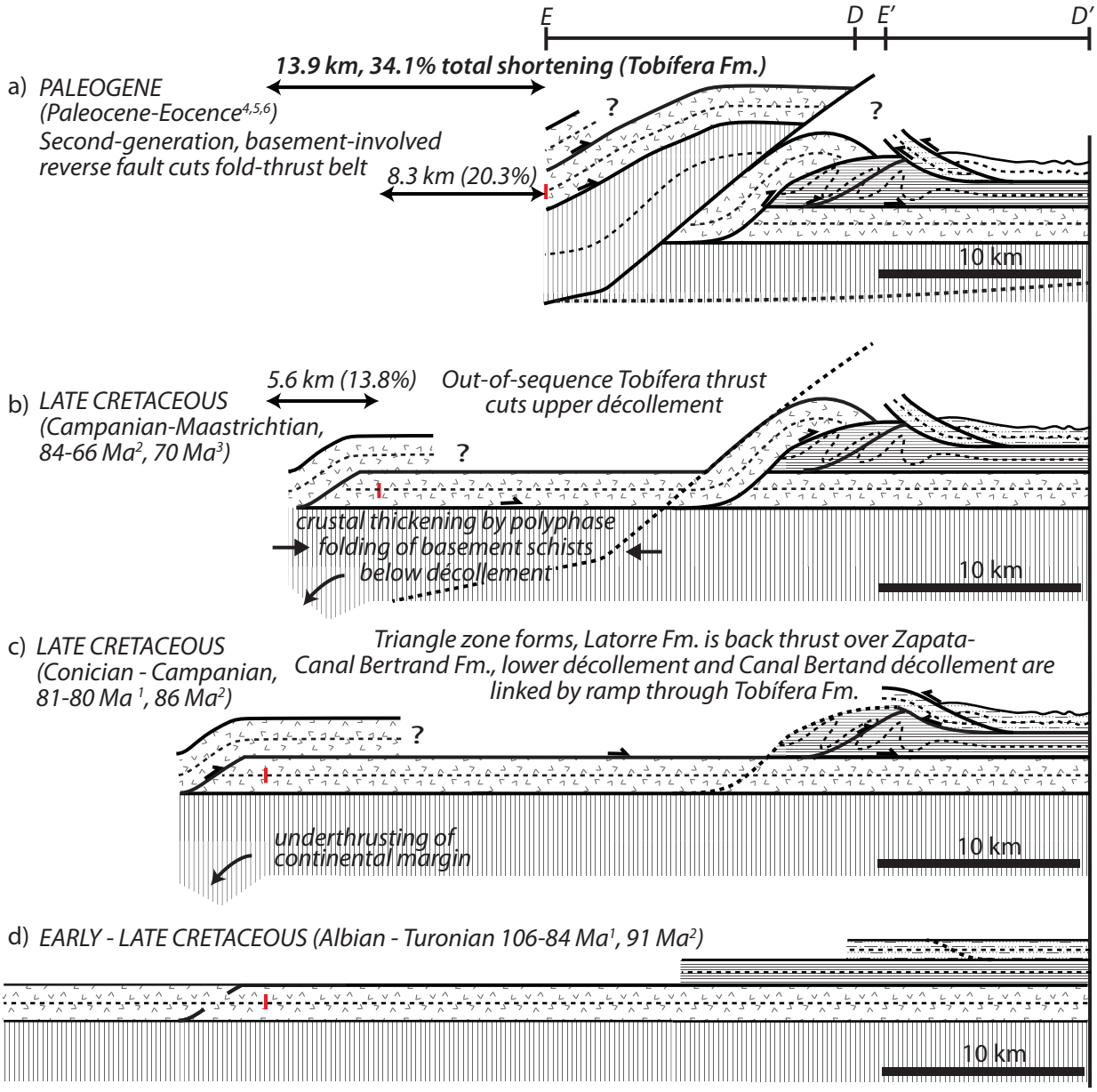

Figure 1.18. (a) Composite profile D-E constructed from profiles D-D' and E-E' at Estuario Wickham presented in this study. (b-d) incrementally restored cross sections showing the kinematic evolution of the thrust belt and positions of the Canal Bertrand triangle zone and Latorre back thrust discussed in text. The red line marks the position of the footwall cutoff in the Tobífera Fm. to which shortening estimates are measured. Incremental shortening estimates are labeled. Data sources as in Figure 1.17.

Formation. Beginning in the Paleogene, removing displacement along the basement-involved reverse fault accounts for 8.3 km (20.3%; Figure 1.17b) of shortening. During the Campanian-Maastrichtian, the active décollement occurred at the base of the Tobífera Formation and ramped up section to cut the Zapata-Canal Bertrand triangle zone. Restoring displacement along the second-generation Tobífera thrust accounts for an additional 5.6 km (13.8%) of shortening, yielding a total of 13.9 km (~34%; Figure 1.18a-c). During the Coniacian-Campanian (Figure 1.18c), the décollement at the base of the Tobífera Formation ramped up section and transferred displacement to the Zapata-Canal Bertrand décollement forming a triangle zone and allowing the propagation of the thrust sheet into the foreland basin. Although the hanging wall cutoffs are eroded, Figure 1.18d shows a schematic restoration of the triangle zone and Zapata-Canal Bertrand décollement to the Early Cretaceous.

5.2.3 Composite Section F-G, Restoration

Exposures along transect F-F' and G-G', >20 km along-strike toward the southeast, include the second-generation basement fault and Zapata-Canal Bertrand triangle zone near Estuario Silva Palma, as well as the basal décollement in the basement schist exposed near Bahía Fortesque. Composite transect F-G was constructed by combining the two sections at the base of the Tobífera Formation where it crops out at the southwestern end of F-F' and northeastern end of G-G' (Figure 1.8, 1.10, 1.14, 1.19a). Beginning in the Paleogene, removing displacement along the second-generation basement thrust accounts for 7.9 km (19.6%) of shortening (Figure 1.19a-b). During the Campanian-Maastrichtian, the active décollement level is the base of the Tobífera Formation where it truncates the Zapata-Canal Bertrand triangle zone. Toward the hinterland, the décollement dips shallowly (~6°) toward the southwest and is defined by a ~1 km thick shear zone exposed near Bahía Fortesque (Figure 1.19b). Restoring displacement along the second-generation Tobífera thrust accounts for an additional 6 km (14.8%) of shortening (Figure 1.19c). By the Conician-Campanian, a ductile décollement that formed below the basement-cover contact ramped up-section through the Tobífera

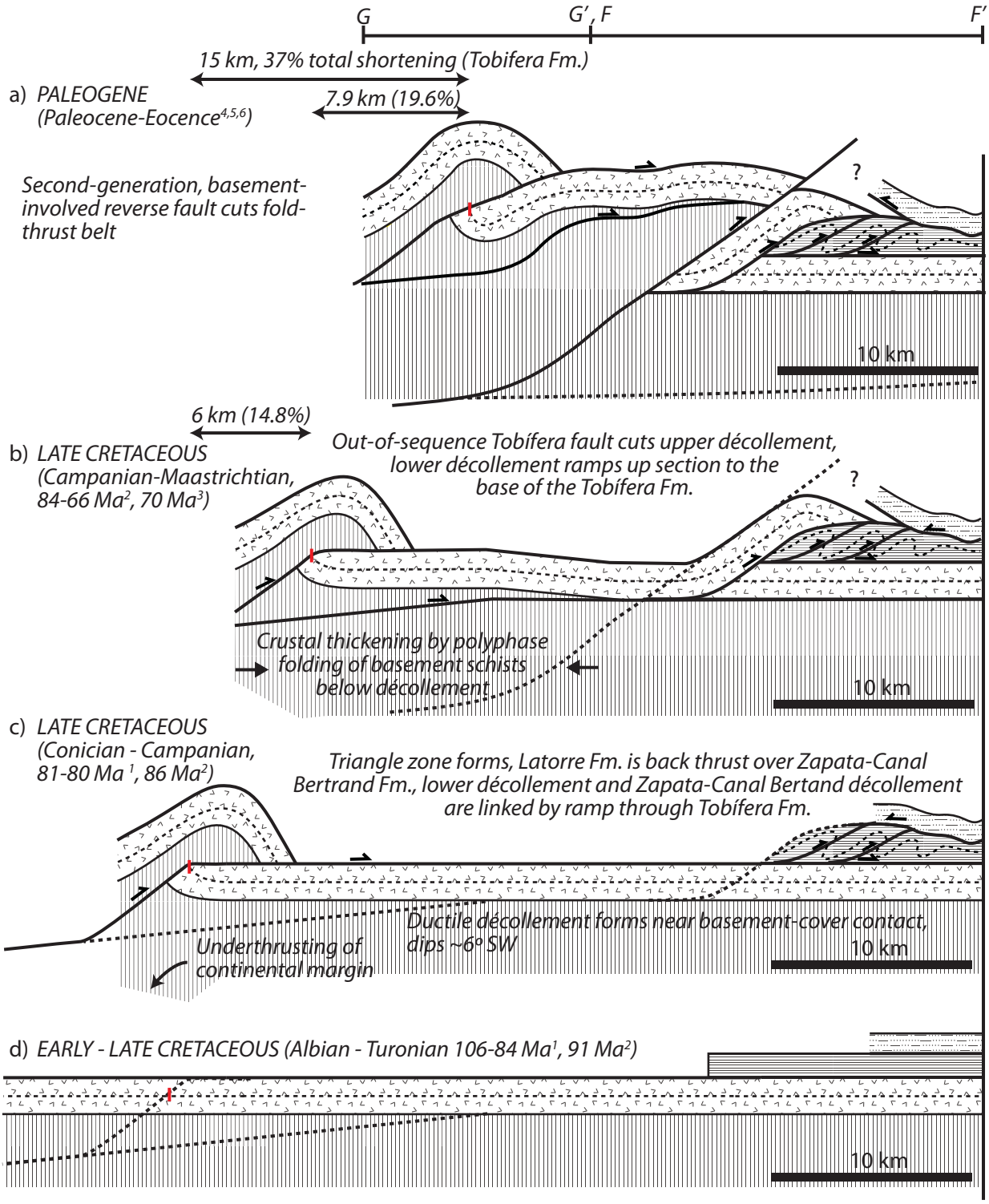
G
G', F
F'
15 km, 37% total shortening (Tobifera Fm.)
a) PALEOGENE
(Paleocene-Eocence[4,5,6])
7.9 km (19.6%)
Second-generation, basement-involved reverse fault cuts fold-thrust belt
?
10 km
6 km (14.8%)
b) LATE CRETACEOUS
(Campanian-Maastrichtian,
84-66 Ma[2], 70 Ma[3])
Out-of-sequence Tobífera fault cuts upper décollement, lower décollement ramps up section to the base of the Tobífera Fm.
?
Crustal thickening by polyphase folding of basement schists below décollement
10 km
c) LATE CRETACEOUS
(Conician - Campanian,
81-80 Ma [1], 86 Ma[2])
Triangle zone forms, Latorre Fm. is back thrust over Zapata-Canal Bertrand Fm., lower décollement and Zapata-Canal Bertand décollement are linked by ramp through Tobífera Fm.
Ductile décollement forms near basement-cover contact, dips ~6° SW
Underthrusting of continental margin
10 km
d) EARLY - LATE CRETACEOUS (Albian - Turonian 106-84 Ma[1], 91 Ma[2])
10 km

Figure 1.19

Figure 1.19. (a) Composite profile F-G constructed from profiles F-F' and G-G' near Estuario Silva Palma and Bahía Fortesque presented in this study. (b-d) Incrementally restored cross sections showing the kinematic evolution of the thrust belt and positions of the basal ductile décollement, Zapata-Canal Bertrand triangle zone and Latorre back thrust discussed in text. The red line marks the position of the footwall cutoff in the Tobífera Fm. to which shortening estimates are measured. Incremental shortening estimates are labeled. Basement shortening and thickening is shown schematically in each step to reflect pervasive strain below the lower décollement. The dip of the lower décollement was determined using the structural modeling software LithoTect™. Data sources as in Figure 1.17.

Formation and transferred material onto the Zapata-Canal Bertrand décollement where a triangle zone formed at the tip of the thrust wedge. Figure 1.19d shows the complete restoration of the thrust belt to the Early Cretaceous and accounts for an additional 1 km (2.6%) shortening in the footwall syncline beneath the basement ramp. Total shortening estimates from composite transect F-G indicates ~14.9 km or 37% shortening (Figure 1.19).

5.2.4 Kinematic Synthesis

Incrementally restored line-balanced cross sections from three composite cross sections in the study area demonstrate that the kinematic evolution of the thrust-belt is characterized by multiple décollement levels that are linked by thrust ramps and get progressively deeper through time. Figure 1.20 highlights elements of the fold-thrust belt that correlate well for over ~100 km along-strike in the study area. The first thrusts to form partially obducted the Rocas Verdes basin rocks onto the continental margin prior to the Campanian and formed an early décollement in the Late Jurassic-Early Cretaceous shale (Zapata-Canal Bertrand Formation) that crops out along sections A-B-C and H (Figure 1.20). During this stage (Conician-Campanian), a low-taper triangle zone developed in the shale at the tip of the propagating thrust wedge, and the earliest synorogenic turbidites (Latorre Formation) were passively back thrust over the tip of the wedge (Figure 1.20, sections D-E, F-G). Continued shortening during the Campanian resulted in the deepening of the basal décollement to <1 km below the basement-cover contact. Thrust ramps cut the Tobífera Formation and linked the basal décollement with the Zapata-Canal Bertrand décollement (Figure 1.20, sections A-B-C, F-G). Shortening of the Tobífera Formation propagated deformation into the foreland basin along the Zapata-Canal Bertrand décollement (Figure 1.20, sections A-B-C, H). Below the basal décollement and toward the hinterland, polyphase folding that was detached from the overlying cover shortened the basement schist. Continued shortening prior to the end of the Maastrichtian resulted in a second phase of out-of-sequence thrusting and the

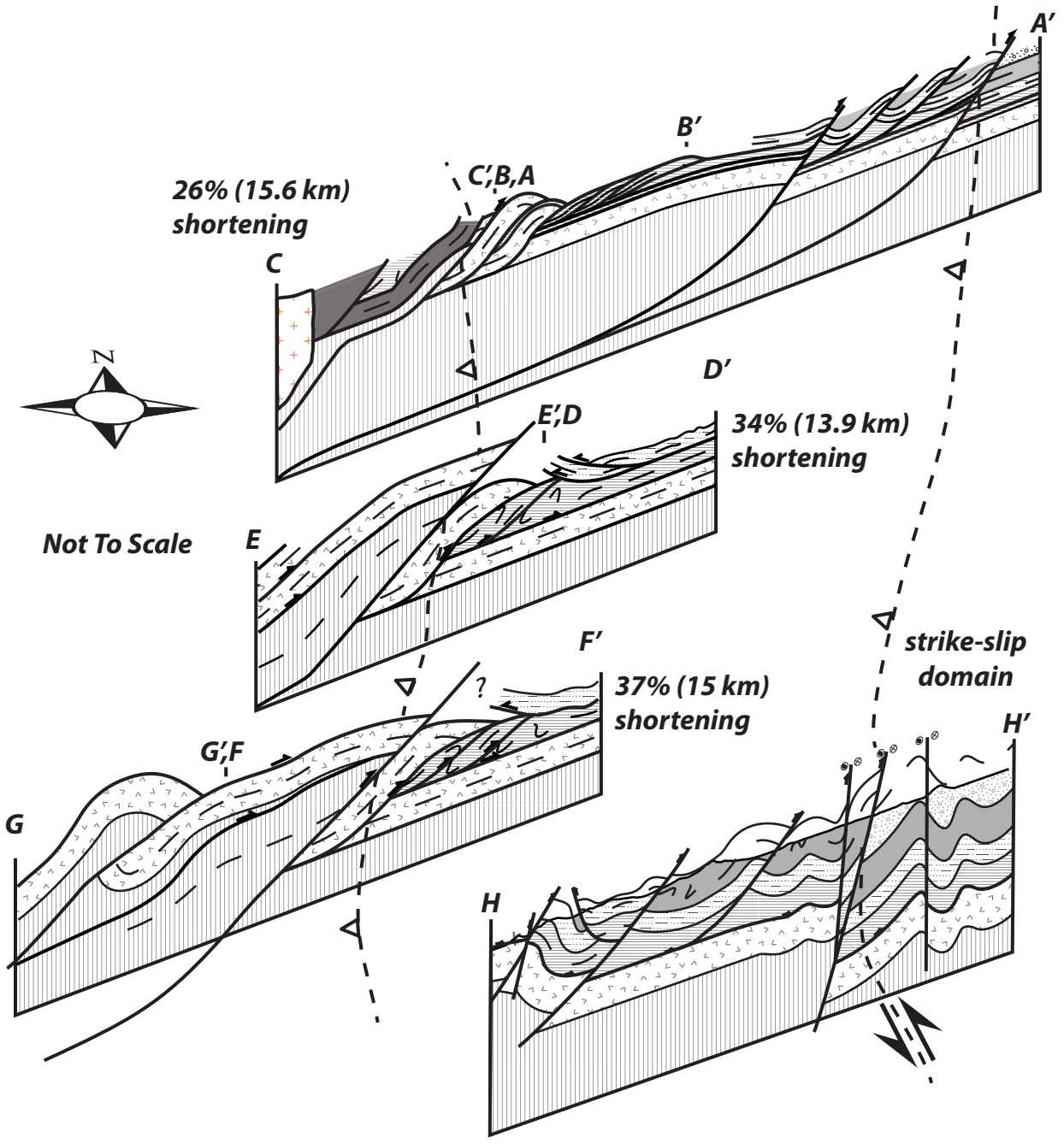

Figure 1.20. Cross-section correlation of the study area showing the approximate relative positions of composite cross sections A-B-C, E-D, F-G and H, not to scale. The dashed line shows the approximate map trace of the second-generation basement fault that exposes the Cordillera Darwin metamorphic complex in the hanging wall. Total shortening estimates for each section are labeled. See text for details.

formation of thick-skinned basement-involved reverse faults that cut the early décollements, culminated in the Paleogene and reactived Jurassic normal faults. Neogene strike-slip deformation overprinted the fold-thrust belt toward the southeast (Figure 1.20, section H). Shortening estimates suggest a systematic along-strike increase in tectonic shortening from ~26% in northwestern localities to ~37% toward the southeast.

Shortening estimates from this study correlate well with regional structural models that predict along-strike increase in tectonic shortening from northwest to southeast that occurred during the Late Cretaceous—Paleogene (*e.g.* Kraemer, 2003). Because the calculated shortening magnitudes are estimates, and are measured in different parts of the fold-thrust belt due to limited exposure, comparing the shortening percentages along-strike is an objective way to evaluate if there is a systematic southeastward increase in shortening. In the Ultima Esperanza region of Chile, Fosdick *et al*. (2011) report minimum shortening of 19% (~32 km), in contrast to ~70% of shortening (~100 km) of the Cordillera Darwin Metamorphic Complex reported by Klepeis *et al*. (2010) near Tierra del Fuego to the southeast. Our results support regional models by showing a ~11% increase in shortening (26-37%) over ~100 km along-strike between Ultima Esperanza and Tierra del Fuego (Figure 1.1).

Regional shortening estimates also are consistent with paleomagnetic data (Dalziel 1973; Burns *et al*., 1980; Rapalini *et al*., 2001, 2007) that suggest a large (up to 90°) counterclockwise rotation of the Patagonian-Fuegian arc since a Cretaceous remagnetization event. Along-strike increase in shortening and bending of the orogen may reflect the closure of an initially wedge-shaped Rocas Verdes basin that was wider toward the south (Stern & De Wit, 2003). Recent plate reconstructions (Dalziel *et al*., 2013) indicate that the Antarctic Peninsula was situated outboard of the Patagonian-Fuegian arc and possibly acted as a collider (*c.f.* Hervé *et al*., 2005), closing the Rocas Verdes basin as the South American plate moved westward relative to the Antarctic plate by the Early Cretaceous. Thus this collision would provide a likely mechanism for the bending of the volcanic arc and for the systematic increase in shortening toward the southeast.

6. Conclusions

New mapping presented in this study reveals the structure and kinematic evolution of the Patagonian fold-thrust belt over 100 km^2 on Peninsula Brunswick within the Magallanes region of Chile that formed between the Late Cretaceous and Paleogene. Results show that the thrust-belt developed during two main phases of deformation characterized by multiple décollement levels that become deeper through time. A preexisting mechanical stratigraphy defined by relatively weak shale deposits from the antecedent Jurassic Rocas Verdes basin and ductilly deformed schist of the continental margin controls the stratigraphic positions of the décollements.

The first phase of deformation occurred in the Conician-Campanian and is characterized by top-northeast thin-skinned thrusting of the mafic floor of the Rocas Verdes basin onto the continental margin along an upper décollement that formed within relatively weak shale deposits. This early stage of thin-skinned thrusting is contemporaneous with the deposition of the first sediments into the Magallanes foreland basin (Latorre and Escarpada Formations). Continued shortening resulted in the formation of a ductile décollement <1 km below the basement-cover contact. By the Campanian, thrust ramps with top-northeast displacements cut competent volcanic rocks of the Tobífera Formation, linked the lower and upper décollements, and transferred displacement into the nascent Magallanes foreland basin. A triangle zone cored by weak shale (Zapata-Canal Bertrand Formation) formed at the tip of the propagating thrust wedge as it advanced into the Magallanes foreland basin. Below the lower décollement and toward the hinterland, shortening in the basement schist was accommodated by polyphase folding and crystal plasticity, and it was entirely detached from the overlying fold-thrust belt. Continued shortening beginning in the Maastrichtian resulted in second phase of out-of-sequence thrusting that cut the early décollements, culminated in the Paleocene-Eocene and was defined by thick-skinned basement-involved faults that juxtapose basement schist of the Cordillera Darwin Metamorphic Complex against the overlying fold-thrust belt. Thick-skinned basement-involved faults are interpreted as

compressional reactivations of Jurassic normal faults and probably reflect the complete closure of the Rocas Verdes basin and collision of the Patagonian arc.

Shortening estimates from three incrementally restored line-balanced cross sections across the Magallanes fold-thrust belt indicate an 11% along-strike increase in tectonic shortening from 26% in the northwest to 37% toward the southeast that occurred between Turonian and Paleogene time. Shortening estimates from this study are consistent with regional tectonic models that predict an along-strike increase in tectonic shortening from the Ultima Esperanza region of Chile (~19%, Fosdick *et al.,* 2011) along the trend of the orogen toward the southeast through the Magallanes region of Chile (this study, 26-37%) to Tierra del Fuego (~70%, Klepeis *et al.,* 2010). Results show good correlations of both thin- and thick-skinned structures along the trend of the Patagonian fold-thrust belt for >400 km from Ultima Esperanza to Tierra del Fuego and suggest that the development of the Patagonian orocline at least partly occurred between the Late Cretaceous and Paleogene. Shortening estimates are also consistent with paleomagnetic data that indicates a post-Cretaceous counterclockwise rotation of the Patagonian arc. Mechanisms that caused increased shortening toward the southeast include the closing an initially wedge-shaped Rocas Verdes basin that was wider and deeper toward the southeast as well as counterclockwise bending of the Patagonian arc as South America moved westward relative to Antarctica by the Cretaceous.

In southeast of the study area near the Estrecho de Magallanes, left-lateral strike-slip faults cut both folds and thrust faults and reactivate Late Cretaceous thrusts. Folds and corresponding axial planar cleavages that formed in the Cretaceous fold-thrust belt are tightened and rotated to upright orientations in close proximity to strike-slip faults. Left-lateral faults strike northwest-southeast parallel to the trend of the thrust belt and are probably right stepping left-lateral splays from the Magallanes-Fagnano fault zone to the south. Strike-slip faults reflect a phase of Neogene wrench tectonics that overprints the Cretaceous fold-thrust belt.

CHAPTER 2: STRUCTURAL EVOLUTION OF A DUCTILE DÉCOLLEMENT AT THE BASE OF A RETROARC FOLD-THRUST BELT, PATAGONIA, CHILE.

Abstract

During Late Cretaceous inversion of the Late Jurassic – Early Cretaceous Rocas Verdes basin in southern Chile between 53°-55° S, a high strain zone formed in continental crust, accommodating northeast-directed thrusting of Rocas Verdes basin rocks onto the continental margin and transferring displacement into a nascent Patagonian retroarc fold-thrust belt. New mapping, Electron Backscatter Diffraction (EBSD) fabric analysis and microstructural data document the kinematic evolution and deformation conditions of the high-strain zone in two locations within the fold-thrust belt.

Toward the hinterland, at Seno Martínez, mafic schists that form part of the Rocas Verdes basin were thrust above garnet-bearing chlorite schist and psammite of the Cordillera Darwin Metamorphic Complex. The schist of the Cordillera Darwin Metamorphic Complex shows a quartz/chlorite composite schistose foliation ($S_{1\text{-}2}$) that is progressively refolded by noncylindrical, tight and isoclinal folds (F_3). Beneath the thrust contact, deformation intensifies in a ~5 km thick high-strain zone that is defined by the tightening of F_3, pronounced southwest-plunging quartz lineations (L_2), and F_3 sheath folds that are subparallel to and fold L_2. C-S fabrics, C' shear bands and rotated porphyroblasts show top-northeast, foreland directed transport. Kink-folds and steeply inclined tight folds (F_4) with both north- and south-dipping axial planes (S_4) overprint D_2 and D_3 structures and are related to subhorizontal contraction during the Paleogene. Quartz textures from D_2 and D_4 fabrics are typical of subgrain rotation and grain boundary migration recrystallization equivalent to Regime 3, and quartz CPO patterns indicate basal <a> and mixed<a> and [c] slip systems. Quartz microstructures suggest deformation temperatures between 500°-650°C during D_2 -D_4 at Seno Martínez.

At Bahía Gallant, ~75 km toward the foreland, volcanoclastic rocks that are part of the Rocas Verdes basin terrane were thrust above Cordillera Darwin Metamorphic Complex schist along a > 1 km thick high-strain zone defined by the tightening of F_2 recumbent isoclinal folds and a prominent southwest plunging quartz lineation. C-S fabrics, C' shear bands and asymmetric quartz boudins indicate top-northeast transport. Quartz textures indicate subgrain rotation recrystallization typical of Regime 2, and quartz CPO patterns suggest dominantly basal <a> slip. Quartz microstructures suggest deformation temperatures between 400°-550°C at Bahía Fortesque. The structural position of the high-strain zone and sequence of deformation of the Cordillera Darwin Metamorphic Complex schist in each locality allows regional correlation of the high-strain zone. Quartz deformation mechanisms indicate the high-strain zone formed under greenschist facies conditions in the foreland and amphibolite facies conditions in the hinterland and thus dipped shallowly (<10°) toward the hinterland. The high-strain zone decoupled the Patagonian fold-thrust belt from the underthrust continental margin and formed a regional décollement at the base of the nascent retroarc fold-thrust belt.

1. Introduction

The Patagonian Andes record a phase of Late Cretaceous-Paleogene crustal contraction that resulted in the closure and inversion of a marginal basin, known as the Rocas Verdes basin, and subsequent formation of the Magallanes foreland basin and Patagonian retroarc fold-thrust belt. These events define the Andean Orogeny in the southernmost Andes (Dalziel and Palmer, 1979, Nelson *et al*., 1980; Klepeis *et al*., 2010). A belt of metamorphic rocks known as the Cordillera Darwin Metamorphic Complex (Kranck, 1932; Nelson *et al*., 1980; Hervé *et al*., 2010) located in Tierra del Fuego in southern Chile, record deformation and syntectonic moderate to high pressure metamorphism that occurred during the late-Cretaceous – Paleogene orogeny (Nelson *et al*., 1980; Kohn, 1993; Klepeis *et al*., 2010; Maloney *et al*., 2011). Metamorphic rocks of

the Cordillera Darwin Metamorphic Complex form the local 'basement' and are tectonically juxtaposed against volcanic and sedimentary 'cover' rocks of the Rocas Verdes basin and Magallanes foreland basin that now form part of the Patagonian retroarc fold-thrust belt (Klepeis, 1994; Kohn *et al*., 1995; Klepeis *et al*., 2010; Maloney *et al*., 2011). The juxtaposition of polydeformed moderate to high pressure metamorphic rocks against a coeval retroarc fold-thrust belt provide a unique opportunity to study possible kinematic relationships between polyphase deformation that occurs in metamorphic 'basement' and the development of an overlying fold-thrust belt. In this chapter, I report on the kinematic evolution of polydeformed schists of the Cordillera Darwin Metamorphic Complex, where they are tectonically interleaved with the Patagonian retroarc fold-thrust belt, to understand how base of a retroarc fold-thrust belt interacts with its plastically deformed 'basement'.

The study areas, located along the western margin of the Cordillera Darwin Metamorphic Complex near Seno Martínez and the southern end of Peninsula Brunswick near Bahía Fortesque and Estuario Silva Palma (Figure 2.1), preserve important contacts between the Cordillera Darwin Metamorphic Complex and overlying volcanic and volcanoclastic strata of the Rocas Verdes marginal basin. Near Bahía Fortesque, the contact is sheared and rocks of Cordillera Darwin Metamorphic Complex are imbricated with the rocks of Rocas Verdes basin to form the hinterland domain of the Patagonian retroarc-fold thrust belt. Retrodeformed line-balanced cross sections of the Patagonian fold-thrust belt predict that the sheared contact is part of a regional décollement that detaches the Patagonian fold-thrust belt from polydeformed 'basement' schist of the Cordillera Darwin Metamorphic Complex (*i.e*. Chapter 1). Here, I test the hypothesis that the shear zone recognized near Bahía Fortesque forms part of a regional décollement between polydeformed basement of the Cordillera Darwin Metamorphic Complex and the overlying strata and structures of the Patagonian retroarc fold-thrust belt. Testing this hypothesis is important for several reasons: 1) previous workers have identified similar shear zones that accommodated Late Cretaceous craton-vergent thrusting of Rocas Verdes rocks onto the continental margin elsewhere in southern

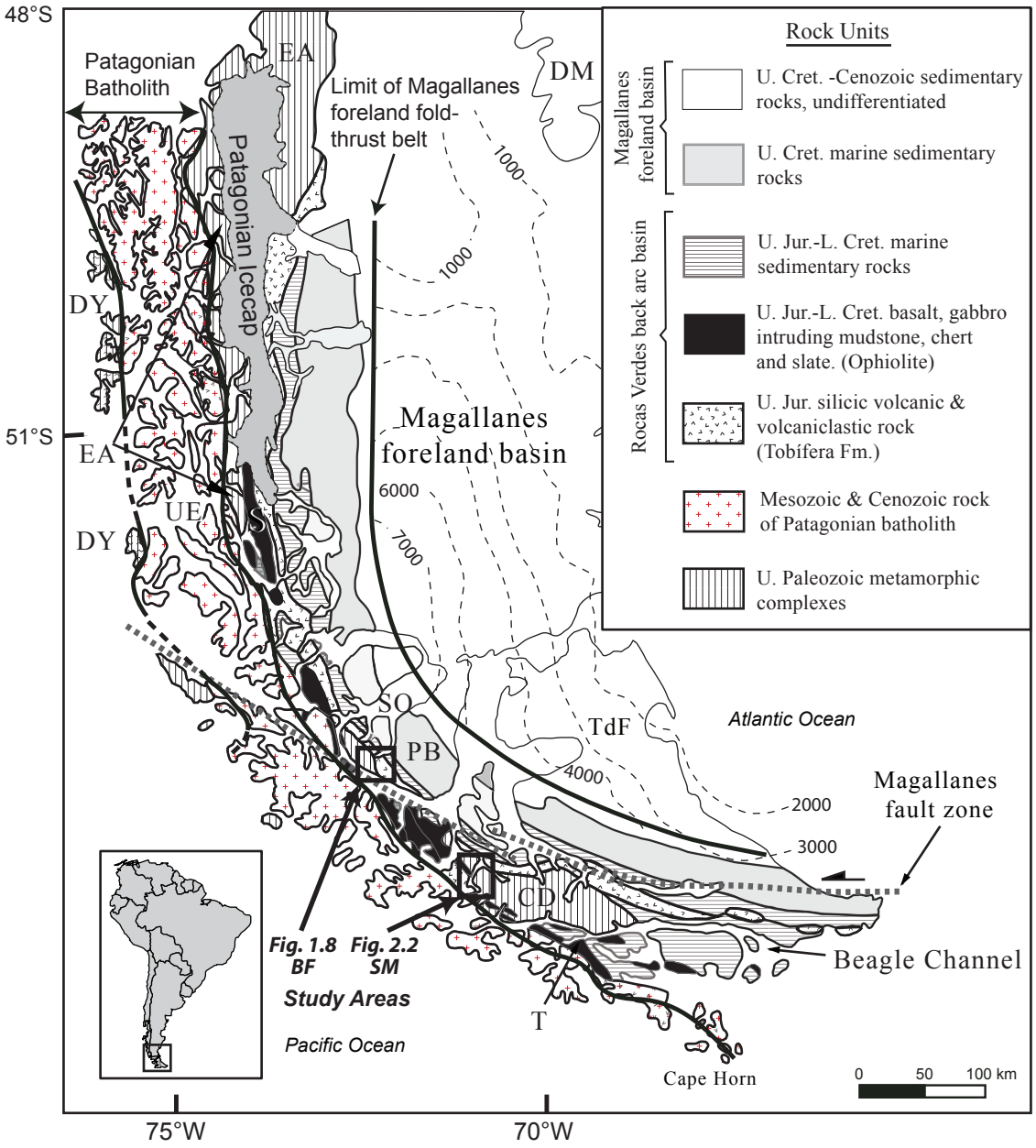

Figure 2.1. Simplified geologic map of the southernmost Andes showing tectonostratigraphic provinces, modified from McAtamney *et al.* (2011); Fildani and Hessler (2005). Contours (thin dashed lines) show sediment isopach overlying Jurassic volcanic rocks after Biddle *et al.* (1986). Metamorphic complexes include Cordillera Darwin (CD), Eastern Andes (EA), Duque de York, (DY), the Deseado Massif (DM). Ophiolitic suites include the Sarmiento (S) and Tortuga (T) complexes. BF, Bahía Fortesque; SM, Seno Martínez; UE, Ultima Esperanza; SS, Seno Skyring; SO, Seno Otway; PB, Peninsula Brunswick; TdF, Tierra del Fuego. Boxes show location of the study areas shown in figure 1.8 and figure 2.2.

Patagonia, indicating that the décollement may be a regional structure (Nelson *et al*., 1980; Calderón *et al*., 2012; Klepeis *et al*., 2010); 2) the depth of the exposure in the study is at the basement-cover contact and provides a good opportunity to study the kinematic relationship between polyphase ductile deformation of 'metamorphic basement' and the development of a coeval retroarc fold-thrust belt; and 3) polyphase deformation below a regional décollement may provide a mechanism for crustal thickening below and toward the hinterland of retroarc fold-thrust belts in other orogenic systems that cannot be entirely accounted for by shortening of a fold-thrust belt (*e.g*. Eastern Cordillera, McQuarrie *et al*., 2005).

I present new mapping and field-based descriptions of polydeformed rocks of the Cordillera Darwin Metamorphic Complex in two study areas near the basement-cover contact. I also contribute new microstructural and crystallographic preferred orientation (CPO) analyses of deformed rocks with the goal of understanding the kinematic development and deformation conditions of the basement schist and their kinematic relationship with the overlying fold-thrust belt. Results from this study confirm the occurrence of a regional décollement at the contact between volcanic rocks of the Rocas Verdes basin and the Cordillera Darwin Metamorphic Complex and constrain its structural evolution.

2. Geologic setting

2.1 The Cordillera Darwin Metamorphic Complex

The Cordillera Darwin is a topographic high that defines the apex of the Fuegian Andes. It is a ~5000 km^2 metamorphic massif of pelite, psammite and orthogneiss of lower greenschist to upper amphibolite grade known as the Cordillera Darwin Metamorphic Complex (Kranck, 1932; Nelson *et al*., 1980; Kohn *et al*., 1995; Hervé *et al*., 2003, 2010; Klepeis *et al*., 2010). Detrital zircon populations from meta-sedimentary rocks of the Cordillera Darwin Metamorphic Complex yield both Ordovician-Devonian and Carboniferous-Permian depositional ages (Barbeau *et al*., 2009; Hervé *et al*., 2010)

and are interpreted to record Paleozoic sedimentation along the continental margin of Gondwana (Hervé *et al*., 2010). Paleozoic sedimentary rocks of the Cordillera Darwin Metamorphic Complex are entirely overprinted by Cretaceous – Paleocene metamorphism and deformation that defines the Andean Orogeny in the southernmost Andes (Klepeis *et al*., 2010; Kohn *et al*., 1993; M. J. Kohn *et al*., 1995; Nelson *et al*., 1980).

Near the Beagle Channel (Figure 2.1), upper amphibolite grade mineral assemblages that include sillimanite, kyanite, staurolite and garnet record Late Cretaceous peak metamorphic conditions of P = 12 kbar and T = 620°C (Kohn *et al*., 1993; Maloney *et al*., 2011). The margins of the Cordillera Darwin Metamorphic Complex are dominantly comprised of chlorite-, biotite- and garnet-bearing lower-greenschist facies pelitic and psammitic rocks, thus forming an antiformal dome with the highest metamorphic grade exposed in the core of the orogen (Klepeis *et al*., 2010; Kohn *et al*., 1993; Nelson *et al*., 1980). A suite of Late Jurassic granitic orthogneiss known as the Darwin Granite intrudes pelitic and psammitic rocks of the Cordillera Darwin Metamorphic Complex and displays equivalent amphibolite-grade metamorphic mineral assemblages as the host rock.

Several generations of Late Cretaceous structures that record crustal shortening and thickening during the Andean Orogeny pervasively deform orthogneiss and schist of the Cordillera Darwin Metamorphic Complex. The pioneering work of Nelson *et al*. (1980) described in detail for the first time three main phases of deformation. An early phase of north-vergent shearing and folding is overprinted by a subsequent phase of bivergent (top-north and south) conjugate folding and shearing. Top-south back thrusting and the development of a pervasive north-dipping crenulation cleavage characterize a latter phase of shortening. Recent work by Klepeis *et al*. (2010) describe imbricated, northeast-vergent first-generation ductile thrusts near the Beagle Channel that place the basaltic floor of the Rocas Verdes basin onto the continental margin. Upper Cretaceous post-tectonic granitic plutonic rocks and pegmatite dikes (~86 Ma, Herve *et al*., 1984; Klepeis *et al*., 2010; *see also* Mukasa and Dalziel, 1996) intrude and cut the thrusts,

indicating that obduction of the Rocas Verdes basin floor occurred by the Late Cretaceous. Two latter stages of deformation reported by Klepeis *et al*., (2010) are characterized by bivergent (north- and south-vergent) folding and thrusting of high-grade rocks in the core of the orogen that are now exposed near the Beagle Channel. Here, back-thrusts and back folds (south-vergent) formed pop-up structures that thickened and uplifted the hinterland of the orogen and accommodated ~70% horizontal shortening (Klepeis *et al*., 2010; *see also* Dalziel and Cortés, 1972; Nelson *et al*., 1980).

In support of these interpretations, pseudosection modeling and *in situ* monazite geochronology of retrogressed mineral assemblages from second-generation fabrics within the high-grade core of the Cordillera Darwin Metamorphic Complex show that exhumation was underway by ~73 Ma [*Maloney et al*., 2011] and is consistent with P-T-t pathways calculated for sillimanite-, kyanite-, staurolite- and garnet-bearing mineral assemblages from the Cordillera Darwin Metamorphic Complex presented by Kohn *et al*. (1995). Uplift and exhumation of the Cordillera Darwin Metamorphic Complex continued well into the Paleogene and was partly accomplished by uplift in the hanging walls of thick-skinned basement involved reverse faults (Barbeau *et al*., 2009; Gombosi *et al*., 2009; Kohn *et al*., 1995).

2.2 The Rocas Verdes basin and Patagonian Batholith

An Upper Jurassic – Lower Cretaceous succession of volcanic, volcanoclastic and marine sedimentary rocks overly the Cordillera Darwin Metamorphic Complex (Figure 2.1). Silicic volcanic and volcanoclastic rocks known as the Tobífera Formation unconformably overlie the Cordillera Darwin Metamorphic Complex and record widespread silicic volcanism associated with a Late Jurassic phase of continental rifting during the breakup of Gondwana (Dalziel and Cortés, 1972; Natland, 1974; Bruhn *et al*., 1978; Gust *et al*., 1985; Hanson and Wilson, 1991; Pankhurst *et al*., 2000; Pankhurst *et al*., 2003). Contemporaneous with rift-related volcanism, a suite of bimodal, calc-alkaline intrusive rocks that are part of the Patagonian Batholith, now preserved in the Ultima Esperanza region of Chile, record the earliest pulses of arc magmatism along the Pacific margin of Gondwana in the southernmost Andes (Hervé *et al*., 1984; Bruce *et al*., 1991;

Hervé *et al*., 2007; Calderón *et al*., 2007). Protracted continental extension during the Jurassic resulted in the formation of a marginal basin located between the Patagonian arc and the extended continental margin; known as the Rocas Verdes basin (Dalziel, *et al*., 1974; Dalziel, 1981). Extension in the Rocas Verdes basin led to the generation of new quasi-oceanic crust that is now preserved in the Sarmiento and Tortuga complexes of southern Chile (Figure 2.1, Stern & De Wit, 2003; Calderón *et al*., 2007) and the Larsen Harbour Complex of South Georgia (Mukasa and Dalziel, 1996). The Rocas Verdes basin was filled with a thick succession (>2 km) of Upper Jurassic – Lower Cretaceous marine hemipelagic mudstones and turbidites (Dalziel *et al*., 1975; Suárez *et al*., 1976; Winn and Dott, 1979; Storey and Macdonald, 1984; Wilson, 1991; Fildani & Hessler, 2005; Mpodozis *et al*., 2007; McAtamney *et al*., 2011).

2.3 The Magallanes foreland basin and Patagonian fold-thrust belt

Crustal thickening recorded by structures and prograde metamorphic textures in the Cordillera Darwin Metamorphic Complex (*e.g*. Nelson *et al*., 1980; Kohn *et al*., 1993; 1995; Mpodozis & Rojas, 2006; Klepeis *et al*., 2010; Maloney *et al*., 2011) was contemporaneous with the development of the Magallanes Foreland basin and Patagonian fold-thrust belt (Figure 2.1, *e.g*. Fildani *et al*., 2003; Fildani and Hessler, 2005; Romans *et al*., 2010; Zahid and Barbeau, 2010; Mpodozis *et al*., 2007; McAtamney *et al*., 2011). Shortening resulted in the development of a thin-skinned thrust belt by the Late Cretaceous that propagated into the foreland basin and imbricated strata of the Rocas Verdes basin with that of the Magallanes Foreland basin (Alvarez-Marrón *et al*., 1993; Klepeis *et al*., 1994; Ghiglione and Ramos, 2005; Rojas and Mpodozis, 2006; Fosdick *et al*., 2011; Chapter 1). A second pulse of deformation characterized by thick-skinned faults dissected the fold-thrust belt and uplifted basement rocks of the Cordillera Darwin Metamorphic Complex and Rocas Verdes terrane, aiding the exhumation, denudation and resedimentation of these rocks into the Magallanes foreland basin by the Paleogene (Klepeis, 1994; Mpodozis and Rojas, 2006; Gombosi *et al*., 2009; Klepeis *et al*., 2010; Zahid and Barbeau, 2010; Romans *et al*., 2010; McAtamney *et al*., 2011; Chapter 1).

3. Field Observations at Seno Martínez

3.1 Overview of Seno Martínez

Seno Martínez is a north-northeast-trending fiord located along the western margin of the Cordillera Darwin in Tierra del Fuego (Figure 2.1). Bedrock exposures of the Cordillera Darwin Metamorphic Complex crop out along the shoreline as a chlorite, biotite and locally garnet-bearing pelitic and psammitic schist of lower-greenschist to lower-amphibolite facies (Figure 2.2). The southern end of the fiord preserves plutonic rocks of the Patagonian Batholith as well as outcrops of epidote-actinolite bearing schist that are interpreted to be part of the Rocas Verdes basin seafloor. The contact with the batholith is not exposed and is inferred to be an intrusive contact. Along the eastern shore of Seno Fontane (Figure 2.2), epidote-actinolite schist is in tectonic contact with the underlying pelitic and psammitic schist of the Cordillera Darwin Metamorphic Complex. Toward the north of the study area, the mouth of Seno Martínez merges with a northwest-trending fiord called Seno Keats. On the northern shore of Seno Keats at Bahía Angelito (Figure 2.2), quartz and chlorite-bearing schist of the Cordillera Darwin Metamorphic Complex are in tectonic contact with the overlying Jurassic volcanic strata of the Tobífera Formation.

Thus, pelitic and psammitic schist of the Cordillera Darwin Metamorphic Complex exposed along Seno Martínez form a structural culmination bound on the north by Jurassic rocks of the Tobífera Formation, and south by mafic schist of the Rocas Verdes basin terrane. Exposed along Seno Martínez in the core of the culmination, pelitic and psammitic schist of the Cordillera Darwin Metamorphic Complex are deformed by at least four generations of ductile noncylindrical folds and associated deformation (D_1 - D_4, discussed below). I divided the study area into four structural domains on the basis of overprinting relationships and intensity of specific structures (Figure 2.2, 2.3): Domain I occurs along Seno Fontane and Seno Martínez on the southwest-dipping limb of a

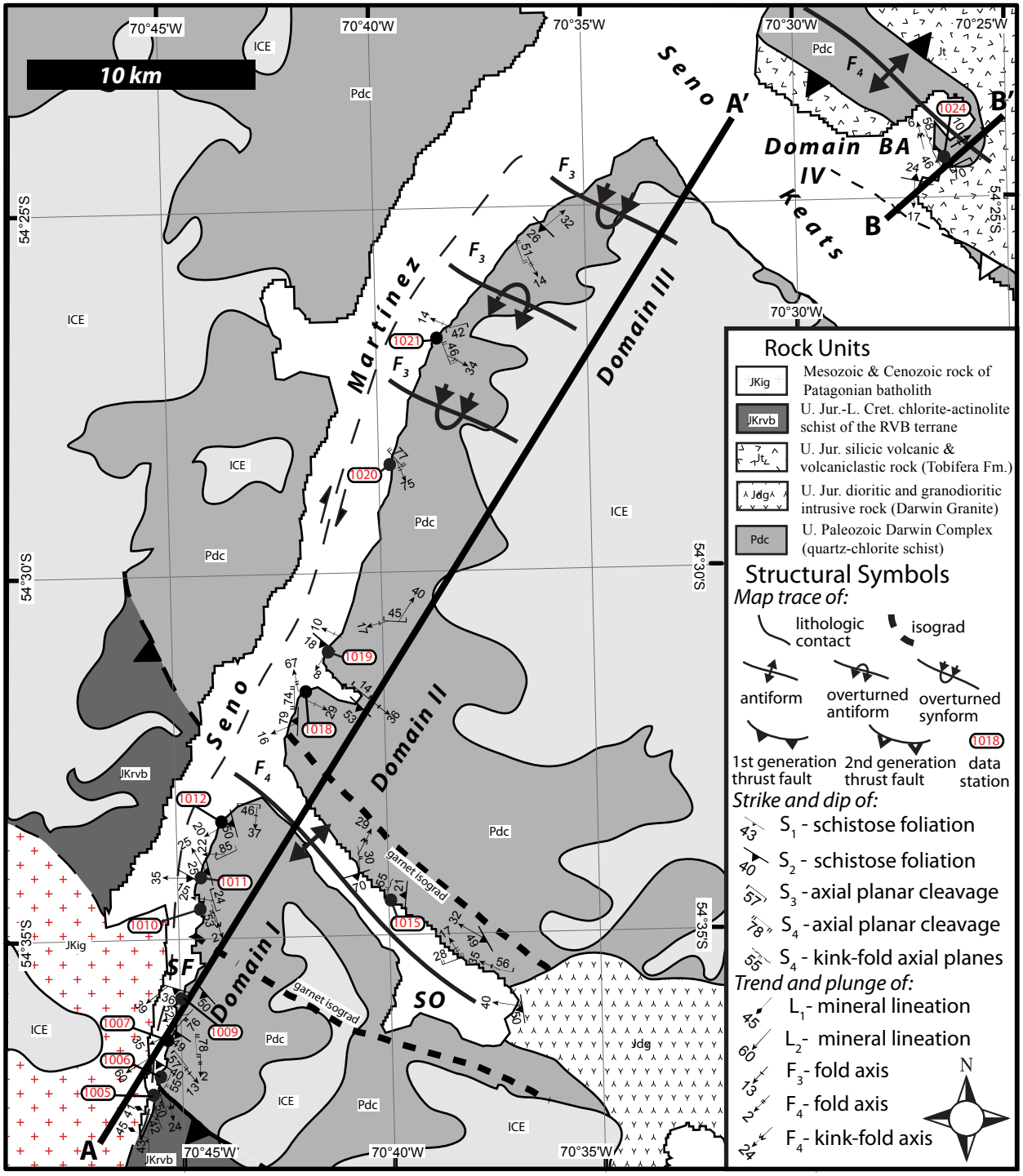

Figure 2.2. Geologic map of Seno Martínez showing data collected in this study, modified after Nelson *et al.*, (1980). Black dots with red numbers refer to data stations mention in the text. The locations of structural domains I-IV are shown as well as the location of cross sections A-A' and B-B'. BA, Bahía Angelito; SO, Seno Oryan; SF, Seno Fontane.

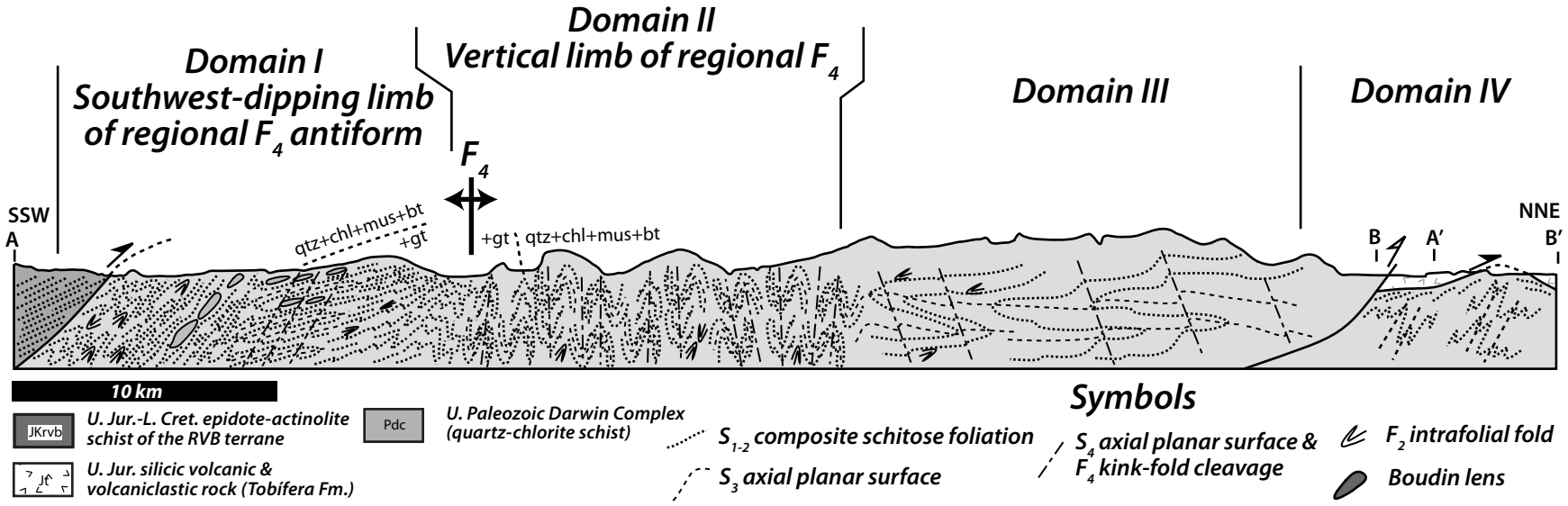

Figure 2.3. Composite cross section A-A' and B-B' showing sketches of superposed structures that are common in each structural domain I-IV. Location on figure 2.2. No vertical exaggeration. All mineral abbreviations henceforth are after Kretz (1983).

regional anitform (F_4) that culminates near Seno Oryan (Figure 2.2, 2.3). Domain II occurs in the core of the regional antiform and on its vertical limb. Domain III is located north of the antiform near the confluence of Seno Martínez and Seno Keats. Domain IV is located at Bahía Angelito along the north shore of Seno Keats where pelitic schist of the Cordillera Darwin Metamorphic Complex is in tectonic contact with the overlying Tobífera formation (Figure 2.2, 2.3).

3.2 Structure of Domain I: the contact between the Rocas Verdes basin terrane and the Cordillera Darwin Metamorphic Complex, D_2 and D_3 high-strain zone

The southeastern end of Seno Fontane (Figure 2.2) exposes outcrops of metavolcanic rocks that are predominantly epidote-actinolite grade greenschist (Figure 2.4a). The mineral assemblage of the schist is epidote, actinolite, (±) hornblende, feldspar, quartz, pyrite and hematite (Figure 2.4c-d). Diabase dikes intrude the schist and are commonly boudinaged (Figure 2.4a). In some locations, metatuffs are preserved that dip gently toward the west-southwest (Figure 2.4b). Here, a subsolidus schistose foliation (S_1) is defined by the alignment of actinolite (±) hornblende and recrystallized quartz (±) feldspar layers that dips gently toward the west-southwest. A poorly developed recrystallized quartz lineation (L_1) plunges gently toward the west-northwest (Figure 2.4e). On the basis of their probable volcanic origin and intermediate-mafic composition mineral assemblage, I interpret the epidote-actinolite schist as reflecting the part of the oceanic floor of the Jurassic Rocas Verdes basin.

Northward and structurally below the epidote-actinolite schist, rocks exposed at site 1006 (Figure 2.2) are chlorite- and- muscovite-bearing schists that have a pelitic composition different than the metavolcanic rocks described above and are thus interpreted as part of the Cordillera Darwin Metamorphic Complex. On the basis of a change in lithology and first appearance of chlorite-grade pelitic schist, the contact between the Rocas Verdes basin terrane (epidote-actinolite schist) and Cordillera Darwin metamorphic complex (quartz-chlorite pelitic schist) is located between sites 1005 and

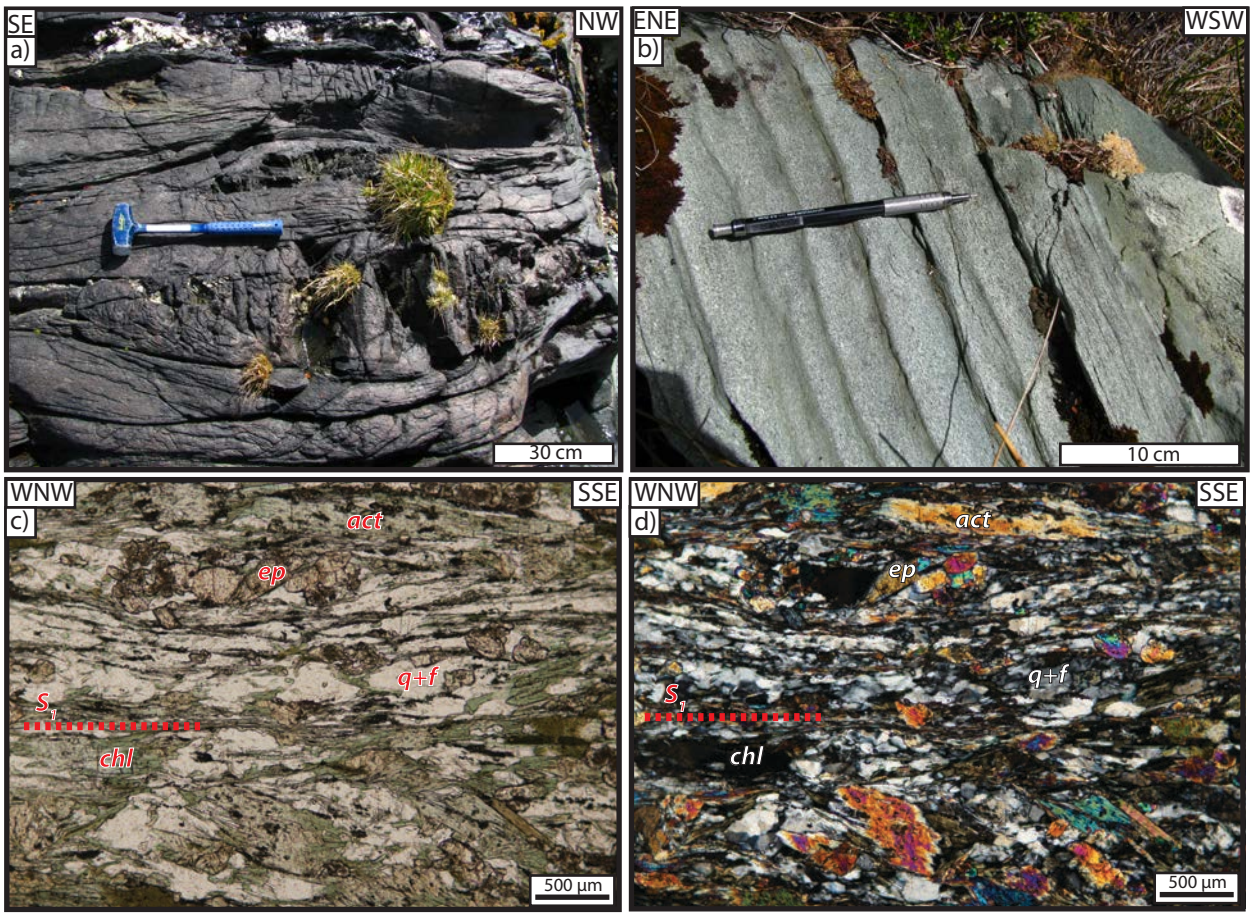

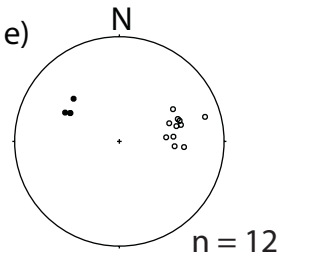

Figure 2.4. Photographs of (a) a diabase dike and (b) metatuffs that comprise part of the Rocas Verdes basin terrane near Seno Fontane, (c) plane light and (d) polarized light photomicrographs of epidote-actinolite schist from the Rocas Verdes basin terrane showing a subsolidus schistose foliation (S_1, parallel to base of each photo) and (e) stereogram plot showing poles to foliation (S_1) and quartz mineral lineation (L_1) from outcrops of the Rocas Verdes basin terrane in Seno Fontane. All stereograms hereafter are equal-area, lower hemisphere stereographic projections. Planar data are represented as poles (open symbols) unless otherwise plotted as great circles. Linear data are represented with solid black symbols.

1006 (Figures, 2.2, 2.3). Northward of the contact between sites 1006 and 1009 (Figure 2.2), lower greenschist facies chlorite- and- muscovite-bearing pelitic schists are tectonically interleaved with epidote-actinolite schists. Here, the pelitic schist contains a pervasive composite schistose foliation (S_2) defined by the alignment of muscovite, quartz and chlorite as well as transposed intrafolial isoclinal folds (F_2) of an early foliation (S_1 , discussed below). Intrafolial folds (F_2) are unique to the pelitic schist and not expressed in the epidote-actinolite schist. Where the pelitic and epidote-actinolite schists are interleaved, they share a pervasive schistose foliation (S_2) that dips moderately southwest and contains a prominent dynamically recrystallized quartz stretching lineation that plunges southwest (S_2 /L_2 , Figure 2.5a-b). Diabase dikes that intrude the pelitic and epidote-actinolite schists are dismembered, forming boudin lenses enveloped by S_2 (Figure 2.5d). Boudin neck extension directions do not have a preferred orientation (Figure 2.5c). Interleaved pods of epidote-actinolite schist that occur within and share a pervasive schistose foliation and quartz stretching lineation (S_2 /L_2) with the quartz-chlorite schist define a shear zone at and below the contact of the Rocas Verdes basin schist with the underlying Cordillera Darwin Metamorphic Complex between sites 1005 and 1009. Epidote-actinolite schist does not occur north of site 1009.

Pelitic schist of the Cordillera Darwin Metamorphic Complex preserves two younger phases of folding that are not expressed in the epidote-actinolite schist of the Rocas Verdes basin terrane. Between sites 1006 and 1012, sets of tight, upright, inclined and reclined folds (F_3) refold the pervasive S_2 schistose foliation (Figures 2.5e-h). F_3 folds generally do not exhibit a well-developed axial planar foliation. F_3 fold axes plunge shallowly either northwest-southeast or east-west (Figures 2.5f-h), indicating dominantly northeast-southwest or north-south shortening. In some locations, F_3 fold axes are subparallel with the L_2 quartz stretching lineation (Figure 2.5b, e, f). Asymmetric, upright kink-bands (F_4) fold the S_2 surface and overprint F_3 (Figure 2.5i). The axial surfaces of F_4 kink-bands are well developed in phylosilicate-rich domains and dominantly dip steeply toward the west-southwest (Figure 2.5j). A subsidiary set of kink-bands dips steeply

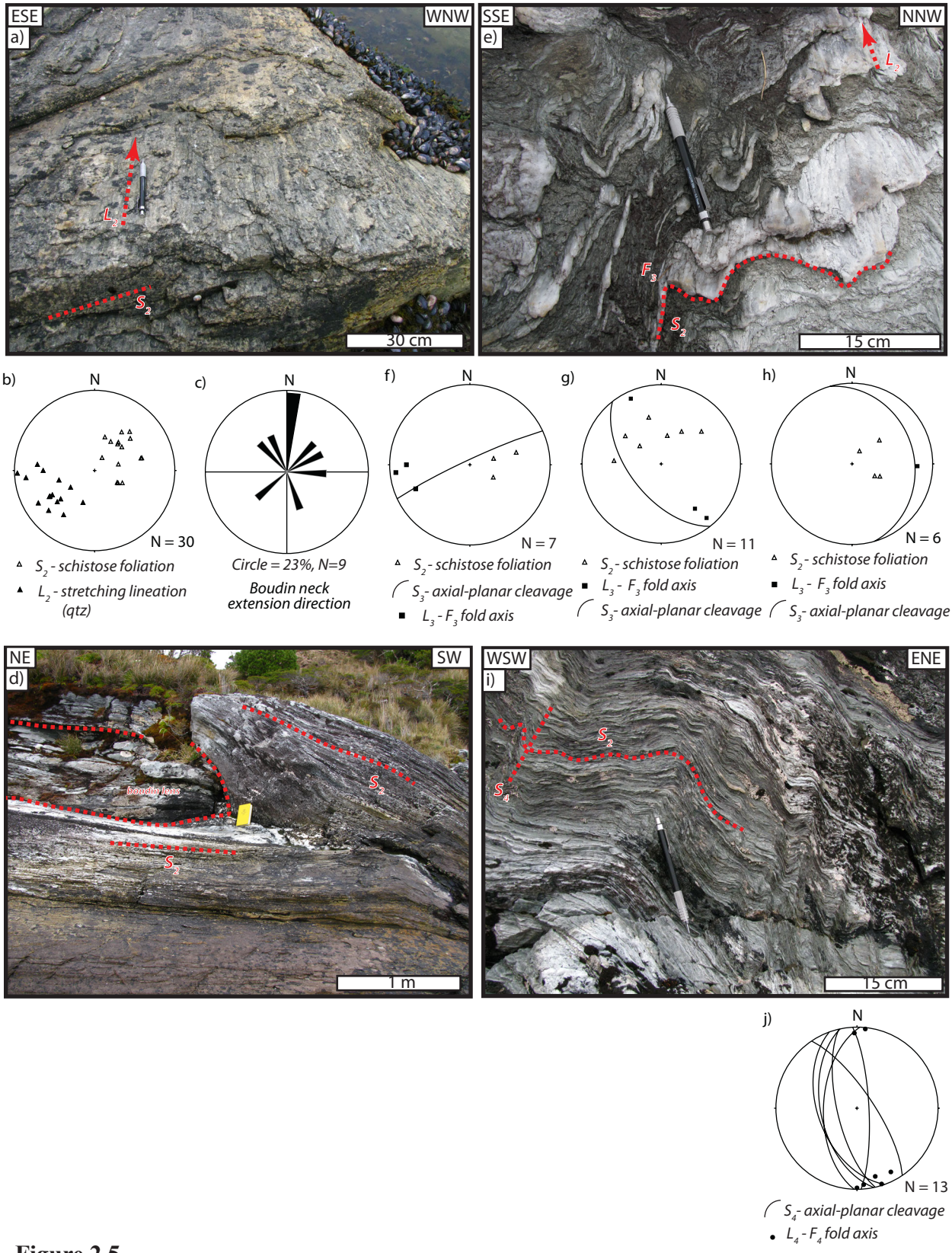
ESE
a)
WNW
L_2
S_2
30 cm
SSE
e)
NNW
L_2
F_3
S_2
15 cm
b)
N
N = 30
S_2 - schistose foliation
L_2 - stretching lineation (qtz)
c)
N
Circle = 23%, N=9
Boudin neck extension direction
f)
N
N = 7
S_2 - schistose foliation
S_3 - axial-planar cleavage
L_3 - F_3 fold axis
g)
N
N = 11
S_2 - schistose foliation
L_3 - F_3 fold axis
S_3 - axial-planar cleavage
h)
N
N = 6
S_2 - schistose foliation
L_3 - F_3 fold axis
S_3 - axial-planar cleavage
NE
d)
SW
boudin lens
S_2
S_2
1 m
WSW
i)
ENE
S_2
S_4
15 cm
j)
N
N = 13
S_4 - axial-planar cleavage
L_4 - F_4 fold axis

Figure 2.5

Figure 2.5. Domain I field photographs and stereograms. (a) Photograph of L-S tectonite defined by a composite schistose foliation (S_2) and prominent quartz stretching lineation (L_2) in an outcrop of epidote-actinolite schist that is interleaved with pelitic schist at site 1009, (b) stereogram showing structural data from sites 1006-1009, (c) rose diagram showing trends of boudin neck extension directions from Domain I, (d) photograph showing mafic boudin lens that is enveloped by S_2, (e) photograph of upright-tight F_3 folds of S_2 and F_2 (upper right) with axes subparallel to the quartz stretching lineation (L_2), (f-h) stereograms showing geometries of F_3 folds in Domain I that occur in upright (f-g) and reclined (h) orientations. (i) Photograph of F_4 kink-folds that overprint S_2 and (j) stereogram showing the geometry of F_4 folds in Domain I.

toward the east-northeast, conjugate to the west-southwest dipping set. Kink-band axes plunge shallowly toward the north and south (Figure 2.5j). F_4 kink folds are asymmetric and show contractional senses of rotation (*i.e.* top-northeast on southwest-dipping S_4 surfaces or top-southwest on northeast-dipping S_4 surfaces).

3.3 Structure of Domain II of the Cordillera Darwin Metamorphic Complex

Rocks exposed along Seno Oryan preserve the highest metamorphic grade in the study area and are located in the core of a regional antiform (F_4, Figure 2.2, 2.3). Between sites 1009 and 1018, garnet-bearing upper greenschist facies pelitic schist are exposed in the core of the antiform where they are deformed and record the superposition of three generations of folds (F_2 -F_4 , Figure 2.6a-e). Here, the pervasive macroscopic foliation (S_2) contains a prominent quartz stretching lineation (L_2) and is defined by the same composite foliation as in Domain I. Near Seno Oryan (Figure 2.2), S_2 is folded, and poles to S_2 define a southwest-northeast trending girdle (F_3 , Figures 2.6f). Here, F_3 fold axes plunge moderately toward the west-northwest or steeply toward the east. Axial surfaces to F_3 folds (S_3) dip steeply and moderately toward the north and east, indicating both upright-horizontal and reclined orientations for F_3 folds, as they are folded by F_4 (Figure 2.6g). Quartz lineations (L_2) are locally parallel to F_3 axes and plunge shallowly toward the west-northwest (Figure 2.6f-g).

Along the upright, northern limb of the regional F_4 antiform between Seno Oryan and site 1021, tight and isoclinal folds (F_3) refold the quartz stretching lineation (L_2) and the schistose foliation (S_2). Here, F_3 folds are commonly isoclinal and occur as upright, reclined and recumbent folds depending on how they are refolded by F_4 (Figure 2.6a-b). L_2 and poles to S_2 define southwest-northeast-trending girdle (Figure 2.6h). F_3 fold axes plunge shallowly toward the southeast, and S_3 axial surfaces occur in both upright and recumbent orientations (Figures 2.6i). In some locations, F_3 folds form sheath folds (Figure 2.6c-d). In outcrops where the limbs of F_3 sheath folds are well preserved, a prominent quartz mineral lineation (L_2) exists on the folded S_2 surface (Figure 2.6e). Here, sheath folds (F_3) refold the S_2 /L_2 surface, have isoclinal limbs and form long-axes

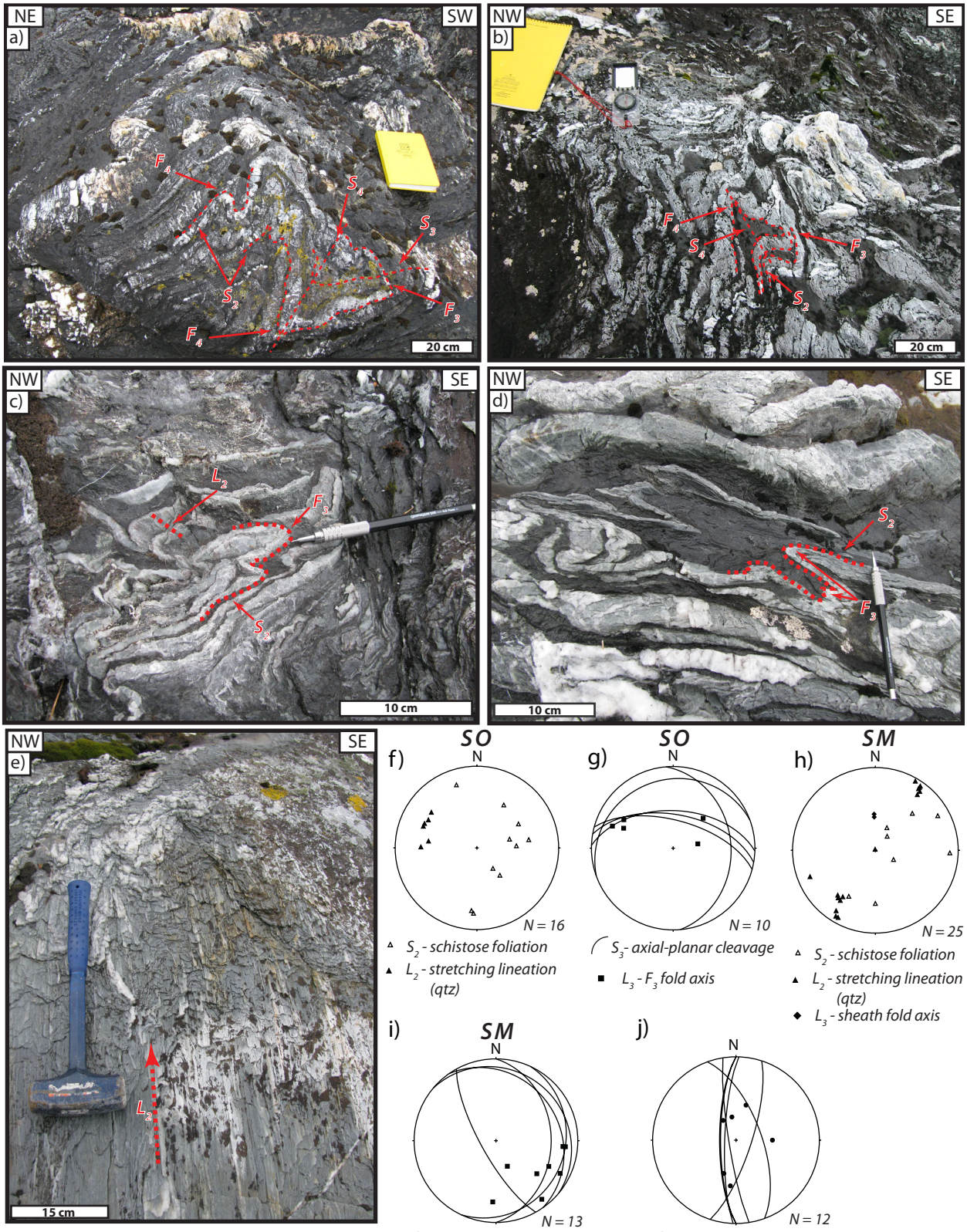
NE
a)
SW
F_4
S_4
S_3
S_2
F_3
F_4
20 cm
NW
b)
SE
F_4
S_4
F_3
S_2
20 cm
NW
c)
SE
L_2
F_3
S_2
10 cm
NW
d)
SE
S_2
F_3
10 cm
NW
e)
SE
L_2
15 cm
SO
f)
N
N = 16
S_2 - schistose foliation
L_2 - stretching lineation (qtz)
SO
g)
N
N = 10
S_3 - axial-planar cleavage
L_3 - F_3 fold axis
SM
h)
N
N = 25
S_2 - schistose foliation
L_2 - stretching lineation (qtz)
L_3 - sheath fold axis
SM
i)
N
N = 13
S_3 - axial-planar cleavage
L_3 - F_3 fold axis
j)
N
N = 12
S_4 - axial-planar cleavage
L_4 - F_4 fold axis

Figure 2.6

Figure 2.6. Domain II field photographs and stereograms. Photographs of (a) Ramsay type-III and (b) type-II superimposed fold relationships formed by the folding of F_3 by F_4, (c-d) F_3 sheath folds with long axes that are subparallel to the local quartz stretching lineation (L_2) and (e) S_2 /L_2 L-S tectonite in the hinge zone of a macroscopic F_3 fold. (f-j) Stereograms showing (f) girdle formed by S_2 with quartz lineation parallel to the predicted fold axis at Seno Oryan (SO), (g) orientation of F_3 folds at Seno Oryan, (h) girdle defined by folding of S_2 /L_2 and sheath fold axes near sites 1018-1020 at Seno Martínez (SM), (i) orientation of F_3 folds near in Domain II at Seno Martínez and (j) orientation of F_4 folds in Domain II.

that are subparallel to the local stretching lineation (L_2 , Figure 2.6c) and plot along the same girdle is S_2 and L_2 (Figure 2.6h). Everywhere in Domain II, the S_2 /L_2 surface and F_3 folds are refolded by upright, steeply plunging tight folds (F_4) that form both Ramsay type II (Figure 2.6b) and type III (Figure 2.6a) superposed fold patterns (Ramsay, 1983). F_4 folds have upright, north-striking axial surfaces and steeply north- and south-plunging fold axes and thus form reclined folds (Figure 2.6j).

3.4 Structure of Domain III of the Cordillera Darwin Metamorphic Complex

North of site 1020 (Figure 2.2), quartz- chlorite- and- muscovite bearing schist contains a pervasive composite schistose foliation (S_2) and recrystallized quartz mineral lineation (L_2) similar to S_2 /L_2 elsewhere along Seno Martínez. Here, regional, gently inclined isoclinal folds (F_3) refold the S_2 /L_2 surface and have amplitudes on the order of 100s of meters (*e.g.* Figure 2.7a). Poles to refolded S_2 /L_2 surfaces form a southwest-northeast-trending girdle (Figure 2.7c). S_3 axial surfaces dip gently toward the north and south, and F_3 axes plunge shallowly toward the west and southeast (Figure 2.7d). Sheath folds (F_3) occur at site 1020 and 1021 where they refold the S_2 /L_2 surface and have long axes that plot along a girdle defined by L_2 and poles to S_2 (F_3 , Figure 2.7c). However, sheath folds do not occur north of site 1021. Everywhere in Domain III, the S_2 /L_2 surface and F_3 folds are overprinted by sets of kink-folds (F_4) that have steeply east-northeast- or northeast-dipping axial surfaces (S_4), and fold axes that plunge both steeply and shallowly toward the south-southeast (Figure 2.7a-b, e). F_4 kink-folds are asymmetric and show a clockwise sense of rotation when viewed down-plunge (toward the SE), indicating top-southwest contraction.

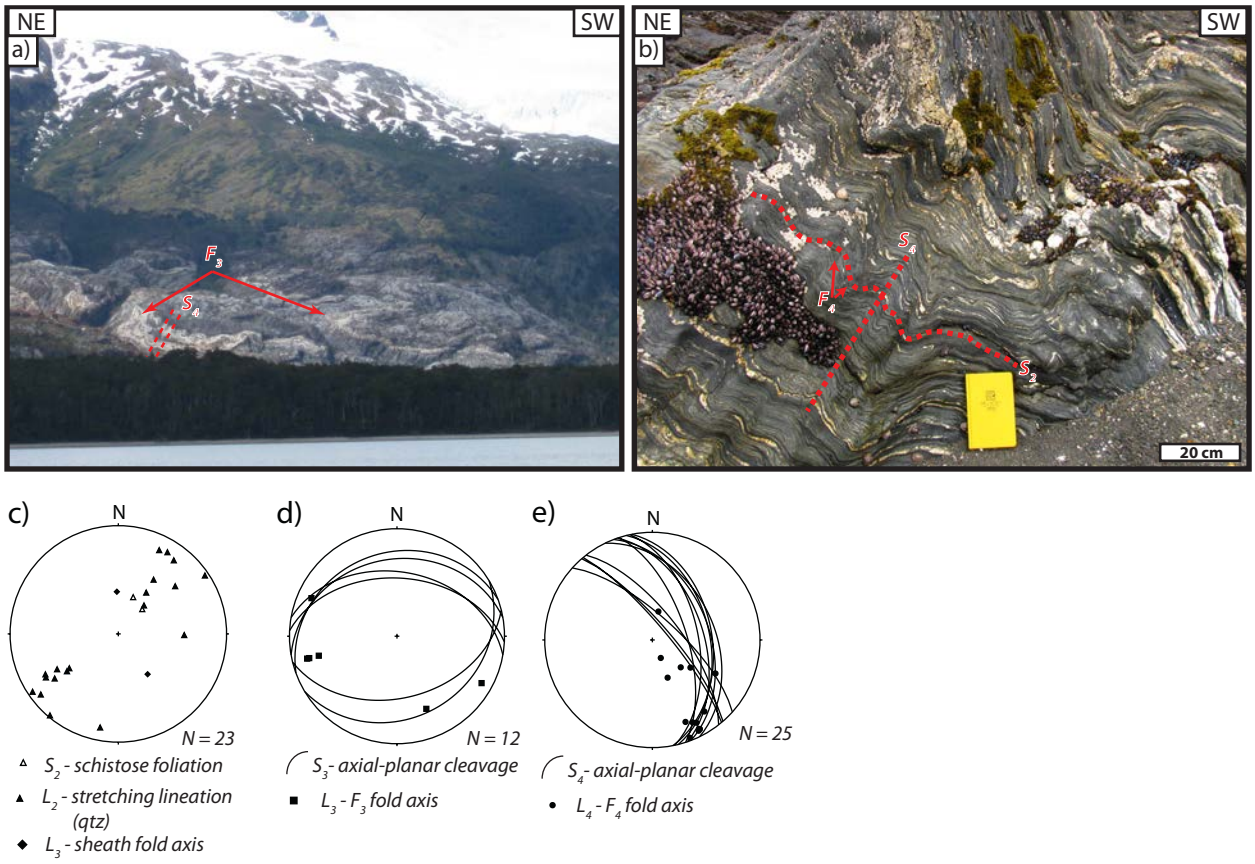

Figure 2.7. Field photographs and stereograms from Domain III. Photographs of (a) regional recumbent isocline F_3 folds and (b) steeply inclined F_4 kink-folds, note top-southwest vergence. Stereograms showing (c) girdle defined by S_2 /L_2 and F_3 sheath folds in Domain III near sites 1020, and 1021, (d) orientations of F_3 folds from Domain III and (e) orientation of F_4 folds in Domain III.

3.5 Domain IV, faulted contact between the Cordillera Darwin Metamorphic Complex and the Tobífera Formation at Bahía Angelito

Along the north shore of Seno Keats in Bahía Angelito, the quartz- and- chlorite-bearing pelitic schist of the Cordillera Darwin Metamorphic Complex is in tectonic contact with the Tobífera Formation (Figure 2.2, 2.8). Here, a 4 m thick conglomerate with pebble and cobble sized clasts supported by a muddy matrix unconformably overlies the Cordillera Darwin Metamorphic Complex. The conglomerates are overlain by 1 m of turbidite sandstones. The conglomerates and sandstones dip southwest and are interpreted to represent a basal clastic unit within the Tobífera Formation that is described elsewhere in Tierra del Fuego (*c.f.* Dalziel & Cortés, 1972; Johnson, 1990).

The contact is sheared and cut by several small thrust faults. Five meters below the contact at site 1024 (Figure 2.2), the pelitic schist is observed in the footwall of a thrust where it preserves structures similar those in Domain I and III in Seno Martínez (Figure 2.8a,d). Here, a pervasive schistose foliation (S_2) contains a recrystallized quartz stretching lineation (L_2), and the S_2 /L_2 surface is folded (F_3), forming a north-trending girdle (Figure 2.8b). F_3 folds are isoclinal, upright folds with steeply north-northwest- and- south-southeast-dipping axial surfaces that form a conjugate set. F_3 fold axes are horizontal and trend toward the east-northeast and west-southwest (Figure 2.8c). Directly below the contact (<5 m) the Cordillera Darwin Metamorphic Complex is sheared and displays schistose foliation (S_2) that dips dominantly toward the southwest (Figure 2.8d). Southwest-dipping C-S fabrics that are parallel to S_2 indicate top-northeast sense of shear. In some locations, lenses of conglomerate are enveloped by the basement schist and are bound on all sides by small thrust faults (Figure 2.8d). Both the conglomeratic lenses and sandstones contain a cleavage defined by pressure solution seams that is coplanar with the foliation in the pelitic schist, indicating that they are also sheared (Figure 2.8d-f).

One hundred meters southwest of site 1024, the conglomerate and sandstone deposits are conformably overlain by volcanoclastic units of the Tobífera Formation (Figure 2.8g). Here, white, silicic ignimbrites overlie dark-grey ash beds and dip

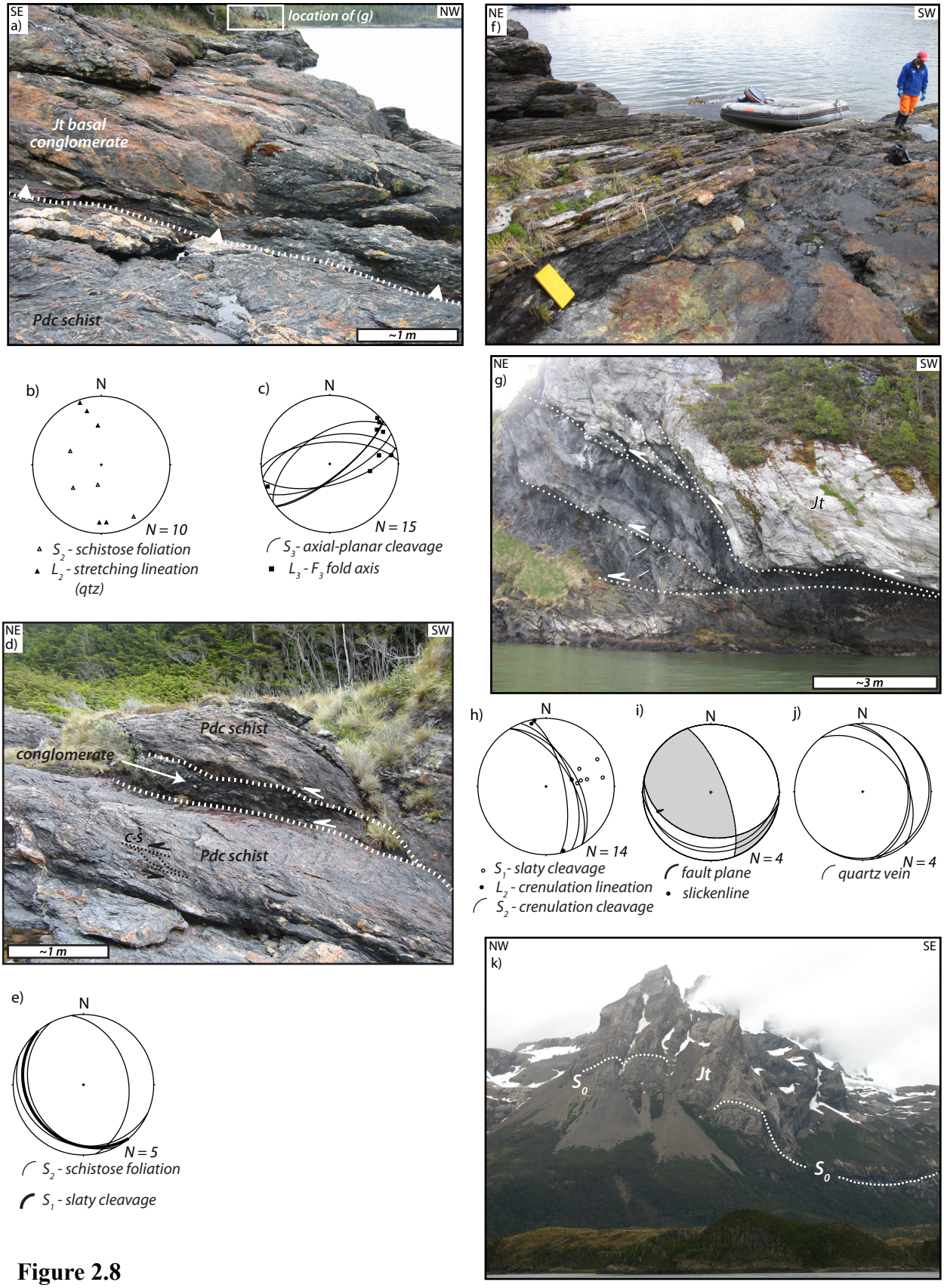
SE
a)
location of (g)
NW
Jt basal conglomerate
Pdc schist
~1 m
NE
f)
SW
b)
N
N = 10
S_2 - schistose foliation
L_2 - stretching lineation (qtz)
c)
N
N = 15
S_3 - axial-planar cleavage
L_3 - F_3 fold axis
NE
g)
SW
Jt
~3 m
NE
d)
SW
Pdc schist
conglomerate
C-S
Pdc schist
~1 m
h)
N
N = 14
S_1 - slaty cleavage
L_2 - crenulation lineation
S_2 - crenulation cleavage
i)
N
N = 4
fault plane
slickenline
j)
N
N = 4
quartz vein
e)
N
N = 5
S_2 - schistose foliation
S_1 - slaty cleavage
NW
k)
SE
S_0
Jt
S_0

Figure 2.8

Figure 2.8. Field photographs and stereograms from Domain IV. (a) Photograph of a thrust contact between the basal conglomerate beds of the Tobifera Fm. (above) and polydeformed pelitic schist (below), (b, c) stereograms showing (b) girdle formed by the refolded S_2 /L_2 surface and (c) geometry of F_3 folds within the pelitic schist, (d) conglomerate lens that is bound my small thrusts and enveloped by pelitic schist; C-S fabric in the schist indicates top-northeast sense of shear, (e) stereogram showing cleavage from the Tobífera Fm., locally coplanar with S_2 in the pelitic schist and (f) photograph of cleavage in basal clastic units of the Tobífera Fm. overlying the pelitic schist of the Cordillera Darwin Metamorphic Complex. (g) Photograph of small thrusts that form an imbricate fan in the Tobífera Fm., and (h-j) stereograms of (h) cleavage and crenulations near the thrusts in (g), (i) fault kinematic data from the thrusts and (j) tensile quartz vein orientations near the thrusts in (g). (k) View toward the north from Bahía Angelito showing folded strata of the Tobífera Fm. forming a regional syncline.

southwest. The ash beds display a cleavage (S_1) defined by pressure solution seams and flattened quartz and feldspar lapilli. Bedding is not distinguishable within the ash beds. S_1 dips toward the southwest and is overprinted by a set of crenulation cleavages (S_2). The crenulations cleavages (S_2) dip steeply toward the east-northeast, and crenulation lineations (L_2) are horizontal, trending north-northwest and south-southeast (Figure 2.8h). The S_2 crenulation cleavage is asymmetric and shows a top-southwest sense of rotation, indicating contraction. S_1 is cut by a set of small brittle thrust faults that form a southwest-dipping imbricate fan (Figure 2.8g). Fault planes dip shallowly toward the south-southwest; one set contains a slickenline that plunges obliquely toward the west-southwest, indicating a thrust-left sense of slip (Figure 2.8i). Sets of tensile quartz veins occur in close proximity to the thrusts and dip towards the east-northeast (Figure 2.8g, j). Some quartz veins are sigmoidal and indicate a top-northeast sense of rotation. Although inaccessible on foot, bedding in the Tobífera Formation is well exposed on the mountainside northeast of Bahía Angelito where it dips toward the northeast and is gently folded to form a regional syncline, suggesting that the sheared contact at the base of the Tobífera Formation is also folded (Figure 2.8k).

4. Microstructures and Kinematic Indicators

4.1 Domain I and II

4.1.1 Kinematic indicators

Mesoscopic kinematic indicators from S_2 fabrics are commonly absent or ambiguous, however, microstructures preserve reliable shear-sense indicators. For example, Figure 2.9 shows examples of microstructures and kinematic indicators associated with the macroscopic schistose foliation (S_2). Compositional layering defined by micaceous, fine-grained quartz and feldspar domains and coarse-grained quartz-rich domains (S_1) is folded by intrafolial, rootless, isoclinal folds (F_2) that are transposed parallel to and partly define the composite S_1/S_2 foliation. Dynamically recrystallized coarse-grained quartz domains have elongate grains parallel to S_2 helping define it.

Kinematic indicators include C' shear bands in micaceous domains and asymmetric muscovite sigma tails on garnet porphyroblasts. Both types of kinematic indicator show top-northeast sense of shear (Figure 2.9a-b). Curved, synkinematic quartz inclusion trails in garnet poryphyroblasts are continuous with S_2 and also indicate top-northeast shear (Figure 2.9c-d).

4.1.2 Quartz microstructure

In quartz-rich domains, alternating layers of dynamically recrystallized fine- and coarse- grained quartz defines S_2 (Figure 2.10a-c). Within coarse-grained S_2 domains, recrystallized quartz grains are typically flattened and have cuspate-lobate shaped irregular grain boundaries. Quartz grains are commonly internally deformed, containing polygonalized subgrain boundaries (*e.g.* Figure 2.10a-c). Fine-grained domains consist of polyphase aggregates of quartz, feldspar and chlorite. Although quartz is also recrystallized in fine-grained domains, pinning microstructures associated with the other phases inhibited grain growth. Quartz textures from S_2 domains indicate both subgrain rotation and grain boundary migration recrystallization consistent with Regime 3 dislocation creep (Hirth and Tullis, 1992) and/or the subgrain rotation recrystallization to grain boundary migration transition of Stipp *et al*. (2002). In samples collected near the core of the F_4 antiform at Seno Oryan (Figure 2.3), some quartz grains also exhibit chessboard extinction indicative of high temperature dislocation creep (Figure 2.10c). Quartz textrures do not exhibit evidence for a separate foliation associated with F_3 folds, consistent with the observation that macroscopic F_3 folds to not display a pervasive foliation (*i.e.* section 3.2).

In quartz-rich domains where F_4 kink-bands are well expressed, quartz exhibits a prominent shape-preferred orientation parallel to the axial surface of F_4 (S_4, Figure 2.10d-f). S_4 is oblique (~65°) to and overprints S_2 (Figure 2.10d-f). Recrystallized, elongate, course-grained quartz grains that contain well-developed subgrain boundaries define S_4 (Figure 2.10d-f). Parallel to S_4 subgrain boundaries, irregular, cuspate-shaped grains protrude into adjacent grains (Figure 2.10d), thus providing textural evidence of grain boundary migration recrystallization associated with the formation of S_4. Quartz

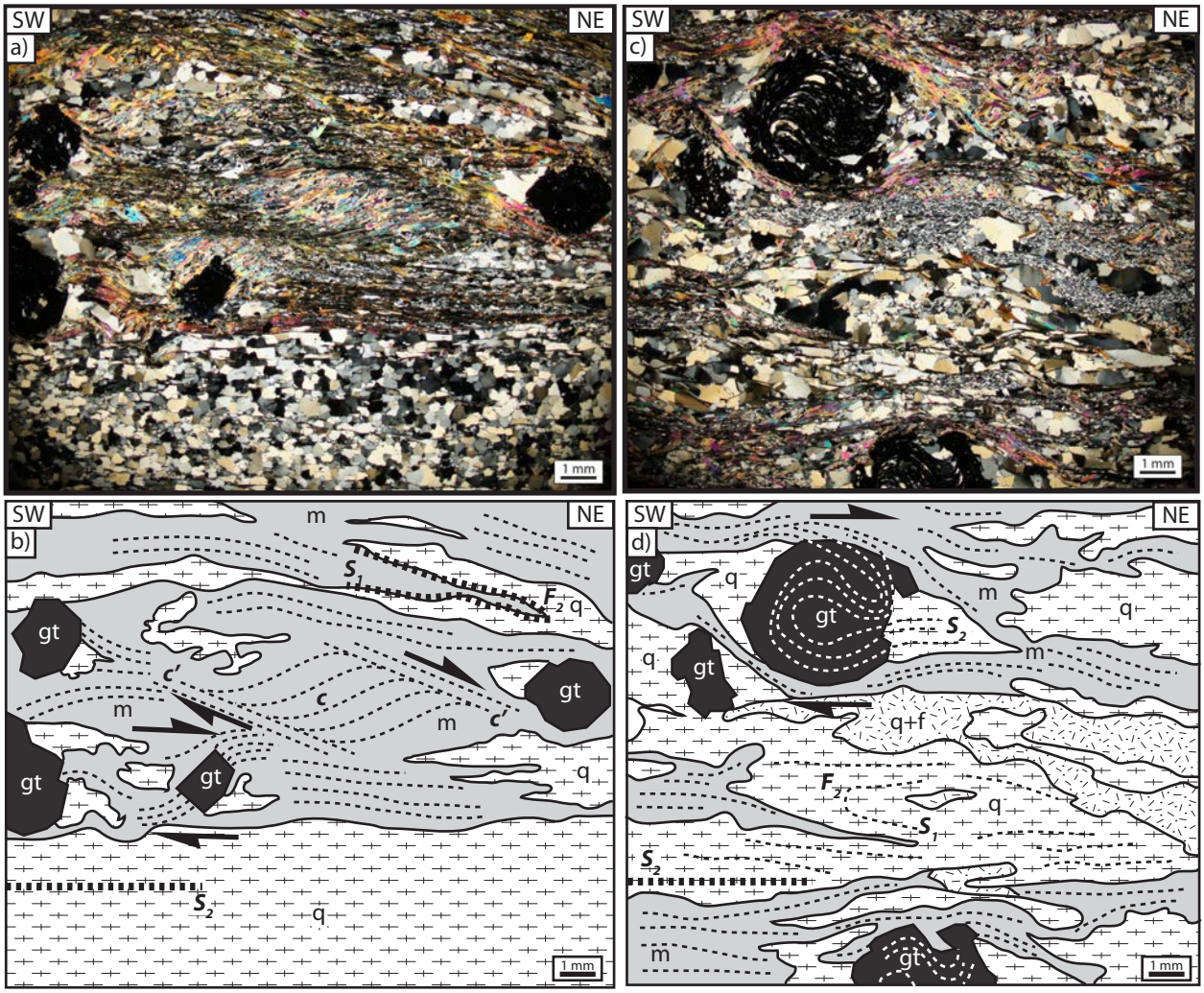

Figure 2.9. Photomicrographs (a) and (c) and sketches (b) and (d), respectively of microscopic kinematic indicators from Domains I and II near Seno Martínez. See text for descriptions. In both samples the composite S_2 foliation is parallel to the base of the photograph. Intrafolial (F_2) folds are highlighted in (b) and (d). Abbreviations: m, micaceous domain; q, quartz domain; q+f, polyphase quartz and feldspar domain; gt, garnet, C and C' refer to shear bands. Cross polarized light.

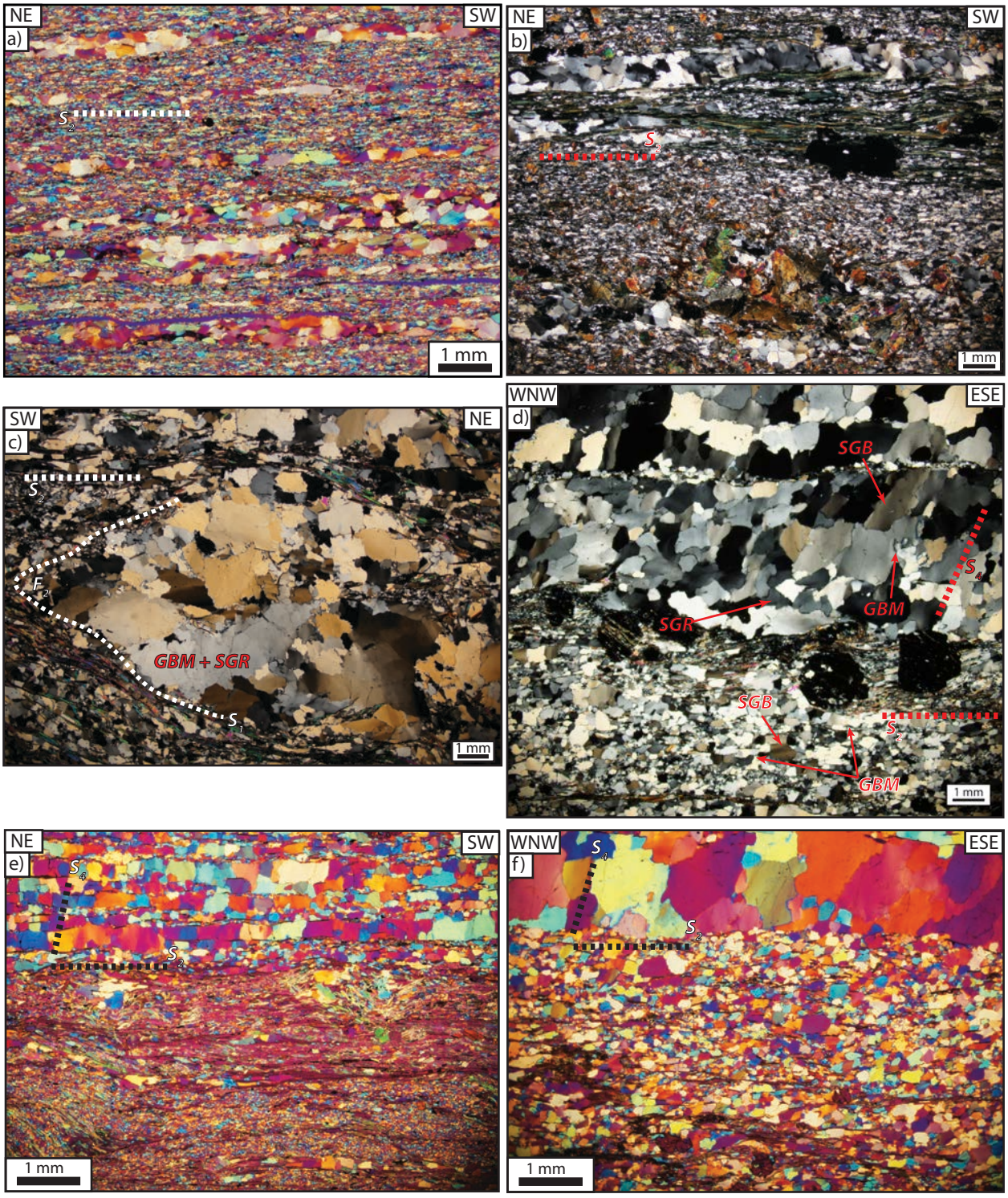

Figure 2.10. Photomicrographs showing quartz recrystallization textures from Domains I and II where S_2 is well preserved (a-c) and (d-f) where S_4 pervasively overprints S_2. See text for descriptions. All photomicrographs are taken in cross-polarized light and (a), (e) and (f) are taken with the lambda plate inserted. GBM, grain boundary migration; SGR, subgrain rotation; SGB, subgrain boundary.

textures from S_4 domains indicate both subgrain rotation and grain boundary migration recrystallization consistent with Regime 3 dislocation creep (Hirth and Tullis, 1992) and/or the subgrain rotation recrystallization to grain boundary migration transition of Stipp *et al*. (2002). Microstructural kinematic indicators parallel to S_4 are ambiguous, however, asymmetric kink-folds that define the macroscopic S_4 foliation always show contractional senses of rotation (*i.e*. top-southwest on northeast dipping surfaces, and visa versa, Figure 2.5i).

4.2 DOMAIN III MICROSTRUCTURES

In domain III, the composite schistose foliation (S_2) is pervasively overprinted by F_4 kink-folds. Here, S_2 is a composite foliation defined by the axial surfaces of transposed intrafolial F_2 folds and dynamically recrystallized quartz layers, similar to the S_2 foliation from Domains I and II (Figure 2.11a,b). Likewise, samples from domain III also lack textural evidence for a foliation associated with F_3 folds. F_4 kink folds are best expressed in micaceous layers where they display top-southwest sense of rotation and a well-developed northeast-dipping axial surface (S_4) that crosscuts S_2 (Figure 2.11a). Coarse-grained quartz exhibits shape-preferred orientations that are parallel to S_4 (Figure 2.11a-c). Subgrain boundaries and flattened recrystallized grains with cuspate, irregular grain boundaries that are parallel to S_4 provide textural evidence for grain boundary migration and subgrain rotation recrystallization (Figure 2.11c). S_4 quartz textures in Domain III are equivalent to those in Domain I and II and reflect Regime 3 of Hirth and Tullis (1992), and/or the subgrain rotation recrystallization to grain boundary migration transition of Stipp *et al*. (2002). Quartz microstructures from Domain IV are similar to those of Domains I-III and are not discussed further.

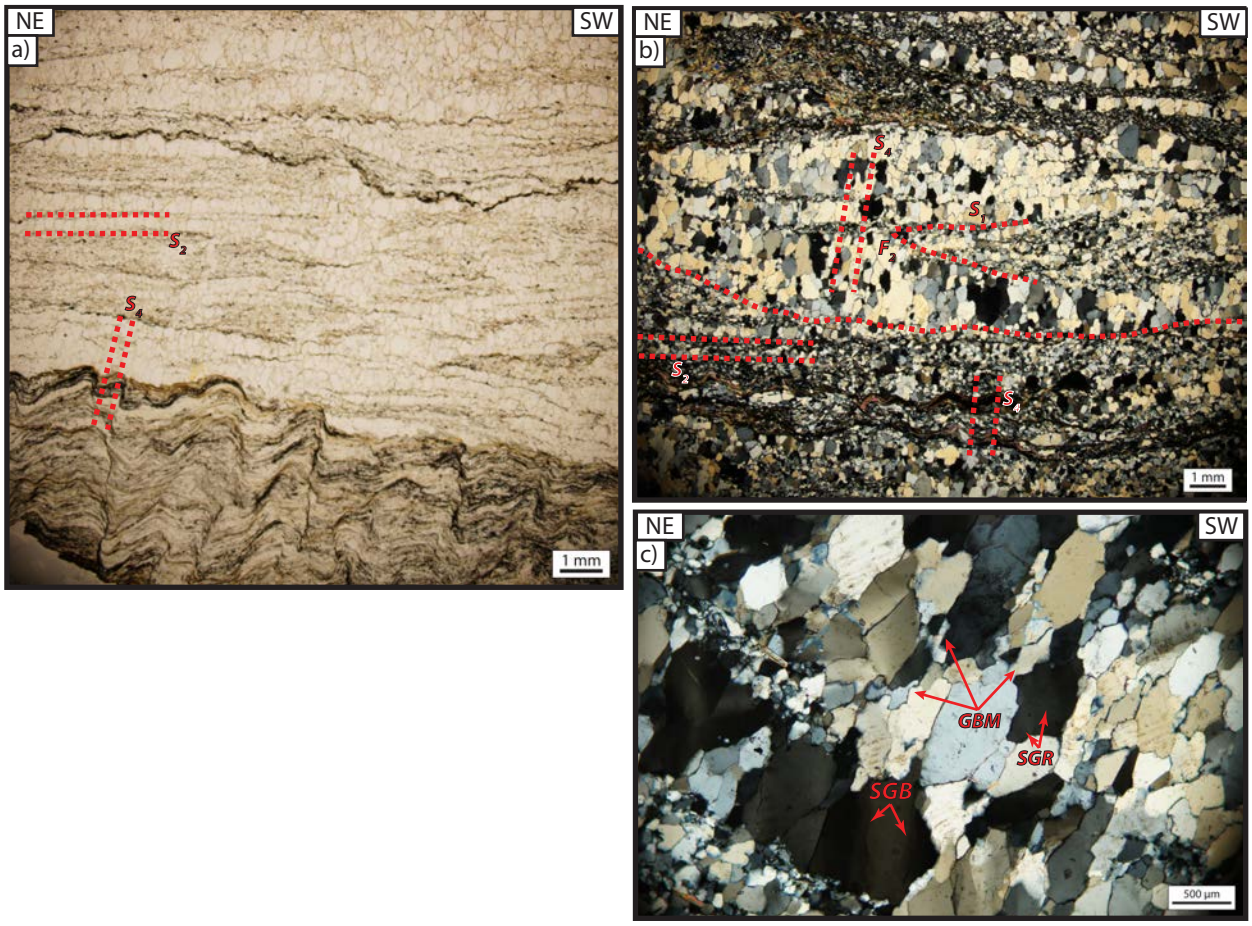

Figure 2.11. Photomicrographs showing quartz recrystallization textures from Domain III where S_4 is pervasive. (a) Plane-light photomicrograph showing axial plane of S_4 kink-folds in micaceous domains that are subparallel to a prominent shape preferred orientation of quartz grains (S_4) that overprints S_2. (b) Cross-polarized light photomicrograph showing S_1 isoclinally folded by F_2 and overprinted by a quartz shape preferred orientation (S_4). (c) Photomicrograph showing quartz recrystallization textures parallel to S_4 (the upright fabric). GBM, grain boundary migration; SGR, subgrain rotation; SGB, subgrain boundary.

5. Quartz crystallographic preferred orientations from S_2 and S_4 fabrics at Seno Martínez

Field and microstructural observations indicate that there are two prominent foliations (S_2 and S_4) in all of the structural Domains (I-IV) along Seno Martinez. To better characterize the deformation temperatures and sense of shear during formation of each foliation, I measured the crystallographic preferred orientations (CPOs) of dynamically recrystallized quartz in 10 samples from S_2 domains and 8 samples from S_4 domains.

CPOs are a function of many factors that describe the deformation path of a rock including the active slip systems, the strain type (*i.e.* plane strain, flattening or constriction), the magnitude of finite strain, the degree of non-coaxial deformation (*i.e.* kinematic vorticity), the activity of recrystallization mechanisms, and the growth of grains from solution (see Passchier and Trouw, 2005 and references therein). Many empirical and experimental studies have attempted to find the relationship between common quartz CPOs in shear zones and each of the above factors (*e.g.* Lister, 1977; Lister *et al.*, 1978; Lister and Hobbs, 1980; Law *et al.*, 1984; Law, 1987; 1990; Law *et al.*, 1990; Schmid and Casey, 1986; Stipp *et al.*, 2002; Barth *et al.*, 2010). Quartz has four primary slip systems: basal {001}-<a>, prism {100}-<a>, rhomb {101}-<a> and prism {010}-[c]. Experimental and empirical studies show that the dominant slip-system is temperature dependent. Basal - <a> and prism - <a> slip-systems are favored under greenschist to lower amphibolite facies conditions, whereas the transition to prism-[c] slip occurs at relatively high homologous temperatures (>600° C for quartz) under upper amphibolite facies conditions (Lister and Dornsiepen, 1982; Law, 1990) and is possibly facilitated by hydrolytic weakening (Mainprice *et al.*, 1986).

The work of Stipp *et al.* (2002) correlated quartz CPOs with quartz recrystallization mechanisms and dislocation creep regimes over a large range of independently determined deformation temperatures (~270 to ~700°C), allowing quartz CPO patterns to be used to infer deformation conditions. These authors found that the

transition from bulge to subgrain rotation recrystallization occurs ~400° C and is coincident with a textural change in quartz c-axis CPOs from c-axis maxima near Z to c-axis gridles in the Z-Y plane, indicating mixed - <a> slip and suggesting a transition from basal - <a> to prism - <a> slip-systems near the bulge to subgrain rotation recrystallization transition with increasing temperatures. The transition from subgrain rotation recrystallization to grain boundary migration occurs ~500° C and correlates with a textural change to dominantly c-axis maxima near Y, indicative to prism-<a> slip. Stipp *et al*. (2002) only observed evidence of prism - [c] slip in the grain boundary migration recrystallization regime above ~630° C where it occurred together with basal - <a> slip, indicating that mixed <a> and [c] slip systems can occur at relatively high temperatures.

The symmetry or asymmetry of c- and a-axis CPO patterns also contains useful information about the type of finite strain and kinematic framework of the deformation. During progressive deformation the a-axes rotate into parallelism with the shear plane, and thus the geometry of c- and a-axis CPOs can be used to evaluate the degree of non-coaxial deformation and shear sense. Pole figures with relatively symmetric patterns reflect coaxial deformation, and those with asymmetric patterns reflect a component of rotation during the deformation (Lister, 1977; Lister *et al*., 1978; Schmid and Casey, 1986). Similarly, the type of strain imposed on quartz-bearing rocks will influence the geometry of the pole figure. Quartzites that have undergone bulk coaxial constriction show broad cleft girdle c-axis patterns in the ZY plane and small-circle a-axis girdles around X. Conversely, samples that have undergone coaxial flattening should exhibit c-axes that form small-circle gridles around Z and a-axis patterns defined by broad cleft-girdles in the XY plane (Lister & Hobbs, 1980; Schmid & Casey, 1986). Samples that experience constriction or flattening under non-coaxial deformation will form similar patterns but also exhibit a degree of asymmetry that is synthetic with the direction of shear. Thus, pole figure patterns can be used to determine the shear sense and type of strain that was imposed on the sample.

Analyses were performed on thin sections cut perpendicular to foliation (either S_2 or S_4) and parallel to the L_2 quartz lineation for analyses of S_2 /L_2 fabrics or perpendicular

to the F_4 kink fold axes for analyses of S_4 fabrics (*i.e.* XZ thin sections). CPOs were measured using the HKL Nordlys Electron Backscatter Detector (EBSD) on the Phillips XL30 Environmental Scanning Electron Micrscopic at the University of Texas at Austin Department of Geosciences. All analyses were conducted using a working distance between 18-25mm and an accelerating voltage of 25-30kv. Background conditions and diffraction patterns were automatically collected using the AztecHKL EBSD software package by Oxford Instruments. Only indexed diffraction patterns with a mean angular deviation <1° were accepted. Data were collected in quartz-rich domains using a variable step size that was appropriate for the grainsize of each sample. The data were reduced using the HKL Channel5 software to one point per grain with a misorientation angle of 10° to define grain boundaries. C-axis and a-axis pole figures were plotted using Pfch5 (Mainprice, 2005) and contoured with multiples of uniform distribution (MUD). Only plots with c-axis pole figures that yield MUD > 2 were considered. Quartz CPO results from 10 samples within S_2 domains and 8 samples within S_4 domains are presented below. Both c- and- a-axis orientations are presented as pole figures (left and middle columns, respectively) whereas the sample coordinate X (parallel to lineation) is presented in an inverse pole figure diagram (right column). The samples are ordered by location to highlight spatial trends in the data, beginning at the southwest end of transect A-A' at site 1006 and continuing toward the northeast to Seno Keats. Sample locations are presented in Figure 2.2.

5.1 S_2 Quartz CPOs, Seno Martinez

Samples 1006, 1007 and 1009 were collected from Domain 1 within 5 km of the contact with overlying rocks of the Rocas Verdes basin terrane (Figure 2.2). C-axis patterns from sample 1006A (Figure 2.12a) form a small-circle girdle that is symmetric around Z. A-axes form a mostly symmetric cross-girdle pattern in the XY plane. The lineation direction (X) is subparallel to or gently inclined toward <a> (210, 120). C-axes from sample 1007A (Figure 2.12b) form a type-I asymmetric cross-girdle, and a-axes form moderately developed small-circle girdles in the ZY plane. The asymmetries of c- and a-axis patterns are sinistral and indicate top-northeast shear sense. The lineation (X)

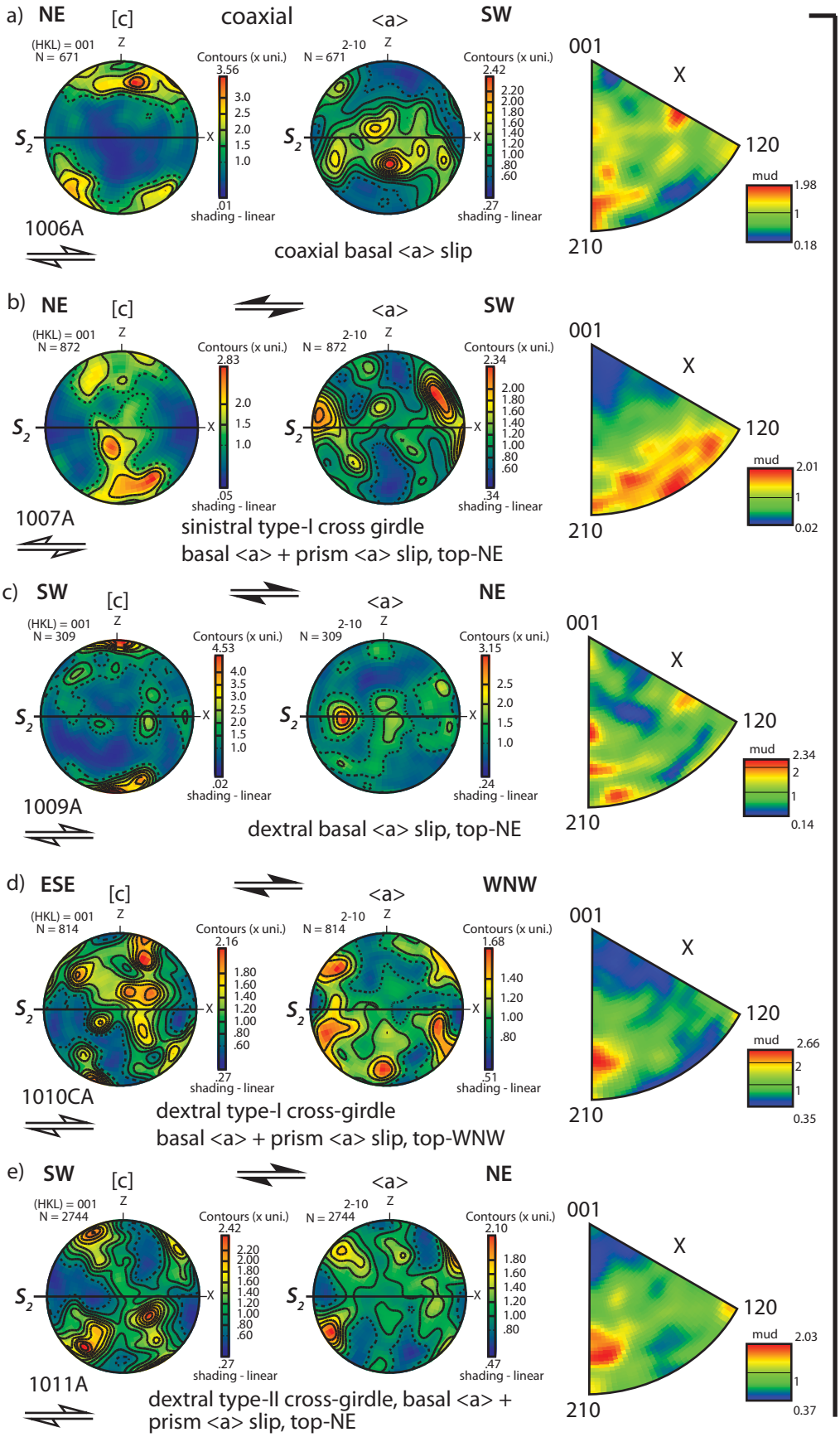
a) NE
[c]
coaxial
<a>
SW
(HKL) = 001
N = 671
Contours (x uni.)
3.56
3.0
2.5
2.0
1.5
1.0
.01
shading - linear
2-10
N = 671
2.42
2.20
2.00
1.80
1.60
1.40
1.20
1.00
.80
.60
.27
001
X
120
210
mud
1.98
1
0.18
1006A
coaxial basal <a> slip
b) NE
[c]
<a>
SW
(HKL) = 001
N = 872
2.83
2.0
1.5
1.0
.05
shading - linear
2-10
N = 872
2.34
2.00
1.80
1.60
1.40
1.20
1.00
.80
.60
.34
001
X
120
210
mud
2.01
1
0.02
1007A
sinistral type-I cross girdle
basal <a> + prism <a> slip, top-NE
c) SW
[c]
<a>
NE
(HKL) = 001
N = 309
4.53
4.0
3.5
3.0
2.5
2.0
1.5
1.0
.02
shading - linear
2-10
N = 309
3.15
2.5
2.0
1.5
1.0
.24
001
X
120
210
mud
2.34
2
1
0.14
1009A
dextral basal <a> slip, top-NE
d) ESE
[c]
<a>
WNW
(HKL) = 001
N = 814
2.16
1.80
1.60
1.40
1.20
1.00
.80
.60
.27
shading - linear
2-10
N = 814
1.68
1.40
1.20
1.00
.80
.51
001
X
120
210
mud
2.66
2
1
0.35
1010CA
dextral type-I cross-girdle
basal <a> + prism <a> slip, top-WNW
e) SW
[c]
<a>
NE
(HKL) = 001
N = 2744
2.42
2.20
2.00
1.80
1.60
1.40
1.20
1.00
.80
.60
.27
shading - linear
2-10
N = 2744
2.10
1.80
1.60
1.40
1.20
1.00
.80
.47
001
X
120
210
mud
2.03
1
0.37
1011A
dextral type-II cross-girdle, basal <a> +
prism <a> slip, top-NE
Domain I

Figure 2.12

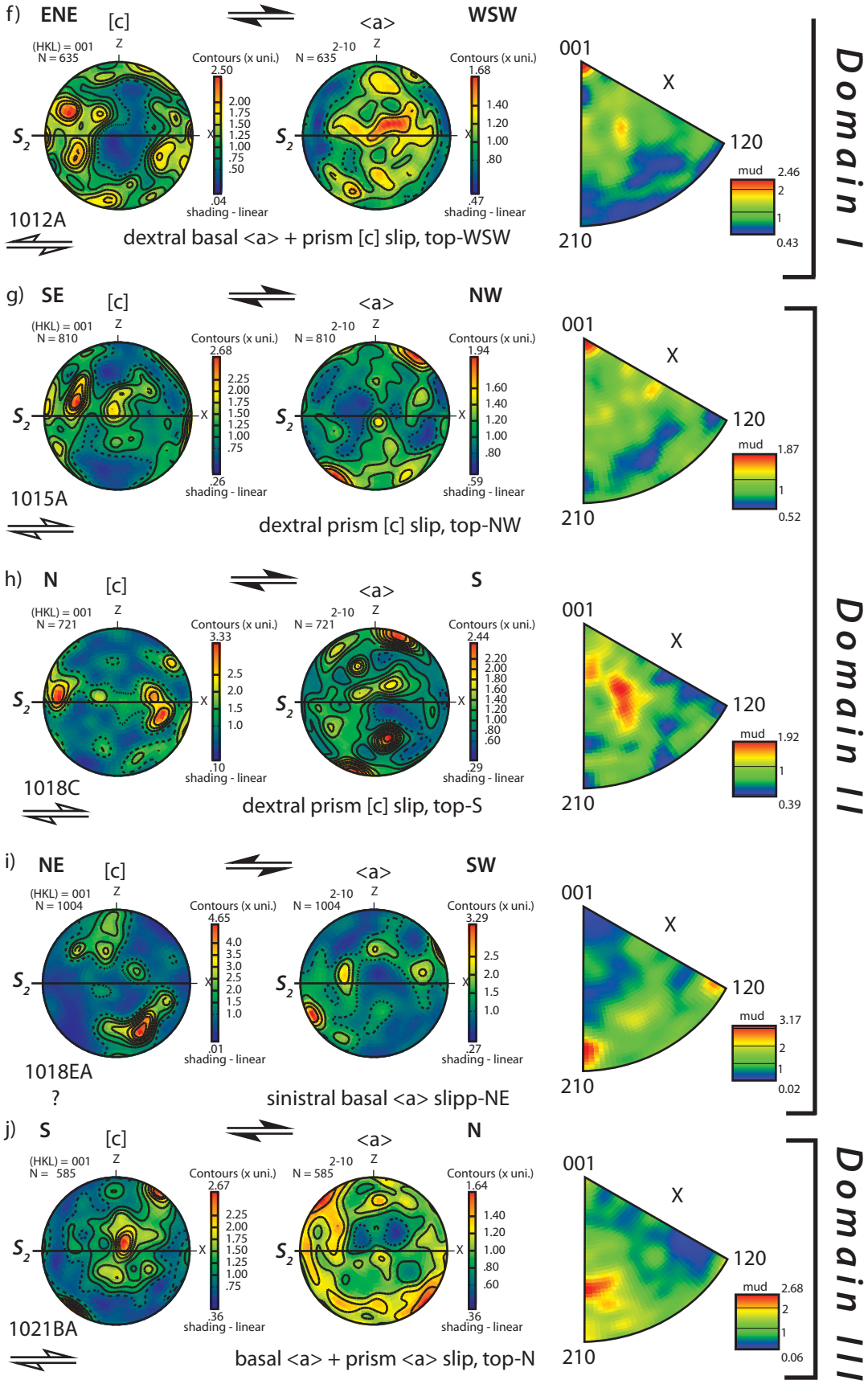
f) ENE
[c]
<a>
WSW
(HKL) = 001
N = 635
2-10
N = 635
Contours (x uni.)
2.50
2.00
1.75
1.50
1.25
1.00
.75
.50
.04
shading - linear
1.68
1.40
1.20
1.00
.80
.47
shading - linear
S2
X
Z
001
X
120
210
mud
2.46
2
1
0.43
1012A
dextral basal <a> + prism [c] slip, top-WSW
Domain I
g) SE
[c]
<a>
NW
(HKL) = 001
N = 810
2-10
N = 810
Contours (x uni.)
2.68
2.25
2.00
1.75
1.50
1.25
1.00
.75
.26
shading - linear
1.94
1.60
1.40
1.20
1.00
.80
.59
shading - linear
001
X
120
210
mud
1.87
1
0.52
1015A
dextral prism [c] slip, top-NW
h) N
[c]
<a>
S
(HKL) = 001
N = 721
2-10
N = 721
Contours (x uni.)
3.33
2.5
2.0
1.5
1.0
.10
shading - linear
2.44
2.20
2.00
1.80
1.60
1.40
1.20
1.00
.80
.60
.29
shading - linear
001
X
120
210
mud
1.92
1
0.39
1018C
dextral prism [c] slip, top-S
Domain II
i) NE
[c]
<a>
SW
(HKL) = 001
N = 1004
2-10
N = 1004
Contours (x uni.)
4.65
4.0
3.5
3.0
2.5
2.0
1.5
1.0
.01
shading - linear
3.29
2.5
2.0
1.5
1.0
.27
shading - linear
001
X
120
210
mud
3.17
2
1
0.02
1018EA
?
sinistral basal <a> slipp-NE
j) S
[c]
<a>
N
(HKL) = 001
N = 585
2-10
N = 585
Contours (x uni.)
2.67
2.25
2.00
1.75
1.50
1.25
1.00
.75
.36
shading - linear
1.64
1.40
1.20
1.00
.80
.60
.36
shading - linear
001
X
120
210
mud
2.68
2
1
0.06
1021BA
basal <a> + prism <a> slip, top-N
Domain III

Figure 2.12

Figure 2.12. CPOs of S_2 quartz from Domains I-III at Seno Martínez. Lower hemisphere pole figures of quartz c-axis (left column), a-axis (center column) and inverse pole figures of X (extension direction, right column). The sample number and sense of shear independently determined from thin sections (open half-arrow pairs) is shown in the lower left corner of each figure. The shear sense interpreted from the pole figures are shown in black half arrow pairs above the pole figures and the type of strain, and slip-systems and shear sense are interpreted below each set of plots. Pole figures are contoured in multiples of uniform distribution and the contour interval is shown to the right of each plot. Hereafter all pole figures are presented the same way.

is strongly parallel with <a> (210, 120). Sample 1009A (Figure 2.12c) exhibits c-axis patterns that cluster around Z, whereas a-axes form a girdle defined by three point maxima in the XY plane. The c-axis plot is slightly asymmetric indicating dextral (top-northeast) sense of shear. The lineation (X) is subparallel to or gently inclined toward <a> (210, 120). CPO patterns from samples 1006A, 1007A and 1009A predominantly indicate basal-<a> slip and top-northeast sense of shear. A secondary c-axis point-maxima near Y in sample 1007A (Figure 2.12b) indicates a minor component of prism-<a> slip.

Samples 1010, 1011, and 1012 were collected from Domain I >5 km north of the contact with the Rocas Verdes basin terrane and are from garnet-bearing schist, which are at a higher grade than samples 1006, 1007, and 1009 (Figure 2.2). C-axis patterns from 1010CA form a poorly developed, asymmetric (dextral, top-west-southwest) type-I cross girdle in the ZY plane with point maxima near to and clockwise from Z and a secondary point maxima near Y. A-axes plot around the primitive circle, and form small-circle girdles around X. The lineation (X) is subparallel to <a> (210 & 120; Figure 2.12d). Sample 1011A has a c-axis pattern that forms a well developed asymmetric (dextral, top-northeast) type-II cross girdle with maxima both along the primitive circle and subparallel to Y. A-axes form small-circle girdles in the ZY plane that are centered around X, and the lineation (X) is gently inclined toward <a> (210 & 120; Figure 2.12e). C-axes from sample 1012A plot around the primitive circle and form maxima near X and secondary maxima near Z. A-axes form a moderately developed girdle in the ZY plane, and both c-axis and a-axis patterns show slightly clockwise asymmetry, indicating dextral (top-west-southwest) shear. The lineation is strongly parallel to [c] (001; Figure 2.12f). CPOs from these samples are indicative of both basal-<a> and prism-<a> slip systems, as well as prism-[c] slip recorded by sample 1012A, suggesting higher temperature deformation conditions than recorded by samples 1006, 1007 and 1009.

Samples from Domain II include 1015A, 1018C and 1018EA (Figure 2.2). Of these, only sample 1015A is from garnet-bearing schist. C-axis patterns from sample 1015A form a girdle in the XY plane that contains primary point maxima near X and a

secondary maxima parallel to Y. A-axes form point maxima near Z and a poorly developed girdle in the ZY plane. The asymmetries of both plots indicate dextral sense of shear (top-northwest). The lineation (X) is well aligned with (001) indicating predominantly prism-[c] slip (Figure 2.12g). C-axis patterns from sample 1018C form a girdle in the XY with point maxima near X, and a-axes form a YZ girdle with maxima near Z. The lineation (X) is moderately inclined [c] (001). Both pole figures are asymmetric and show dextral (top-south) shear sense (Figure 2.12h). Sample 1018EA records c-axis patterns that form two point maxima that plunge gently (~20°) toward Z. A-axis form point maxima on the primitive circle near X and a girdle in the XY plane. Both c-axis and a-axis plots show counterclockwise asymmetry, indicating sinistral (top-northeast) sense of shear. The lineation (X) is well aligned with <a> (210 & 120; Figure 2.12i). CPO patterns from Domain II samples are indicative of prism-[c] and rhomb-<a> (*i.e.* sample 1018EA) slip systems, suggesting higher-temperature deformation than samples from the southern end of Domain I. This difference is compatible with the observation that samples exhibiting evidence of prism-[c] slip (1012A, 1015A, 1018C) were collected from a structurally lower position in the core of the F_4 antiform.

S_2 CPOs in Domain III are pervasively overprinted by S_4, as a result only one sample from Domain III preserves quality S_2 data (1021BA). C-axes from sample 1021BA form a ZY girdle that is asymmetric (dextral, top-north) and contains point maxima that plot along the primitive circle and parallel to Y. A-axes are distributed near the primitive circle and form two point maxima that are moderately inclined from X. The lineation is plunges shallowly toward <a> (210; Figure 2.12j). CPO patterns from sample 1021BA indicate both basal-<a> and prism-<a> slip, indicating cooler D_2 deformation temperatures than in Domain II.

5.2 S_4 Quartz CPOs, Seno Martinez

Domain I includes samples 1010AA, 1010CA, and 1012A (Figure 2.2). C-axes from sample 1010AA form a point maximum near X, and a-axis are well aligned and form a girdle defined by three point maxima in the ZY plane. The lineation (X) is parallel with [c], and the asymmetry of the plots indicates dextral (top-southwest) sense of shear

(Figure 2.13a). Sample 1010CA yielded c-axis orientations that form a point maximum parallel to Y, and a-axes that plot around the primitive circle. The lineation (X) is parallel to <a>. The sense of shear is unclear (Figure 2.13b). Sample 1012A yielded c-axis orientations that cluster near X, and a symmetric a-axis cross girdle in the ZY plane that is poorly defined by point maxima and indicates coaxial shear. The lineation (X) is parallel with [c]. Results from domain I suggest both prism-[c] and prism-<a> slip systems were active during D_4 top-southwest or coaxial shear.

Quartz CPOs from domain II were measured on samples 1018C, 1018EA, and 1019BA. Sample 1018C yields c-axis maxima that cluster near Z, and an a-axis girdle in the XY plane. Both c- and a-axis plots are asymmetric and indicate dextral (top-south) shear. The lineation (X) is subparallel with <a> (Figure 2.13d). C-axis orientations from sample 1018EA form a dextral (top-southwest) type-I cross-girdle with maxima near Z, X and Y. A-axes plot near the primitive circle, and the lineation is subparallel to and moderately inclined toward <a> (Figure 2.13e). C-axes from sample 1019BA form an inclined girdle in the ZY plane, and a-axes form point maxima that are inclined ~30° clockwise from X. The asymmetry of each plot is dextral indicating top-north shear. The lineation (X) plunges moderately toward <a> (Figure 2.13f). Results from domain II are indicative of both basal-<a> (Figure 2.12d,e,f) and prism-<a> (Figure 2.13d-f) slip associated with top-southwest or top-north shear sense.

Quartz CPOs from Domain III were measured on sample 1020A and 1021A (Figure 2.2). Sample 1020A yields c-axes that form a point maximum near X and a secondary maximum near Z. A-axes form a girdle in the ZY plane, and the asymmetry of c-axis and a-axis plots indicates dextral (top-southwest) shear. The lineation (X) is parallel with [001] (Figure 2.13g). C-axes from sample 1021BA form a poorly defined girdle in the XY plane with secondary maxima near Z. A-axes are not well aligned, but form moderately developed point maxima near Z and X. The slight asymmetry of c- and a-axis pole figures suggests sinistral (top-northeast) sense of shear. The lineation (X) is subparallel to both <a> and [c] (Figure 2.13h). CPO patterns from S_4 foliations in domain III provide evidence of the concurrent activity of basal-<a>, prism-<a> and prism-[c] slip

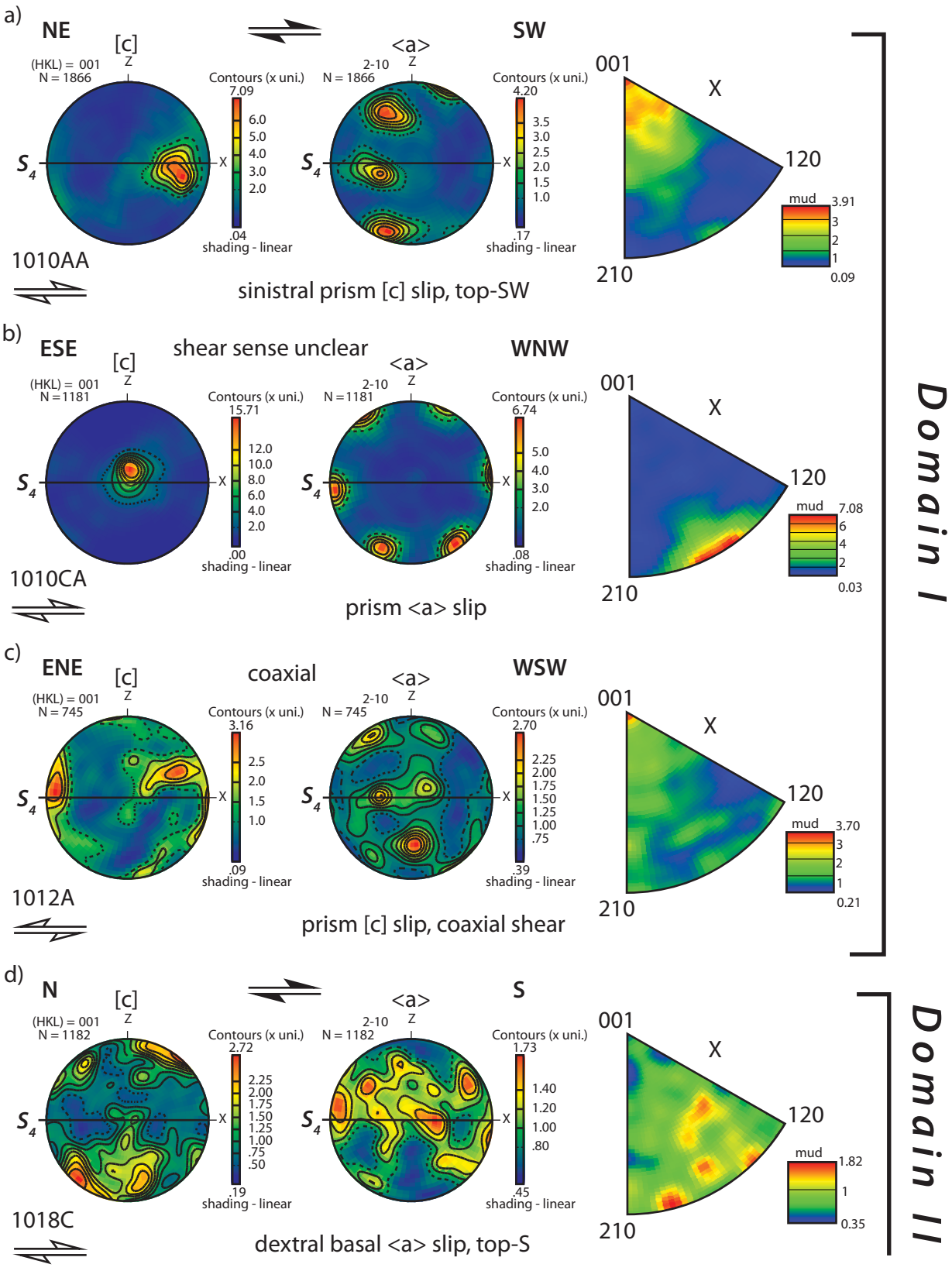

Figure 2.13. CPOs of S_4 quartz from Domains I-III at Seno Martínez (continued on next page).

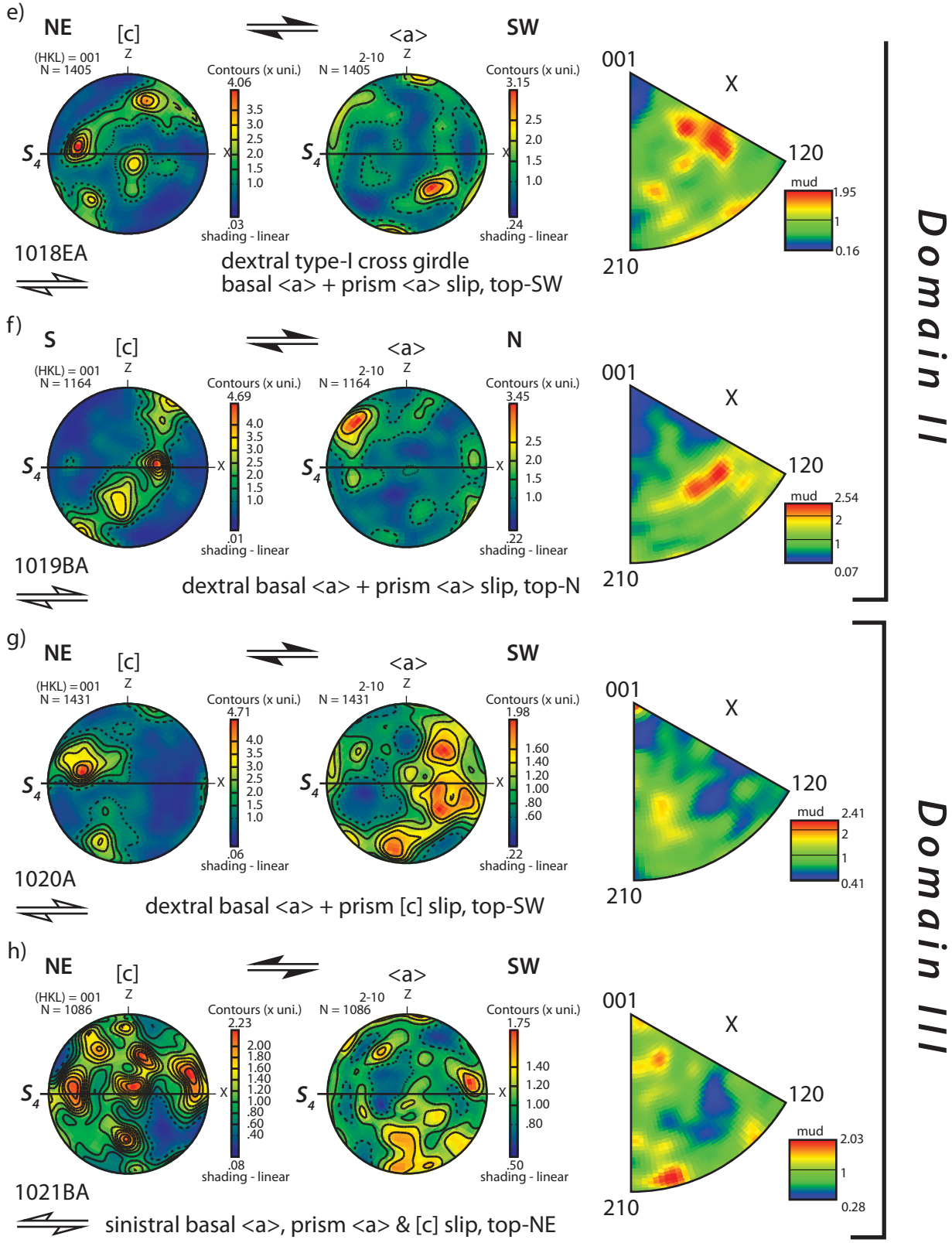
e)
NE
[c]
SW
<a>
(HKL) = 001
N = 1405
2-10
N = 1405
Contours (x uni.)
4.06
3.5
3.0
2.5
2.0
1.5
1.0
.03
shading - linear
3.15
2.5
2.0
1.5
1.0
.24
shading - linear
S4
X
Z
1018EA
dextral type-I cross girdle
basal <a> + prism <a> slip, top-SW
001
X
120
210
mud
1.95
1
0.16
f)
S
N
(HKL) = 001
N = 1164
2-10
N = 1164
4.69
4.0
3.5
3.0
2.5
2.0
1.5
1.0
.01
3.45
2.5
2.0
1.5
1.0
.22
1019BA
dextral basal <a> + prism <a> slip, top-N
mud
2.54
2
1
0.07
g)
(HKL) = 001
N = 1431
2-10
N = 1431
4.71
4.0
3.5
3.0
2.5
2.0
1.5
1.0
.06
1.98
1.60
1.40
1.20
1.00
.80
.60
.22
1020A
dextral basal <a> + prism [c] slip, top-SW
mud
2.41
2
1
0.41
h)
(HKL) = 001
N = 1086
2-10
N = 1086
2.23
2.00
1.80
1.60
1.40
1.20
1.00
.80
.60
.40
.08
1.75
1.40
1.20
1.00
.80
.50
1021BA
sinistral basal <a>, prism <a> & [c] slip, top-NE
mud
2.03
1
0.28
Domain II
Domain III

Figure 2.13

along with both top-northeast and top-southwest shear. Quartz CPO results from D_4 domains show evidence for all three of the important quartz slip systems (basal-<a>, prism-<a> and prism-[c]) and have no apparent spatial trend, suggesting D_4 deformation temperatures were high enough to allow multiple slip systems.

5.3 S_2 AND S_4 CPO SYNTHESIS AT SENO MARTÍNEZ

S_2 and S_4 microstructural observations and quartz CPO data from Domains I-III in Seno Martínez are synthesized in Figure 14. Dynamically recrystallized quartz elongate parallel to S_2 is locally recrystallized and overprinted by S_4 (Figure 14a-c; see also Figure 2.10). In S_2 domains (lower portions of Figures 2.14a-c), shear sense indicators and quartz CPOs are commonly well preserved. Here, quartz CPOs indicate dominantly top-northeast shear sense associated with S_2 fabrics. Slip-systems indicated by CPO patterns in S_2 domains include basal-<a>, prism-<a> and prism-[c] slip. Any affect of recrystallization during F_3 folding on CPOs from S_2 fabrics is unclear, however, on the basis of subparallelism of F_3 sheath folds with the L_2 stretching lineation (*i.e.* section 3.3) it is inferred that the transport direction was parallel and that F_3 recrystallization would probably have enhanced S_2 CPOs.

Coarse-grained quartz domains are commonly recrystallized and overprinted by S_4 (upper portions of Figure 2.14a-c). The shear sense associated with S_4 domains is dependent on the vergence of F_4 kink-folds that define them, but is commonly antithetic to (*i.e.* top-southwest) the sense-of-shear associated with S_2 (Figure 14c). Slip-systems associated with the formation of S_4 include, basal-<a>, prism-<a> and prism-[c] slip and show no apparent spatial trends, suggesting mixed slip-systems were active during the formation of S_4.

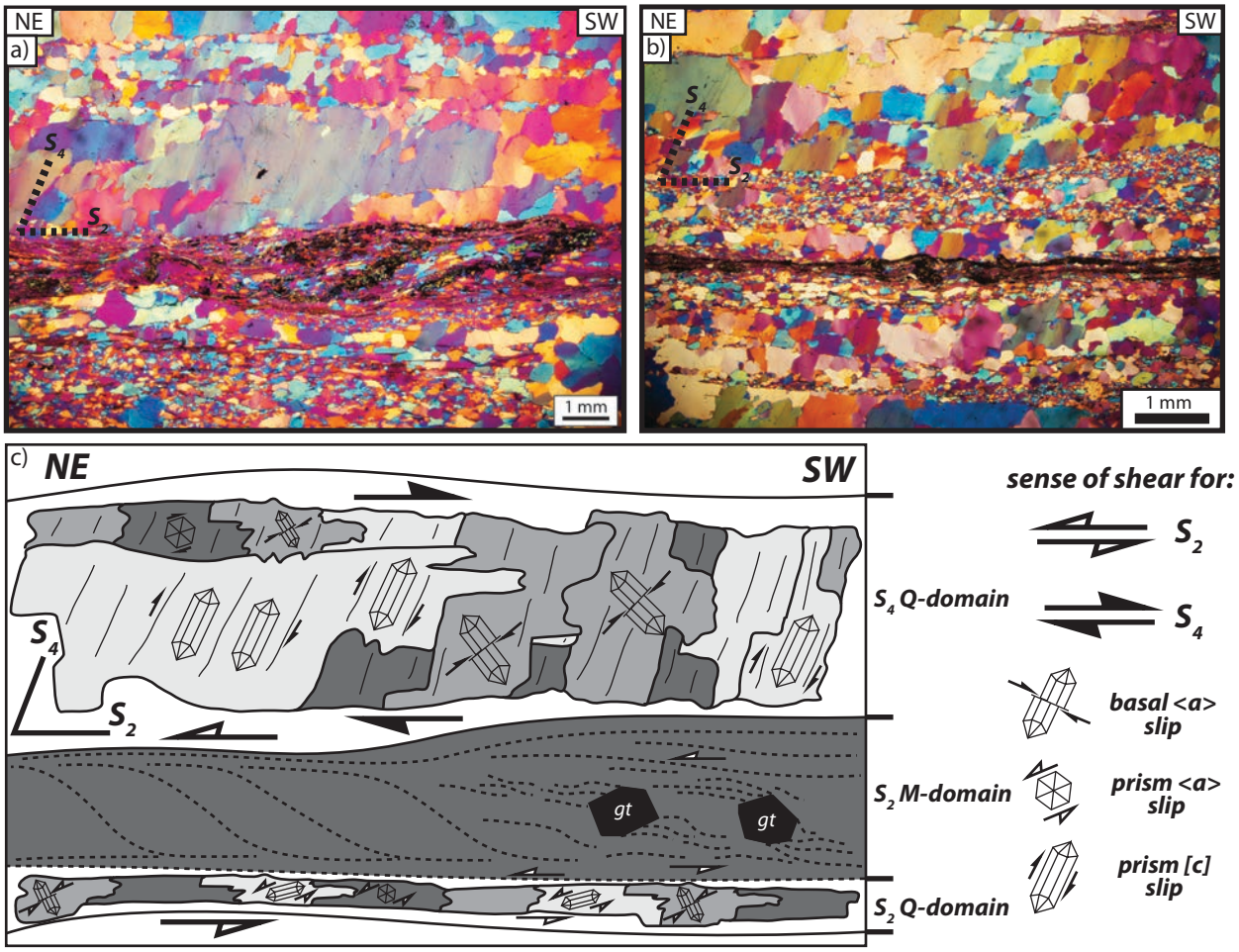

Figure 2.14. Synthesis of CPO data from S_2 and S_4 fabrics in Domains I-III near Seno Martínez. (a-b) Photomicrographs showing examples of samples that exhibit good preservation of both S_2 (parallel to base of slide) and S_4 (steeply inclined toward the NE) fabrics and (c) sketch showing interpretation of CPO results for S_2 and S_4 fabrics. In regions where S_2 is well preserved (*i.e.* lower part of (a) and (c)), CPO results indicate the activity of all three major slip-systems, basal <a>, prism <a> and prism <c> and dominantly top-northeast shear that is sympathetic with other microstructural shear sense indicators. In regions where S_4 is pervasive (*i.e.* (b) and the upper part of (a) and (c)) relict S_2 fabrics are reoriented by the S_4 fabric that is indicative of all three slip-systems and dominantly top-southwest shear.

6. The Cordillera Darwin Metamorphic Complex near Bahía Fortesque and Estuario Silva Palma

Along-strike ~75 km toward the northwest from Seno Martínez, rocks of the Cordillera Darwin Metamorphic Complex are exposed on Peninsula Brunswick where they are tectonically interleaved with Jurassic rocks of the Rocas Verde basin (Tobífera Formation). Near Bahía Fortesque (Figure 2.1), a ~1 km thick ductile high strain zone known as the Bahía Fortesque shear zone juxtaposes the Cordillera Darwin Metamorphic Complex above the Tobífera Formation (see Chapter 1). Near Estuarios Silva Plama and Wickham (> 10 km northeast of Bahía Fortesque), the Cordillera Darwin Metamorphic Complex is exposed in the hanging wall of an out-of-sequence fault that juxtaposes it above rocks of the Magallanes fold-thrust belt and Upper-Cretaceous to Paleocene foreland basin strata (see chapter 1). In both locations, chlorite-quartz schist of the Cordillera Darwin Metamorphic Complex are pervasively deformed by several generations of structures (see Chapter 1) that are similar to those at Seno Martínez. To determine the deformation conditions associated with structures in the Cordillera Darwin Metamorphic Complex on Peninsula Brunswick and compare them with those at Seno Martínez, I describe the quartz recrystallization textures and performed EBSD analyses of five samples from Bahía Fortesque, five samples from Estuario Silva Palma and one sample from Estuario Wickham. For a detailed description of the macroscopic structures in these locations see Chapter 1.

6.1 Quartz microstructures and kinematic indicators from the Cordillera Darwin Metamorphic Complex on Peninsula Brunswick

6.1.1 The Bahía Fortesque high-strain zone

The Bahía Fortesque shear zone is defined by a southwest-dipping, composite schistose foliation (S_2) that contains a prominent southwest-plunging, recrystallized quartz lineation (L_2, Figure 1.14, chapter 1). Macroscopic kinematic indicators include C-S fabrics and C' shear bands that indicate and top-northeast shear (see Chapter 1). In thin section, the S_1 foliation is defined by compositional layering between quartz-rich and

phylosilicate-rich domains. The S_1 surface is commonly transposed by C-S type shear bands to form a composite foliation (S_2). The asymmetry of C-S fabrics indicates top-northeast shear (Figure 2.15a). S_1 is commonly folded by intrafolial isoclinal folds (F_2) that are also transposed parallel to S_2 (Figure 2.15a). A sample collected from below the Bahía Fortesque shear zone (1116) preserves upright, tight F_2 folds that do not have a pervasive S_2 (Figure 2.15b), indicating qualitatively lower strains than samples from within the Bahía Fortesque high-strain zone.

Quartz occurs in layers parallel to S_2 in the Bahía Fortesque high-strain zone and has undergone substantial recrystallization and subgrain formation. Recrystallized subgrains are commonly polygonal and have approximately uniform grain size (Figure 2.15a, d). In some locations, layers of recrystallized, elongate grains form a second foliation (S_2) that is oblique to S_1 and indicates top-northeast shear (Figure 2.15c). Feldspar grains are not common, but where observed they are not substantially recrystallized (Figure 2.15d). Quartz microstructures from the Bahía Fortesque shear zone are characteristic of subgrain rotation recrystallization and Regime 2 dislocation creep of Hirth and Tullis (1992) and/or the subgrain rotation regime of Stipp *et al*. (2002).

6.1.2 Estuario Silva Palma

The Cordillera Darwin Metamorphic Complex at Estuario Silva Palma is deformed by two generations of structures similar to those at Bahía Fortesque. Here, the pervasive schistose foliation (S_1) contains a prominent quartz stretching lineation (L_1), and both structures are folded by isoclinal F_2 folds (see chapter 1). In phylosilicate domains, S_2 is commonly defined by pressure solution seams that overprint an older crenulated surface (S_1, Figure 2.15e). In quartz-rich domains, quartz occurs in layers that are extensively recrystallized to form polygonal subgrains of approximately uniform grain size (Figure 2.15e-f). In the hinges of F_2 folds, recrystallized quartz grains are elongate parallel to the axial plane (S_2) of the folds (Figure 2.15f). Quartz microstructures from the Cordillera Darwin Metamorphic Complex in Estuario Silva Palma are indicative subgrain rotation recrystallization and regime 2 dislocation creep of Hirth and

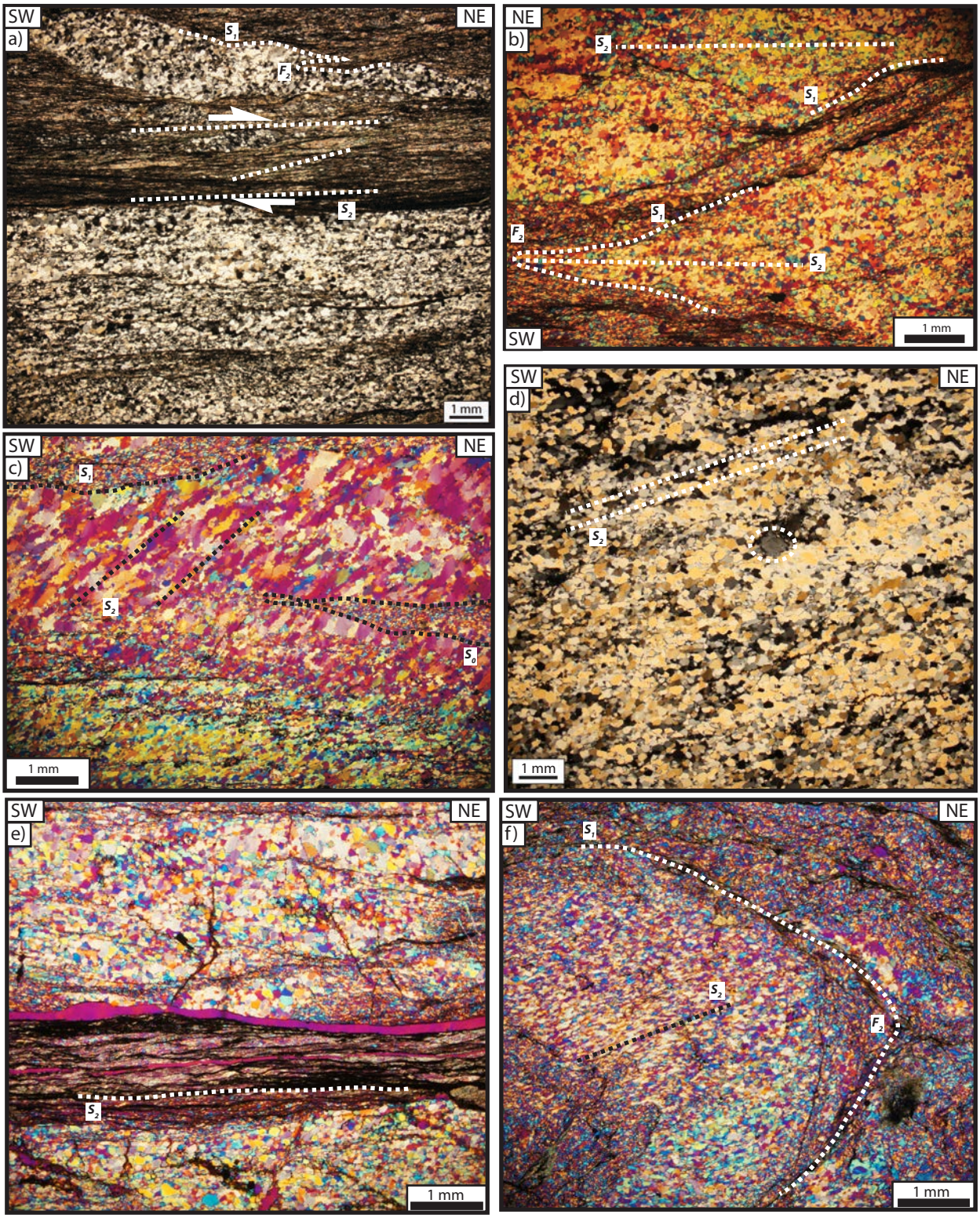

Figure 2.15. Photomicrographs showing quartz subgrain rotation recrystallization textures, superposed fabric relationships and/or kinematic indicators from the Bahía Fortesque shear zone (a-d) and from pelitic schist of the Cordillera Darwin Metamorphic Complex at Estuario Silva Palma (e-f). Oval in (d) highlights a rigid feldspar grain. See text for descriptions.

Tullis (1992) and/or the subgrain rotation regime of Stipp *et al*. (2002). Microstructural shear sense indicators are absent or ambiguous in samples form Estuario Silva Palma.

7. Quartz CPOs from the Cordillera Darwin Metamorphic Complex on Peninsula Brunswick

7.1 Bahía Forestque high-strain zone

Quartz CPOs were measured in five samples from the Bahía Fortesque high-strain zone to determine the slip-systems, sense of shear and deformation temperatures associated with the shear zone. Results are presented in Figure 2.16. Samples 11105A-D are from within the high-strain zone (Figure 2.16a-d) and sample 11116 (Figure 2.16e) is from below it. C-axes from sample 11105A form a small circle girdle centered on Z, and a-axes form a symmetric cross girdle in the XY plane. The lineation (X) is inclined ~30° toward <a> (Figure 2.16a). The symmetry of the plots indicates coaxial shear. C-axes from sample 11105B form primary point maxima near Z and a secondary maximum near Y (Figure 2.16b). A-axes form a poorly defined girdle in the XY plane, and X plunges moderately toward <a>. Both c- and a-axis plots show clockwise asymmetry, indicating dextral (top-northeast) shear. Samples 11105C and D are very similar (Figure 2.16c-d). C-axis orientations form point-maxima near Z, and a-axes form a girdle in the XY plane. Each plot is asymmetric and indicates a sinistral (top-northeast) sense of shear. The lineation (X) is subparallel to or gently inclined toward <a> (Figure 2.16c-d). Sample 1116 was collected below the high-strain zone. Point maxima for c-axes are subparallel to Y and X, and for a-axes, subparallel to Y and Z. The lineation (X) is inclined toward <a> suggesting <a>-slip, however, the c- and a- axis patterns from this sample are not diagnostic of a particular slip-system (Figure 2.16e). Poorly developed patterns in sample 1116 (Figure 2.16e) probably reflect its position in a relatively low strain zone outside of the Bahía Fortesque shear zone.

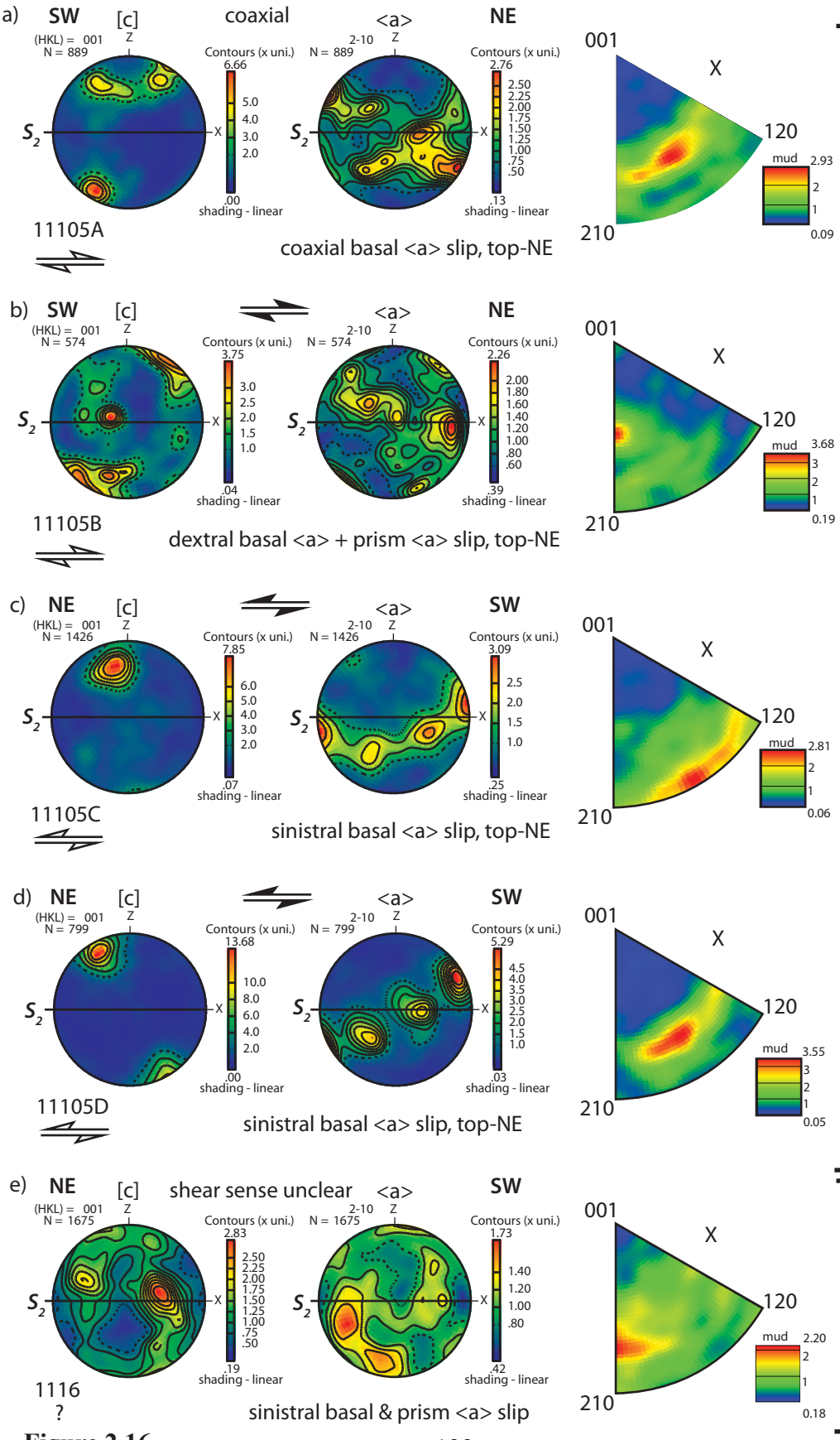
a) SW [c] coaxial <a> NE
(HKL) = 001 N = 889
Contours (x uni.) 6.66
5.0 4.0 3.0 2.0
.00 shading - linear
2-10 N = 889
Contours (x uni.) 2.76
2.50 2.25 2.00 1.75 1.50 1.25 1.00 .75 .50
.13 shading - linear
001 X 120 210
mud 2.93 2 1 0.09
11105A
coaxial basal <a> slip, top-NE
b) SW [c] <a> NE
(HKL) = 001 N = 574
Contours (x uni.) 3.75
3.0 2.5 2.0 1.5 1.0
.04 shading - linear
2-10 N = 574
Contours (x uni.) 2.26
2.00 1.80 1.60 1.40 1.20 1.00 .80 .60
.39 shading - linear
001 X 120 210
mud 3.68 3 2 1 0.19
11105B
dextral basal <a> + prism <a> slip, top-NE
c) NE [c] <a> SW
(HKL) = 001 N = 1426
Contours (x uni.) 7.85
6.0 5.0 4.0 3.0 2.0
.07 shading - linear
2-10 N = 1426
Contours (x uni.) 3.09
2.5 2.0 1.5 1.0
.25 shading - linear
001 X 120 210
mud 2.81 2 1 0.06
11105C
sinistral basal <a> slip, top-NE
d) NE [c] <a> SW
(HKL) = 001 N = 799
Contours (x uni.) 13.68
10.0 8.0 6.0 4.0 2.0
.00 shading - linear
2-10 N = 799
Contours (x uni.) 5.29
4.5 4.0 3.5 3.0 2.5 2.0 1.5 1.0
.03 shading - linear
001 X 120 210
mud 3.55 3 2 1 0.05
11105D
sinistral basal <a> slip, top-NE
e) NE [c] shear sense unclear <a> SW
(HKL) = 001 N = 1675
Contours (x uni.) 2.83
2.50 2.25 2.00 1.75 1.50 1.25 1.00 .75 .50
.19 shading - linear
2-10 N = 1675
Contours (x uni.) 1.73
1.40 1.20 1.00 .80
.42 shading - linear
001 X 120 210
mud 2.20 2 1 0.18
1116
?
sinistral basal & prism <a> slip
Bahía Fortesque high strain zone
Below HSZ

Figure 2.16

Figure 2.16. CPOs of S_2 quartz from pelitic schist within (a-d) and below (e) the Bahía Fortesque high-strain zone.

7.2 Estuarios Silva Palma and Wickham

Four samples (1053 and 1054A-C, Figure 2.17a-d) from the Cordillera Darwin Metamorphic Complex near Estuario Silva Palma and one sample from Estuario Wickham (11086B, Figure 2.17e) were selected for EBSD fabric analysis of quartz. C-axis orientations from sample 11053 form point maxima that are symmetric around Z and a secondary maxima near Y. A-axes form a symmetric cross girdle in the XY plane. The symmetry of these plots are indicative of coaxial deformation. The lineation (X) is subparallel to <a> (210, Figure 2.17a). C-axis patterns from sample 1054A form an asymmetric (dextral, top-northeast) type-I cross girdle; a-axes form a cross-girdle in the XY plane, and the lineation is subparallel to <a> (210; Figure 2.17b). Sample 11054B yields c-axis patterns that define point maxima near Z and a weak ZY girdle; a-axes form a girdle in the XY plane, and both plots are asymmetric indicating dextral (top-southwest) shear. The lineation (X) is plunges moderately toward <a> (Figure 2.17c). Sample 11054C has c-axis orientations that form a ZY girdle with point maxima near both Z and Y. A-axes define small circle girdles centered around X. The lineation plunges shallowly toward <a>, and the asymmetry of the pole figures indicates dextral shear (top-northeast; Figure 2.17d). Sample 11086B from Estuario Wickham gives c-axis orientations that form point maxima near Z, and a-axes that are poorly organized. The lineation is also poorly defined in the crystallographic reference frame. The asymmetry of the c-axis pole figure indicates sinistral (top-northeast) shear.

7.3 Synthesis of quartz CPOs from the Cordillera Darwin Metamorphic Complex on Peninsula Brunswick

All pole figures from Estuario Silva Palma (Figure 2.17a-d) and Estuario Wickham (Figure 2.17e) are indicative of predominantly basal-<a> slip. Data from Estuario Silva Palma (Figure 2.17a-d) also include some evidence for prism-<a> slip (*e.g.* Figure 2.17a & d). CPOs are consistent with quartz textural evidence that suggest subgrain rotation recrystallization and Regime 2 dislocation creep, indicating deformation temperatures equivalent to those from the Bahía Fortesque high-strain zone but cooler than those from Domains I-III near Seno Martínez.

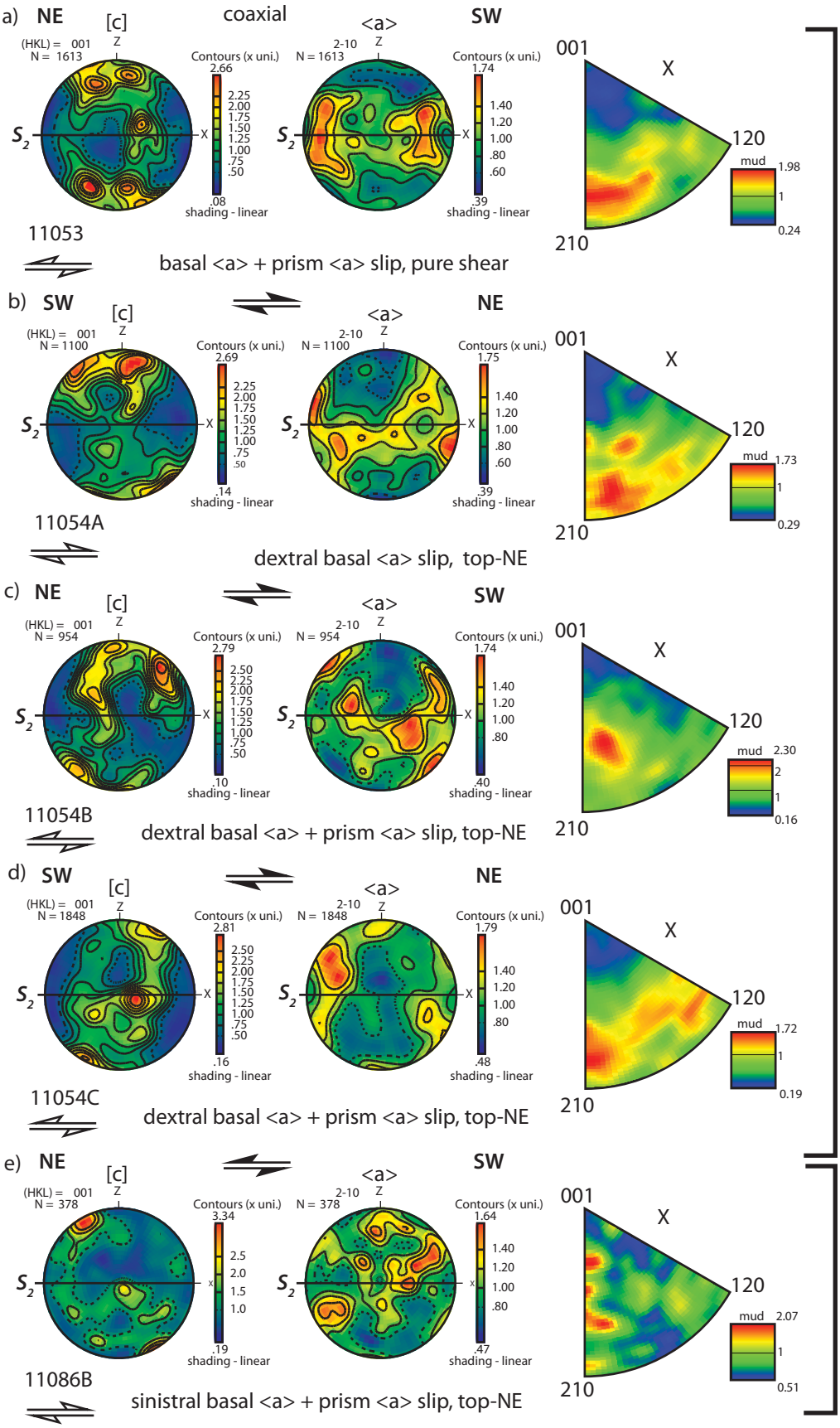
a) NE
[c]
coaxial
<a>
SW
(HKL) = 001
N = 1613
Contours (x uni.)
2.66
2.25
2.00
1.75
1.50
1.25
1.00
.75
.50
.08
shading - linear
2-10
N = 1613
Contours (x uni.)
1.74
1.40
1.20
1.00
.80
.60
.39
shading - linear
001
X
120
mud
1.98
1
0.24
210
11053
basal <a> + prism <a> slip, pure shear
b) SW
[c]
<a>
NE
(HKL) = 001
N = 1100
Contours (x uni.)
2.69
2.25
2.00
1.75
1.50
1.25
1.00
.75
.50
.14
shading - linear
2-10
N = 1100
Contours (x uni.)
1.75
1.40
1.20
1.00
.80
.60
.39
shading - linear
001
X
120
mud
1.73
1
0.29
210
11054A
dextral basal <a> slip, top-NE
c) NE
[c]
<a>
SW
(HKL) = 001
N = 954
Contours (x uni.)
2.79
2.50
2.25
2.00
1.75
1.50
1.25
1.00
.75
.50
.10
shading - linear
2-10
N = 954
Contours (x uni.)
1.74
1.40
1.20
1.00
.80
.40
shading - linear
001
X
120
mud
2.30
2
1
0.16
210
11054B
dextral basal <a> + prism <a> slip, top-NE
d) SW
[c]
<a>
NE
(HKL) = 001
N = 1848
Contours (x uni.)
2.81
2.50
2.25
2.00
1.75
1.50
1.25
1.00
.75
.50
.16
shading - linear
2-10
N = 1848
Contours (x uni.)
1.79
1.40
1.20
1.00
.80
.48
shading - linear
001
X
120
mud
1.72
1
0.19
210
11054C
dextral basal <a> + prism <a> slip, top-NE
e) NE
[c]
<a>
SW
(HKL) = 001
N = 378
Contours (x uni.)
3.34
2.5
2.0
1.5
1.0
.19
shading - linear
2-10
N = 378
Contours (x uni.)
1.64
1.40
1.20
1.00
.80
.47
shading - linear
001
X
120
mud
2.07
1
0.51
210
11086B
sinistral basal <a> + prism <a> slip, top-NE
Estuario Silva Palma
Estuario Wickham

Figure 2.17

Figure 2.17. CPOs of S_2 quartz from pelitic schist of the Cordillera Darwin Metamorphic Complex at Estuario Silva Palma (a-d) and Estuario Wickham (e).

8. Discussion

8.1 Correlation of structures in the Cordillera Darwin Metamorphic Complex near Seno Martínez.

Pelitic schists of the Cordillera Darwin Metamorphic Complex exposed near Seno Martínez are everywhere deformed by at least four generations of structures (D_1 -D_4). The sequence of deformation allows for correlation between structural domains. Everywhere along Seno Martínez the pelitic schist of the Cordillera Darwin Metamorphic Complex displays a prominent composite schistose foliation (S_1/S_2) and quartz stretching lineation (L_2) that are refolded. Therefore structures from each domain can be correlated relative to this surface. In Domain I the composite $S_{1\text{-}2}$ fabric in the pelitic schist is subparallel with S_1 in the epidote-actinolite schists, thus both fabrics are interpreted to reflect the same deformation. S_1 that is unique to the Paleozoic pelitic schists of the Cordillera Darwin Metamorphic Complex is transposed by intrafolial folds (F_2) that partly define the composite foliation ($S_{1\text{-}2}$). Therefore, S_1 in the pelitic schist must reflect an older deformation than S_2 /L_2 in the pelitic schist and S_1 /L_1 in the epidote-actinolite schist (D_1; *c.f.* 'pre-Andean' fabric of Nelson *et al*., 1980) and are not discussed further. Relative to the S_2 /L_2 surface, F_3 folds are equivalent in age across all four of the structural domains (D_3). Similarly, F_4 folds are interpreted to be coeval everywhere in the study area (D_4).

Each structural domain displays evidence for each of the main phases of deformation (D_2 -D_4), however, the magnitude of each deformation is spatially variable between domains and is evaluated on the basis of tightness of folds and occurrences of structures commonly associated with high-strain zones such as prominent mineral lineations and/or sheath folds. Below I correlate the macroscopic and microscopic structures from Seno Martínez and interpret them in terms of qualitative high- and low-strain zones associated with each deformation (D_2 –D_4).

8.1.1 D_2 macroscopic structures

Everywhere along Seno Martíez D_2 structures are defined by a pervasive schistose foliation that is defined by the alignment of quartz, chlorite and muscovite and contains a prominent quartz stretching lineation (S_2 /L_2). This surface occurs in all four of the

structural domains at Seno Martínez where it is everywhere refolded by F_3 and F_4. The common occurrence of this surface across all domains at Seno Martínez suggests that D_2 deformation was relatively homogeneous across the study area.

8.1.2 D_3 macroscopic structures

D_3 structures along Seno Martínez are spatially heterogeneous. In Domain I, F_3 are generally tight folds that occupy upright, inclined and reclined orientations that refold the S_2 /L_2 surface (*e.g.* Figure 2.5e-h). In contrast, F_3 folds in Domain II are tight to isoclinal and include sheath folds with axes that are parallel to the local quartz stretching lineation (L_2; *e.g.* Figures 2.6a-d). Thus relative to Domain I, F_3 fold limbs have been tightened and the fold hinges sheared to form the sheaths. On this basis, a qualitative increase in strain is inferred toward the northeast from Domain I to Domain II with regard to D_3 structures. The parallelism of F_3 sheath folds in Domain II with the L_2 stretching lineation is interpreted to reflect progressive deformation during D_2 and D_3 where the highest intensity of D_3 deformation is localized in Domain II. Farther to the north in Domain III, sheath folds disappear and regional, recumbent tight and isoclinal folds characterize F_3 (*e.g.* Figure 2.7a). Although the regional folds reflect large amounts of shortening, the absence of the sheath folds suggests qualitatively lower shear strains in Domain III than in Domain II and defines a negative strain gradient from Domain II to III. In Domain IV, F_3 folds are upright tight folds (*e.g.* Figure 2.8b, c) that are similar in geometry and structural-style to upright folds observed in Domain I and thus reflect lower strains than Domain II and III.

8.1.3 D_2 microstructure and quartz CPOs

Quartz microstructures associated with D_2 fabrics everywhere near Seno Martínez show textural evidence for subgrain rotation recrystallization and grain boundary migration that are equivalent to Regime 3 dislocation creep (Hirth and Tullis, 1992) and/or the subgrain rotation recrystallization to grain boundary migration transition of Stipp *et al*. (2002) (Figure 2.10a-c). Quartz CPOs from S_2 fabrics in domains I and II suggest a systematic increase in deformation temperature structurally down-section from

the sheared contact with the Rocas Verdes basin terrane (near site 1006, Figure 2.2) toward the core of the D_4 antiform near Seno Oryan (Figure 2.2, 2.3). In Domain I, Quartz CPOs from D_2 structures record a southwest to northeast change in quartz slip systems from basal-<a> slip (Figure 2.12a-c) to basal-<a> + prism-<a> slip (Figure 2.12 d-e) and prism-[c] slip near site 1012 (Figure 2.12f). The occurrence of prism-[c] slip in two samples from domain II near Seno Oryan near sites 1015 and 1018 (Figure 2.3,m 12g-h) record the highest temperature slip-systems in the study area. This trend in quartz slip systems is consistent with textural evidence (*i.e.* chessboard extinction, Figure 2.10c) for high-temperature dislocation creep that only occurs in Seno Oryan near the core of the F_4 antiform. North of Seno Oryan, near sites 1018 and 1021 quartz CPOs reflect basal-<a> and prism-<a> slip (*e.g.* figures 2.12i, j) and suggest D_2 deformation conditions that are equivalent of those in located in Domain I on the southwest dipping limb of the regional F_4 antiform (*i.e.* Figures 2.12a-e). Quartz slip systems and CPOs from Domains I-III are indicative deformation temperatures ranging from ~500-650° C during D_2.

Microstructural kinematic indicators from the Cordillera Darwin Metamorphic Complex in Domain I and II include C-S and C' shear bands and asymmetric tails on synkinematic garnet porphyroblasts that are compatible with top-northeast shear during D_2 (Figure 2.9). Supporting these observations, pole figures from D_2 recrystallized quartz fabrics in Domain I and II are commonly asymmetric and indicate either dominantly coaxial or top-northeast sense of shear (Figure 2.12a-c, e, i). However, quartz CPOs from several samples collected in Domains I and II have asymmetries that indicate a different sense of shear, either top-west or northwest (Figures 2.12 d, f-g) or top-S (Figure 2.12h). These samples probably reflects reorientation of the D_2 fabrics as they were folded around later (F_3 and F_4) folds. The dominance to top-NE kinematic indicators from microstructures and quartz CPOs is interpreted to reflect bulk top-northeast shear during D_2 in domains I and II.

8.1.4 D_4 macroscopic structures

Evidence for D_4 occurs in Domains I-III near Seno Martínez and is also spatially heterogeneous. In Domains I and III, F_4 is defined by sets of upright kink-bands with axial surfaces that dip steeply toward the east and west (Figures 2.5i-j and 2.7b, e). F_4 kink-folds in Domains I and III are localized to phylosilicate-rich lithologies. The geometry of F_4 folding in Domain II contrasts sharply with Domains I and III. In Domain II, F_3 structures are refolded by steeply plunging reclined folds with upright axial surfaces (F_4) and form Ramsay type II and III superposed fold patterns (Figures 2.6a-d, j). In Domain II, F_4 deformation is pervasive and defines a D_4 high-strain zone relative to Domains I and III.

8.1.5 D_4 microstructure and quartz CPOs

Quartz CPOs associated with D_4 fabrics from Domain I in Seno Martínez (Figure 2.13a-c) record both prism-<a> and prism-[c] slip parallel to the S_4 foliation. Quartz CPOs from D_4 fabrics in Domain II indicate both basal-<a> and prism-<a> slip (Figure 2.12d-f) and Domain III CPOs record basal-<a>, prism-<a> and prism-[c] slip (Figure 2.12g-h). The asymmetry of pole figures for D_4 fabrics indicates either top-south to southwest or top-north to northeast shear that is compatible with the asymmetry of local F_4 kink bands that define the S_4 foliation.

Pole figures from D_4 fabrics in Domains I-III show evidence for all of the quartz slip systems and do not reflect any spatial trend, suggesting deformation temperatures were regionally high enough (> ~500°C, Stipp *et al*., 2002) to allow mixed slip. This interpretation is compatible with quartz recrystallization textures from D_4 fabrics everywhere in Domains I, II and III near Seno Martínez that indicate subgrain rotation recrystallization and grain boundary migration dislocation creep were dominant recrystallization mechanisms, equivalent with Regime 3 dislocation creep (Hirth and Tullis, 1992) and/or the subgrain rotation recrystallization to grain boundary migration transition of Stipp *et al*. (2002) (Figure 2.10d-f). Quartz slip systems and CPOs from D_4 structures are indicative of deformation temperatures ranging from ~500-650° C, equivalent to those of D_2.

8.1.6 Domain IV: structure of Bahía Angelito

Field relations at Bahía Angelito indicate that the contact between the Cordillera Darwin Metamorphic Complex and Tobífera Formation is a sheared unconformity that forms a thrust flat. F_3 folds in the Cordillera Darwin Metamorphic Complex below the contact are upright, tight folds that indicate south-north shortening. Here, top-northeast C-S fabrics that occur parallel to S_2 (Figure 2.8d) are interpreted to reflect top-northeast shearing of the Tobífera Formation over the Cordillera Darwin Metamorphic Complex during D_2 and D_3.

Above the contact, a set of south-southwest dipping brittle thrust faults imbricate the Tobífera Formation. Kink folds and quartz veins associated with the brittle thrusts (*i.e.* Figure 2.8h-j) share the same northeast-southwest shortening direction as F_4 kink-bands in the Cordillera Darwin Metamorphic Complex to the south (*i.e.* Figure 2.7e), suggesting that the structures reflect the same shortening event. Consequently, the shear zone below the contact is interpreted to be coeval with D_2 and D_3 deformation near Seno Martínez, and brittle faults that crosscut the ductile fabrics in the schist are interpreted to reflect the progressive deformation of the contact as it was sheared and uplifted during D_3 –D_4 (discussed below).

8.2 Synthesis of microstructures from the Cordillera Darwin Metamorphic Complex on Peninsula Brunswick

Microstructural observations from the Bahía Fortesque shear zone show differences in deformation conditions from those in the Cordillera Darwin Metamorphic Complex taken near Estuario Silva Palma and Estuario Wickham on Peninsula Brunswick (Figure 2.2).

Quartz CPO results from the Bahía Fortesque high-strain zone (Figure 2.16a-d) indicate ubiquitous basal-<a> slip with minor evidence for the occurrence of prism-<a> slip (*i.e.* Figures 2.16b), and microstructural observations indicate dominantly subgrain rotation recrystallization mechanisms for quartz in each sample (Figure 2.15a-d). The sense of shear from CPO patterns are top-northeast in every sample (Figure 2.16), consistent with macroscopic kinematic indicators from the shear zone (see chapter 1).

Quartz recrystallization textures and CPOs are indicative of Regime 2 dislocation creep of Hirth and Tullis (1992) and/or the SGR recrystallization regime of Stipp *et al*., (2002), suggesting deformation temperatures between 400°-500° C during the formation of the Bahía Fortesque high-strain zone.

Samples of the Cordillera Darwin Metamorphic Complex taken near Estuario Silva Palma and Estuario Wickham preserve quartz recrystallization textures that are similar to those observed at the Bahía Fortesque high-strain zone. Here, subgrain rotation recrystallization is the dominant deformation mechanism for quartz (Figure 2.15 e-f). Quartz CPOs from these locations indicate dominantly basal-<a> slip. Pole figures from some samples near Estuario Silva Palma also record prism-<a> slip and thus suggest slightly higher deformation temperatures than those at the Bahía Fortesque high-strain zone where prism-<a> slip is mostly absent. Quartz textural observations and CPOs are indicative of deformation temperatures between 400°-550° C. Slightly warmer deformation conditions at Estuario Silva Palma are interpreted to reflect the position of the samples structurally below the Bahía Fortesque high strain zone (*i.e*. Chapter 1 Figure 2.10).

8.3 Regional synthesis of structures, definition of the Magallanes décollement

Structures of the Cordillera Darwin Metamorphic Complex near Seno Martínez and Peninsula Brunswick share many common structural and geologic elements that allow regional correlation on the basis of their stratigraphic position, sense of shear, and sequence of deformation. Most importantly, the Bahía Fortesque high-strain zone, the D_2 -D_3 high-strain zones at Seno Martínez, and the Bahía Angelito shear zone each accommodated top-northeast thrusting of rocks from the Rocas Verdes basin terrane (Tobífera Formation at Bahías Fortesque and Angelito, mafic-intermediate volcanic rocks of the Rocas Verdes basin seafloor at Seno Martínez) over the Cordillera Darwin Metamorphic Complex schist. In each of these localities, the earliest macroscopic structure in the Cordillera Darwin Metamorphic Complex is a pervasive schistose foliation that contains a prominent down-dip quartz mineral lineation that is refolded (*i.e*.

S_2 /L_2 at Seno Martínez, S_{1-2} composite and L_2 at Bahía Fortesque and S_1 /L_1 at Estuario Silva Palma) and displays dominantly top-northeast shear shear-sense indicators. Similarly, D_3 is characterized by the transposition of D_2 structures by northeast-vergent tight and/or isoclinal noncylindrical folds that are interpreted to reflect progressive deformation during top-northeast D_2 and D_3 shearing. Qualitative strain gradients defined by the tightness of D_3 folds and/or occurrence of F_3 sheath folds indicate D_3 high strain zones in Domain II at Seno Martínez and at Bahía Fortesque (*i.e.* Chapter 1). Upright or steeply inclined kink-folds and/or tight folds characterize D_4 structures everywhere in the study area and indicate a regional pulse of northeast-southwest horizontal shortening that is superimposed on D_2 /D_3 structures (discussed below). Table 1 summarizes the structural elements that are unique to each structural domain and sequence of deformation in the study area.

Progressive, top-northeast D_2 /D_3 shearing appears to have occurred regionally near the top of the Cordillera Darwin Metamorphic Complex and at the contact with the volcanic and volcanoclastic rocks of the Rocas Verdes basin terrane. At Seno Martínez, Bahía Fortesque and Bahía Angelito the contact is sheared and separates polydeformed and metamorphosed basement schist below the high-strain zones from overlying rocks of the Rocas Verdes basin terrane that do not express the same degree of deformation and superposed folding (see also Chapter 1), indicating that a regional structural detachment separates Jurassic rocks of the Rocas Verdes basin from the underlying pre-Jurassic basement and thus defining a regional décollement at the base of the Patagonian fold-thrust belt (see also Chapter 1). The décollement occurs at a major stratigraphic and rheological contact between relatively strong ignimbrite and volcanic units of the Tobífera Formation and Rocas Verdes basin seafloor with weaker pelitic schists of the underlying Cordillera Darwin Metamorphic Complex, which is thought to reflect either a pre-Jurassic accretionary complex (Dalziel & Cortés, 1972; Nelson *et al*., 1980) or a succession of clastic passive margin deposits (Hervé *et al*., 2008) before it was metamorphosed during the Cretaceous Andean Orogeny. Deformed rocks in the Cordillera Darwin Metamorphic Complex within and below the décollement have the

same top-northeast shear sense during $D_{2\text{-}3}$ as the first generation structures of the Patagonian fold-thrust belt above the décollement and toward the foreland (*i.e.* Chapter 1). Within and below the décollement, shortening was accomodated by crystal plasticity while above it and toward the foreland by formation of the fold-thrust belt.

Defined here for the first time, the Magallanes décollement (new name) is exposed at Seno Martínez, Bahía Angelito and Bahía Fortesque and is interpreted to have accommodated top-northeast thrusting of the Rocas Verdes basin onto the continental margin (*i.e.* Cordillera Darwin Metamorphic Complex), underthrusting of the continental margin, and the development of the Patagonian fold-thrust belt during the Andean Orogeny (*c.f.* Klepeis *et al.*, 2010; see also Chapter 1). Quartz microstructures and CPOs presented in this study indicate the deformation temperatures associated with D_2 -D_4 stages of the décollement at Seno Martínez were ~100° C warmer (500-650° C) than at Bahía Fortesque (400-550° C), suggesting that the décollement dipped shallowly (~6°) toward the south-southwest (present-day coordinates, Figure 2.18) during its formation.

8.4 Model of the evolution of polyphase structures in the Cordillera Darwin Metamorphic Complex and regional significance

Integrating the new data presented in this study with previous work (Klepeis *et al.,* 2010), I present a model to describe the structural evolution of the Magallanes décollement and polyphase deformation of the Cordillera Darwin Metamorphic Complex (Figure 2.19). In the Late Jurassic, the Rocas Verdes basin existed Pacficward of the continental margin of South America but inboard of the Patagonian arc (*e.g.* Dalziel, *et al.,* 1974; Dalziel, 1981; Fildani and Hessler, 2005; Figure 2.19a). The onset of the Andean Orogeny in the southernmost Andes is defined by the closure and inversion of the Rocas Verdes basin (Dalziel *et al.*, 1974; Nelson *et al.*, 1980; Fildani and Hessler, 2005; Klepeis *et al.*, 2010). Regional-scale obduction of the mafic seafloor of the Rocas Verdes basin and underthrusting and metamorphism of the continental margin were underway by ~86 Ma (Figure 2.19b; Klepeis *et al.*, 2010). Obduction of the Rocas Verdes basin terrane was partly facilitated by the development of the Magallanes décollement

Table 1 - Correlation of structures from the Cordillera Darwin Metamorphic Complex near Seno Martínez, Bahía Angelito and Peninsula Brunswick

Regional Event	Seno Martínez				Peninsula Brunswick	
	Domain I	Domain II	Domain III	Domain IV	Bahía Fortesque high-strain zone	Estuario Silva Palma
D4	Upright kink-folds that form conjugate sets; localized to phylosilicate-rich lithologies SGR + GBM, basal-<a>, and prism-[c] slip *T* ~500-650° Top-SW dominant	***High-strain zone*** steeply-dipping tight and isoclinal reclined folds; Ramsay type II and III superposed fold patterns SGR + GBM, basal-<a>, and prism-<a> *T* ~500-650° Top-SW dominant	upright kink-folds that form conjugate sets; localized to phylosilicate lithologies SGR + GBM, basal-<a>, prism-<a>, and prism-[c] slip *T* ~500-650° Top-SW dominant	crenulation cleavage and brittle faulting	kink-folds (local F_3)* Top-SW	not recognized
D3	upright, inclined and reclined tight folds refold S_2/L_2 Top-NE dominant	***High-strain zone*** upright, reclined and recumbent tight and isoclinal folds and sheath folds refold S_2/L_2; sheath fold axes are parallel to the local L_2 Top-NE dominant	regional, recumbent tight and isoclinal folds Top-NE dominant	upright tight folds refold S_2/L_2; C-S fabric	***High-strain zone*** isoclinal inclined folds (local F_2) transposed parallel to $S_{1\text{-}2}$* Top-NE	isoclinal recumbent folds (local F_2) * Top-NE
D2	pervasive schistose foliation and quartz mineral lineation (S_2/L_2); S_2/L_2 is subparallel and coeval with S_1/L_1 in epidote-actinolite schist of the RVB terrane SGR + GBM, basal-<a>, prism-<a>, and prism-[c] slip *T* ~500-650° Top-NE dominant	pervasive schistose foliation and quartz mineral lineation (S_2/L_2) SGR + GBM, basal-<a>, prism-<a> and prism-[c] slip *T* ~500-650° Top-NE dominant	pervasive schistose foliation and quartz mineral lineation (S_2/L_2) SGR + GBM, basal-<a>, prism-<a> slip *T* ~500-650° Top-NE dominant	pervasive schistose foliation and quartz mineral lineation (S_2/L_2) Top-NE dominant	composite schistose foliation (local $S_{1\text{-}2}$) and quartz mineral lineation (local L_2)* SGR, basal-<a> + minor prism-<a> slip *T* ~400-550° Top-NE	schistose foliation (local S_1) and quartz mineral lineation (local L_1)* SGR, basal-<a> + minor prism-<a> slip *T* ~400-550° Top-NE
D1	intrafolial foliation (S_1); not present in epidote-actinolite schist of the RVB terrane	intrafolial foliation (S_1)	intrafolial foliation (S_1)	intrafolial foliation (S_1)	not recognized	not recognized

* data source from Chapter 1

Dashed line is intended to represent progressive deformation between D_2 and D_3 events

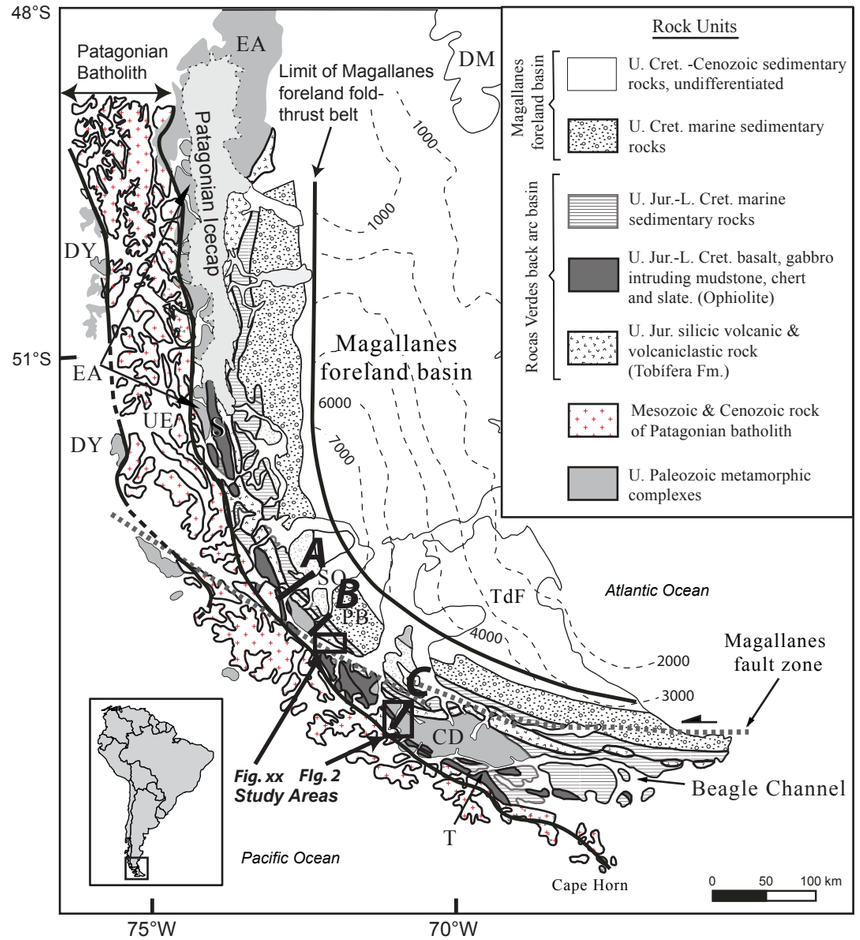
48°S
51°S
75°W
70°W
Patagonian Batholith
EA
Limit of Magallanes foreland fold-thrust belt
DM
Patagonian Icecap
DY
EA
UEA
DY
Magallanes foreland basin
1000
1000
6000
7000
A
B
SO
PB
C
CD
TdF
4000
2000
3000
Atlantic Ocean
Magallanes fault zone
Beagle Channel
T
Cape Horn
0 50 100 km
Fig. xx Fig. 2 Study Areas
Pacific Ocean
Rock Units
Magallanes foreland basin
U. Cret. -Cenozoic sedimentary rocks, undifferentiated
U. Cret. marine sedimentary rocks
Rocas Verdes back arc basin
U. Jur.-L. Cret. marine sedimentary rocks
U. Jur.-L. Cret. basalt, gabbro intruding mudstone, chert and slate. (Ophiolite)
U. Jur. silicic volcanic & volcaniclastic rock (Tobífera Fm.)
Mesozoic & Cenozoic rock of Patagonian batholith
U. Paleozoic metamorphic complexes

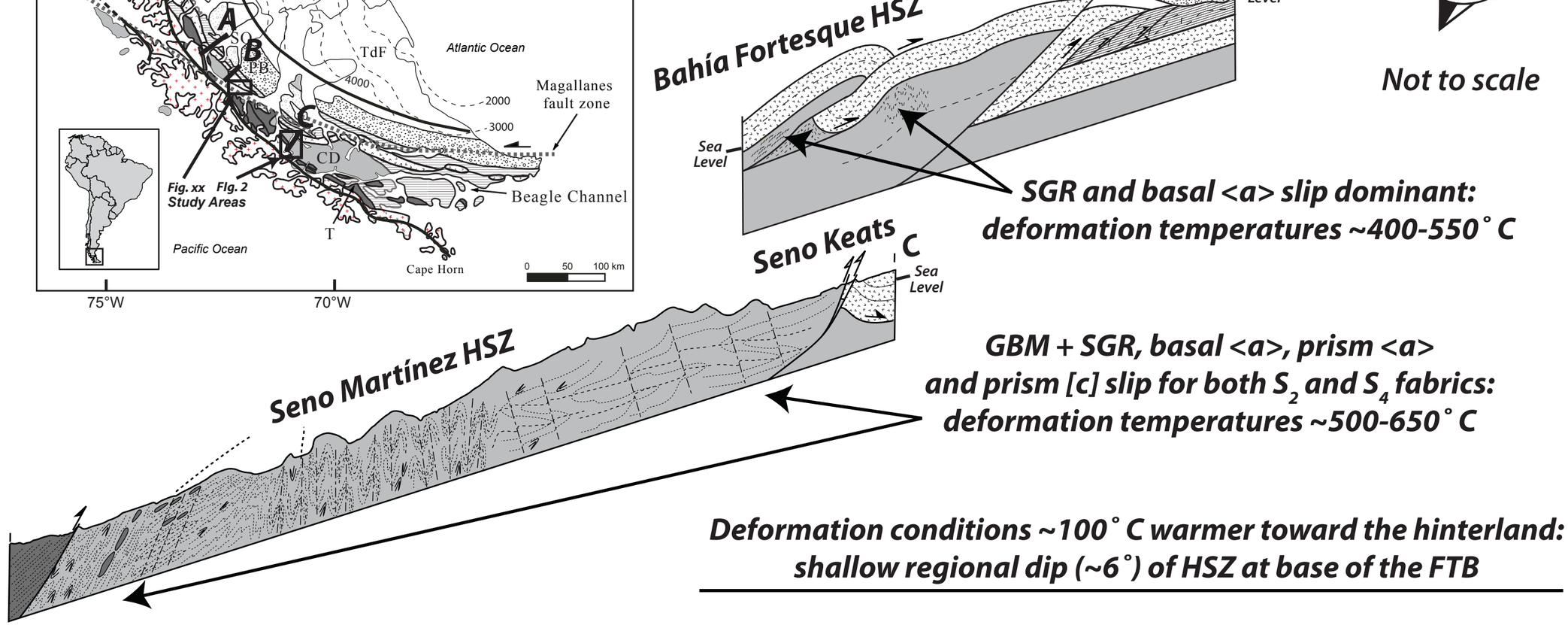
Patagonian FTB
Seno Otway
A
Canal Jeronimo
Sea Level
Estuario Silva Palma
B
Sea Level
Bahía Fortesque HSZ
Sea Level
N
Not to scale
SGR and basal <a> slip dominant:
deformation temperatures ~400-550˚ C
Seno Keats
C
Sea Level
Seno Martínez HSZ
GBM + SGR, basal <a>, prism <a>
and prism [c] slip for both S_2 and S_4 fabrics:
deformation temperatures ~500-650˚ C
Deformation conditions ~100˚ C warmer toward the hinterland:
shallow regional dip (~6˚) of HSZ at base of the FTB

Figure 2.18

Figure 2.18. Regional correlation of structures between Seno Martínez, Bahía Fortesque and the Patagonian fold-thrust belt. Cross-sections A and B are from Chapter 1 and are shown in their relative positions with respect to Seno Martínez (the locations are shown on the inset map). Sea level is indicated on each cross section to provide a sense of the structural level of each cross section. The Magallanes décollement (new name, see text) is exposed at Bahía Fortesque where it ramped up section and fed displacement into the Patagonian fold-thrust belt. Southwest of Bahía Fortesque at Seno Martínez, the décollement is defined several-kilometer-wide high strain zones that accommodated the thrusting of Rocas Verdes basin terrane rocks above the Cordillera Darwin metamorphic complex. Deformation conditions from fabrics within the décollement were ~100° warmer at Seno Martínez and indicate that the décollement dipped shallowly toward the hinterland.

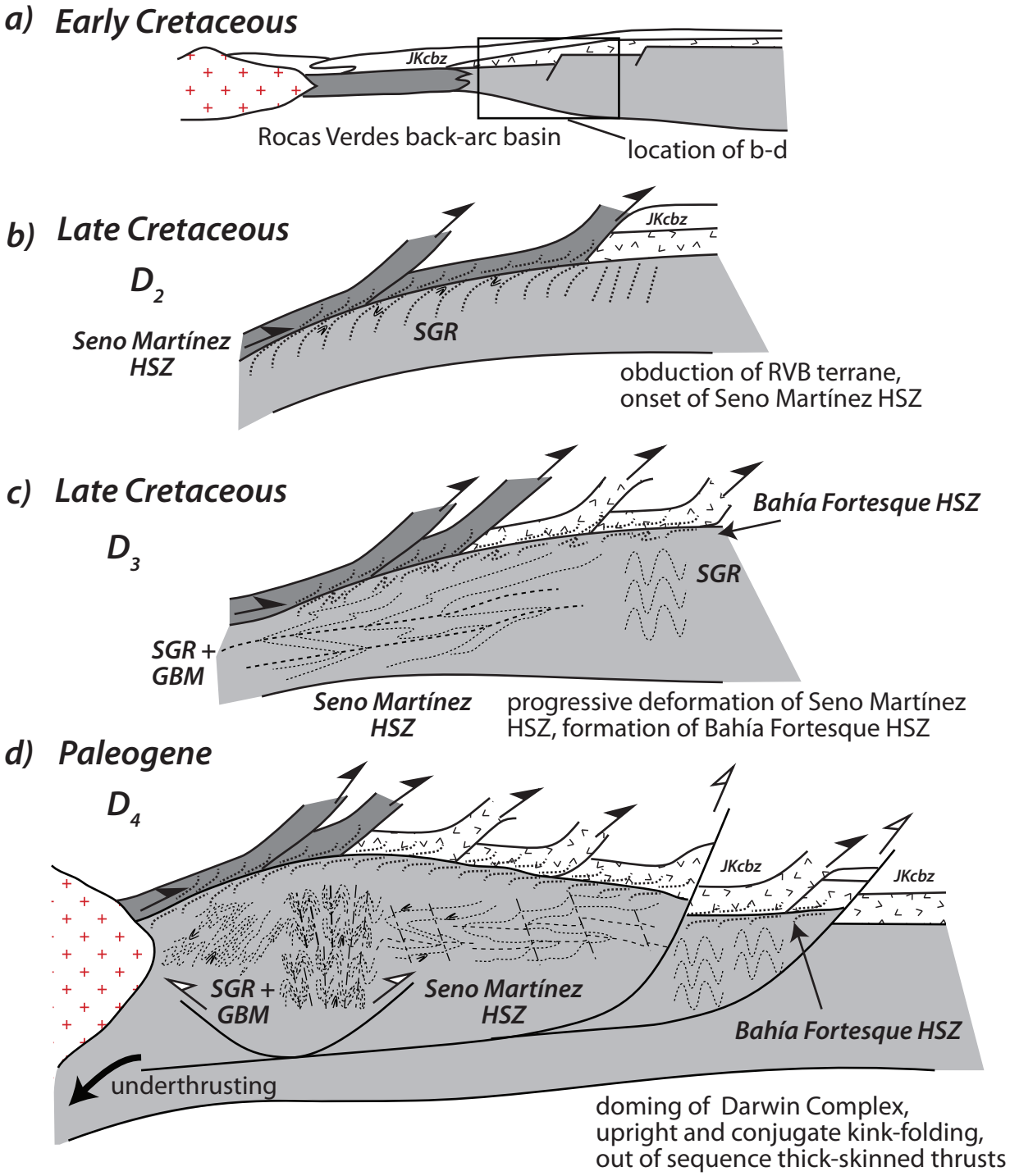
a) Early Cretaceous
JKcbz
Rocas Verdes back-arc basin
location of b-d
b) Late Cretaceous
D2
JKcbz
Seno Martínez
HSZ
SGR
obduction of RVB terrane,
onset of Seno Martínez HSZ
c) Late Cretaceous
D3
Bahía Fortesque HSZ
SGR
SGR +
GBM
Seno Martínez
HSZ
progressive deformation of Seno Martínez
HSZ, formation of Bahía Fortesque HSZ
d) Paleogene
D4
JKcbz
JKcbz
SGR +
GBM
Seno Martínez
HSZ
Bahía Fortesque HSZ
underthrusting
doming of Darwin Complex,
upright and conjugate kink-folding,
out of sequence thick-skinned thrusts

Figure 2.19

Figure 2.19. Cartoon model showing the possible development of the Magallanes décollement and tectonic significance of superposed fabrics at Seno Martínez. Modified after Klepeis *et al.* (2010). (a) Extension, diking and bimodal magmatism formed the Rocas Verdes basin during the Late Jurassic. The basin is filled with a thick sequence of Upper Jurassic - Lower Cretaceous mudstone and turbidites. (b) By the Late Cretaceous, closure of the Rocas Verdes basin resulted in the obduction of its quasi-oceanic floor onto the continental margin and formation of a regional décollement at the basement-cover contact that is reflected by D_2 fabrics at Seno Martínez. (c) Continued shortening resulted in the imbrication of the Rocas Verdes basin terrane and propagation of thin-skinned thrust wedge toward the foreland (*i.e.* Bahía Fortesque high-strain zone and other first generation structures of Patagonian fold-thrust belt, Chapter 1). Within the décollement zone at Seno Martínez, progressive deformation was accomplished by the transposition of D_2 fabrics by noncylindrical and/or sheath folds (D_3). The décollement dipped shallowly (~6°) toward the hinterland. Below the décollement, regional F_3 folds thicken the Cordillera Darwin metamorphic complex. (d) Complete closure of the Rocas Verdes basin and docking of the Patagonian arc in the Paleogene resulted in thick-skinned deformation of the thrust wedge. At Seno Martínez, horizontal shortening was accommodated by doming and pervasive refolding (F_4) of D_3 structures that resulted in the uplift and partial exhumation of high-grade rocks in the core of the Cordillera Darwin Metamorphic Complex. Thick-skinned deformation propagated toward the foreland where a phase of out-of-sequence basement-involved reverse faulting occurred (*i.e.* second-generation structures of the Patagonian fold-thrust belt, Chapter 1).

that formed near the basement-cover contact. At this time, pre-Andean fabrics (*i.e.* S_1 at Seno Martínez) were transposed into parallelism with the pervasive composite schistose foliation (S_2) and prominent quartz stretching lineation (L_2) associated with D_2 fabrics near Seno Martínez. Displacement was transferred toward the northeast resulting in the shearing and imbrication of the Tobífera Formation, development of the Bahía Fortesque high-strain zone and the earliest first-generation thrusts of the Patagonian fold-thrust belt (see Chapter 1). The D_2 fabrics from the Magallanes décollement are considered to be contemporaneous and correlative with first generation obduction structures described by Klepeis *et al*. (2010) along the Beagle Channel and to reflect regional underthrusting of the continental margin beneath the Rocas Verdes basin terrane (see also, D_1 of Nelson *et al*., 1980).

Continued shortening and underthrusting of the continental margin resulted in the progressive deformation, burial and synkinematic metamorphism of the Cordillera Darwin Metamorphic Complex schists, and the transposition of third-generation folds (F_3, D_3) into D_2 structures. Within the Seno Martínez D_3 high-strain zone (Table 1), F_3 folds are expressed as both isoclinal and sheath folds that are both compatible with southwest-northeast shortening and bulk top-northeast shearing. Below the D_3 high-strain zone at Seno Martínez, F_3 folds occurred as regional recumbent folds that thickened the Cordillera Darwin Metamorphic Complex. Displacement during D_3 was transferred toward the northeast along the Magallanes décollement toward the Bahía Foretesque high-strain zone where D_3 is characterized by the isoclinal folding and shearing of S_2 /L_2. Displacement ramped over the Bahía Fortesque high-strain zone and was transferred into the Patagonian fold-thrust belt (see Chapter 1). Craton-directed (top-northeast) $D_{2\text{-}3}$ progressive deformation documented in this study is correlative with a phase of north-vergent first-generation thrusting reported near the Beagle Channel that accomodated the partial obduction of the Rocas Verdes terrane onto the continental margin prior to ~86 Ma (Klepeis *et al*., 2010; see also, Nelson *et al*., 1980). Deformation conditions during $D_{2\text{-}3}$ near Seno Martínez were between 500-650° C, suggesting the Magallanes décollement occurred at ~20-25 km depth (assuming a 25° C/km geothermal gradient).

These deformation conditions are compatible with thermobarometry and pseudosection modeling from amphibolite-grade rocks exposed in the high-grade core of the Cordillera Darwin Metamorphic Complex near the Beagle Channel that were buried to depths ~35 km (P = 12 kbar and T = 620°C, Malonely *et al*., 2011; *see also* Kohn *et al*., 1993) and were structurally below garnet-bearing rocks near Seno Martínez. $D_{2\text{-}3}$ events recorded at Seno Martínez are part of a regional tectonic event that partially obducted rocks of the Rocas Verdes terrane and resulted in the underthrusting and buriel of the continental margin (*c.f*. obduction thrusts of Klepeis *et al*., 2010; D_1 of Nelson *et al*., 1980; D_1 of Calderón *et al*., 2012; prograde (S_1) fabrics of Maloney *et al*., 2011). The Bahía Fortesque shear zone transferred displacement up-section and toward the northeast into the nacent Patagonian fold-thrust belt during $D_{2\text{-}3}$ (*c.f*. Chapter 1).

Fourth-generation structures at Seno Martínez reflect the complete closure of the Rocas Verdes basin and collision of the Patagonian arc by the Paleogene (*c.f*. Nelson *et al*., 1980; Klepeis *et al*., 2010). At Seno Martínez, D_4 is defined by the sets of upright north- and south-dipping kink bands that overprint D_2 and D_3 structures and record horizontal southwest-northeast shortening and subvertical extension. D_4 strains localized in Domain II where upright, isoclinal F_4 folds refold D_2 and D_3 structures and form a high strain zone that uplifts garnet-grade rocks in the core of a regional F_4 antiform. Folding of the garnet isograd at Seno Martínez probably correlates with the antiformal doming of amphibolite-grade isograds near the Beagle Channel (*i.e*. Kohn *et al*., 1993; Klepeis *et al*., 2010) that resulted in the uplift and partial exhumation of high-grade rocks in the core of the Cordillera Darwin Metamorphic Complex by the Paleogene (*c.f*. exhumation fabrics (S_2) of Maloney *et al*., 2011; second generation bivergent structures of Klepeis *et al*., 2010; D_2 and D_3 of Nelson *et al*., 1980) and is compatible with Late-Cretaceous – Paleogene cooling of the high-grade core of the Codillera Darwin Metamorphic Complex (Maloney *et al*., 2011; Kohn *et al*., 1995). At Seno Martínez, D_4 shortening is interpreted to cause the uplift and partial exhumation Cordillera Darwin Metamorphic Complex and be coincident with the propagation of out-of-sequence thick-skinned basement-involved reverse faults that cut first generations structures of the Magallanes décollement and fold-

thrust belt (Figure 2.19d; *c.f.* Klepeis *et al*., 2010, see Chapter 1). The timing of D_4 is also coincident with the depositional ages of sediments in the Magallanes forland basin that reflect rapid Paleogene exhumation and denudation of the Cordillera Darwin (Gombosi *et al*., 2009; Zahid *et al*., 2010).

9. Conclusions

A newly defined regional ductile shear zone named the Magallanes décollement is several kilometers thick and decoupled an underthrust continental margin from an overlying retroarc fold-thrust belt during the Late Cretaceous inversion of a marginal basin and formation of Patagonian Andes. The décollement is defined by the transposition of several generations of noncylindrical folds including sheath folds, northeast-vergent L-S tectonites, C-S fabrics and C'-type shear bands that indicate dominantly top-northeast transport. The structural evolution of the décollement occurred in two phases of Late Cretaceous-Paleogene progressive deformation that resulted in the folding, synkinematic metamorphism and burial of the underlying Cordillera Darwin Metamorphic Complex (D_2 -D_3). These first two phases of deformation (D_2 -D_3) are interpreted to record the obduction of the Rocas Verdes Terrane and propagation of displacement into the Patagonian fold-thrust belt. A later stage of deformation (D_4) records regional southwest-northeast horizontal contraction and vertical extension that resulted in the uplift and doming of high-grade rocks of the Cordillera Darwin Metamorphic Complex and folded the Magallanes décollement. The latter stage of deformation is coincident with a pulse of thick-skinned out of sequence thrusting the cut the décollement and first-generation thrusts in the Patagonian fold-thrust belt. D_4 shortening is interpreted to reflect complete closure of the Rocas Verdes basin

and collision of the Patagonian Arc with the continental margin.

The décollement is a regional structure that is exposed in at least three locations over 100 km^2 of the Patagonian Andes where it separates Late Jurassic and Early Cretaceous rocks of the Rocas Verdes basin above from the underlying Paleozoic Cordillera Darwin Metamorphic Complex. Quartz microstructures and CPOs record deformation temperatures of the décollement that are ~500-650° C in hinterland localities and ~400-550° C toward the foreland, indicating a regional hinterland dip of ~6°. Below the décollement and toward the hinterland, tectonic shortening was accommodated polyphase folding and crustal thickening of the basement schist. Above the décollement and toward the foreland shortening was accomplished by the formation of a retroarc fold-thrust belt. The Magallanes décollement is a well exposed example of the kinematic link between polyphase 'basement' shortening and the development of a retroarc fold thrust belt during an 'Andean-style' orogeny.

CHAPTER 3: FAULT KINEMATICS OF THRUST, STRIKE-SLIP AND NORMAL FAULTS ALONG THE MAGALLANES-FAGNANO FAULT SYSTEM; IMPLICATIONS FOR LATE TERTIARY SINISTRAL TRANSTENSION

Abstract

The present tectonic setting of the southernmost Andes between 52° and 55°S latitude is dominated by a system of left-lateral faults that separates the South American and Scotia plates, known as the Magallanes-Fagnano fault system. Crosscutting relationships, modern fault scarps, and geomorphic lineaments indicate that recent strike-slip deformation is superimposed on a Late Cretaceous – Paleogene Patagonian fold-thrust belt that formed as a result of crustal shortening during the Andean orogeny. Fault kinematic data and crosscutting relationships from a population of thrust, strike-slip and normal faults located in a ~100 km^2 region of the Magallanes fold-thrust belt, presented herein, show possible kinematic and temporal relationships between thrust and sets of coeval strike-slip and normal faults. Results indicate that thrust fault kinematics are spatially homogeneous in the study area and record subhorizontal northeast-trending shortening. Strike-slip faults form two kinematically distinct populations. The dominant set consists of northeast-striking right-lateral faults as well as east-northeast- and northwest-striking left lateral faults. The dominant set of strike-slip faults form a Riedel and less common P-shear geometry that is compatible with left-lateral slip on a west-northwest trending principal fault zone, inferred to be the main splay of the Magallanes-Fagnano fault system. A subsidiary set of strike-slip faults has kinematic axes opposite the dominant set and is older. Normal faults strike east and record north-south trending extension. Normal faults are generally kinematically compatible with the dominant set of strike-slip faults and are inferred to be coeval. Normal and strike-slip faults crosscut thrust faults and associated folds. A newly mapped, left-lateral fault zone termed the Bahía del Indio fault strikes northwest for ~100 km across the study area and reactivates

a Paleogene high-angle reverse fault. The study area occurs in a releasing step-over between overlapping left-lateral, left-stepping segments of the Bahía del Indio fault and the Magallanes-Fagnano fault. Results indicate that strike-slip and normal faults record a tectonic event defined by sinistral transtension that post-dates all contractional structures. Results are consistent with regional tectonic models that suggest sinistral shearing in the southernmost Andes was probably contemporaneous with the opening of the Drake Passage and the onset of seafloor spreading in the Western Scotia Sea during the Early Miocene.

1. Introduction

Three major sinistral transform systems accommodate present-day plate motions between the South American, Antarctica and Scotia plates including the Magallanes-Fagnano fault – North Scotia ridge transform, South Scotia Ridge transform and the Shakleton fracture zone (*e.g.* Barker and Burrell, 1977; Pelayo & Wiens, 1989; Barker, 2001; Smalley *et al.*, 2003; 2007; Dalziel *et al.*, 2013). The Magallanes-Fagnano fault system is located in southern Argentina and Chile between 52° and 55° S latitude (Figure 3.1; Pelayo & Wiens, 1989) and accommodates most of the motion between the South American and Scotia plates (Smalley *et al.*, 2003; 2007). Modern geomorphic lineaments and fault scarps of the Magallanes-Fagnano fault system are superimposed on the trend of the Patagonian retroarc fold-thrust belt, a ~700 km long orogenic belt that extends from Tierra del Fuego to the Pacific margin of Chile and records crustal contraction from the Late-Cretaceous to Tertiary Andean Orogney (*e.g.* Dalziel and Palmer, 1979; Nelson, 1980; Klepeis, 1994; Ghiglione and Ramos, 2005; Klepeis *et al.*, 2010; Fosdick *et al.*, 2011).

The tectonic origin and timing of the onset of sinistral deformation along the Magallanes-Fagnano fault system has been the subject of some debate for several decades (*e.g.* Cunningham, 1993; Cunningham *et al.*, 1995; Diraison *et al.*, 2000; Kraemer, 2003; Ghiglione & Cristallini, 2007). Some interpretations suggest that sinistral deformation

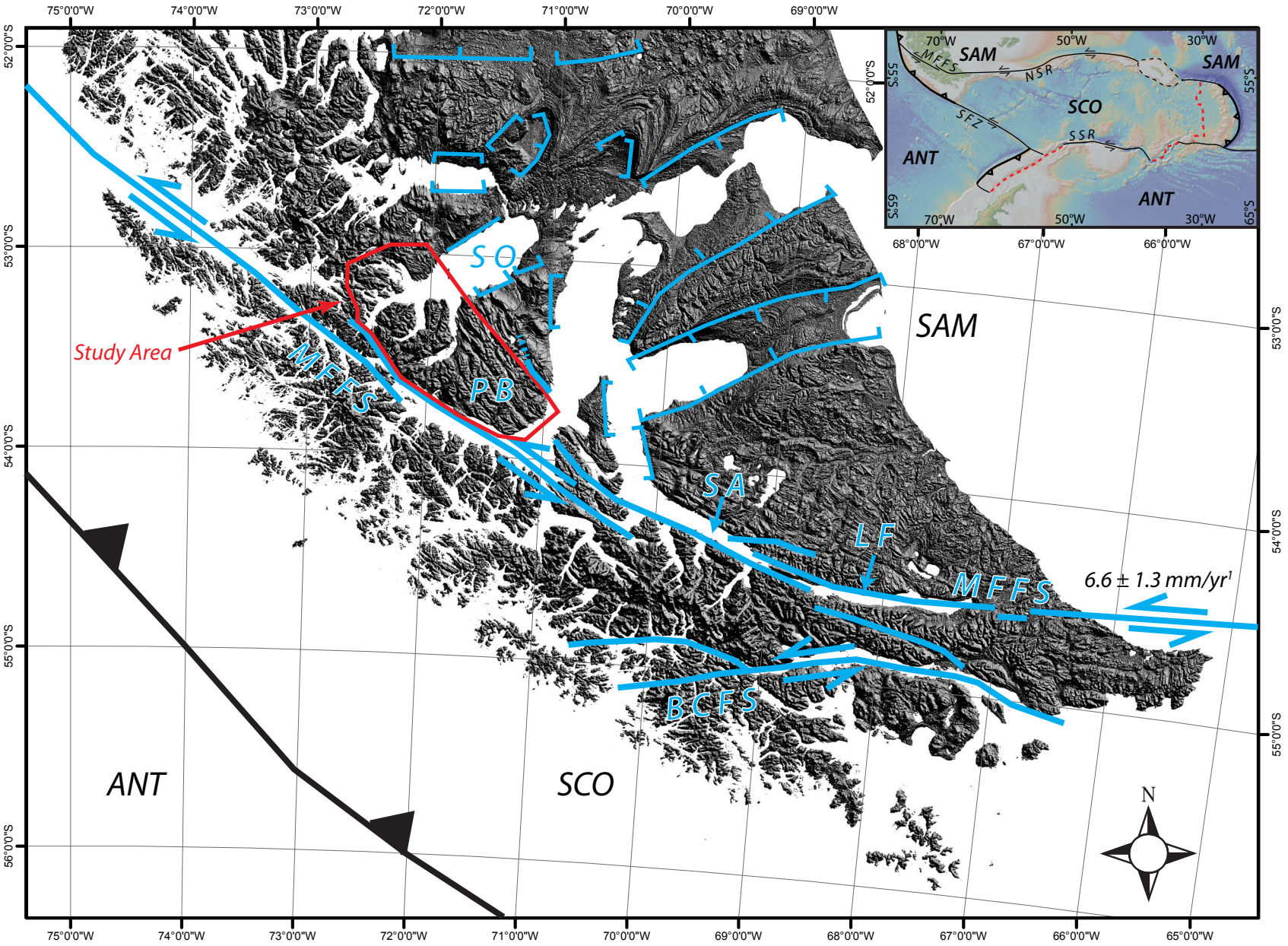
75°0'0"W
74°0'0"W
73°0'0"W
72°0'0"W
71°0'0"W
70°0'0"W
69°0'0"W
68°0'0"W
67°0'0"W
66°0'0"W
65°0'0"W
52°0'0"S
53°0'0"S
54°0'0"S
55°0'0"S
56°0'0"S
SO
Study Area
MFFS
PB
SAM
SA
LF
MFFS
6.6 ± 1.3 mm/yr[1]
BCFS
ANT
SCO
N
70°W
50°W
30°W
55°S
65°S
SAM
MFFS
NSR
SCO
SFZ
SSR
ANT
ANT

Figure 3.1

Figure 3.1. Shaded relief image of the southernmost Andes complied from SRTM topography data. Location of the study area is shown. Thick blue line indicates map trace of the Magallanes-Fagnano and Beagle Channel fault systems after Cunningham (1993), Klepeis, (1994), Klepeis and Austin (1997), Smalley *et al*. (2003) and Lodolo *et al*. (2007). Thin blue lines indicate map trace of Neogene normal faults (tick on down-dropped block) after Diraison *et al*. (1997). Thick black line represents location of trench between the Antarctic and Scotia plates, teeth on overriding plate. Inset, physiography of the Scotia Arc region showing major plate bounding structures after Dalziel *et al*. (2013) and Smalley *et al*. (2003). Bold black lines are subduction zones with teeth in the upper plate, solid black lines are transform faults and dashed red lines are modern spreading centers. Abbreviations as follows: SAM, South American Plate: SCO, Scotia Plate; ANT, Antarctic Plate; MFFS, Magallanes-Fagnano fault system; BCFS, Beagle Channel fault system; NSR, North Scotia Ridge; SSR, South Scotia Ridge; SFZ, Shackleton Fracture Zone; LF, Lago Fagnano; SA, Seno Almirantazgo; PB, Peninsula Brunswick; SO, Seno Otway. Data sources: Digital Elevation Model, Farr *et al*. (2007); inset basemap from GeoMapApp (http://www.geomapapp.org, Ryan *et al*., 2009); 1, Smalley *et al*. (2003); 2, DeMets *et al*. (1990).

occurred since the Late Cretaceous and that the Patagonian fold-thrust belt is product of ongoing wrench tectonics that occurred during and since the Andean Orogeny (Cunningham 1993; Cunningham *et al*., 1995; Menichetti *et al*., 2008). Other authors interpret the development of the thrust belt and onset of strike-slip deformation as having occurred as two separate tectonic events and conclude that strike-slip deformation has overprinted the thrust belt since the Oligocene (Klepeis, 1994; Klepeis & Austin, 1997; Lodolo *et al*., 2003; Ghiglione & Ramos, 2005). Most studies of the Magallanes-Fagnano fault system focus on a region of Tierra del Fuego near Lago Fagnano or the Beagle Channel where the fault strands are well exposed (Figure 3.1), however, the spatial extent and field relations of strike-slip deformation in the Patagonian fold-thrust belt beyond Tierra del Fuego is not well understood.

This paper presents the results of a kinematic analysis of a population (n=235) of thrust, strike-slip and normal faults that occur within a previously unmapped ~100 km^2 region of the Patagonian fold-thrust belt between the Magallanes Straits and Isla Riesco in southern Chile (Figure 3.1). The goals of this study were to 1) determine the spatial extent of strike-slip deformation along-strike to the northwest from where it is well described on Tierra del Fuego, 2) test for kinematic compatibility between populations of thrust, strike-slip and normal faults in the study area and, 3) document field crosscutting relationships between thrust, strike-slip and normal faults. The results document the occurrence of coeval sets of strike-slip and normal faults that record sinistral transtension within a left-lateral, left-stepping segment of the Magallanes-Fagnano fault system. The results are discussed in the context of a tectonic transition from contraction to left-lateral shear that probably occurred in the early Miocene.

2. Tectonic setting and geologic background

2.1 MAGALLANES-FAGNANO FAULT SYSTEM

The Magallanes-Fagnano fault system transects Isla Grande of Tierra del Fuego and occupies the northwest-trending segment of the Magallanes Strait near the Pacific margin (Figure 3.1). Toward the northwest, the Magallanes-Fagnano fault system terminates at a trench-transform triple junction between the Antarctic, South American and Scotia plates. East of Tierra del Fuego, the Magallanes-Fagnano fault system joins the North Scotia Ridge, a sinistral transform boundary that extends from Tierra del Fuego >1700 km east toward South Georgia island and defines the northern boundary of the Scotia Sea plate (Pelayo & Wiens, 1989). On Tierra del Fuego, GPS data indicate that the present-day slip rate along the Magallanes-Fagnano transform is 6.6 ± 1.3 mm/yr and that an additional 1-2 mm/yr of sinistral slip is accommodated by diffuse deformation in Tierra del Fuego and southern Patagonia (Smalley *et al*., 2003). Relative plate motions are consistent with earthquake focal mechanism solutions from two events that occurred along the Magallanes-Fagnano fault segment on Tierra del Fuego (Smalley *et al*., 2007) and offshore toward the east (Pelayo & Wiens, 1989) that both indicate nearly pure strike-slip sinistral motion.

In Tierra del Fuego and the Magallanes region of Chile, the Magallanes-Fagnano fault system consists of an array of steeply-dipping, sinistral transform faults that strike west near Tierra del Fuego and northwest near the Pacific margin of Chile (Figure 3.1). Individual fault strands are arranged in an en-echelon arrays that contain both right- (restraining step-over) and left- (releasing step-over) stepping segments. Asymmetric, normal fault bounded basins are commonly associated with releasing step-overs and oblique contractile folds are documented within restraining step-overs (Figure 3.1, Winslow, 1982; Klepeis & Austin, 1997; Lodolo *et al*., 2003; Menichetti *et al*., 2008). Lago Fagnano and Seno Almirantazgo (Figure 3.1) form prominent west trending lineaments that occupy oblique-normal fault bounded basins within a left-stepping

segment of the fault zone (Klepeis, 1994; Klepeis & Austin, 1997; Lodolo *et al*., 2003; Menichetti *et al*., 2008).

Klepeis (1994) conducted the first detailed field-based kinematic analysis of the Magallanes-Fagnano fault system and demonstrated that it is characterized by dominantly sinistral strike-slip motion with a lesser component of normal-slip. He reported 20-25 km of sinistral separation and as much as 3 km of throw based on an offset thrust contact exposed near the western end of Lago Fagnano. Lodolo *et al*. (2003) postulated that the Magallanes-Fagnano fault system accommodated as much as 40 km of sinistral offset by extrapolating a GPS-based slip rate (~0.5 mm/yr after Del Cogliano *et al*., 2000) back to the cessation of seafloor spreading in the Scotia Sea at 8 Ma (after Barker and Burrell, 1977). Kinematic analyses of brittle faults along the Magallanes-Fagnano fault segment near Lago Fagnano reported by Menichetti *et al*. (2008) indicate a dominant population of sinistral strike-slip faults and a smaller population of normal faults that is also consistent with the kinematic data of Klepeis (1994) and Klepeis and Austin (1997).

2.2 TIMING OF STRIKE-SLIP DEFORMATION

Field-based constraints on the age of the onset of strike-slip deformation are limited. Klepeis (1994) postulated that sinistral strike-slip deformation on Tierra del Fuego occurred after 60 Ma and dominantly since 30 Ma based on field observations indicating that strike-slip structures consistently crosscut Late Cretaceous contractional structures. In support of field observations, reflection seismic data across the Magallanes-Fagnano transform fault, collected along the north trending segment of the Magallanes Strait, demonstrates that the main strand of the Magallanes-Fagnano fault overprints Cretaceous contractional structures (Klepeis and Austin, 1997) and is interpreted by the authors to be a result of the Oligocene onset of seafloor spreading in the Scotia Sea (*i.e*. ~30 Ma; Barker and Burrell, 1977). In contrast, Lodolo *et al*. (2003; 2006) proposed a late Miocene (<9.5-6 Ma) age for the onset of sinistral translation along the Magallanes-Fagnano fault system. These authors postulate a causal response between the cessation of

sea floor spreading in the western Scotia Sea (Lodolo *et al*., 2006) and the onset of strike-slip deformation in Tierra del Fuego.

On South Georgia (a displaced continental fragment of the Fuegian Cordillera now located at the eastern terminus of the North Scotia Ridge, see Dalziel *et al*., 1975), Curtis *et al*. (2010) described a ductile shear zone known as the Cooper Bay dislocation that formed under sinistral transpression during the first phase of the Andean Orogeny. These authors reported an 83.7 ± 1.2 Ma Rb/Sr age from synkinematic biotite within the shear zone and cite this as a minimum age for sinistral shearing (Curtis *et al*., 2010).

A tectonic model proposed by Cunningham (1993) suggests that the Andean Orogeny in Tierra del Fuego was defined by sinistral transpression since 120 Ma as South America moved westward relative to the Antarctic Peninsula. This model is in part supported by a plate reconstruction that indicates a total of 1320 km of left-lateral strike-slip displacement has occurred between southern South America and the Antarctic Peninsula since the relative westward rate of motion of southern South America increased *c*. 84 Ma. The model suggests that ~900 km of the motion occurred after 50 Ma (Cunningham *et al*., 1995). Although the absolute timing of the onset of strike-slip deformation in the southern Andes remains under debate, most authors agree that it is probably spatially variable and occurred mostly during the Cenozoic (see discussions by Klepeis 1994; Cunningham *et al*., 1995; Lodolo *et al*., 2003; Menichetti *et al*., 2008; and review by Dalziel *et al*., 2013).

3. Methodology

Fault-slip data including the attitudes of fault planes and striae as well as sense-of-slip was collected from faults everywhere they were observed in the field. Sense-of-slip was determined using observed offsets and common fault-slip indicators including fault surface asperities ('steps'), secondary fractures such as Riedel-shears as well as tensile and/or sigmoidal vein orientations (*e.g*. Petit, 1987). Where possible, multiple

sense-of-slip indicators were noted. The quality of shear-sense indicators were ranked on a three-point scale and considered when interpreting the dataset. Where available, the magnitudes of displacement and thickness of fault gouge was measured.

Kinematic analyses of the fault-slip data were conducted using the methods of Marrett and Allmendinger (1990), which facilitates a graphical comparison of the distribution and orientations of average incremental strain axes among populations of kinematically scale-invariant faults. Shortening and extension axes were calculated for each fault by bisecting the angle between the pole to the fault plane and the slip lineation and thus always lie within the movement plane (defined by the pole to fault and slip-lineation, Aleksandrowski, 1985) at 45° to those features. Directional maxima for a population of shortening and extension axes representing a set of faults were calculated using the linked Bingham distribution statistics function of *FaultKin* and considered to reflect the average incremental strain axes of the population (Marrett and Almendinger, 1990). Fault-slip data were weighted equally and assumed to be scale-invariant, the latter assumption is supported by both theoretical (*e.g.* Turcotte, 1986) and natural (*e.g.* Marrett & Allmendinger, 1992) examples of fault populations and is qualitatively testable by the 'Weighting test' of Marrett and Allmendinger (1990). Fault plane solutions were constructed from the linked Bingham axes and plotted to illustrate the average kinematics from a population of faults.

To test for spatial homogeneity of faulting, the scale-invariance of fault populations and the kinematic compatibility of fault-slip data in the study area, stereograms of faults and striae as well as kinematic axes and fault plane solutions from different field locations were graphically compared. Fault populations with subparallel kinematic axes and/or slip directions were considered to be kinematically compatible and scale-invariant. Subsets of fault populations with anomalous kinematic axes and/or slip directions were considered separately. Both brittle and semi-brittle fault zones are considered in this study. Because this study only considers fault kinematics and does not address the mechanical behavior of the faults, it is considered reasonable to compare kinematic axes from both brittle and semi-brittle fault zones and discuss them in the

context of understanding the orientation and distribution of average incremental strain axes for fault populations. Graphical analyses of fault-slip data and field observations of crosscutting relationships between fault sets were evaluated to understand the geologic significance of faults in the study area.

4. Fault kinematic data

A population (n=235) of fault kinematic data was collected from three study areas located between Seno Otway and the Magallanes Straits. The data are organized into separate populations of thrust, strike-slip and normal faults and are presented according to location for three study areas: 1) Canal Jeronimo, Seno Otway and Estuario Wickham to the northwest, 2) Estuario Silva Palma, Seno Cordes and Bahía Fortesque near central Peninsula Brunswick and 3) Cabo Forward and the Magallanes Straits toward the southeast (Figure 3.1). Refer to Chapter 1 for the names and significance of the structures mentioned.

4.1 Faults near Canal Jeronimo, Seno Otway and Estuario Wickham

4.1.1 Thrust faults

Fault kinematic data were collected from 29 thrust faults exposed along the shores of Canal Jeronimo and Seno Otway (Figure 3.2). Near Canal Jeronimo, first generation thrust faults from the Tobífera duplex (Figure 3.2a) and a thrust that imbricates the Rocas Verdes basin terrane (Figure 3.2c) all display moderately southwest-dipping fault surfaces with down-dip, southwest-plunging or oblique south-southwest plunging slip lineations. Shortening axes are subhorizontal and plunge shallowly southwest and northeast and extension axes are subvertical. Minor fault planes associated with second-generation thrusts near Canal Jeronimo dip steeply toward the southwest and

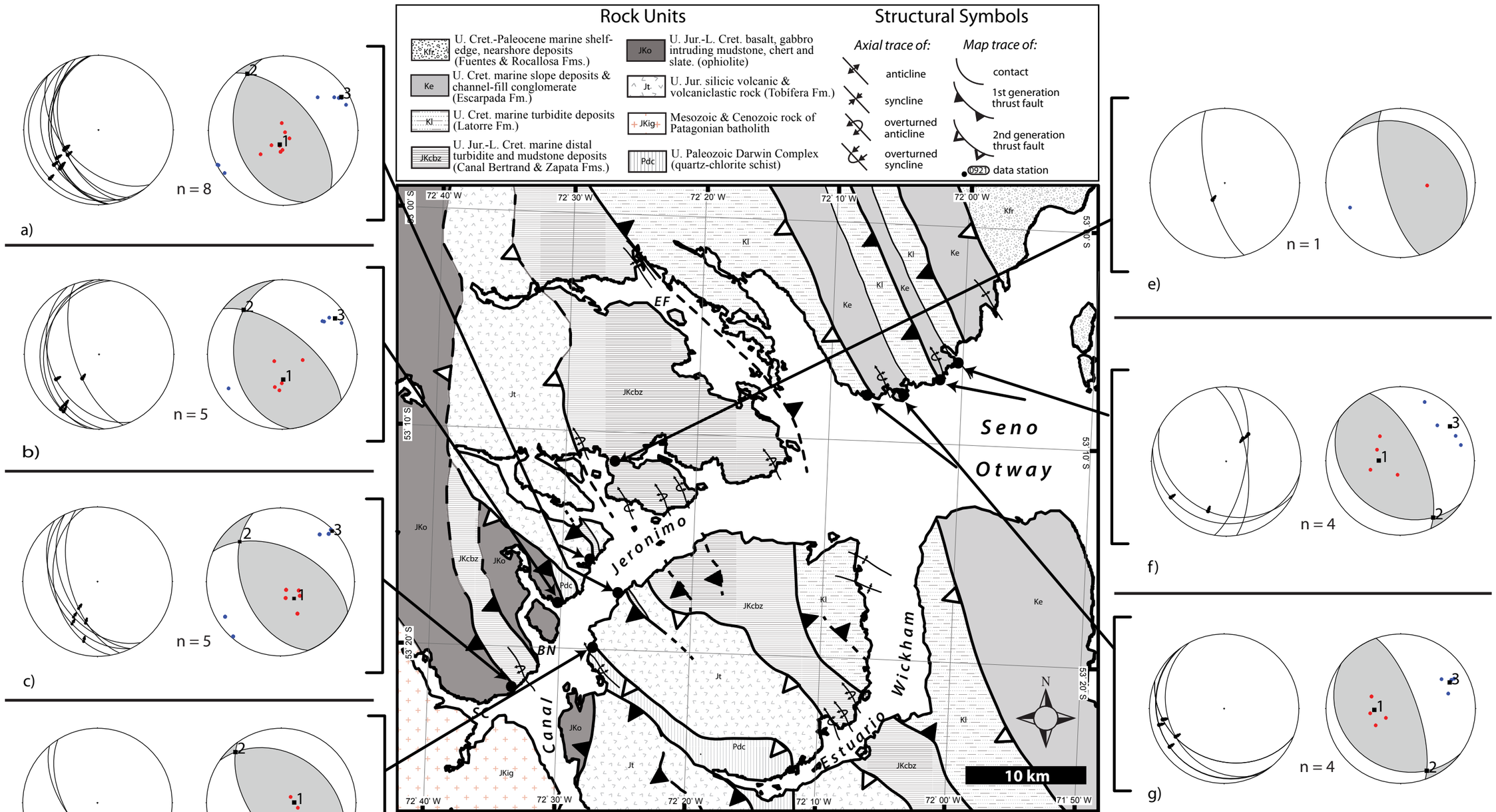

Figure 3.2. Map showing spatial distribution and orientations of thrust fault populations and kinematic axes in the northwestern part of the study area near Canal Jeronimo and Seno Otway. (a-g, left) Equal area stereographic projections of: attitudes of fault surfaces (great circles) and striae (solid black dots). Arrows on striae shows motion of the hanging wall; (a-g, right) equal area stereographic projection showing attitudes of shortening (blue dots) and extension (red dots) axes, linked Bingham axes (black squares: 1, extension; 2, intermediate; 3, shortening), and fault plane solution constructed from the linked Bingham axes (gray shaded areas show extension dihedra, white areas show shortening dihedra). Hereafter, all stereograms are presented the same way unless otherwise indicated.

have down-dip slip lineations. Kinematic axes of the second generation thrusts are subparallel to those of first generation thrusts (Figure 3.2d). Toward the northeast, a steeply dipping out-of-syncline thrust is exposed within the Zapata-Canal Bertrand décollement (Figure 3.2e), fault planes, striae and kinematic axes from this fault are subparallel to those from first generation structures toward the southwest (Figures 3.2a-c).

Near Seno Otway, eight first-generation minor thrust faults are located in the footwalls of map scale thrusts that imbricate Late Cretaceous foreland basin strata. The minor faults form both synthetic and antithetic fault sets (Figure 3.2 f-g). Synthetic faults dip shallowly south-southwest and southwest and contain down-dip to obliquely plunging striae. Antithetic faults dip steeply toward the east-northeast and contain steeply north plunging striae. Shortening axes from first-generation thrusts within foreland basin strata plunge shallowly northeast, and extension axes are subvertical to steeply east-southeast plunging (Figures 3.2f-g).

Near Estuario Wickham (Figure 3.3), minor thrust faults occur in the hanging wall of the second-generation Tobífera thrust. The fault planes dip shallowly to the west-southwest and contain down-dip striae. Shortening axes from this thrust plunge shallowly northeast, and extension axes are subvertical (Figure 3.3a). In the hanging wall of the Tobífera thrust, first-generation thrust-sense shear bands that thicken the Cordillera Darwin Metamorphic Complex are axial planar to F_1 folds (see Chapter 1), dip steeply toward the southwest, and contain down-dip quartz and mica mineral lineations. Shortening axes from thrusts in the Cordillera Darwin Metamorphic Complex plunge shallowly northeast and southwest and extension axes are subvertical (Figure 3.3b-c). Second-generation reverse faults that juxtapose the Cordillera Darwin Metamorphic Complex above the Tobífera Formation dip steeply toward the west and contain down-dip quartz stretching lineations. Shortening axes plunge shallowly to the east and extension axes are subvertical (Figure 3.3d).

In the footwall of the Tobífera thrust, minor thrusts that shear the limbs of first-generation overturned folds within the Zapata-Canal Bertrand Formation (see chapter 1),

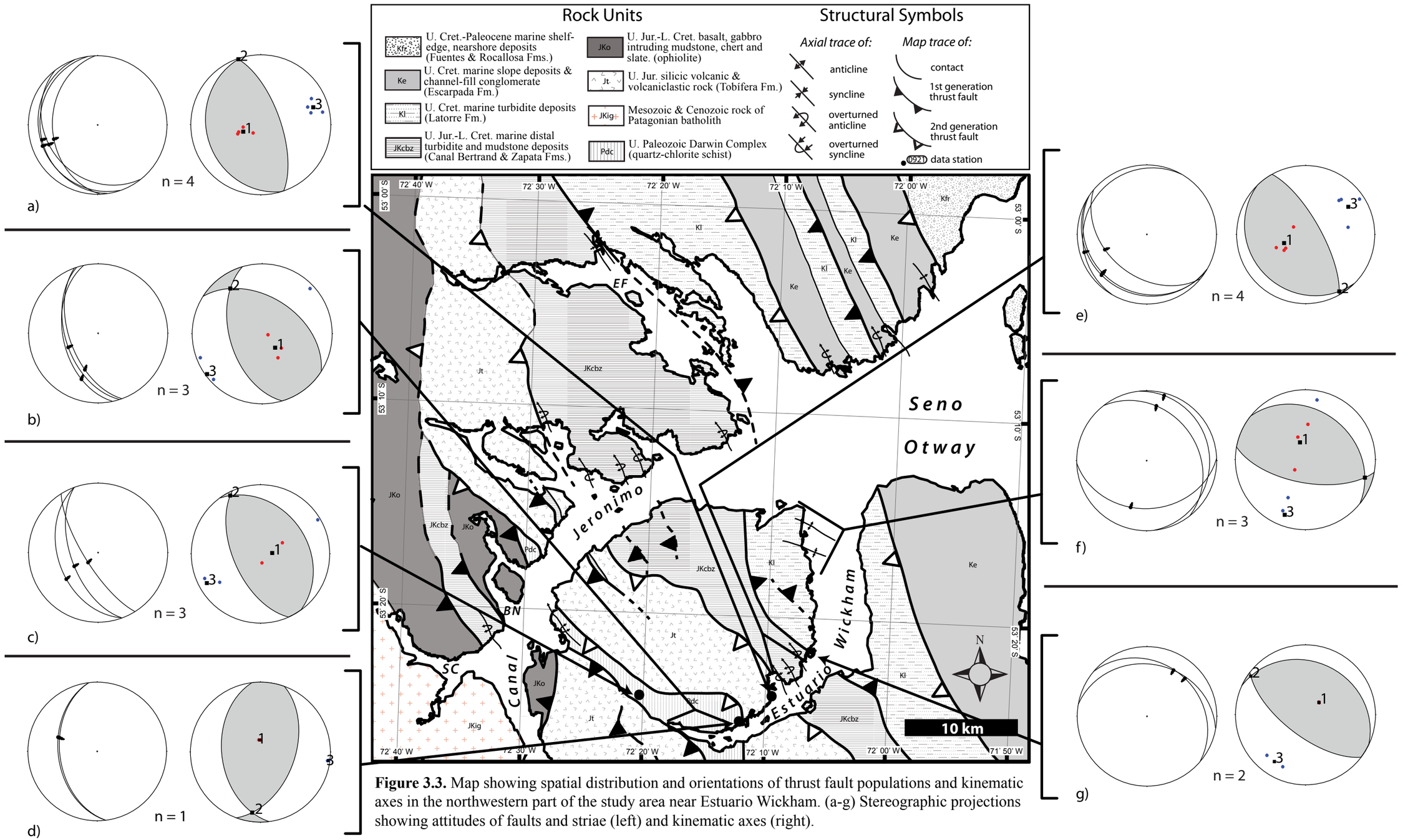

Figure 3.3. Map showing spatial distribution and orientations of thrust fault populations and kinematic axes in the northwestern part of the study area near Estuario Wickham. (a-g) Stereographic projections showing attitudes of faults and striae (left) and kinematic axes (right).

dip shallowly toward the southwest and contain down-dip white mica lineations and tool marks. Shortening axes from minor thrusts in the Zapata-Canal Bertrand Formation plunge shallowly to the northeast and extension axes are subvertical (Figure 3.3e). A small population of minor back thrusts (n=5) occur within the Latorre Formation. The back thrusts dip dominantly toward the north-northeast and contain down-dip slip lineations (Figure 3.3f-g). One antithetic thrust dips shallowly toward the south-southwest. Shortening axes from back thrusts within the Latorre Formation plunge shallowly south-southeast, and extension axes are subvertical (Figures 3.3f-g).

4.1.2 Strike-slip and normal faults

A relatively small population (n=21) of strike-slip faults crop out near Seno Otway and Estuario Wickham (Figure 3.4). In Seno Condor at the southwest corner of Canal Jeronimo, five strike-slip faults are exposed. Four of the faults strike northeast and are right-lateral, and one fault strikes west-northwest and is left-lateral. Slip lineations on all of the fault planes are subhorizontal. Shortening axes plunge shallowly east-northeast and west-southwest. Extension axes are also subhorizontal and trend north and south (Figure 3.4a).

Evidence for strike-slip deformation is absent along Canal Jeronimo between Seno Condor and Seno Otway. Strike-slip faults occur again in the eastern part of the study area near Seno Otway and Estuario Wickham (Figure 3.4). In Estuario Wickham, strike-slip faults occupy two dominant orientations. A set of west-striking faults is left-lateral and north-northeast-striking faults are right-lateral. Trends of kinematic axes from strike-slip faults are mutually subparallel. Shortening axes plunge shallowly to moderately northeast and southwest. Extension axes are subhorizontal and plunge northwest or southeast (Figures 3.4b-c). At site 11071 (Figure 3.4), a right-lateral fault crosscuts a first-generation back thrust.

Near Seno Otway, strike slip faults occupy similar orientations to those in Estuario Wickham. Sets of right-lateral faults strike northeast or north-

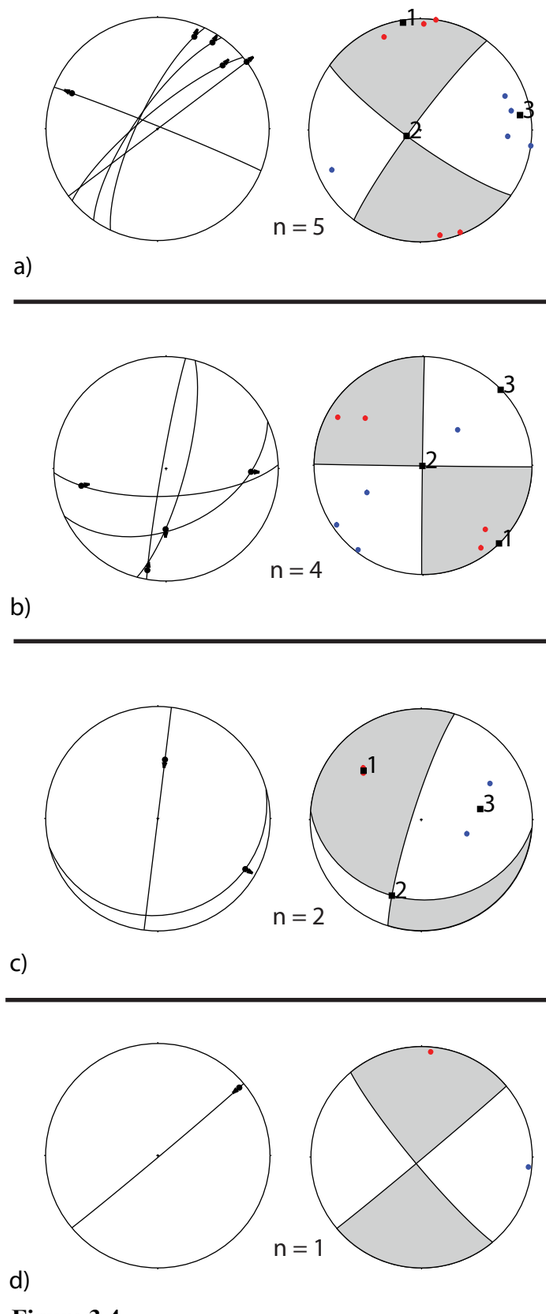
a)
n = 5
1
2
3
b)
n = 4
3
2
1
c)
n = 2
1
3
2
d)
n = 1

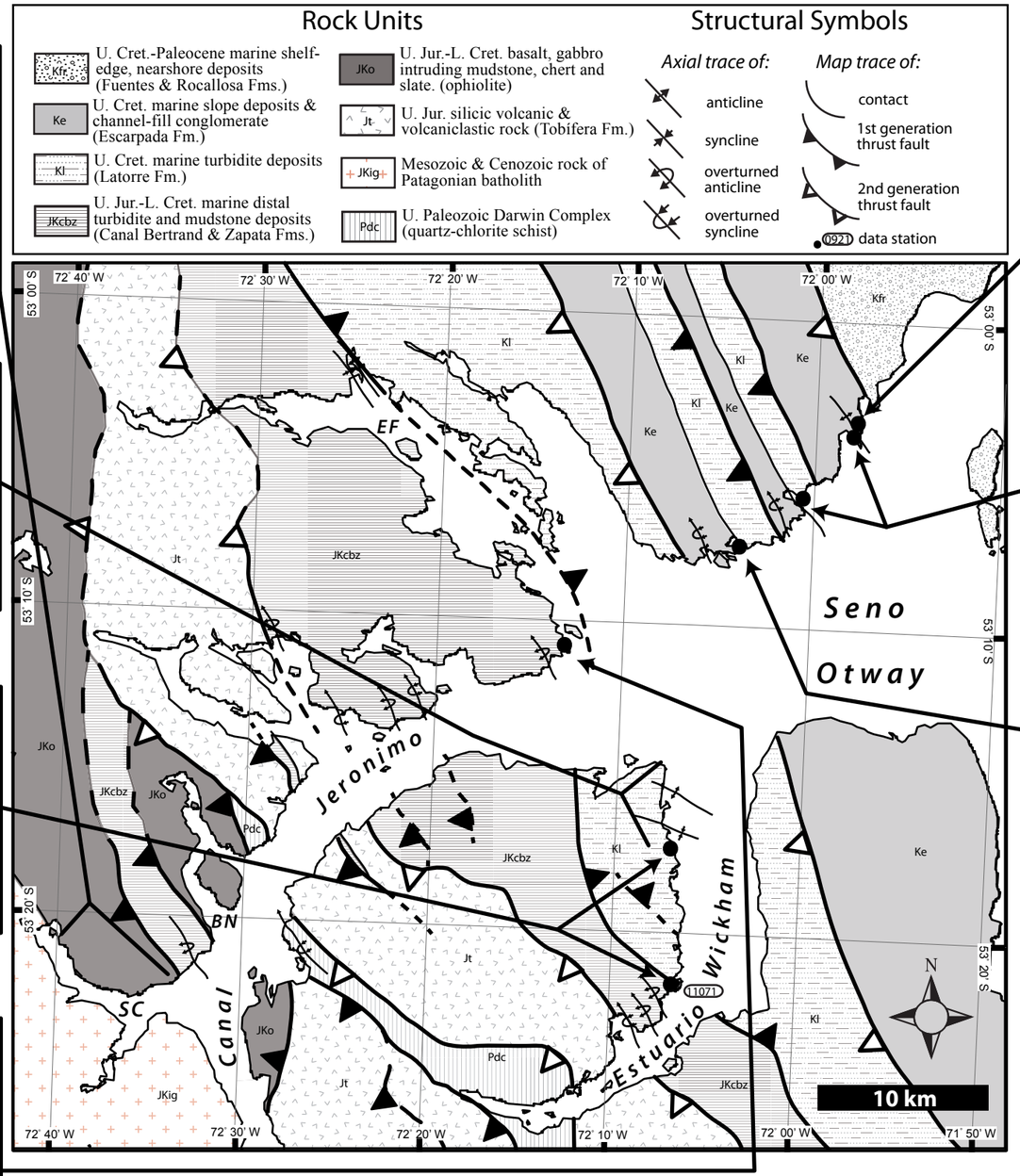
Rock Units
Kfr U. Cret.-Paleocene marine shelf-edge, nearshore deposits (Fuentes & Rocallosa Fms.)
Ke U. Cret. marine slope deposits & channel-fill conglomerate (Escarpada Fm.)
Kl U. Cret. marine turbidite deposits (Latorre Fm.)
JKcbz U. Jur.-L. Cret. marine distal turbidite and mudstone deposits (Canal Bertrand & Zapata Fms.)
JKo U. Jur.-L. Cret. basalt, gabbro intruding mudstone, chert and slate. (ophiolite)
Jt U. Jur. silicic volcanic & volcaniclastic rock (Tobifera Fm.)
JKig Mesozoic & Cenozoic rock of Patagonian batholith
Pdc U. Paleozoic Darwin Complex (quartz-chlorite schist)
Structural Symbols
Axial trace of:
anticline
syncline
overturned anticline
overturned syncline
Map trace of:
contact
1st generation thrust fault
2nd generation thrust fault
0921 data station
72° 40' W
72° 30' W
72° 20' W
72° 10' W
72° 00' W
71° 50' W
53° 00' S
53° 10' S
53° 20' S
Kfr
Kl
Ke
JKcbz
Jt
JKig
JKo
Pdc
EF
Jeronimo
Seno
Otway
Wickham
Canal
Estuario
BN
SC
1107
N
10 km

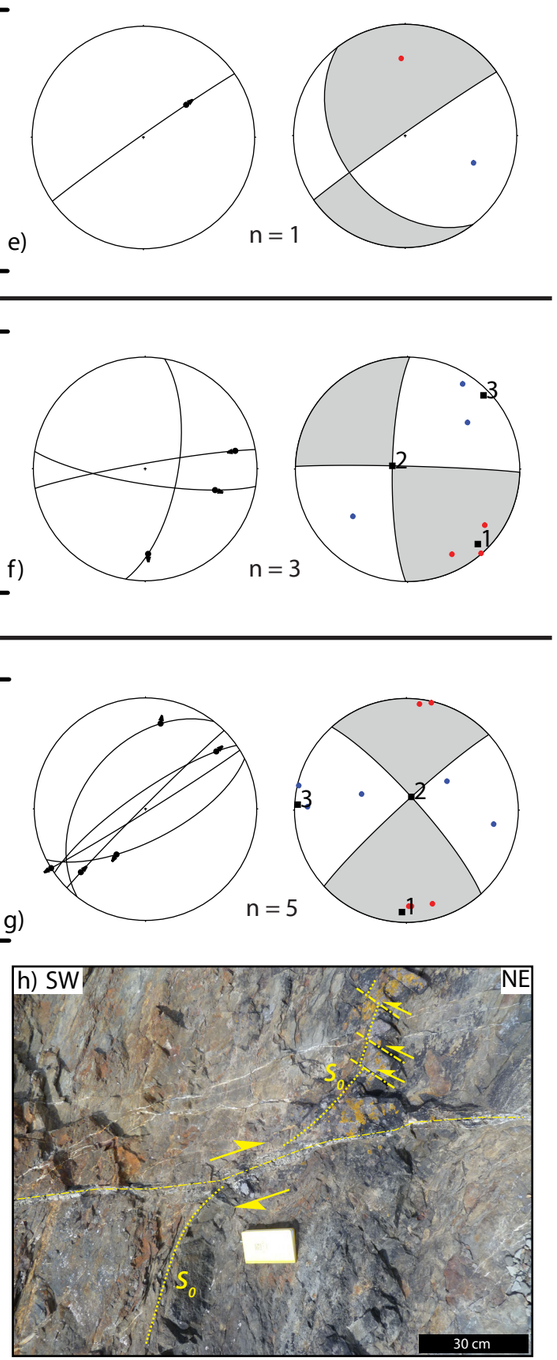
e)
n = 1
f)
n = 3
3
2
1
g)
n = 5
3
2
1

h) SW
NE
S_0
S_0
30 cm

Figure 3.4

Figure 3.4. Map showing spatial distribution and orientations of strike-slip fault populations and kinematic axes in the northwestern part of the study area near Canal Jeronimo, Seno Otway and Estuario Wickham. (a-g) Stereographic projections showing attitudes of faults and striae (left) and kinematic axes (right). (h) Field photograph showing map view of a right-lateral strike-slip fault (horizontal trace in photo) with three subsidiary left-lateral faults. S_0, bedding, field book for scale.

northeast and left-lateral faults are west-striking (Figure 3.4d-h). Kinematic axes for fault sets dominated by right-lateral slip are mutually subparallel and have north- and south-plunging extension axes and shortening axes that plunge both east and west (Figures 3.4d, f, g). One set of left-slip faults has shortening axes that plunge northeast and southwest as well as southeast-trending extension axes (Figure 3.4f). Figure 3.4h shows an example of both right-lateral and left-lateral minor faults that are characteristic of those exposed near Seno Otway and Estuario Wickham. Displacements are on the order of centimeters to decimeters where they can be measured.

4.2 Faults near Estuario Silva Palma, Bahía Fortesque and Seno Cordes

4.2.1 Thrust faults

A population of 16 thrust faults from Estuario Silva Palma and 11 thrust-sense ductile shear bands from the Cordillera Darwin Metamorphic Complex schist exposed in Bahía Fortesque and Seno Cordes were measured. Near Estuario Silva Palma, the second generation Tobífera thrust is well exposed at sea level in three locations (Figure 3.5a). Everywhere this thrust dips shallowly to the southwest and contains down-dip quartz stretching lineations. Shortening axes plunge shallowly northeast and southwest, and extension axes are subvertical to steeply southwest plunging (Figure 3.5a). In the footwall, out of syncline thrusts that thicken the Zapata-Canal Bertrand Formation dip dominantly toward the southwest and contain down-dip to oblique south-southwest plunging calcite slip lineations. Shortening axes from thrusts in the Zapata-Canal Bertrand Formation plunge shallowly northeast and southwest, and extension axes are subvertical (Figure 3.5b).

In Seno Cordes toward the south, a first generation shear zone is exposed at the base of the Tobífera Formation where it dips steeply to the west-southwest and contains down-dip quartz stretching lineations. Shortening axes plunge shallowly to the west-southwest and extension axes are subvertical (Figure 3.5c). In Bahía Fortesque, thrust-sense shear bands that are axial-planar to isoclinal F_1 folds (*i.e.* Chapter 1, Figure 3.13f) dip shallowly to the southwest and contain down-dip to oblique southwest to south-

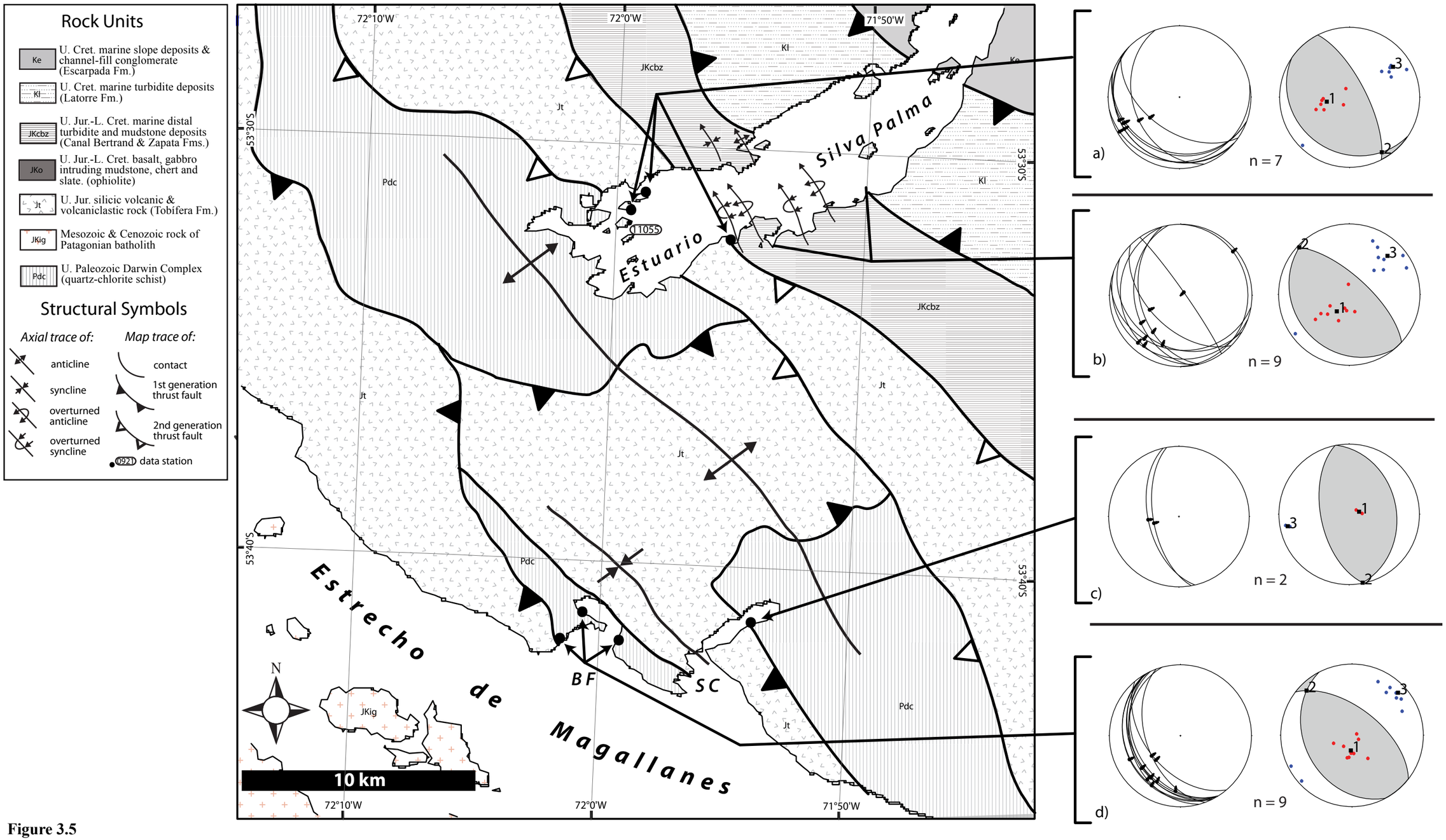
Rock Units
Ke
U. Cret. marine slope deposits & channel-fill conglomerate (Escarpada Fm.)
Kl
U. Cret. marine turbidite deposits (Latorre Fm.)
JKcbz
U. Jur.-L. Cret. marine distal turbidite and mudstone deposits (Canal Bertrand & Zapata Fms.)
JKo
U. Jur.-L. Cret. basalt, gabbro intruding mudstone, chert and slate. (ophiolite)
Jt
U. Jur. silicic volcanic & volcaniclastic rock (Tobífera Fm.)
JKig
Mesozoic & Cenozoic rock of Patagonian batholith
Pdc
U. Paleozoic Darwin Complex (quartz-chlorite schist)
Structural Symbols
Axial trace of:
anticline
syncline
overturned anticline
overturned syncline
Map trace of:
contact
1st generation thrust fault
2nd generation thrust fault
0921 data station
72°10'W
72°0'W
71°50'W
53°30'S
53°40'S
Silva Palma
Estuario
Estrecho de Magallanes
BF
SC
11055
N
10 km
a)
n = 7
b)
n = 9
c)
n = 2
d)
n = 9

Figure 3.5

Figure 3.5. Map showing spatial distribution and orientations of thrust fault populations and kinematic axes in the central part of the study area near Estuario Silva Palma, Bahía Fortesque (BF) and Seno Cordes (SC). (a-d) Stereographic projections showing attitudes of faults and striae (left) and kinematic axes (right).

southwest plunging quartz stretching lineations. Shortening axes from the Bahía Fortesque shear zone plunge shallowly northeast and southwest, and extension axes are subvertical (Figure 3.5d).

4.2.2 Strike-slip and normal faults

In Estuario Silva Palma, a small population (n=8) of strike-slip and normal faults crosscut contractional structures (Figure 3.6). Strike-slip faults are not common in Estuario Silva Palma, however, where they occur they crosscut F_1 folds within the Zapata-Canal Bertrand Formation and occupy similar orientations to those observed at Seno Otway. North-northeast-striking faults are right-lateral, and northwest-striking faults are left-lateral. Shortening axes plunge shallowly to the east, and extension axes are subhorizontal and plunge north and south (Figure 3.6a). A small population of normal faults also occurs at Estuario Silva Palma (Figure 3.6b-e). Normal faults occupy two west-striking orientations, one set dips moderately toward the south, and a second dips shallowly toward the north to form a conjugate-style geometry. Striae have both down-dip and oblique rakes on normal fault planes. Shortening axes cluster and are subvertical to steeply plunging. Extension axes plunge north and south (Figures 3.6b, c). At site 11055 (Figure 3.6), a set of minor brittle faults with normal-sense displacements offsets the contact between a silicic dike that intrudes psammitic schist of the Cordillera Darwin Metamorphic Complex. Here, both the dike and the psammite share a subsolidus foliation that is interpreted to reflect the first phase Andean contractional deformation (S_1, Figure 3.6e), indicating that normal faulting postdated thrusting.

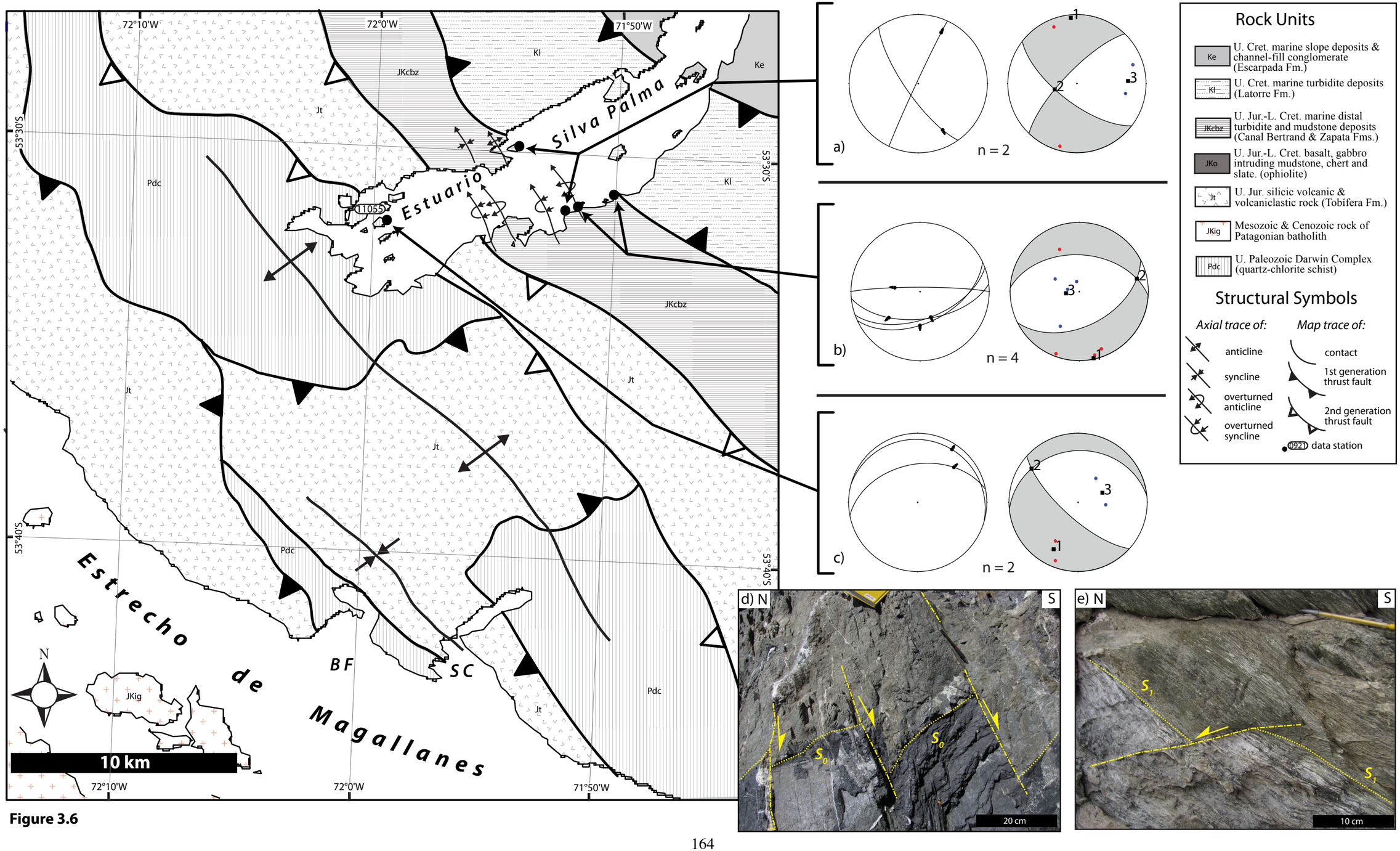
72°10'W
72°0'W
71°50'W
53°30'S
53°40'S
Silva Palma
Estuario
Estrecho de Magallanes
BF
SC
11055
Kl
Ke
JKcbz
Jt
Pdc
JKig
N
10 km
a)
n = 2
b)
n = 4
c)
n = 2
1
2
3
Rock Units
Ke
U. Cret. marine slope deposits & channel-fill conglomerate (Escarpada Fm.)
Kl
U. Cret. marine turbidite deposits (Latorre Fm.)
JKcbz
U. Jur.-L. Cret. marine distal turbidite and mudstone deposits (Canal Bertrand & Zapata Fms.)
JKo
U. Jur.-L. Cret. basalt, gabbro intruding mudstone, chert and slate. (ophiolite)
Jt
U. Jur. silicic volcanic & volcaniclastic rock (Tobífera Fm.)
JKig
Mesozoic & Cenozoic rock of Patagonian batholith
Pdc
U. Paleozoic Darwin Complex (quartz-chlorite schist)
Structural Symbols
Axial trace of:
anticline
syncline
overturned anticline
overturned syncline
Map trace of:
contact
1st generation thrust fault
2nd generation thrust fault
0921 data station
d) N
S
S_0
20 cm
e) N
S
S_1
10 cm

Figure 3.6

Figure 3.6. Map showing spatial distribution and orientations of strike-slip and normal fault populations and kinematic axes in the central part of the study area near Estuario Silva Palma, Bahía Fortesque and Seno Cordes. (a-c) Stereographic projections showing attitudes of faults and striae (left) and kinematic axes (right). (d-e) Field photographs of an outcrop face showing examples of brittle normal faults offsetting bedding (d) and a subsolidus S_1 foliation (e).

4.3 Faults near Cabo Froward and the Magallanes Straits

4.3.1 Thrust faults

Eleven thrust faults were measured near Cabo Froward from exposures within the Zapata-Canal Bertrand Formation and Late Cretaceous foreland basin strata (Figure 3.7). At Cabo Froward, a set of four out-of-syncline thrust faults truncate overturned F_1 tight folds within the Zapata-Canal Bertrand Formation (Figure 3.7a). Here, thrust faults dip shallowly toward the west and contain down-dip calcite slip lineations and tool marks. Shortening axes plunge shallowly east, and extension axes are subvertical (Figure 3.7b). A set of tensile calcite veins that formed adjacent to the thrust faults trends east and helps to confirm a top-northeast thrust sense of motion (Figure 3.7c). Northward along the Magallanes Straits, sets of both synthetic and antithetic minor thrust faults imbricate the Latorre and Escarpada Formations and dip moderately toward the northeast and southwest. Slip lineations defined by calcite fibers and mechanical grooves trend down-dip. Shortening axes plunge shallowly northeast and southwest, and extension axes are subvertical (Figure 3.7d-e). North of Cabo Froward along the Magallanes Straits, fault populations are dominated by strike-slip and normal faults (discussed below).

4.3.2 Strike-slip faults

Along the Magallanes Straits for 30 km northeast of Cabo Froward (Figure 3.8), folds and thrusts of the Cretaceous foreland thrust belt (see Chapter 1) are overprinted by a substantial ($n > 100$) population of brittle strike-slip faults. Near Cabo Froward, several left-lateral strike-slip faults strike west and crosscut contractional F_1 folds and thrusts that thicken the Zapata-Canal Bertrand Formation (Figure 3.8a, 3.9a). At this locality, one right-lateral fault strikes northeast in a conjugate-style orientation to the left-lateral set. Shortening axes from the population of 5 faults plunge shallowly northeast and southwest; extension axes are also shallowly plunging northwest and southeast (Figure 3.8a). Between Cabo Froward and Bahía Rosa (Figure 3.8), a set of both right-lateral and left-lateral minor strike-slip faults crosscut tilted Late Cretaceous strata of the Latorre

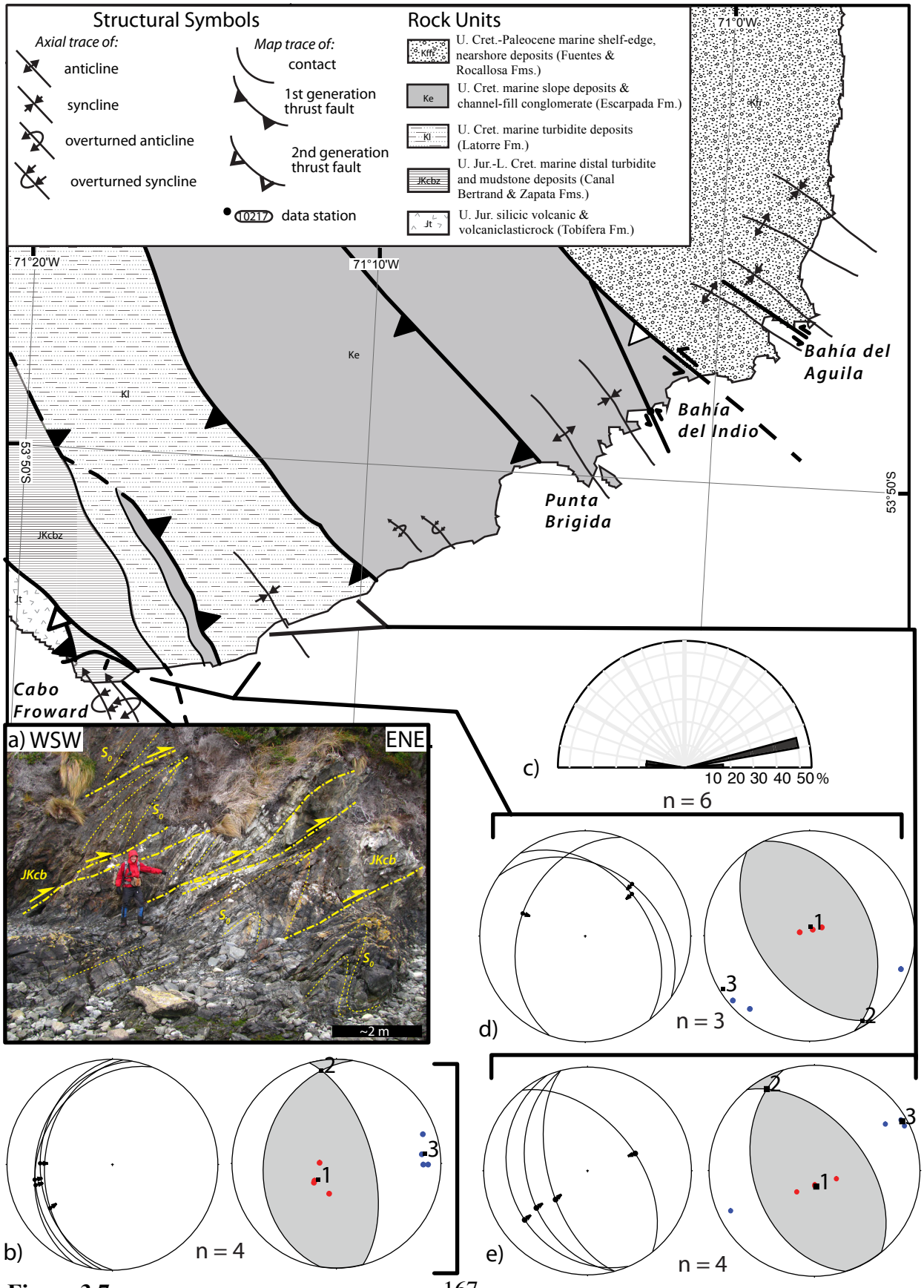
Structural Symbols
Axial trace of:
anticline
syncline
overturned anticline
overturned syncline
Map trace of:
contact
1st generation thrust fault
2nd generation thrust fault
10217 data station
Rock Units
Kff U. Cret.-Paleocene marine shelf-edge, nearshore deposits (Fuentes & Rocallosa Fms.)
Ke U. Cret. marine slope deposits & channel-fill conglomerate (Escarpada Fm.)
Kl U. Cret. marine turbidite deposits (Latorre Fm.)
JKcbz U. Jur.-L. Cret. marine distal turbidite and mudstone deposits (Canal Bertrand & Zapata Fms.)
Jt U. Jur. silicic volcanic & volcaniclastic rock (Tobífera Fm.)
71°0'W
71°20'W
71°10'W
53°05'S
53°50'S
Bahía del Aguila
Bahía del Indio
Punta Brigida
Cabo Froward
a) WSW
ENE
JKcb
~2 m
c)
10 20 30 40 50%
n = 6
d)
n = 3
b)
n = 4
e)
n = 4

Figure 3.7

Figure 3.7. Map showing spatial distribution and orientations of thrust fault populations and kinematic axes in the southeastern part of the study area near Cabo Froward and the Magallanes Straits. (a) Field photograph showing F_1 folds within the Zapata-Canal Bertrand Fm. near Cabo Froward that are truncated by thrust faults. (b, d-e) Stereographic projections showing attitudes of faults and striae (left) and kinematic axes (right). (c) Rose diagram showing trends of tensile calcite veins associated with thrust faults.

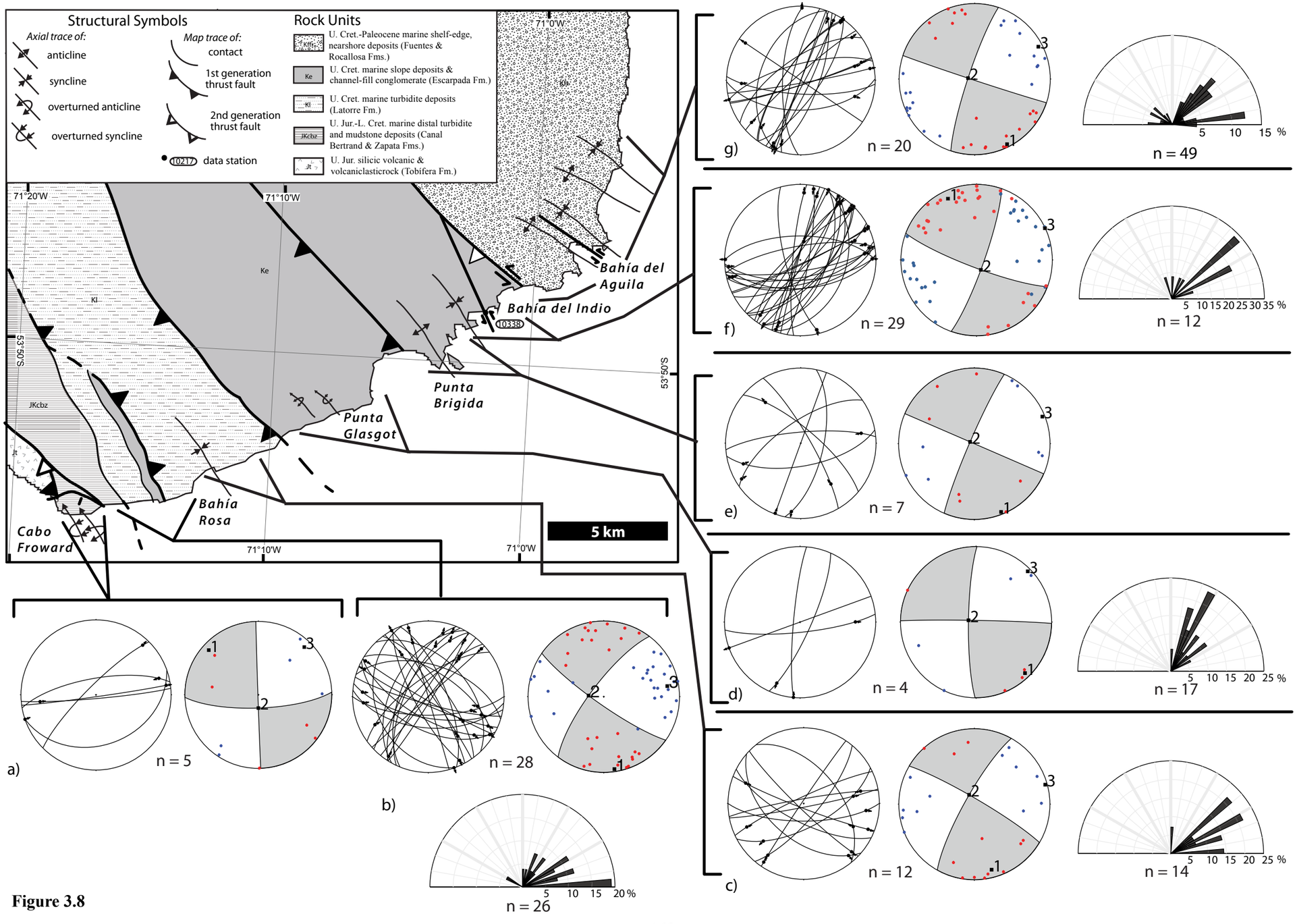
Structural Symbols
Axial trace of:
anticline
syncline
overturned anticline
overturned syncline
Map trace of:
contact
1st generation thrust fault
2nd generation thrust fault
10217 data station
Rock Units
Kfr
U. Cret.-Paleocene marine shelf-edge, nearshore deposits (Fuentes & Rocallosa Fms.)
Ke
U. Cret. marine slope deposits & channel-fill conglomerate (Escarpada Fm.)
Kl
U. Cret. marine turbidite deposits (Latorre Fm.)
JKcbz
U. Jur.-L. Cret. marine distal turbidite and mudstone deposits (Canal Bertrand & Zapata Fms.)
Jt
U. Jur. silicic volcanic & volcaniclasticrock (Tobífera Fm.)
71°0'W
71°20'W
71°10'W
53°50'S
Bahía del Aguila
Bahía del Indio
10338
Punta Brigida
Punta Glasgot
Bahía Rosa
Cabo Froward
5 km
a)
n = 5
b)
n = 28
n = 26
c)
n = 12
n = 14
d)
n = 4
n = 17
e)
n = 7
f)
n = 29
n = 12
g)
n = 20
n = 49

Figure 3.8

Figure 3.8. Map showing spatial distribution and orientations of the dominant strike-slip fault populations and kinematic axes in the southeastern part of the study area near Cabo Froward and the Magallanes Straits. (a-g) Stereographic projections showing attitudes of faults and striae (left) and kinematic axes (right). Rose diagrams in (b-d, f-g) show trends of tensile and sigmoidal calcite veins associated with the strike-slip faults in each location.

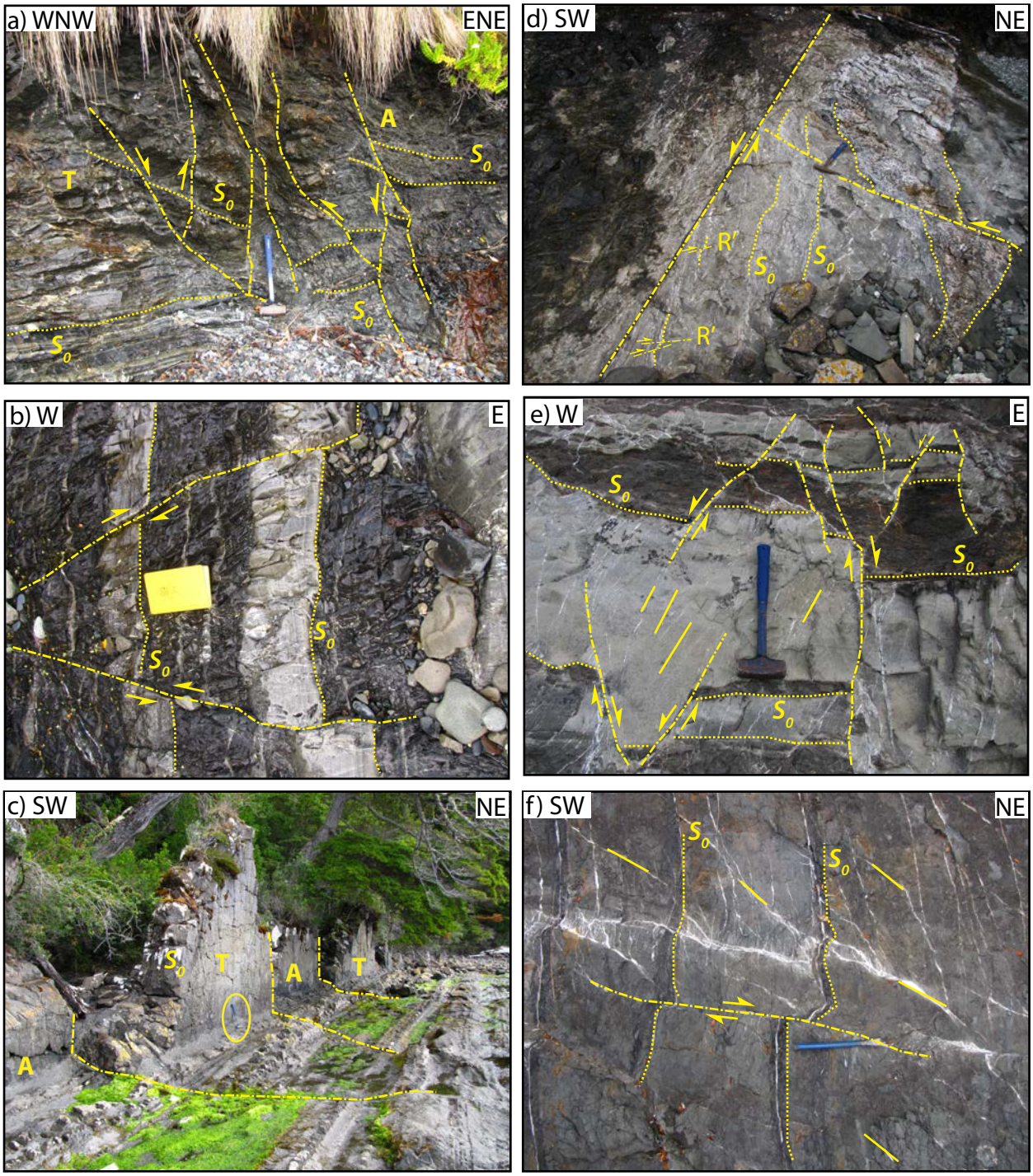

Figure 3.9. Field photographs showing examples of strike-slip faults near Cabo Froward (a) and the Magallanes Straits (b-f). Faults are marked by broken lines and bedding (S_0) by dotted lines. (a) Strike-slip faults crosscutting deformed bedding of the Zapata-Canal Bertrand Fm. near Cabo Froward, senses of displacement are apparent; here slickenlines are subhorizontal (see figure 3.8a), (b-c) conjugate sets of strike-slip faults near Bahía Rosa crosscutting strata of the Latorre (b, map view) and Escarpada (c) Fms., (d) map view of cataclasite in a ~5 m wide left-lateral fault zone at site 10338, (e-f) map view of conjugate sets of strike-slip faults displacing bedding of the Fuentes-Rocallosa Fms., short solid lines highlight trends of tensile calcite veins.

and Escarpada Formations (Figure 3.8b, 3.9b). Left-lateral faults occupy two common orientations, one set strikes west-northwest and the second set strikes north-northwest (Figure 3.8b). All right-lateral faults are northeast striking (Figure 3.8b). Kinematic axes from this population of right- and left-lateral faults cluster well. Shortening axes are shallowly east and west plunging, and extension axes plunge shallowly north and south (Figure 3.8b). Less than 5 km northeast of Bahía Rosa (Figure 3.8), F_1 folds that thicken the Latorre Formation are crosscut by a set of right- and left-lateral faults that occupy similar orientations to those toward the southwest. Here, left lateral faults are east-northeast and northwest striking, and all right-lateral faults strike northeast (Figure 3.8c). Kinematic axes are subparallel for both right- and left-lateral fault sets; shortening axes trend east-northeast and west-southwest, and extension axes trend north-northwest and south-southeast (Figure 3.8c). Near Punta Glasgot and Punta Brigida (Figure 3.8d,e), a small population of strike slip faults crosscuts F_1 folds within the Escarpada Formation Here, left-lateral faults strike east-northeast and northwest, and right-lateral faults strike north-northeast. The kinematic axes are subhorizontal; shortening axes trend east to northeast and southeast, and extension axes plunge shallowly northwest and southwest or north and south.

North of Punta Brigida near Bahía del Indio and Bahía del Aguila, strike-slip deformation intensifies. Between Punta Brigida and Bahía del Indio, a large set (n=49) of both left- and right-lateral faults crosscut steeply dipping strata of the Escarpada Formation (Figure 3.8f, g, 3.9c). Here, left-lateral faults strike dominantly east-northeast. Near site 10338 (Figure 3.8), a ~5 m wide intensely fractured zone that contains cataclasite defines a map-scale left-lateral fault that strikes northwest (Figure 3.9d). All right-lateral faults in this population are north- or northeast-striking. Kinematic axes from both right- and left-lateral faults cluster and are subhorizontal. Shortening axes plunge northeast and southwest; extension axes plunge north to northwest and south to southeast (Figure 3.8f). Near Bahía del Aguila, both right- and left-lateral fault sets crosscut folded Maastrichtian strata of the Fuentes-Rocallosa Formations (Figure 3.8g, 3.9e, f). Here all right-lateral faults strike north to northeast, and all left-lateral faults strike east-northeast.

One left-lateral fault strikes northwest (Figure 3.8g). Kinematic axes from strike-slip faults near Bahía del Aguila cluster and are subhorizontal. Shortening axes plunge northeast and southwest; extension axes plunge northwest and southeast (Figure 3.8g).

4.3.3 Veins

Calcite-filled veins are commonly associated with strike-slip faults everywhere along the Magallanes Straits. Calcite veins occur either in tensile (*i.e.* mode-I fractures) or in sigmoidal geometries. The asymmetric orientations of mode-I veins and asymmetry of sigmoidal veins relative to fault planes was used to help determine the shear sense of associated of strike-slip faults. Calcite veins dominantly strike east to northeast. The dominant strikes are generally parallel to shortening axes associated with the strike-slip faults, indicating that veining and faulting were probably contemporaneous and lending credence to kinematic interpretations of the faults that are based on fault surface asperities and/or secondary fractures (Figure 3.8b-d, f-g; 3.9e-f).

4.3.4 Anomalous strike-slip faults

A small population (n=15) of strike-slip faults occurs along the Magallanes Straits with shear senses opposite those of the dominant sets discussed above. East of Cabo Froward, three left-lateral faults strike northeast, and one right-lateral fault strikes northwest (Figure 3.10a). At Punta Brigida, three left-lateral faults strike northeast or north (Figure 3.10b). A set of five faults near Bahía del Indio (Figure 3.10c) and three faults near Bahía del Aguila (Figure 3.10d) consist of right-lateral faults striking southeast and left-lateral faults striking northeast. Kinematic axes from the population (n=15) of anomalous faults cluster well and are subhorizontal. Shortening axes plunge north and south, and extension axes plunge east and west (Figures 10a-d). Crosscutting relationships between the dominant and anomalous sets of faults were only observed in two localities at site 10315 (location in Figure 3.10). Here, two northeast-striking right-lateral faults from the dominant set crosscut southeast-striking right lateral-faults of the anomalous set. On this basis, it is inferred that the dominant set of right- and left-lateral

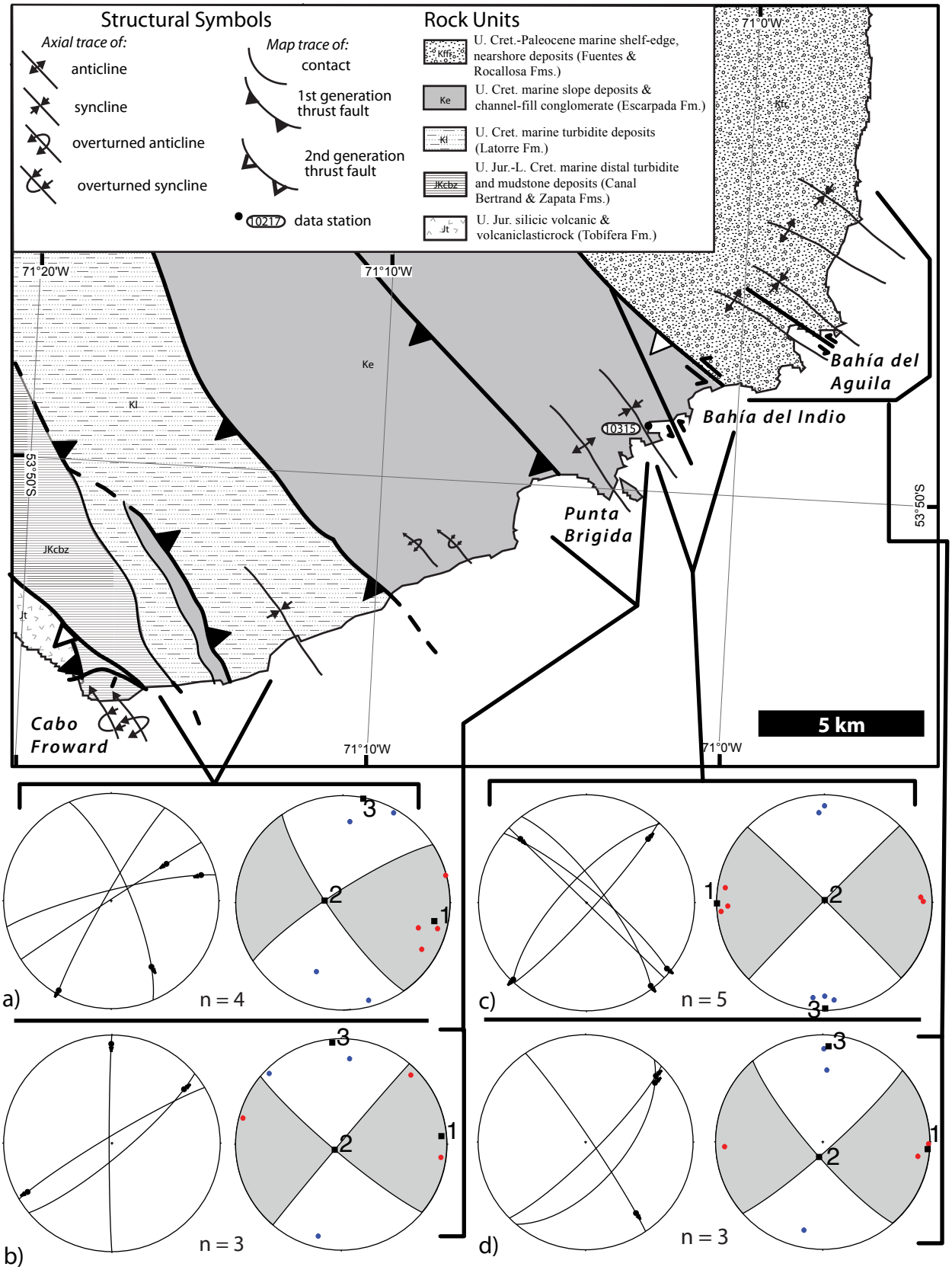
Structural Symbols
Axial trace of:
anticline
syncline
overturned anticline
overturned syncline
Map trace of:
contact
1st generation thrust fault
2nd generation thrust fault
10217 data station
Rock Units
U. Cret.-Paleocene marine shelf-edge, nearshore deposits (Fuentes & Rocallosa Fms.)
U. Cret. marine slope deposits & channel-fill conglomerate (Escarpada Fm.)
U. Cret. marine turbidite deposits (Latorre Fm.)
U. Jur.-L. Cret. marine distal turbidite and mudstone deposits (Canal Bertrand & Zapata Fms.)
U. Jur. silicic volcanic & volcaniclastic rock (Tobífera Fm.)
71°20'W
71°10'W
71°0'W
53°05'S
53°50'S
Ke
Kl
JKcbz
Jt
Bahía del Aguila
Bahía del Indio
10315
Punta Brigida
Cabo Froward
5 km
a)
n = 4
b)
n = 3
c)
n = 5
d)
n = 3

Figure 3.10

Figure 3.10. Map showing spatial distribution and orientations of the anomalous strike-slip fault populations and kinematic axes in the southeastern part of the study area near Cabo Froward and the Magallanes Straits. (a-d) Stereographic projections showing attitudes of faults and striae (left) and kinematic axes (right).

faults discussed above (*i.e*. Figure 3.8) are everywhere younger than the anomalous set discussed here (*i.e*. Figure 3.10).

4.3.5 Normal Faults

A small population (n=13) of minor normal faults also occurs along the Magallanes Straits between Cabo Froward and Bahía del Aguila (Figure 3.11). At Cabo Froward, one minor normal fault crosscuts sheared ignimbrite deposits near the contact between the Tobífera and Zapata-Canal Bertrand Formations (Figure 3.11a). Along the shore of the Magallanes Strait <5 km east of Cabo Froward, at least seven normal faults occur (*e.g*. Figure 3.11b). Here, striae have steep rakes on normal fault planes that indicate oblique slip. One east-northeast-striking and three northwest-striking faults have a left-normal sense of slip. Three northeast-striking faults have a right-normal sense of slip (Figure 3.11b). Near Punta Brigida, two west-striking normal faults have down-dip striae, and one northeast-striking oblique slip fault has a normal-right sense of shear (Figure 3.11c). Only two normal faults were observed north of Punta Brigida (Figure 3.11d). Here, an east-northeast-striking fault has a right-normal shear sense, and a northwest-striking fault has a left-normal sense of shear. Throughout the study area, shortening axes are clustered and subvertical. Most west-striking normal faults have extension axes that are subhorizontal and plunge north or south. East of Cabo Froward, extension axes are subhorizontal and generally trend north or south (Figure 3.11a-d).

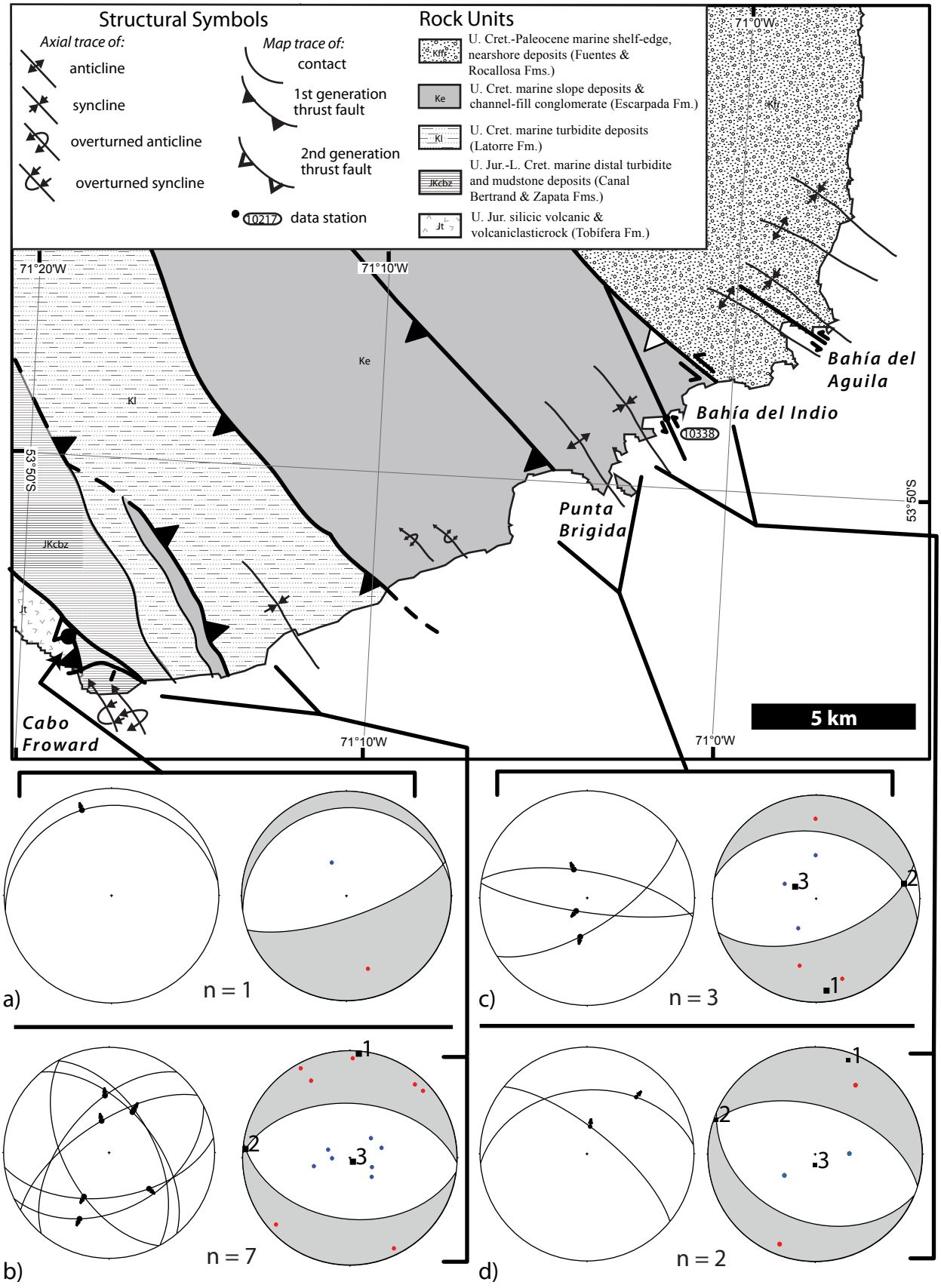
Structural Symbols
Axial trace of:
anticline
syncline
overturned anticline
overturned syncline
Map trace of:
contact
1st generation thrust fault
2nd generation thrust fault
10217 data station
Rock Units
Kff U. Cret.-Paleocene marine shelf-edge, nearshore deposits (Fuentes & Rocallosa Fms.)
Ke U. Cret. marine slope deposits & channel-fill conglomerate (Escarpada Fm.)
Kl U. Cret. marine turbidite deposits (Latorre Fm.)
JKcbz U. Jur.-L. Cret. marine distal turbidite and mudstone deposits (Canal Bertrand & Zapata Fms.)
Jt U. Jur. silicic volcanic & volcaniclasticrock (Tobífera Fm.)
71°20'W
71°10'W
71°0'W
53°05'S
53°50'S
Ke
Kl
JKcbz
Jt
Bahía del Aguila
Bahía del Indio
10338
Punta Brigida
Cabo Froward
5 km
a)
n = 1
b)
n = 7
c)
n = 3
d)
n = 2
1
2
3

Figure 3.11

Figure 3.11. Map showing spatial distribution and orientations of normal fault populations and kinematic axes in the southeastern part of the study area near Cabo Froward and the Magallanes Straits. (a-d) Stereographic projections showing attitudes of faults and striae (left) and kinematic axes (right).

5. Results: Test for kinematic compatibility among fault sets

To test for kinematic compatibility among faults sets in different locations along-strike, the attitudes of fault planes and striae as well as orientations of kinematic axes are graphically compared using the methods of Marrett and Allmendinger (1990).

5.1 THRUST FAULTS

Thrust faults near Canal Jeronimo, Seno Otway and Estuario Wickham dip dominantly toward the southwest and contain down-dip or steeply oblique striae. A subsidiary northeast-dipping set of faults occurs that forms a conjugate orientation with the main set. Shortening axes are subhorizontal and trend northeast, and extension axes are subvertical (Figure 3.12a, b). Thrust faults exposed near Estuario Silva Palma, Bahía Fortesque and Seno Cores have similar orientations. Here, thrusts dip dominantly southwest and contain down-dip or steeply oblique striae. Shortening axes plunge shallowly northeast and southwest, and extension axes are subvertical or steeply southwest-plunging (Figure 3.12c, d). Thrust faults exposed near Cabo Froward and along the Magallanes Straits also have similar orientations. Both west-southwest and northeast dipping faults form a conjugate geometry. Subhorizontal shortening axes plunge northeast and southwest; extension axes are subvertical (Figure 3.12e). A plot of all thrust faults in the study area highlights a high degree of kinematic compatibility within the population (Figure 3.12f). It is clear that thrust faults have a dominant orientation that dips shallowly toward the southwest and contains striae with high-angle rakes on the fault surfaces. Kinematic axes from the total population (n=88) of thrust faults form point maxima indicating that they show kinematic homogeneity throughout the study area. Shortening axes are subhorizontal and trend northeast. Extension axes are subvertical. The plunge and trend of mean principal strain axes calculated by the linked Bingham method are 1) extension = 78°, 216°; 2) intermediate = 4°, 325°; and 3) shortening = 11°, 056° (Figure 3.12f), which are compatible with the regional trends of

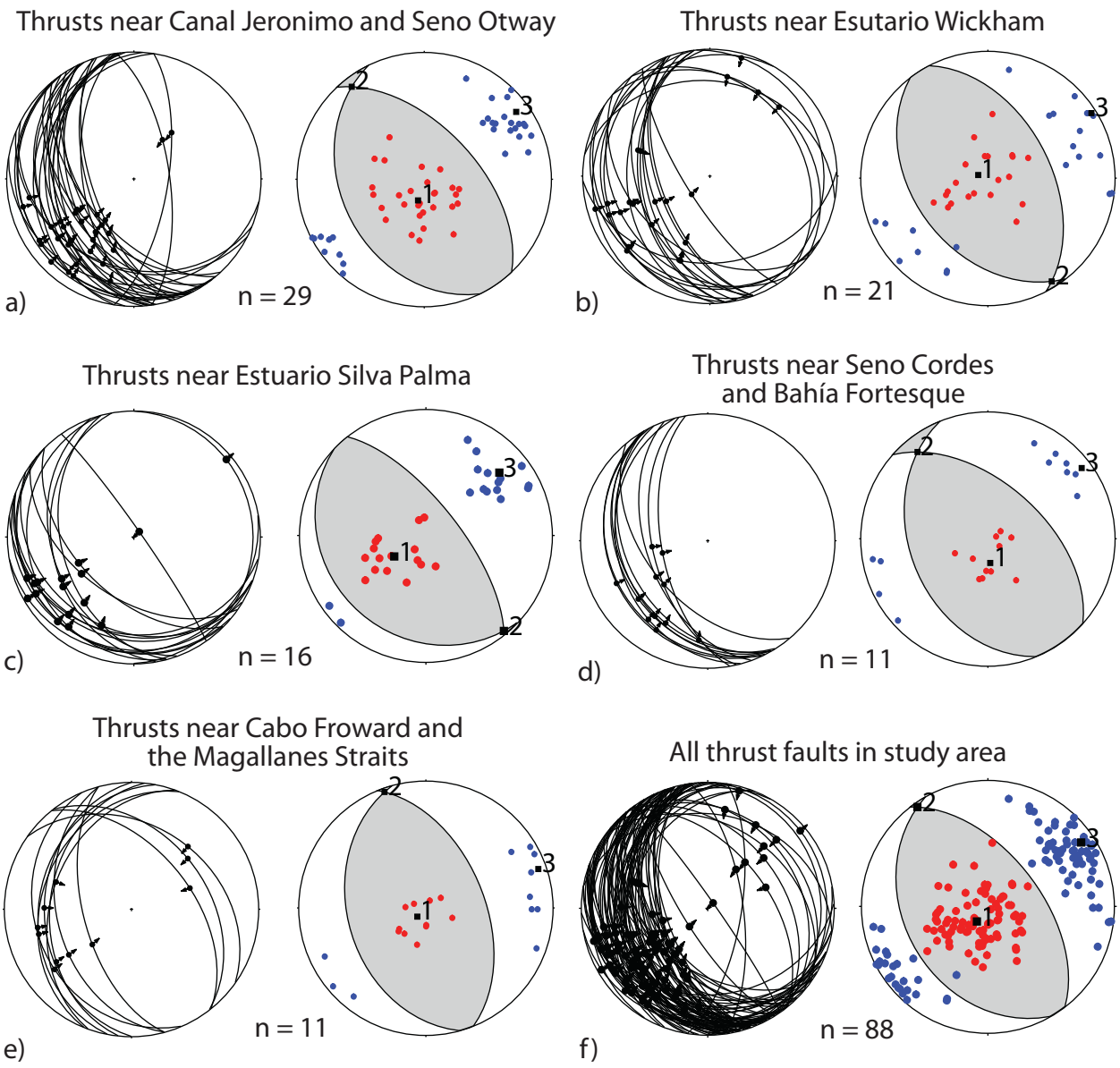

Figure 3.12. Stereographic projections showing attitudes of faults and striae (left) and kinematic axes (right) from all thrust faults near (a) Canal Jeronimo and Seno Otway, (b) Estuario Wickham, (c) Estuario Silva Palma, (d) Seno Cordes and Bahía Fortesque, (e) Cabo Froward and the Magallanes Straits and (f) all thrust faults in the study area.

contractional structures of the Cretaceous to Paleocene Magallanes fold-thrust belt (see Chapter 1).

5.2 STRIKE-SLIP FAULTS

Strike-slip faults occupy two dominant orientations near Canal Jeronimo and Seno Otway (Figure 3.13a), Estuario Wickham (Figure 3.13b) and Estuario Silva Palma (Figure 3.13c). North to northeast-striking faults sets are all right-lateral, northwest- and east-northeast-striking sets are left-lateral. Striae are always moderately to shallowly plunging on fault surfaces, indicating a small component of either normal or reverse displacement that depends on the dip-direction of the fault surface and plunge direction of the slickenline. However, faults with small components of either normal or reverse senses of motion have subparallel kinematic axes and are therefore considered kinematically compatible and part of the same deformation. Kinematic axes from strike-slip fault populations near Canal Jeronimo, Seno Otway, Estuarios Wickham and Silva Palma are subparallel. Shortening axes plunge generally northeast and southwest; extension axes plunge generally northwest and southeast (Figures 13a-c).

Two populations of strike-slip faults occur near Cabo Froward and the Magallanes Straits. The dominant set (n=105) is subparallel to strike-slip faults elsewhere in the study area. Right-lateral faults all strike northeast, and left-lateral faults strike east-northeast, forming a conjugate-style set, or northwest. Shortening axes from this population generally plunge shallowly east-northeast or west-southwest; extension axes generally plunge shallowly north-northwest and south-southeast (Figure 3.13e). The anomalous set of strike-slip faults (n=15) have opposite senses of shear for their orientations compared with the dominant population (Figure 3.13d). For this reason the kinematic axes from this population of faults is also opposite those of the dominant set. Where observed, strike-slip faults from the dominant set always crosscut strike-slip faults of the anomalous set, indicating that the anomalous set probably reflects an earlier phase of strike-slip deformation than the dominant set. Thus the two sets of strike-slip faults are discussed separately.

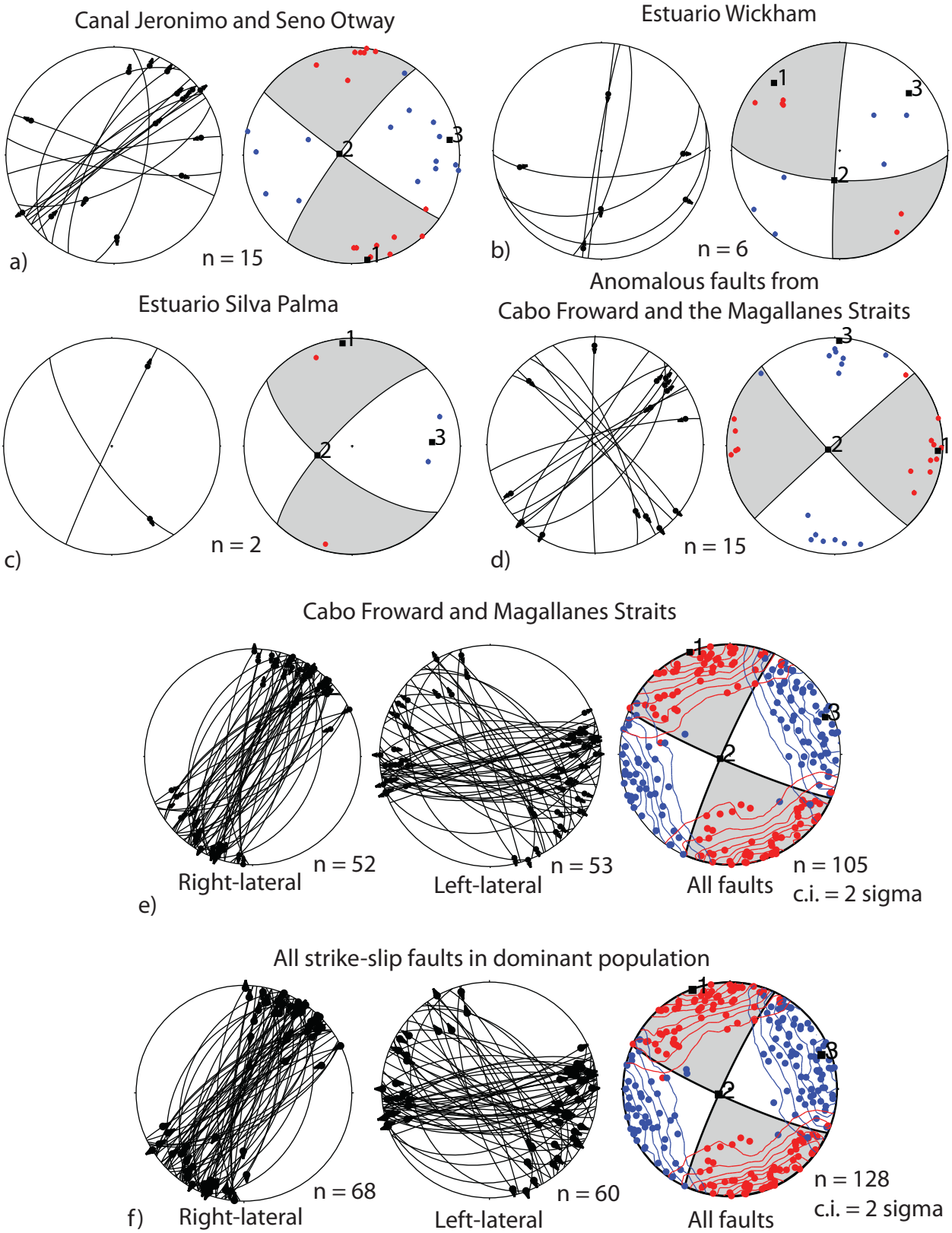
Canal Jeronimo and Seno Otway
a)
n = 15
Estuario Wickham
b)
n = 6
Estuario Silva Palma
c)
n = 2
Anomalous faults from
Cabo Froward and the Magallanes Straits
d)
n = 15
Cabo Froward and Magallanes Straits
Right-lateral
n = 52
Left-lateral
n = 53
All faults
n = 105
c.i. = 2 sigma
e)
All strike-slip faults in dominant population
f)
Right-lateral
n = 68
Left-lateral
n = 60
All faults
n = 128
c.i. = 2 sigma

Figure 3.13

Figure 3.13. Stereographic projections showing attitudes of faults and striae (left) and kinematic axes (right) from all strike-slip faults near (a) Canal Jeronimo and Seno Otway, (b) Estuario Wickham, (c) Estuario Silva Palma, (d) Cabo Froward and the Magallanes Straits, (e) all anomalous strike-slip faults and (f) all strike-slip faults from the dominant population in the study area.

The attitudes of faults and striae, as well as the orientations of kinematic axes, from the dominant set of faults near Cabo Froward and the Magallanes Straits (*i.e.* Figure 3.13e) are generally parallel to those elsewhere in the study area (Figure 3.13f). The total population of strike-slip faults in the study area (n=128, excluding the anomalous set) is internally kinematically homogeneous based on the subparallelism of shallowly plunging kinematic axes that form statistically distinct point maxima defined by north-northwest-trending extension axes and east-northeast-trending shortening axes (Figure 3.13f). The plunge and trend of the mean principal strain axes calculated by the linked Bingham method are 1) extension = 01°, 339°; 2) intermediate = 81°, 244°; and 3) shortening = 09°, 070° (Figure 3.13f).

Right- and left-lateral strike-slip faults from the dominant population form a conjugate set such that right-lateral faults have a mean strike of 030° and left-lateral faults have a mean strike of 085°. A small sub-population of left-lateral faults strikes toward 300° (Figure 3.14a). The orientations and sense of slip of the dominant faults are sympathetic with the predicted attitudes and shear senses expected for a population of faults that form Riedel shears. Northeast-striking right-lateral faults form R'-shears and east-northeast striking left lateral faults form R-shears. The small set of northwest-striking left-lateral faults has an orientation consistent with P-shears (Figure 3.14a). Tensile calcite veins associated with strike-slip faults exposed along the Magallanes Straits trend dominantly northeast and have a mean strike of 043° (Figure 3.14b) that is subparallel to the expected orientation of T-shears. The orientations of R-, R'-, P- and T-shears in the study are compatible with a principal fault plane that strikes west-northwest (~280°) and has a left-lateral sense of slip. The predicted principal fault zone is strikingly parallel to the trend of the Magallanes-Fagnano fault system (~275° near Tierra del Fuego and ~300° in the Magallanes Straits, Figure 3.1), thus strongly suggesting a genetic relationship between strike-slip faulting in the study area and the development of the Magallanes-Fagnano fault system.

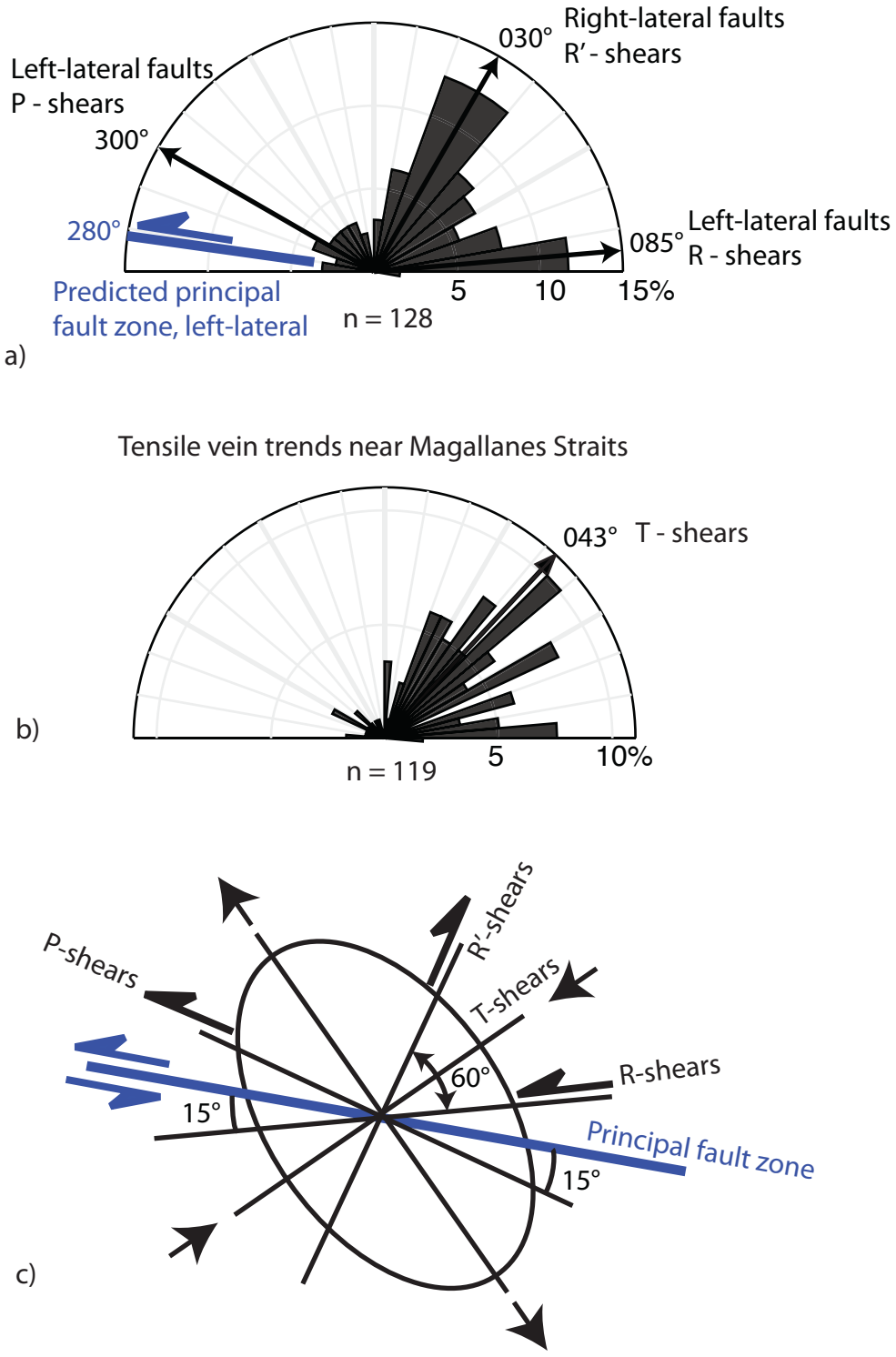

Figure 3.14. Kinematic synthesis of the dominant set of strike-slip faults, (a) rose diagram showing strikes of the dominant sets of right- and left-lateral faults in the study area, thick blue line shows trend of predicted principle fault zone based on Riedel shear geometry, (b) rose diagram showing trends of tensile veins in the study area, (c) diagram synthesizing trends of right- and left-lateral faults as well as tensile veins according to Riedel shear theory, ellipse is a schematic strain ellipse and thick black arrows show expected shortening and extension directions.

5.3 NORMAL FAULTS

Normal faults in the study area were only observed near Estuario Silva Palma or along the Magallanes Straits (Figure 3.15a-b). In both locations they occupy three common orientations that strike west, northeast or northwest. Normal faults commonly dip steeply (~60°) and form conjugate-style sets that contain steeply plunging to oblique striae on the fault surfaces (Figure 3.15a-c). Kinematic axes from all normal faults in the study area form moderately defined point maxima such that shortening axes are subvertical, and extension axes are subhorizontal and north- or south-plunging. The plunge and trend of principal kinematic axes of normal faults calculated by the linked Bingham method are 1) extension = 3°, 183°; 2) intermediate = 2°, 093°; and 3) shortening = 86°, 332° (Figure 3.15c).

5.4 RELATIVE TIMING OF NORMAL, STRIKE-SLIP AND THRUST FAULTS

Minor normal faults were only observed in close proximity to strike-slip faults. In many cases oblique-slip normal faults have the same strike-slip component of shear as parallel sets strike-slip faults discussed above. For example, east of Cabo Froward, the northwest-striking set of normal faults has a component of left-lateral slip, consistent with northwest-striking strike-slip faults from the same location (*i.e.* Figures 3.8b, 3.11b). Similarly, northeast-striking normal faults in this locality have a component of right-lateral slip, consistent with the set of right-lateral faults that also strike northeast (*i.e.* Figures 3.8b, 3.11b). Extension axes for normal fault populations plunge northward and southward and are subparallel, similar to the north-northwest and south-southeast plunges of those from the dominant set of strike-slip faults in the study area (Figure 3.15d) and indicating a degree of kinematic compatibility between strike-slip and normal fault sets. On this basis it is interpreted that strike slip and normal faults are kinematically related and reflect a phase of bulk transtensional strain (*c.f.* Klepeis, 1994; Lodolo *et al.*, 2003; Menichetti *et al.*, 2008).

Although the orientation of shortening axes from strike-slip faults is subparallel to that of thrust faults (Figure 3.15d), the extension axes are perpendicular. Also, cross-

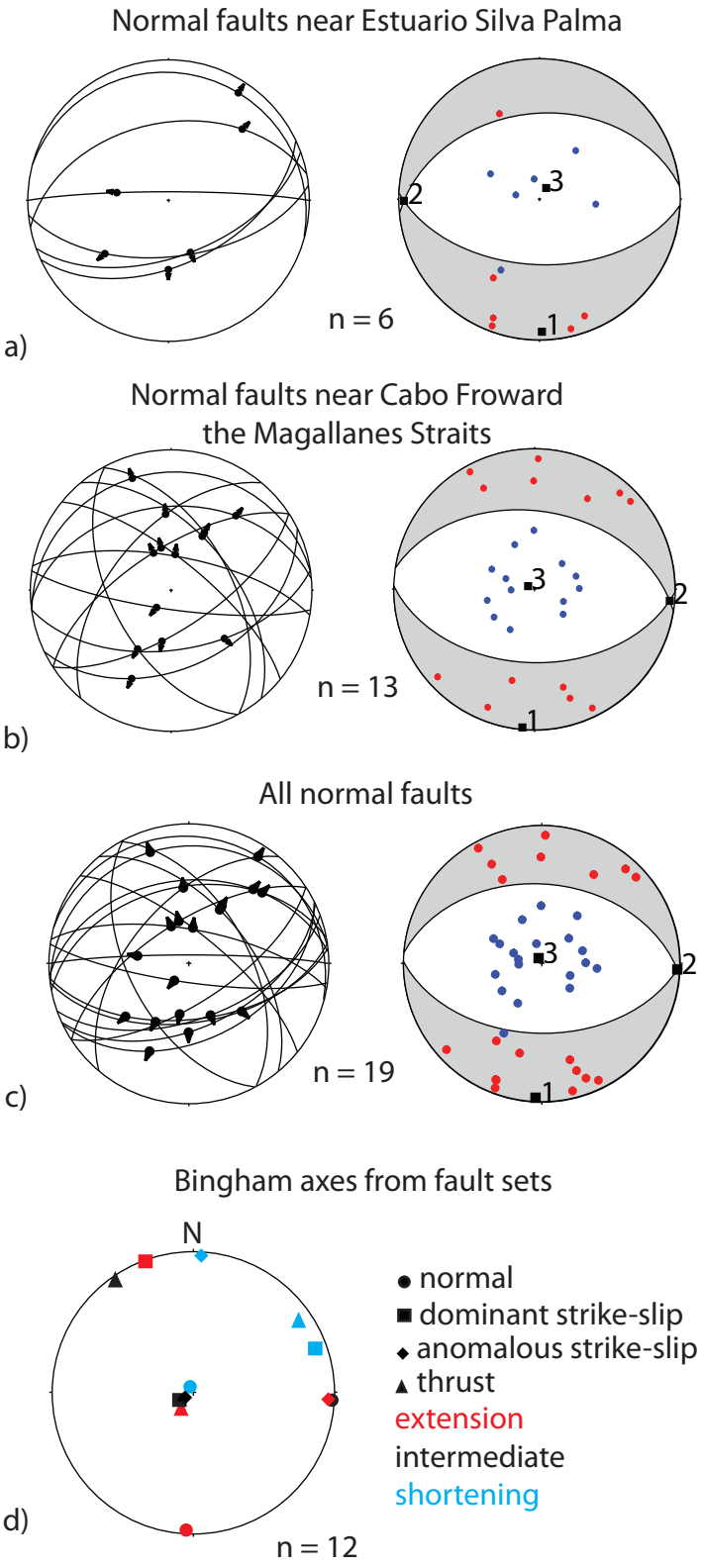
Normal faults near Estuario Silva Palma
2
3
1
n = 6
a)
Normal faults near Cabo Froward
the Magallanes Straits
3
2
1
n = 13
b)
All normal faults
3
2
1
n = 19
c)
Bingham axes from fault sets
N
normal
dominant strike-slip
anomalous strike-slip
thrust
extension
intermediate
shortening
d)
n = 12

Figure 3.15

Figure 3.15. Stereographic projections showing attitudes of faults and striae (left) and kinematic axes (right) from all normal faults near (a) Estuario Silva Palma, (b) Cabo Froward and the Magallanes Straits, (c) all normal faults in the study area, and (d) equal area stereographic projection of linked Bingham axes calculated for the total normal fault population (solid circles), the total population of dominant strike-slip faults (solid squares), the population of anomalous strike-slip faults (solid diamonds), and the total population of thrust faults (solid triangles) in the study area. Red indicates principal extension axes, black indicates intermediate axes and blue indicates principal shortening axes.

cutting relationships clearly indicate that strike-slip faulting everywhere overprints F_1 folds and thrusts from the Magallanes fold-thrust belt (*i.e.* Figure 3.9a, c). Consistent with this observation, the deformation conditions for strike-slip and normal faults were not the same as those for thrust faults. Many thrust faults in the study are defined by subsolidus quartz and feldspar foliations and recrystallized quartz stretching lineations (*e.g.* Bahía Fortesque, Figure 3.6b; Chapter 1, 2), indicating deformation temperatures >300°C (see Chapter 2). In contrast, all strike-slip and normal faults observed are brittle shear fractures indicating that they formed under much cooler deformation conditions and probably shallower levels of the crust, thus requiring substantial exhumation of the thrust belt to have occurred prior to the onset of strike-slip deformation. On the basis of crosscutting relationships and deformation conditions for each set of faults, it is deduced that strike-slip- and normal- faulting probably initiated during the Oligocene after the main pulse of Late-Cretaceous to Eocene contractional deformation ceased (*c.f.* Klepeis, 1994; Klepeis and Austin, 1997; Torres Carbonell *et al.*, 2008) and significant exhumation of the fold-thrust belt occurred (Fosdick *et al.*, 2013).

The small population (n=15, Figure 3.10) of anomalous strike-slip faults exposed near the Magallanes Straits is not kinematically compatible with any other fault set in the study area. The kinematic axes from these faults reflect north-south shortening and east-west extension (Figure 3.15d). Bingham analysis indicates that the intermediate principal strain axes of both sets of strike slip faults are subparallel however, the shortening and extension axes of the anomalous set occur ~65° CCW from those of the dominant set (Figure 3.15d). It is possible that the anomalous set of strike-slip faults reflects the earliest motions of sinistral strike-slip deformation associated with the Magallanes-Fagnano fault system and records north-trending shortening and east-trending extension that occurred in a restraining bend that developed near the northwest-striking segment of the Magallanes-Fagnano fault zone near Bahía del Indio. This interpretation is supported by the observation that northeast-vergent inclined folds of bedding that are common in the fold-thrust belt (*i.e.* Chapter 1) are tighter and occur in more upright orientations near the map trace of strike-slip faults at Bahía del Indio (Chapter 1 Figure 1.15, 1.16a, g-j).

Furthermore, the dominant set of strike-slip faults that is kinematically compatible with normal faults always crosscuts the anomalous set, indicating that transtensional deformation is younger. This interpretation is favored because it does not require complicating regional tectonic interpretations based on a relatively small population of minor faults.

6. Discussion

6.1 Spatial distribution of strike-slip and normal faults, implications for extent of the Magallanes fault system

Strike-slip deformation is heterogeneously distributed throughout the study area. The highest density of strike-slip faults occurs along the Magallanes Straits, probably because of their close proximity to the of the Magallanes-Fagnano fault system (*e.g.* Figure 3.8). Winslow (1982) used areal photos to identify several young (Holocene?) fault scarps that she interpreted as left-lateral splays from the Magallanes fault system. One splay transects Isla Dawson and trends northwest toward Peninsula Brunswick (Figure 3.16). A second fault scarp truncates stream meanders of the Río San Juan, located on Peninsula Brunswick north of the study area (Figure 3.16). New data presented in this study discerns a high-density of minor strike-slip faults near Bahía del Indio and Bahía Aguila that are kinematically compatible with a left-lateral, west-northwest striking principal fault zone. Bahía del Indio is exactly on strike from the trace of the fault splay on Isla Dawson interpreted by Winslow (1982), and thus minor faults in the area are interpreted to be associated with as the same structure (Figure 3.16).

Subsurface seismic data collected along the north-trending segment of the Magallanes Straits between Isla Dawson and Peninsula Brunswick (Figure 3.1) confirm the occurrence of a steeply southwest-dipping fault plane along strike from Bahía del Indio and the map trace of a the fault picked by Winslow (1982) (Klepeis and Austin, 1997; Lodolo *et al.*, 2003). Lodolo *et al.* (2003) interpret a component of normal down-to-the-southwest displacement in addition to left-lateral shear based on growth strata that

fill a small graben in the hanging wall of the fault (Figure 3.15 of Lodolo *et al*., 2003). Similarly, Klepeis and Austin (1997) interpret normal-sense offset of bright reflectors between 1 and 5 second TWT. However, the data are not migrated because of problems with seafloor reverberation and sidewall echoes making the actual position of the reflectors somewhat ambiguous (Figure 6 of Klepeis and Austin, 1997). These seismic interpretations conflict with field mapping along the shore of Peninsula Brunswick near Bahía del Indio. Here, the stratigraphic separation across the fault requires a substantial reverse component of motion on a southwest-dipping fault that I interpret to be a thick-skinned second-generation basement uplift with ~3 km of throw (see Chapter 1). A possible explanation for the apparently conflicting interpretations lies in knowing the age of the reflectors that are interpreted by Lodolo *et al*. (2003) and Klepeis and Austin (1997). The former authors had interpretable seismic resolution to 1 second TWT, and the sediment water interface is located at 0.8 second TWT, suggesting that the growth strata in the fault graben are probably very young (Quaternary?, Lodolo *et al*., 2003). On the basis of field mapping along the shore of Peninsula Brunswick that requires a substantial component of reverse motion on the fault (~3 km of throw), my interpretation is that a high-angle Cretaceous reverse fault was reactivated by left-normal slip described by Klepeis and Austin (1997) and Lodolo *et al*. (2003). This interpretation is consistent with field observations from this study that indicate strike-slip faults consistently crosscut contractional structures of the Magallanes fold-thrust belt as well as recent seismicity (Pelayo and Wiens, 1989) and geodetic data (Smalley *et al*., 2003) that indicate left-lateral deformation is presently active.

The map trace of the reverse fault near Bahía del Indio is inferred to continue for ~100 km toward the northwest, where it crops out again at Seno Otway (Figure 3.16). Here, strike-slip deformation is localized in the eastern part of the map area (*i.e*. Figure 3.4) near Seno Otway and Estuario Wickham. Faults from these locations are kinematically compatible with the population of Riedel shears that form under bulk left lateral shear (*i.e*. Figure 3.14). For this reason, it is inferred that minor strike-slip faults that occur near Seno Otway and Estuario Wickham are Riedel shears associated with left-

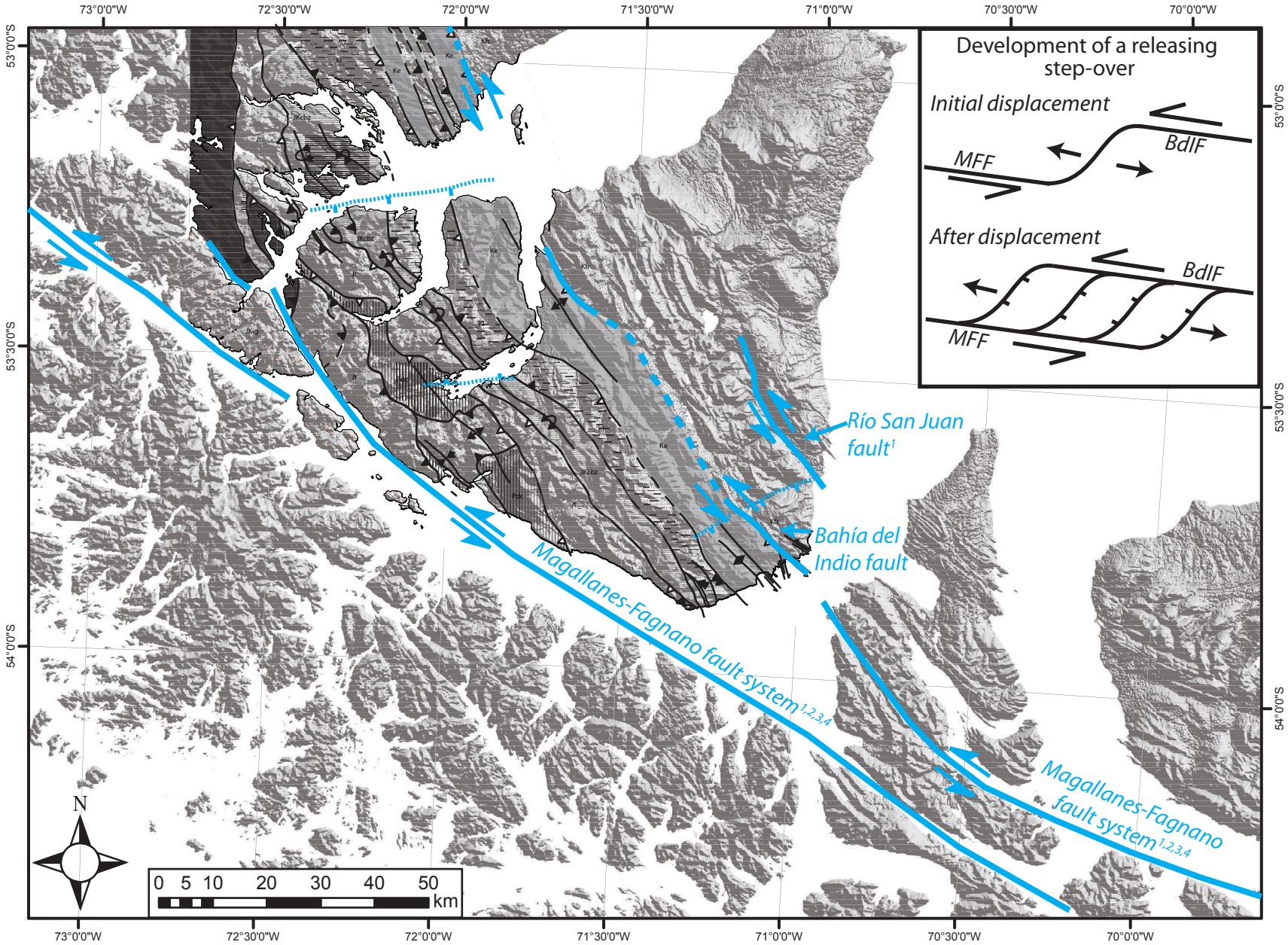
73°0'0"W
72°30'0"W
72°0'0"W
71°30'0"W
71°0'0"W
70°30'0"W
70°0'0"W
53°0'0"S
53°30'0"S
54°0'0"S
Development of a releasing step-over
Initial displacement
MFF
BdlF
After displacement
BdlF
MFF
Río San Juan fault[1]
Bahía del Indio fault
Magallanes-Fagnano fault system[1,2,3,4]
Magallanes-Fagnano fault system[1,2,3,4]
N
0 5 10 20 30 40 50
km

Figure 3.16

Figure 3.16. Shaded relief image showing trace of the newly mapped Bahía del Indio fault and correlation with splay of the Magallanes-Fagnano fault system as mapped by 1, Winslow (1982); 2, Klepeis (1994); 3, Klepeis and Austin (1997) and 4, Lodolo *et al*. (2003). Thin dashed lines show traces of normal faults inferred from the shaded relief image or from apparent changes in the depth of exposure that are observed in the field (see Chapter 1). The geologic map of Peninsula Brunswick (see Chapter 1) is shown to demonstrate the superposition of strike-slip deformation along the trend of the Cretaceous-Paleogene fold-thrust belt. Inset, schematic showing the development of a releasing step-over, modified after Twiss and Moores (2007). MFF, Magallanes-Fagnano fault; BdIF, Bahía del Indio fault.

lateral slip along the Bahía del Indio fault, suggesting that left-lateral deformation persists northwestward across Peninsula Brunswick along the Bahía del Indio fault for ~100 km farther than previously mapped. On the basis of the much lower density of strike-slip deformation near Seno Otway than the Magallanes Straits, I infer that the fault probably loses its strike-slip component of displacement toward the northwest (Figure 3.16). Strike-slip faults also occur in Seno Condor northwest of Canal Jeronimo. Here, I interpret them to reflect a left-lateral splay fault from the Magallanes-Fagnano fault system toward the south that probably formed along the boundary between the Patagonian Batholith and mafic rocks of the Rocas Verdes basin, which may have localized strain (Figure 3.4a, 3.16).

Figure 3.16 shows map traces of three east-northeast- or northeast-striking faults that are inferred from lineaments in the DEM or from changes in the depth of exposure across a fiord (i.e. Canal Jeronimo, see Chapter 1). The faults are inferred to have normal-sense displacements based on their orientation relative to the Magallanes-Fagnano fault system, the strikes of minor normal faults presented in this study (Figure 3.15) and the strikes of regional normal faults interpreted by Diraison *et al*. (1997) and shown in Figure 3.1. Northeast-striking normal faults are located between overlapping strands of the Magallanes-Fagnano fault and the Bahía del Indio fault and strike ~45° counterclockwise to the strike-slip faults, thus occupying the expected orientation for a system of normal faults that formed between two strands of a left-stepping left lateral fault system (Figure 3.16, see inset). On this basis, it is concluded that the Magallanes-Fagnano fault segment in the Magallanes straits south of Peninsula Brunswick and the newly mapped Bahía del Indio fault strand form a left-stepping, left-lateral fault segment from Isla Dawson to Seno Otway. Thus the study area on Peninsula Brunswick occurs in releasing zone of the Magallanes-Fagnano fault system. This interpretation is consistent with fault kinematic results from strike-slip and normal fault sets in the study area near Estuario Silva Palma, Cabo Froward and the Magallanes Straits that are apparently coeval and record left-lateral shear along a northwest striking fault system and north-south extension (Figures 3.6, 3.8, 3.11, 3.15d, 3.16). Left-stepping releasing segments of

the Magallanes-Fagnano fault system are well documented near Mt. Hope and Lago Fagnano and Isla Dawson (Klepeis and Austin, 1997; Lodolo *et al*., 2003; Menichetti *et al*., 2008), and near Isla Desolación along the Pacific margin of Chile (Lodolo *et al*., 2003), indicating that transtensional deformation occurred in many places along the Magallanes-Fagnano fault system.

6.2 TIMING OF TRANSTENSION

Although the absolute timing of the onset of strike-slip deformation in the southernmost Andes is not well constrained, most authors agree that sinistral transtension has occurred dominantly since Oligocene time (*e.g*. Klepeis, 1994; Lodolo *et al*., 2003; Menichetti *et al*., 2008) and probably shares a genetic relationship with the opening of the Drake Passage and development of the Scotia Plate (*e.g*. Barker, 2001; Geletti *et al*., 2005; Lodolo *et al*., 2006). Crosscutting relationships presented in this paper are consistent with those reported by many authors (*e.g*. Klepeis *et al*., 1994; Klepeis and Austin, 1997; Lodolo *et al*., 2003; Menichetti *et al*., 2008; Torres Carbonell, 2008) that indicate strike-slip deformation overprints the Late-Cretaceous to Eocene retroarc fold-thrust belt. Time-constrained balanced cross sections of the Fuegian retroarc thrust belt indicate that the last pulse of thrusting occurred during the Late Oligocene or Early Miocene (Torres Carbonell *et al*., 2011). This author reports that contractional structures of the Fuegian fold and thrust belt are offset by ~48km of sinistral displacement across the Magallanes-Fagnano fault system, indicating a maximum Miocene age for the development of the fault system based on the age of offset strata. The magnitude of offset and crosscutting relationships that indicate a Miocene age for the onset of strike-slip deformation are consistent with an extrapolation of the present slip-rate (~6.6 mm/yr after Smalley *et al*., 2003) combined with the obtained offset to ~7 Ma. (Torres Carbonell, 2008; *c.f*. Lodolo *et al*., 2003). A Miocene age for the onset of strike-slip deformation on Tierra del Fuego coincides with a widespread pulse of uplift and exhumation of the Patagonian fold-thrust belt near Ultima Esperanza (Fosdick *et al*., 2013) and the emergence of the North Scotia Ridge and Tierra del Fuego (Barker, 2001; Eagles, 2005;

Lagabrielle *et al*., 2009), suggesting a regional response to changes in the tectonic setting of the Scotia Arc during the opening of the Drake Passage and development of the West Scotia Sea (*c.f.* Dalziel *et al*., 2013).

7. Conclusions

Fault slip data collected over a ~100 km^2 of the Magallanes retroarc fold thrust belt near Peninsula Brunswick and Seno Otway fall into four well defined populations: 1) thrust faults strike northwest and have subhorizontal, northeast-trending shortening axes; 2) a dominant set strike-slip faults form a conjugate set that consists of northeast-striking right-lateral faults and east-northeast left-lateral faults as well as less common northwest-striking left-lateral faults; 3) normal faults for a population that strike east to east-northeast and northwest and have subhorizontal north- or south-plunging extension axes; 4) an anomalous set of strike-slip faults consisting of northeast-striking left-lateral faults and northwest-striking right lateral faults that is crosscut by the dominant set.

Strike-slip faults form Riedel, T- and P-shear geometries and have subhorizontal east-northeast trending shortening axes, kinematically compatible with the west-northwest-trending map trace of the sinistral Magallanes-Fagnano fault system. A population of oblique-slip normal faults is kinematically compatible with strike-slip faults of the dominant set and together both fault sets reflect regional bulk transtension. An older, subsidiary set of left- and right-lateral strike-slip faults is crosscut by the dominant set and has horizontal shortening axes that trend northward. The subsidiary set is interpreted to reflect the earliest stages strike-slip motion and to reflect north-trending shortening in a restraining bend.

A newly mapped left-lateral fault segment named the Bahía del Indio fault strikes northwest for ~100 km across Peninsula Brunswick between the Magallanes Straits and Seno Otway. The map trace of this fault is continuous with a prominent lineament that appears in areal photographs and satellite imagery to transect Isla Dawson (Winslow,

1982) and a left-normal fault that appears in reflection seismic data below the Magallanes Straits (Klepeis and Austin, 1997; Lodolo *et al*., 2003), indicating that the Bahía del Indio fault is part of the Magallanes-Fagnano fault system. The southwestern end of Peninsula Brunswick occurs in a left-lateral, left-stepping releasing zone between the Bahía del Indio fault and the Magallanes-Fagnano fault trace in the northwestern trending segment of the Magallanes Straits.

Strike-slip and normal faults crosscut thrust faults and contractional folds of the Magallanes retroarc fold-thrust belt everywhere they were observed, indicating that the onset of strike-slip deformation on Peninsula Brunswick postdates the Late-Cretaceous – Eocene fold-thrust belt. Crosscutting relationships and fault kinematic data from Peninsula Brunswick support a growing body of literature that place the Magallanes-Fagnano fault system in a tectonic framework defined regional sinistral transtension that occurred in response to the opening of the Western Scotia Sea and the Drake Passage during the Early Miocene.

APPENDIX A: UTM COORDINATES OF DATA STATIONS, WGS84

Station No.	Zone (S)	Easting	Northing	Station No.	Zone (S)	Easting	Northing	Station No.	Zone (S)	Easting	Northing
900	19	372308	4057416	**938**	18	668548	4081800	**975**	18	671664	4101772
901	19	326083	4034414	**939**	18	668333	4082804	**976**	18	671928	4101105
902	19	303028	4045636	**940**	18	669741	4082787	**977**	18	671532	4100027
903	19	302377	4047274	**941**	18	670390	4082997	**978**	18	672172	4099054
904	18	697954	4047685	**942**	18	670972	4083763	**979**	18	675821	4097744
905	18	656996	4085314	**943**	18	670504	4084895	**980**	18	676280	4097738
906	18	657174	4085231	**944**	18	670108	4085660	**981**	18	676866	4098326
907	18	657569	4084581	**945**	18	670233	4086451	**982**	18	677813	4098389
908	18	657676	4084470	**946**	18	670538	4087812	**983**	18	678155	4098706
909	18	657927	4083601	**947**	18	670357	4088589	**984**	18	678791	4099095
910	18	657837	4082623	**948**	18	670984	4088954	**986**	18	685395	4101220
911	18	656746	4084009	**949**	18	671951	4089550	**987**	18	685828	4102029
912	18	658134	4082415	**950**	18	672088	4089818	**989**	18	686718	4102466
913	18	658380	4081967	**951**	18	664591	4090309	**990**	18	686349	4102895
914	18	658069	4082262	**952**	18	664169	4089645	**991**	18	673963	4117151
915	18	658955	4082788	**953**	18	664442	4088338	**992**	18	674533	4118182
916	18	660386	4082545	**954**	18	665000	4089452	**994**	18	674960	4118573
917	18	661703	4082336	**955**	18	667474	4090468	**995**	18	676272	4118017
918	18	662925	4082894	**956**	18	668065	4090448	**996**	18	676546	4116824
919	18	663131	4082889	**957**	18	669242	4091126	**997**	18	677737	4116891
920	18	663794	4083110	**958**	18	668601	4090941	**998**	18	700321	4110547
921	18	663912	4083248		18	668831	4091063	**999**	18	700332	4110318
923	18	665743	4084724	**959**	18	669586	4091698	**9100**	18	700415	4110229
924	18	680054	4096138	**960**	18	669896	4092799	**9101**	18	699474	4109661
925	18	679631	4096119	**961**	18	670152	4093235	**9102**	18	699190	4108963
926	18	679440	4095635	**962**	18	670417	4093961	**9103**	18	699097	4108887
927	18	677495	4094209	**963**	18	670675	4094123		18	700007	4109860
929	18	676663	4093676	**964**	18	670887	4094363	**9104**	18	692455	4107656
930	18	675544	4093038	**966**	18	671054	4094630	**9105**	18	693739	4107377
931	18	674206	4091890	**968**	18	671990	4095881	**9106**	18	694037	4107375
932	18	673373	4091605	**969**	18	669601	4100591	**9107**	18	695100	4107972
933	18	673462	4091716	**970**	18	670562	4100918	**9108**	18	694543	4107890
934	18	673219	4091480	**971**	18	669319	4102143	**9109**	18	695876	4107850
935	18	673024	4091266	**972**	18	669421	4102689	**9110**	18	696617	4108478
936	18	672707	4090987	**973**	18	670245	4102911	**9112**	18	697363	4108474
937	18	667877	4081190	**974**	18	671582	4101853	**9113**	18	694763	4108137

Station No.	Zone (S)	Easting	Northing	Station No.	Zone (S)	Easting	Northing	Station No.	Zone (S)	Easting	Northing
9114	18	693041	4107728	**10009**	19	386850	3948659	**10178**	19	355242	4028200
9115a	18	695393	4107951	**10010**	19	387464	3951021	**10179**	19	355313	4028242
9115b	18	695457	4107949	**10011**	19	387387	3951868	**10180**	19	355288	4028235
9115c	18	695823	4107833	**10012**	19	388010	3953160	**10181**	19	355322	4028250
9115d	18	695883	4107872	**10013**	19	395570	3948669	**10182**	19	355375	4028280
9115e	18	695964	4107857	**10014**	19	394275	3949556	**10183**	19	355411	4028308
9115f	18	696030	4107857	**10015**	19	392193	3951255	**10184**	19	355456	4028328
9115g	18	696245	4107831	**10016**	19	391549	3951878	**10185**	19	355501	4028358
9116	18	696466	4108634	**10017**	19	391521	3956206	**10186**	19	355561	4028392
9118	18	696936	4108270	**10018**	19	390067	3956519	**10187**	19	355618	4028426
9119	18	691981	4095727	**10019**	19	390599	3957604	**10188**	19	355685	4028468
9121	18	692163	4094962	**10020**	19	392300	3962413	**10189**	19	348438	4025923
9124	18	692053	4094214	**10021**	19	393446	3965551	**10190**	19	347890	4026704
9125	18	692420	4093453	**10022**	19	395599	3968177	**10191**	19	347368	4027102
9126	18	692233	4092640	**10023**	19	392446	3958501	**10192**	19	347324	4027057
9127	18	692073	4092331	**10024**	19	406529	3970064	**10193**	19	347286	4027050
9129	18	692929	4090132	**10025**	19	406463	3969948	**10194**	19	347271	4026896
9131	18	693227	4087365	**10Pb001**	19	354251	4027968	**10195**	19	348355	4026318
9134	18	693278	4083915	**10PB002**	19	354437	4027910	**10196**	19	354091	4027930
9136	18	692135	4081784	**10155**	19	354458	4027917	**10197**	19	354052	4027904
9138	18	692113	4081341	**10156**	19	354504	4027929	**10198**	19	354026	4027878
9140	18	689364	4078791	**10157**	19	354549	4027938	**10199**	19	353989	4027842
9142	18	688745	4077900	**10158**	19	354564	4027937	**10200**	19	353958	4027818
9143	18	688066	4077326	**10159**	19	354483	4027923	**10201**	19	353848	4027720
9145	18	686699	4076990	**10160**	19	354626	4027933	**10202**	19	353808	4027689
9147	18	685075	4075952	**10161**	19	354663	4027951	**10203**	19	353766	4027620
9148	18	683617	4075812	**10162**	19	354683	4027980	**10204**	19	349260	4025632
9149	18	681552	4076471	**10163**	19	354715	4027985	**10205**	19	349345	4025647
	18	680339	4076408	**10164**	19	354780	4028005	**10206**	19	349388	4025660
9151	18	679787	4076573	**10165**	19	354815	4028029	**10207**	19	349431	4025706
9152	18	679681	4076542	**10166**	19	354845	4028047	**10208**	19	350180	4026119
9153	18	679917	4077242	**10168**	19	354898	4028070	**10209**	19	350228	4026122
9154	18	680707	4076732	**10169**	19	354920	4028092	**10210**	19	350261	4026124
10001	19	363516	4033446	**10170**	19	354928	4028092	**10211**	19	350323	4026131
10002	19	363510	4033698	**10171**	19	354953	4028102	**10212**	19	350338	4026141
10003	19	385961	3945185	**10172**	19	354963	4028109	**10213**	19	350401	4026145
10004	19	386162	3945740	**10173**	19	355000	4028142	**10214**	19	350460	4026159
10005	19	386268	3946169	**10174**	19	355046	4028148	**10215**	19	350503	4026124
10006	19	386369	3946698	**10175**	19	355062	4028152	**10216**	19	350661	4026147
10007	19	386597	3947602	**10176**	19	355086	4028159	**10217**	19	350736	4026168
10008	19	386753	3947834	**10177**	19	355134	4028183	**10218**	19	350787	4026196

Station No.	Zone (S)	Easting	Northing	Station No.	Zone (S)	Easting	Northing	Station No.	Zone (S)	Easting	Northing
10219	19	350840	4026201	**10260**	19	350036	4028282	**10301**	19	363674	4033930
10220	19	350886	4026219	**10261**	19	350118	4028285	**10302**	19	363751	4033950
10221	19	351012	4026284	**10262**	19	350369	4028391	**10303**	19	363698	4034017
10222	19	351056	4026288	**10263**	19	350966	4028552	**10304**	19	363634	4034104
10223	19	351108	4026299	**10264**	19	351232	4028399	**10305**	19	363551	4034242
10224	19	351201	4026334	**10265**	19	351473	4028479	**10306**	19	363484	4034317
10225	19	351286	4026370	**10266**	19	351734	4028551	**10307**	19	363963	4034319
10226	19	351707	4026362	**10267**	19	352260	4028900	**10308**	19	363934	4034410
10227	19	352108	4026426	**10268**	19	353002	4028804	**10309**	19	363876	4034448
10228	19	352181	4026385	**10269**	19	353410	4028745	**10310**	19	363937	4034600
10229	19	352228	4026400	**10270**	19	358258	4030158	**10311**	19	363886	4034936
10230	19	352271	4026397	**10271**	19	358365	4030208	**10312**	19	364772	4034962
10231	19	352295	4026452	**10272**	19	358453	4030255	**10313**	19	364688	4035047
10232	19	352356	4026452	**10273**	19	358537	4030302	**10314**	19	364441	4035022
10233	19	352448	4026456	**10274**	19	358603	4030332	**10315**	19	364390	4035141
10234	19	352692	4026534	**10275**	19	358654	4030366	**10316**	19	364591	4035458
10235	19	352758	4026569	**10276**	19	358720	4030405	**10317**	19	364781	4035365
10236	19	352804	4026603	**10277**	19	358865	4030500	**10318**	19	364892	4035410
10237	19	352853	4026620	**10278**	19	358983	4030557	**10319**	19	365063	4035447
10238	19	352878	4026624	**10279**	19	359057	4030602	**10320**	19	365128	4035496
10239	19	352911	4026637	**10280**	19	359509	4030838	**10321**	19	365137	4035578
10240	19	352951	4026640	**10281**	19	359535	4030869	**10322**	19	365244	4035673
10241	19	353025	4026666	**10282**	19	359710	4030893	**10323**	19	365449	4035703
10242	19	353046	4026680	**10283**	19	359945	4030890	**10324**	19	365523	4035629
10243	19	353080	4026693	**10284**	19	360009	4030903	**10325**	19	365578	4035560
10244	19	353121	4026715	**10285**	19	360049	4030932	**10326**	19	365661	4035949
10245	19	353158	4026759	**10286**	19	360141	4030983	**10327**	19	365697	4035900
10246	19	353194	4026777	**10287**	19	360185	4031037	**10328**	19	365676	4035907
10247	19	353215	4026795	**10288**	19	360272	4031118	**10329**	19	365653	4035854
10248	19	351653	4027144	**10289**	19	360362	4031148	**10330**	19	365646	4035802
10249	19	350896	4027083	**10290**	19	360544	4031145	**10331**	19	365612	4035734
10250	19	350785	4027106	**10291**	19	360623	4031248	**10332**	19	365626	4035679
10251	19	350718	4027136	**10292**	19	360644	4031333	**10333**	19	365561	4035986
10252	19	350530	4027084	**10293**	19	360519	4031803	**10334**	19	365313	4035719
10253	19	349819	4027113	**10294**	19	362788	4033360	**10335**	19	365177	4035667
10254	19	349725	4027211	**10295**	19	362951	4033245	**10336**	19	365135	4035614
10255	19	349472	4027514	**10296**	19	363302	4032992	**10337**	19	365130	4035574
10256	19	349547	4027618	**10297**	19	363347	4033001	**10338**	19	365122	4035557
10257	19	349577	4027653	**10298**	19	363536	4033287	**10339**	19	365087	4035451
10258	19	349856	4028076	**10299**	19	363511	4033527	**10340**	19	365091	4035471
10259	19	349955	4028227	**10300**	19	363550	4033884	**10341**	19	365695	4036222

Station No.	Zone (S)	Easting	Northing	Station No.	Zone (S)	Easting	Northing	Station No.	Zone (S)	Easting	Northing
10342	19	367847	4036609	**11005**	19	305203	4046846	**11046**	19	302643	4065210
10343	19	367729	4036578	**11006**	19	304934	4046804	**11047**	19	301931	4065369
10344	19	368141	4036678	**11007**	19	306286	4046875	**11048**	19	302118	4065504
10345	19	368101	4036600	**11008**	19	306486	4047250	**11049**	18	691992	4063088
10346	19	368213	4036844	**11009**	19	307093	4047156	**11050**	18	692755	4062827
10347	19	368240	4036923	**11010**	19	307102	4047080	**11051**	18	691519	4062172
10348	19	368162	4037170	**11011**	19	309105	4047105	**11052**	18	693963	4062644
10349	19	368239	4037175	**11012**	19	309279	4047933	**11053**	18	695947	4063496
10350	19	368808	4037381	**11013**	19	308627	4046845	**11054**	18	697659	4063438
10351	19	368859	4037486	**11014**	19	308360	4046501	**11055**	19	301909	4064025
10352	19	368811	4037618	**11015**	19	302368	4047304	**11056**	19	301639	4064528
10353	19	368744	4037792	**11016**	19	302206	4047377	**11057**	18	698248	4064421
10354	19	368657	4037858	**11017**	18	697877	4046749	**11058**	19	312072	4086598
10355	19	368576	4037930	**11018**	19	313230	4066166	**11059**	18	690698	4080169
10356	19	368582	4038176	**11019**	19	312265	4065994	**11060**	18	691379	4080464
10357	19	368379	4038406	**11020**	19	311938	4065723	**11061**	18	691595	4080522
10358	19	368339	4038485	**11021**	19	311666	4065603	**11062**	18	691967	4080779
10359	19	370149	4042704	**11022**	19	311324	4065293	**11063**	18	691995	4080859
10360	19	370257	4042229	**11023**	19	310730	4065140	**11064**	18	692112	4081337
10361	19	370217	4041905	**11024**	19	310595	4065125	**11065**	18	692081	4081753
10362	19	370105	4041856	**11025**	19	310112	4064869	**11066**	18	692147	4082157
10363	19	369856	4041335	**11026**	19	310153	4064295	**11067**	18	692985	4082596
10364	19	369736	4041038	**11027**	19	305274	4062758	**11068**	18	693183	4082833
10365	19	369592	4040831	**11028**	19	305358	4062918	**11069**	18	692647	4082726
10366	19	369475	4040546	**11029**	19	305716	4063211	**11070**	18	692723	4082877
10367	19	369523	4039735	**11030**	19	306337	4063624	**11071**	18	692727	4082986
10368	19	369941	4039083	**11031**	19	306551	4063211	**11072**	18	692789	4083085
10369	19	369933	4039002	**11032**	19	306547	4063245	**11073**	18	693259	4083814
10370	19	370001	4038780	**11033**	19	306995	4064080	**11074**	18	693126	4084575
10371	19	369913	4038624	**11034**	19	307338	4064114	**11075**	18	693074	4085516
10372	19	369598	4038594	**11035**	19	307596	4064426	**11076**	18	693203	4087421
10373	19	369348	4038569	**11036**	19	312138	4065838	**11077**	18	692691	4091148
10374	19	369346	4038494	**11037**	19	312265	4065932	**11078**	18	692748	4090842
10375	19	369264	4038439	**11038**	19	312194	4065882	**11079**	18	692913	4089523
10376	19	366582	4042172	**11039**	19	308442	4063355	**11080**	18	679578	4077752
10377	19	366718	4041600	**11040**	19	308615	4063890	**11081**	18	679505	4078351
10378	19	366762	4043000	**11041**	19	307884	4067828	**11082**	18	679715	4078947
11001	19	306037	4046033	**11042**	19	307477	4067198	**11083**	18	679068	4079469
11002	19	305912	4046055	**11043**	19	306679	4066420	**11084**	18	678811	4079602
11003	19	305870	4046036	**11044**	19	305573	4066488	**11085**	18	678706	4079655
11004	19	305569	4046697	**11045**	19	303131	4066096	**11086**	18	678268	4079626

Station No.	Zone (S)	Easting	Northing
11087	18	678204	4079585
11088	18	677733	4079715
11089	18	677425	4079839
11090	18	676985	4080108
11091	18	676806	4080470
11092	18	676529	4080543
11093	18	677286	4081123
11094	18	677522	4080753
11095	18	700372	4111017
11096	19	300409	4112331
11097	19	300535	4112605
11098	19	301417	4114913
11099	19	301490	4114859
11100	19	301446	4114857
11101	19	301689	4114986
11102	19	301825	4115349
11103	19	301738	4116195
11104	19	302669	4116844

APPENDIX B. FAULT KINEMATIC DATA FROM CHAPTER 3

Table of thrust fault kinematic data from Peninsula Brunswick									
Field No.	**Fault strike**	**Fault dip**	**Striae trend**	**Striae plunge**	**Sense of Slip**	**T trend**	**T plunge**	**P trend**	**P plunge**
902	155	32	215	28	TR	183	69	46	15
902	148	32	207	28	TR	174	69	39	15
921	170	41	193	19	TR	152	50	40	18
921	163	60	215	54	TR	115	68	238	13
921	154	53	196	42	TR	126	64	221	3
921	154	39	211	34	TR	162	71	45	9
921	145	44	214	42	TR	145	79	44	2
935	157	26	232	25	TR	219	70	57	20
935	142	9	225	9	TR	224	54	46	36
936	162	48	231	46	TR	141	79	242	2
936	137	49	242	48	TL	349	82	234	4
947	148	56	205	51	TR	106	71	224	9
947	140	57	226	57	TR	57	78	228	12
956	189	27	212	11	TR	185	50	52	29
956	184	22	215	12	TR	193	53	50	31
956	176	31	214	20	TR	181	58	52	21
956	161	63	215	58	TR	105	67	238	16
958	155	34	240	34	TR	230	79	62	11
961	174	37	236	34	TR	193	73	68	10
961	173	34	225	28	TR	187	67	60	15
961	172	37	226	31	TR	182	69	61	11
962	155	46	240	46	TR	132	87	243	1
975	171	57	216	47	TR	134	65	241	8
9100	117	30	200	30	TR	191	75	23	15
9102	352	67	36	59	TR	296	62	66	19
9102	9	68	39	51	TR	321	55	75	17
9103	100	18	237	12	TL	253	56	46	31
9114	112	31	260	18	TL	293	55	60	23
9115	152	26	240	26	TR	238	71	61	19
9115	145	12	256	11	TL	261	56	72	34
9115	140	12	235	12	TL	236	57	54	33
9121	322	28	10	22	TR	342	62	204	21
9126	354	11	15	4	TR	4	48	204	40

Field No.	Fault strike	Fault dip	Striae trend	Striae plunge	Sense of Slip	T trend	T plunge	P trend	P plunge
9126	88	32	199	30	TL	226	73	11	14
9140	178	35	252	34	TR	222	77	79	11
9140	172	18	255	18	TR	252	63	77	27
9140	161	16	249	16	TR	248	61	69	29
9140	142	26	248	25	TL	262	69	63	20
9145	173	45	290	42	TL	0	76	97	2
9145	173	43	290	40	TL	352	76	97	4
9148	162	51	245	51	TR	99	83	249	6
9149	160	56	200	44	TR	127	62	227	5
9155	168	48	200	30	TR	147	56	47	7
11014	170	60	255	60	TR	87	75	258	15
11014	167	54	264	54	TL	59	80	260	9
11017	153	22	245	22	TL	246	67	64	23
11017	150	23	210	20	TR	192	63	39	24
11017	150	30	230	30	TR	217	74	54	15
11022	170	35	235	32	TR	198	73	65	12
11022	165	42	217	35	TR	162	69	54	7
11025	325	85	45	85	TR	236	50	54	40
11025	165	17	216	13	TR	202	57	45	31
11025	110	12	222	11	TL	228	56	38	34
11025	100	24	220	21	TL	239	64	31	23
11030	160	35	240	35	TR	219	79	64	10
11032	125	50	235	48	TL	337	79	224	4
11032	80	10	240	3	TL	250	48	51	41
11037	135	52	245	50	TL	356	78	234	6
11038	0	6	50	5	NL	234	40	46	49
11040	121	27	200	27	TR	189	71	24	18
11046	111	23	245	17	TL	267	59	53	26
11046	110	20	245	14	TL	263	57	54	29
11056	135	12	240	12	TL	244	56	57	33
11056	130	12	249	11	TL	256	55	64	34
11062	124	17	229	16	TL	235	61	46	28
11062	120	14	228	13	TL	234	58	44	32
11065	210	10	254	7	TR	246	51	80	38
11065	130	40	250	36	TL	302	73	57	7
11071	310	24	45	24	TL	49	69	223	21
11073	280	26	30	25	TL	47	68	204	20

Field No.	Fault strike	Fault dip	Striae trend	Striae plunge	Sense of Slip	T trend	T plunge	P trend	P plunge
11086	160	42	230	40	TR	170	79	59	4
11087	160	58	240	58	TR	86	76	246	13
11088	148	74	225	74	TR	63	61	235	29
11105	165	29	217	24	TR	188	64	50	20
11105	160	50	235	49	TR	122	81	243	5
11105	140	50	225	50	TR	74	84	228	5
11106	150	36	185	23	TR	146	58	26	17
10pb001	321	51	70	49	TL	178	79	60	5
10pb166	157	25	232	24	TR	220	69	57	21
10pb183	165	59	228	56	TR	110	72	244	13
10pb187	165	41	234	39	TR	179	78	64	5
10pb205	202	30	259	26	TR	229	67	91	18
10pb205	191	28	255	26	TR	232	68	84	19
10pb205	180	32	271	32	TL	273	77	91	13
10pb206	186	36	235	29	TR	193	66	71	13
10pb232	200	37	290	37	TR	290	82	110	8
10pb243	322	40	48	40	TR	28	85	230	5
10pb243	305	34	42	34	TL	56	78	219	11

Table of strike-slip fault kinematic data from Peninsula Brunswick									
Field No.	Fault strike	Fault dip	Striae trend	Striae plunge	Sense of Slip	T trend	T plunge	P trend	P plunge
10pb342	80	87	80	6	NL	125	2	35	6
10pb355	73	85	75	26	NL	122	14	26	22
10pb368	72	85	73	16	NL	119	8	27	15
10pb368	89	57	107	25	NL	321	5	56	43
10pb373	304	90	304	11	NL	350	8	258	8
10pb373	255	72	255	0	NL	119	13	211	13
10pb373	93	75	267	21	TL	316	26	224	4
10pb316	270	64	270	1	NL	132	17	228	19
10pb316	81	78	84	16	NL	128	3	37	20
10pb321	79	71	256	9	TL	301	20	34	7
10pb332	79	59	256	4	TL	298	25	37	18
10pb332	86	59	89	5	NL	308	18	47	25
10pb332	87	68	265	6	TL	309	19	43	11
10pb332	76	64	80	8	NL	300	12	36	24

Field No.	Fault strike	Fault dip	Striae trend	Striae plunge	Sense of Slip	T trend	T plunge	P trend	P plunge
10pb332	260	75	77	13	TL	123	20	214	2
10pb332	65	86	65	7	NL	110	2	20	8
10pb340	165	74	167	6	NL	30	7	122	15
10pb294	80	65	250	20	TL	299	33	31	3
10pb299	330	80	143	33	TL	197	31	98	15
10pb304	265	78	81	20	TL	129	23	37	5
10pb309	310	74	319	29	NL	2	9	266	33
10pb274	84	79	90	27	NL	135	11	39	27
10pb282	250	90	250	0	NL	295	0	205	0
10pb210	152	75	154	7	NL	17	6	109	15
10pb210	120	86	300	5	TL	345	6	255	1
10pb214	316	47	344	27	NL	192	9	294	53
10pb216	323	72	125	43	TL	189	44	84	15
10pb217	164	90	344	6	TL	29	4	299	4
10pb220	95	56	265	15	TL	310	35	48	12
10pb223	331	83	331	0	NL	196	5	286	5
10pb226	100	67	274	14	TL	320	27	53	6
10pb227	105	82	109	27	NL	155	13	59	25
10pb236	118	54	122	5	NL	339	21	81	29
10pb236	120	67	130	22	NL	350	1	80	33
10pb236	338	70	143	35	TL	201	40	103	9
10pb237	287	55	293	9	NL	150	17	251	31
10pb237	302	62	101	34	TL	159	47	65	4
10pb238	160	30	160	0	NL	7	38	133	38
10pb238	90	70	108	40	NL	148	12	46	44
10pb239	114	81	116	13	NL	160	3	70	16
10pb256	325	86	328	35	NL	17	21	276	27
10pb192	82	88	82	6	NL	127	3	37	6
10pb194	85	86	263	26	TL	312	21	216	15
10pb207	260	72	75	14	TL	122	23	213	3
10pb204	71	33	251	0	TL	280	36	42	36
10pb199	117	70	289	20	TL	338	29	248	0
10pb202	90	71	96	18	NL	318	1	48	27
10pb001	321	51	115	28	TL	167	51	265	6
10pb002	134	84	135	11	NL	180	3	89	12
10pb002	111	85	112	9	NL	157	3	66	10
10pb163	260	85	78	24	TL	126	20	32	13

Field No.	Fault strike	Fault dip	Striae trend	Striae plunge	Sense of Slip	T trend	T plunge	P trend	P plunge
10pb163	131	51	139	10	NL	354	19	98	35
10pb187	79	86	82	34	NL	130	20	30	26
11078	75	15	120	11	NL	309	33	107	55
9119	88	70	259	24	TL	309	32	218	3
9127	65	46	92	25	NL	299	11	44	52
11041	145	75	152	25	NL	195	7	102	29
920	292	88	293	18	NL	339	11	246	14
11098	99	79	107	35	NL	152	16	52	33
10pb342	228	84	229	14	TR	183	14	274	6
10pb346	22	90	202	4	NR	157	3	247	3
10pb351	200	44	220	18	TR	177	47	69	17
10pb353	215	72	34	4	NR	171	10	78	15
10pb354	216	72	34	6	NR	171	9	79	17
10pb354	235	66	50	11	NR	189	9	95	25
10pb356	195	80	197	11	TR	151	15	241	1
10pb367	182	70	1	3	NR	138	12	45	16
10pb370	25	80	203	9	NR	339	1	249	13
10pb374	20	70	24	10	TR	338	22	246	7
10pb375	35	70	35	0	TR	352	14	258	14
10pb375	20	90	200	2	NR	155	1	245	1
10pb378	28	86	29	9	TR	343	9	74	3
10pb313	20	39	34	11	TR	358	43	242	24
10pb314	61	70	70	24	TR	20	32	111	3
10pb315	227	79	44	15	NR	0	3	91	18
10pb315	202	86	11	70	NR	310	38	92	45
10pb315	199	87	199	3	TR	154	4	64	0
10pb315	33	85	34	9	TR	348	10	79	3
10pb315	10	81	11	5	TR	326	10	235	3
10pb316	215	85	216	11	TR	170	11	261	4
10pb316	30	52	199	14	NR	344	15	242	37
10pb316	45	82	46	4	TR	0	8	270	3
10pb317	195	88	15	14	NR	329	8	61	11
10pb318	217	80	35	9	NR	171	1	81	13
10pb324	185	82	3	12	NR	319	3	50	14
10pb327	43	63	43	1	TR	2	19	265	18
10pb332	30	62	31	2	TR	349	21	252	18
10pb332	22	61	22	0	TR	341	20	243	20

Field No.	Fault strike	Fault dip	Striae trend	Striae plunge	Sense of Slip	T trend	T plunge	P trend	P plunge
10pb332	45	65	45	0	TR	3	17	267	17
10pb332	64	85	64	0	TR	19	4	289	4
10pb340	30	79	209	3	NR	345	6	254	10
10pb294	235	67	239	9	TR	194	23	100	10
10pb304	200	90	200	1	TR	155	1	245	1
10pb310	12	65	188	9	NR	327	11	232	24
10pb272	24	78	201	15	NR	157	2	248	19
10pb282	185	83	185	0	TR	140	5	50	5
10pb210	32	86	33	12	TR	347	11	78	6
10pb223	213	84	214	6	TR	168	8	78	0
10pb227	202	60	13	15	NR	155	10	59	32
10pb227	209	50	20	10	NR	166	19	61	35
10pb227	212	65	21	22	NR	162	2	71	34
10pb227	205	66	8	33	NR	330	6	65	42
10pb227	226	77	37	33	NR	353	13	92	33
10pb229	234	70	242	22	TR	193	30	283	1
10pb229	39	90	39	36	TR	348	25	90	25
10pb243	48	90	48	6	TR	3	4	93	4
10pb191	225	80	43	10	NR	179	0	89	14
10pb001	62	64	227	28	NR	189	1	280	40
10pb162	214	88	214	7	TR	169	6	259	4
10pb177	40	74	215	18	NR	172	1	263	24
10pb183	245	83	248	20	TR	200	19	293	9
11071	7	90	7	46	TR	312	31	62	31
9119	15	76	180	45	NR	136	19	244	42
9129	190	87	190	9	TR	145	8	236	4
11025	205	88	24	20	NR	338	13	71	15
914	230	78	46	20	NR	2	5	94	23
915	215	74	32	9	NR	169	5	78	18
916	205	75	22	12	NR	159	2	68	19
989	50	89	50	6	TR	5	5	95	4
9116	63	67	213	50	NR	177	15	290	55
9118	225	88	226	20	TR	179	15	272	13
9118	218	42	10	23	NR	164	14	54	53
9118	58	88	238	0	NR	13	1	283	1
9118	235	78	51	19	NR	7	5	99	22
989	50	89	50	6	TR	5	5	95	4

Field No.	Fault strike	Fault dip	Striae trend	Striae plunge	Sense of Slip	T trend	T plunge	P trend	P plunge
11095	10	66	178	25	NR	139	1	229	36
11098	260	86	79	19	NR	33	10	126	16
11102	235	88	53	50	NR	357	31	112	34
10pb356	45	81	47	11	NL	91	1	1	14
10pb363	326	86	145	20	NR	99	11	192	17
	40	60	50	16	NL	267	9	3	33
10pb315	323	76	142	3	NR	278	8	187	12
10pb315	223	72	224	2	NL	87	11	180	14
10pb315	42	84	44	19	NL	89	9	357	18
10pb315	310	80	129	4	NR	265	4	174	10
10pb315	314	90	314	16	TR	268	11	0	11
10pb227	256	82	74	14	TL	121	16	29	4
10pb227	237	89	56	38	TL	108	27	5	25
10pb235	337	75	149	29	NR	105	9	201	32
10pb235	210	85	210	4	NL	75	1	165	6
10pb307	50	80	53	18	NL	98	5	6	20
10pb309	180	88	360	9	TL	45	8	315	5
10pb309	239	85	240	11	NL	285	4	194	11

Table of normal fault kinematic data from Peninsula Brunswick									
Field No.	**Fault strike**	**Fault dip**	**Striae trend**	**Striae plunge**	**Sense of Slip**	**T trend**	**T plunge**	**P trend**	**P plunge**
10pb332	265	40	41	30	NR	202	11	89	64
10pb315	309	72	7	69	NL	30	26	235	61
10pb296	280	70	335	66	NL	360	24	211	63
10pb294	98	79	220	77	NR	194	34	359	56
10pb294	57	67	190	60	NR	162	20	295	63
10pb242	152	55	210	50	NL	228	8	113	72
10pb239	82	55	132	48	NL	154	7	47	68
10pb239	331	55	30	51	NL	48	8	291	72
10pb236	64	44	204	32	NR	2	8	257	62
10pb227	237	66	347	65	NR	333	21	131	68
10pb227	220	55	356	45	NR	331	5	73	65
10pb213	320	55	30	53	NL	42	9	268	77
10pb191	262	17	341	17	NL	164	28	336	62
11055	259	44	46	28	NR	201	10	95	57

Field No.	Fault strike	Fault dip	Striae trend	Striae plunge	Sense of Slip	T trend	T plunge	P trend	P plunge
11055	285	10	33	10	NR	210	35	37	54
11023	84	57	230	41	NR	200	4	297	58
11023	65	52	180	49	NR	166	6	280	76
11023	70	57	157	57	NL	159	12	346	78
11018	270	85	279	60	NL	335	33	209	42

REFERENCES

Aleksandrowski, P. (1985), Graphical determination of principal stress directions for slickenside lineation populations; an attempt to modify Arthaud's method, Journal of Structural Geology, 7, 73-82.

Allmendinger, R., T. E. Jordan, S. M. Kay, and B. L. Isacks (1997), The evolution of the Altiplano-Puna plateau of the central Andes, Annual Review of Earth and Planetary Sciences, 25, 139-174.

Alvarez Marron, J., K. R. McClay, S. Harambour, L. Rojas, and J. Skarmeta (1993), Geometry and evolution of the frontal part of the Magallanes foreland thrust and fold belt (Vicuña Area), Tierra del Fuego, southern Chile, American Association of Petroleum Geologists Bulliten, 77, 1904-1921.

Banks, C. J., and J. Warburton (1986), 'Passive-roof' duplex geometry in the frontal structures of the Kirthar and Sulaiman mountain belts, Pakistan, Journal of Structural Geology, 8 (3/4), 229-237.

Barbeau, D. L., E. B. Olivero, N. L. Swanson-Hysell, K. M. Zahid, K. E. Murray, and G. E. Gehrels (2009), Detrital-zircon geochronology of the eastern Magallanes foreland basin: Implications for Eocene kinematics of the northern Scotia Arc and Drake Passage, Earth and Planetary Science Letters, 284 (3-4), 489-503.

Barker, P. F., J. Burrell (1977), The opening of Drake Passage, in Marine Geology, 25, pp. 15-34.

Barker, P. F. (2001), Scotia Sea regional tectonic evolution; implications for mantle flow and palaeocirculation, in Earth-Science Reviews, 55, pp. 1-39.

Barth, N. C., B. R. Hacker, G. G. E. Seward, E. O. Walsh, D. Young, and S. Johnston (2010), Strain within the ultrahigh-pressure Western Gneiss region of Norway recorded by quartz CPOs, Geological Society of London, Special Publications, 335 (1), 663-685.

Bernhardt, A., Z. R. Jobe, and D. R. Lowe (2011), Stratigraphic evolution of a submarine channel-lobe complex system in a narrow fairway within the Magallanes foreland basin, Cerro Toro Formation, southern Chile, Marine and Petroleum Geology, 28, 785-806.

Biddle, K. T., M. A. Uliana, R. M. Mitchum Jr., M. G. Fitzgerald, and R. C. Wright (1986), The strati- graphic and structural evolution of the central and eastern Magallanes basin, southern South America, Special Publication, International Association of Sedimentology, 8, 41-61.

Bruce, R. M., E. P. Nelson, S. G. Weaver and D. R. Lux (1991), Temporal and spatial variations in the southern Patagonian Batholith; constraints on magmatic arc development, in Special Paper - Geological Society of America, 265, pp. 1-12.

Bruhn, R. L., C. R. Stern, and M. J. D. Wit (1978), Field and Geochemical data Bearing on the Development of a Mesozoic Volcano-Tectonic Rift Zone and Back-Arc Basin in Southernmost South America, Earth and Planetary Science Letters, 41, 32-46.

Burns, K. L., M. J. Rickard, L. Belbin and F. Chamalaun (1980), Further palaeomagnetic confirmation of the Magellanes Orocline, Tectonophysics, 63, pp. 75-90.

Butler, R., E. Tavarnelli, and M. Grasso (2006), Structural inheritance in mountain belts: An Alpine–Apennine perspective, Journal of Structural Geology, 28 (11), 1893-1908.

Calderon, M., A. Fildani, F. Herve, C. M. Fanning, A. Weislogel, and U. Cordani (2007), Late Jurassic bimodal magmatism in the northern sea-floor remnant of the Rocas Verdes basin, southern Patagonian Andes, Journal of the Geological Society, 164 (5), 1011-1022.

Calderón, M., *et al*. (2012), The low-grade Canal de las Montañas Shear Zone and its role in the tectonic emplacement of the Sarmiento Ophiolitic Complex and Late Cretaceous Patagonian Andes orogeny, Chile, Tectonophysics, 524-525, 165-185.

Carbonell, P. J. T., L. V. Dimieri, and E. B. Olivero (2011), Progressive deformation of a Coulomb thrust wedge: the eastern Fuegian Andes Thrust-Fold Belt, Geological Society, London, Special Publications, 349 (1), 123-147.

Clark, M. K., and L. H. Royden (2000), Topographic ooze: Building the eastern margin of Tibet by lower crustal flow, Geology, 28 (8), 703-706.

Cotton, J. T., and H. A. Koyi (2000), Modeling of thrust fronts above ductile and frictional detachments: Application to structures in the Salt Range and Potwar Plateau, Pakistan, Geological Society of America Bulletin, 112 (3), 351-363.

Couzens, B. A., and D. V. Wiltschko (1996), The control of mechanical stratigraphy on the formation of triangle zones, Bulletin of Canadian Petroleum Geology, 44 (2), 165-179.

Covault, J. A., B. W. Romans, and S. A. Graham (2009), Outcrop expression of a continental margin-scale shelf-edge delta from the Cretaceous Magallanes Basin, Chile, Journal of Sedimentary Research, 79, 523-539.

Cunningham, W. D. (1993), Strike-slip faults in the southernmost Andes and the development of the Patagonian Orocline, Tectonics, 12, pp. 186-169.

Cunningham, W. D. (1994), Uplifted ophiolitic rocks on Isal Gordon, southernmost Chile: implications for the closure history of the Rocas Verdes marginal basin and the tectonic evolution of the Beagle Channel region, Journal of South American Earth Sciences, 7 (2), 135-147.

Cunningham, W. D. (1995), Orogenesis at the southern tip of the Americas; the structural evolution of the Cordillera Darwin Metamorphic Complex, southernmost Chile, in Tectonophysics, 244, pp. 229-197.

Cunningham, W. D., I. W. Dalziel, T.-Y. Lee, and L. A. Lawver (1995), Southernmost South America-Antarctic Peninsula relative plate motions since 84 Ma: Implications for the tectonic evolution of the Scotia Arc region, Journal of Geophysical Research, 100 (B5), 8257-8266.

Curtis, M. L., M. J. Flowerdew, T. R. Riley, M. J. Whitehouse, and J. S. Daly (2010), Andean sinistral transpression and kinematic partitioning in South Georgia, Journal of Structural Geology, 32 (4), 464-477.

Dahlstrom, C. D. A. (1969), Balanced cross-sections, Canadian Journal of Earth Sciences, 6, 743-757.

Dalziel, I. W. D., M. J. De Wit and K. F. Palmer (1974), Fossil marginal basin in the southern Andes, Nature, pp. 291-294.

Dalziel, I. W. D., R. H. Dott, Jr., R. D. Winn, Jr. and R. L. Bruhn (1975), Tectonic relations of South Georgia Island to the southernmost Andes, Geological Society of America Bulletin, 86, pp. 1034-1040.

Dalziel, I. W. D., K. F. Palmer (1979), Progressive deformation and orogenic uplift at the southern extremity of the Andes, in Geological Society of America Bulletin, 90, p. 259-280.

Dalziel, I. W. D. (1981), Back-Arc Extension in the Southern Andes: A Review and Critical Reappraisal, Philosophical Transactions of the Royal Society A: Mathematical, Physical and Engineering Sciences, 300 (1454), 319-335.

Dalziel, I. W. D., and R. Cortés (1972), Tectonic style of the southernmost Andes and the Antarctandes, paper presented at 24th International Geological Congress, 3, pp. 316-327.

Dalziel, I. W. D., R. Kligfield, W. Lowrie, and N. D. Opdyke (1973), Palaeomagnetic Data the Southernmost Andes and the Antarctandes, 87-101 pp., Acad. Press, London, United Kingdom.

Dalziel, I. W. D., L. A. Lawver, I. O. Norton, and L. M. Gahagan (2013), The Scotia Arc: Genesis, Evolution, Global Significance, Annual Review of Earth and Planetary Sciences, 41 (1), 767-793.

Darwin, C. R. (1846), Geological Observations on South America. Being the Third Part of the Geology of the Voyage of the Beagle, Under the Command of Capt. FitzRoy, R.N. During the Years 1832 to 1836, 279 pp., Smith Elder, London.

Davis, D. M., and T. Engelder (1985), The Role of Salt in Fold-and-Thrust Belts, Tectonophysics, 119, 67-88.

del Cogliano, D., R. Perdomo, J. Hormaechea, E. Olivero, J. Strelin and D. Martinioni (2000), GPS detection of movements between SCO and SAM plates in Tierra del Fuego Island, Congres Geologique International, Resumes, 31, p.

DeMets, C., R. G. Gordon, D. F. Argus, and S. Stein (1990), Current plate motions, Geophysical Journal International, 101, 425-478.

Diraison, M., P. R. Cobbold, E. A. Rossello, and A. J. Amos (1998), Neogene dextral transpression due to oblique convergence across the Andes of northwestern Patagonia, Argentina, Journal of South American Earth Sciences, 11, 519-532.

Diraison, M., P. R. Cobbold, D. Gapais, E. A. Rossello, and C. Le Corre (2000), Cenozoic crustal thickening, wrenching and rifting in the foothills of the southernmost Andes, Tectonophysics, 316, 119-191.

Diraison, M., P. R. Cobbold, D. Gapais, and E. A. Rossello (1997), Magellan Strait: Part of a Neogene rift system, Geology, 25 (8), 703-706.

Eagles, G. (2005), Tectonic evolution of the west Scotia Sea, Journal of Geophysical Research, 110 (B2).

Farr, T. G., *et al*. (2007), The Shuttle Radar Topography Mission, edited by C. I. o. T. Jet Propulsion Laboratory, Pasadena, CA.

Farzipour-Saein, A., A. Yassaghi, S. Sherkati, and H. Koyi (2009), Mechanical stratigraphy and folding style of the Lurestan region in the Zagros Fold-Thrust Belt, Iran, Journal of the Geological Society, 166 (6), 1101-1115.

Fildani, A. (2003), Initiation of the Magallanes foreland basin; timing of the southernmost Patagonian Andes orogeny revised by detrital zircon provenance analysis, in Geology, 31 (12) pp. 1081-1084.

Fildani, A., and A. M. Hessler (2005), Stratigraphic record across a retroarc basin inversion: Rocas Verdes–Magallanes Basin, Patagonian Andes, Chile, Geological Society of America Bulletin, 117 (11), 1596.

Fildani, A., S. M. Hubbard, and B. W. Romans (2009), Stratigraphic Evolution of Deep-Water Architecture: Examples of Controls and Depositional Styles From the Magallanes Basin, Southern Chile, in SEPM Field Trip Guidebook, 10, p. 73, Society of Sedimentary Geology, Tulsa, OK.

Fosdick, J. C., M. Grove, J. K. Hourigan, and M. Calderón (2013), Retroarc deformation and exhumation near the end of the Andes, southern Patagonia, Earth and Planetary Science Letters, 361, 504-517.

Fosdick, J. C., B. W. Romans, A. Fildani, A. Bernhardt, M. Calderon, and S. A. Graham (2011), Kinematic evolution of the Patagonian retroarc fold-and-thrust belt and Magallanes foreland basin, Chile and Argentina, 51 30'S, Geological Society of America Bulletin, 123 (9-10), 1679-1698.

Geletti, R., E. Lodolo, A. A. Schreider, and A. Polonia (2005), Seismic structure and tectonics of the Shackleton Fracture Zone (Drake Passage, Scotia Sea), Marine Geophysical Researches, 26 (1), 17-28.

Ghiglione, M., and V. Ramos (2005), Progression of deformation and sedimentation in the southernmost Andes, Tectonophysics, 405 (1-4), 25-46.

Ghiglione, M., and V. Ramos (2005), Progression of deformation and sedimentation in the southernmost Andes, Tectonophysics, 405 (1-4), 25-46.

Ghiglione, M. C., and E. O. Cristallini (2007), Have the southernmost Andes been curved since Late Cretaceous time? An analog test for the Patagonian Orocline, Geology, 35 (1), 13.

Ghiglione, M. C., J. Quinteros, D. Yagupsky, P. Bonillo-Martínez, J. Hlebszevtich, V. A. Ramos, G. Vergani, D. Figueroa, S. Quesada, and y. T. Zapata (2010), Structure and tectonic history of the foreland basins of southernmost South America, Journal of South American Earth Sciences, 29 (2), 262-277.

Gombosi, D. J., D. L. Barbeau Jr, and J. I. Garver (2009), New thermochronometric constraints on the rapid Palaeogene exhumation of the Cordillera Darwin complex and related thrust sheets in the Fuegian Andes, Terra Nova, 21 (6), 507-515.

Gust, D. A., K. T. Biddle, D. W. Phelps, and M. A. Uliana (1985), Associated Middle to Late Jurassic Volcanism and Extension in Southern South America, Tectonophysics, 116, 223-253.

Hanson, R. E., and T. J. Wilson (1991), Submarine rhyolitic volcanism in a Jurassic proto-marginal basin; southern Andes, Chile and Argentina, 265, 13-28.

Herve, F. (2003), Detrital zircon age patterns and provenance of the metamorphic complexes of southern Chile, Journal of South American Earth Sciences, 16 (1), 107-123.

Herve, F., R. J. Pankhurst, C. M. Fanning, M. Calderon, and G. M. Yaxley (2007), The South Patagonian Batholith; 150 my of granite magmatism on a plate margin, Lithos, 97, 373-394.

Herve, F., C. M. Fanning, R. J. Pankhurst, C. Mpodozis, K. Klepeis, M. Calderon, and S. N. Thomson (2010), Detrital zircon SHRIMP U-Pb age study of the Cordillera Darwin Metamorphic Complex of Tierra del Fuego: sedimentary sources and implications for the evolution of the Pacific margin of Gondwana, Journal of the Geological Society, 167 (3), 555-568.

Herve, F., H. Miller, and C. Pimpirev (2005), Patagonia - Antarctic Connections before Gondwana Break-Up, Springer-Verlag, Berlin Heidelberg, New York.

Hervé, F., E. Nelson, K. Kawashita, and M. Suárez (1981), New isotopic ages and the timing of orogenic events in the Cordillera Darwin, southernmost Chilean Andes, Earth and Planetary Science Letters, 55, 257-265.

Hervé, F., R. J. Pankhurst, C. M. Fanning, M. Calderón, and G. M. Yaxley (2007), The South Patagonian batholith: 150 my of granite magmatism on a plate margin, Lithos, 97 (3-4), 373-394.

Herve, M., M. Suarez, and A. Puig (1984), The Patagonian Batholith S of Tierra del Fuego, Chile: timing and tectonic implications, Journal of the Geological Society, 141 (5), 909-917.

Hirth, G., and J. Tullis (1992), Dislocation creep regimes in quartz aggregates, Journal of Structural Geology, 14, 145-159.

Hubbard, S. M., B. W. Romans, and S. A. Graham (2008), Deep-water foreland basin deposits of the Cerro Toro Formation, Magallanes basin, Chile: architectural elements of a sinuous basin axial channel belt, Sedimentology, 55 (5), 1333-1359.

Johnson, C. (1990), Antecedentes estratigráficos de la ribera Sur del Seno Almirantazgo, Thesis, Universidad de Chile, Santiago.

Katz, H. R. (1963), Revision of Cretaceous Stratigraphy in Patagonian Cordillera of Ultima Esperanza, Magallanes Province, Chile, Bulletin of the American Association of Petroleum Geologists, 47 (3), 506-524.

Klepeis, K., P. Betka, G. Clarke, M. Fanning, F. Hervé, L. Rojas, C. Mpodozis, and S. Thomson (2010), Continental underthrusting and obduction during the Cretaceous closure of the Rocas Verdes rift basin, Cordillera Darwin, Patagonian Andes, Tectonics, 29 (3).

Klepeis, K. A. (1994a), Relationship between uplift of the metamorphic core of the southernmost Andes and shortening in the Magallanes foreland fold and thrust belt, Tierra del Fuego, Chile, Tectonics, 13, 882-904.

Klepeis, K. A (1994b), The Magallanes and Deseado fault zones; major segments of South American-Scotia transform plate boundary in southernmost South America, Tierra del Fuego, Journal of Geophysical Research, 99, 22.

Klepeis, K. A., and J. Austin (1997), Contrasting styles of superposed deformation in the southernmost Andes, Tectonics, 16, 776-755.

Kohn, M. J., F. S. Spear, and I. D. Dalziel (1993), Metamorphic P-T Paths from Cordillera Darwin, a Core Complex in Tierra del Fuego, Chile, Journal of Petrology, 34, 519-542.

Kohn, M. J., F. S. Spear, T. M. Harrison, and I. W. D. Dalziel (1995), 40Ar/39Ar geochronology and P-T-t paths from the Cordillera Darwin Metamorphic Complex, Tierra del Fuego, Chile, J. metamorphic geology, 13, 251-270.

Kraemer, P. E. (1998), Structure of the Patagonian Andes; regional balanced cross section at 50 degrees S, Argentina, in International Geology Review, 40, pp. 896-915.

Kraemer, P. E. (2003), Orogenic shortening and the origin of the Patagonian orocline (56° S. Lat.) Journal of South American Earth Sciences, 15, 731-748.

Kranck, E. H. (1932), Geological investigations in the Cordillera of Tierra del Fuego, Acta Geogr., Soc. Geogr. Fenniae, 4(2), 1-231, Helsinski.

Kretz, R. (1983), Symbols for rock-forming minerals, American Mineralogist, 68, 277-279.

Lagabrielle, Y., Y. Goddéris, Y. Donnadieu, J. Malavieille, and M. Suarez (2009), The tectonic history of Drake Passage and its possible impacts on global climate, Earth and Planetary Science Letters, 279 (3-4), 197-211.

Law, R. D. (1987), Crystallographic fabrics and deformation histories, Journal of the Geological Society, 144 (4), 675-678.

Law, R. D. (1990), Crystallographic fabrics: a selective review of their applications to research in structural geology, Geological Society of London, Special Publications, 54 (1), 335-352.

Law, R. D., and R. J. Knipe (1984), Strain path partitioning within thrust sheets: microstructural and petrofabric evidence from the Moine Thrust zone at Loch Eriboll, northwest Scotland, Journal of Structural Geology, 6 (5), 477-497.

Law, R. D., S. M. Schmid, and J. Wheeler (1990), Simple shear deformation and quartz crystallographic fabrics: a possible natural example from the Torridon area of NW Scotland, Journal of Structural Geology, 12 (1), 29-45.

Lister, G. S. (1977), Crossed-girdle C-axis fabrics in quartzites plastically deformed by plane strain and progressive simple shear, Tectonophysics, 39, 51-54.

Lister, G. S., and U. F. Dornsiepen (1982), Fabric transitions in the Saxony granulite terrain, Journal of Structural Geology, 4 (1), 81-92.

Lister, G. S., and B. E. Hobbs (1980), The simulation of fabric development during plastic deformation and its application to quartzite: the influence of deformation history, Journal of Structural Geology, 4 (3), 355-370.

Lister, G. S., M. S. Paterson, and B. E. Hobbs (1978), The simulation of fabric development in plastic deformation and its applicaiton to quartzite: the model, Tectonophysics, 45, 107-158.

Lodolo, E. (2003), Magallanes-Fagnano continental transform fault (Tierra del Fuego, southernmost South America), Tectonics, 22 (6).

Lodolo, E., F. Donda, and A. Tassone (2006), Western Scotia Sea margins: Improved constraints on the opening of the Drake Passage, Journal of Geophysical Research, 111(B6).

Lowell, J. D. (1995), Mechanics of basin inversion from worldwide examples, Geological Society, London, Special Publications, 88 (1), 39-57.

MacKay, P. A. (1996), The Highwood Structure: a tectonic wedge at the foreland edge of the southern Canadian Cordillera, Bulletin of Canadian Petroleum Geology, 44 (2), 215-232.

Mainprice, D. (2005), Pfch5, [computer software], ftp://www.gm.univ-montp2.fr/mainprice//CareWare_Unicef_Programs/

Mainprice, D., J.-L. Bouchez, P. Blumenfeld, and J. M. Tubia (1986), Dominant c slip in naturally deformed quartz: Implications for dramatic plastic softening at high temperature, Geology, 14, 819-822.

Maloney, K. T., G. L. Clarke, K. A. Klepeis, C. M. Fanning, and W. Wang (2011), Crustal growth during back-arc closure: Cretaceous exhumation history of Cordillera Darwin, southern Patagonia, Journal of Metamorphic Geology, 29 (6), 649-672.

Marrett, R., and R. Allmendinger (1990), Kinematic analysis of fault-slip data, Journal of Structural Geology, 12, 973-986.

Marrett, R., and R. W. Allmendinger (1992), Amount of extension on "small" faults: An example from the Viking graben, Geology, 20, 47-50.

Marshak, S., and G. Mitra (1998), Basic Methods of Structural Geology, Prentice-Hall, Inc., Upper Saddle River, New Jersey.

McAtamney, J., K. Klepeis, C. Mehrtens, S. Thomson, P. Betka, L. Rojas, and S. Snyder (2011), Along-strike variability of back-arc basin collapse and the initiation of sedimentation in the Magallanes foreland basin, southernmost Andes (53–54.5°S), Tectonics, 30 (5).

McMechan, M. E. (1985), Low-taper triangle-zone geometry: an interpretation for the Rock Mountain Foothills, Pine Pass - Peace River Area, British Columbia, Bulletin of Canadian Petroleum Geology, 33 (1), 31-38.

McQuarrie, N., B. K. Horton, G. Zandt, S. Beck, and P. G. DeCelles (2005), Lithospheric evolution of the Andean fold-thrust belt, Bolivia, and the origin of the central Andean Plateau, Tectonophysics, 399, 15-37.

Menichetti, M., E. Lodolo, and A. Tassone (2008), Structural geology of the Fuegian Andes and Magallanes fold-and-thrust belt - Tierra del Fuego Island, Geologica Acta, 6 (1), 19-42.

Mouthereau, F., and O. Lacombe (2006), Inversion of the Paleogene Chinese continental margin and thick-skinned deformation in the Western Foreland of Taiwan, Journal of Structural Geology, 28 (11), 1977-1993.

Mpodozis, C., P. Alvarez, S. Elgueta, P. Mella, F. Hervé, and M. Fanning (2007), Revised Cretaceous Stratigraphy of the Magallanes Foreland Basin at Seno Skyring: Regional Implicaitons of New SHRIMP Age Data on Detrital Zircon Populations, in GEOSUR 2007 International Congress on the Geology and Geophysics of the Southern Hemisphere, edited, Univ. Católica de Chile, Santiago. Nov. 20-21

Mpodozis, C., C. Arriagada, M. Basso, P. Roperch, P. Cobbold, and M. Reich (2005), Late Mesozoic to Paleogene stratigraphy of the Salar de Atacama Basin, Antofagasta, Northern Chile: Implications for the tectonic evolution of the Central Andes, Tectonophysics, 399 (1-4), 125-154.

Mpodozis, C., and L. Rojas (2006), Orogénesis en los Andes Patagónicos Australes de Tierra del Fuego: Cierre de una "Cuenca Marginal" o Colisión Intracontinental?, in XI Congreso Geológico Chileno, Antofagasta, Chile. Aug. 7-11.

Mukasa, S. B., and I. W. D. Dalziel (1996), Southernmost Andes and South Georgia Island, North Scotia Ridge: Zircon U-Pb and muscovite 40Ar/39Ar age constrains on tectonic evolution of Southwestern Gondwanaland, Journal of South American Earth Sciences, 9 (5/6), 349-365.

Natland, M. L., E. Gonzalez P, A. Canon and M. Ernst (1974), A system of stages for correlation of Magallanes Basin sediments, Memoir - Geological Society of America, 139, 126 pp.

Nelson, E. P., I. W. D. Dalziel, and A. G. Milnes (1980), Stuctural geology of the Cordillera Darwin - collisional-style orogenesis in the southernmost Chilean Andes, Eclogae Geologicae Helvetiae, 73 (3), 727-751.

Olivero, E. B., D. R. Martinioni (2001), A review of the geology of the Argentinian Fuegian Andes, Journal of South American Earth Sciences, 14, pp. 188-175.

Pankhurst, R. (2003), Chronological study of the pre-Permian basement rocks of southern Patagonia, Journal of South American Earth Sciences, 16 (1), 27-44.

Pankhurst, R. J., T. R. Riley, C. M. Fanning, S. P. Kelley (2000), Episodic silicic volcanism in Patagonia and the Antarctic Peninsula; chronology of magmatism associated with the break-up of Gondwana, Journal of Petrology, 41, pp. 605-625.

Pankhurst, R. J., P. T. Leat, P. Sruoga, C. W. Rapela, M. Márquez, B. C. Storey, and T. R. Riley (1998), The Chon Aike silicic igneous province of Patagonia and related rock in Antarctica: a silicic LIP, Journal of Volcanology and Geothermal Research, 81, 113-136.

Passchier, C. W., and R. A. J. Trouw (2005), Micro-tectonics 2nd edition, Springer Berlin Heidelberg, New York.

Pelayo, A. M., and D. A. Wiens (1989), Seismotectonics and relative plate motions in the Scotia Sea region, Journal of Geophysical Research, 94 (B6), 7293-7320.

Petit, J. P. (1987), Criteria for the sense of movement on fault surfaces in brittle rocks, Journal of Structural Geology, 9 (5/6), 597-608.

Ramos, V. A. (1989), Foothills structure in northern Magallanes Basin, Argentina, American Association of Petroleum Geologists Bulliten, 73, 887-903.

Ramsay, and Huber (1983), The Techniques of Modern Structural Geology, Academic Press Inc. (London) Ltd.

Rapalini, A. E., F. Herve, V. A. Ramos and S. E. Singer (2001), Paleomagnetic evidence for a very large counterclockwise rotation of the Madre de Dios Archipelago, southern Chile, in Earth and Planetary Science Letters, 184, pp. 471-487.

Rapalini, A. E. (2007), A paleomagnetic analysis of the Patagonian Orocline, in Geologica Acta, 5, pp. 294-287.

Rojas, L., and C. Mpodozis (2006), Geología Estructural de la Faja Plegada y Corrida del sector Chileno de Tierra del Fuego, Andes Patagónicos Australes, in XI Congreso Geológico Chileno, edited, Antofagasta, Chile. Aug. 7-11.

Romans, B. W., A. Fildani, S. A. Graham, S. M. Hubbard, and J. A. Covault (2010), Importance of predecessor basin history on sedimentary fill of a retroarc foreland basin: provenance analysis of the Cretaceous Magallanes basin, Chile (50-52°S), Basin Research, 22 (5), 640-658.

Romans, B. W., A. Fildani, S. M. Hubbard, J. A. Covault, J. C. Fosdick, and S. A. Graham (2011), Evolution of deep-water stratigraphic architecture, Magallanes Basin, Chile, Marine and Petroleum Geology, 28 (3), 612-628.

Ryan, W. B. F. (2009), Global Multi-Resolution Topography synthesis, Geochemistry Geophysics Geosystems, 10 (Q03014).

Sans, M., J. A. Muñoz, and J. Vergés (1996), Triangle zone and thrust wedge geometries related to evaporitic horizons (southern Pyrenees), Bulletin of Canadian Petroleum Geology, 44 (2), 375-384.

Saunders, A. D., J. Tarney, C. R. Stern and I. W. D. Dalziel (1979), Geochemistry of Mesozoic marginal basin floor igneous rocks from southern Chile, in Geological Society of America Bulletin, 90, p. 237.

Schmid, S. M., and M. Casey (1986), Complete fabric analysis of some commonly observed quartz c-axis patterns, in Mineral and Rock Deformation: Laboratory Studies - The Paterson Volume, edited by B. E. Hobbs and H. C. Heard, pp. 263-286, American Geophysical Union Geophysical Monograph.

Scott, K. M. (1966), Sedimentoogy and dispersal patterns of a Cretaceous flysch sequence, Patagonian Andes, southern Chile, American Association of Petroleum Geologists Bulliten, 50, 72-107.

SERNAGEOMIN (2002), Mapa Geológico de Chile, Servicio Nacional de Geología y Minería, Chile, Santiago.

Smalley, R., I. W. D. Dalziel, M. G. Bevis, E. Kendrick, D. S. Stamps, E. C. King, F. W. Taylor, E. Lauría, A. Zakrajsek, and H. Parra (2007), Scotia arc kinematics from GPS geodesy, Geophysical Research Letters, 34 (21).

Smalley, R., E. Kendrick, M. G. Bevis, I. W. D. Dalziel, F. Taylor, E. Lauría, R. Barriga, G. Casassa, E. Olivero, and E. Piana (2003), Geodetic determination of relative plate motion and crustal deformation across the Scotia-South America plate boundary in eastern Tierra del Fuego, Geochemistry, Geophysics, Geosystems, 4 (9).

Sobornov, K. O. (1996), Lateral variations in structural styles of tectonic wedging in the northeastern Caucasus, Russia, Bulletin of Canadian Petroleum Geology, 44 (2), 385-399.

Stern, C. R., and M. J. De Wit (2003), Rocas Verdes ophiolites, southernmost South America: remnants of progressive stages of development of oceanic-type crust in a continental margin back-arc basin, Geological Society of London, Special Publications, 218 (1), 665-683.

Stipp, M., H. Stunitz, R. Heilbronner, and S. M. Schmid (2002), The eastern Tonale fault zone: a 'natural loboratory' for crystal plastic deformation of quartz over a temperature range of 250 to 700 C, Journal of Structural Geology, 24, 1861-1884.

Stockmal, G. S., D. Lebel, M. E. McMechan, and P. A. MacKay (2001), Structural style and evolution of the triangle zone and external Foothills, southwestern Alberta: Implications for thin-skinned thrust-and-fold belt mechanics, Bulletin of Canadian Petroleum Geology, 49 (4), 472-496.

Storey, B. C., and D. I. M. Macdonald (1984), Processes of formation and filling of a Mesozoic back-arc basin on the island of South Georgia, Geological Society, London, Special Publications, 16(1), 207-218.

Suárez, M., and T. H. Pettigrew (1976), An upper Mesozoic island-arc-backarc system in the southern Andes and South Georgia, Geological Magazine, 113 (305-328).

Teixell, A., and H. A. Koyi (2003), Experimental and field study of the effects of lithological contrasts on thrust-related deformation, Tectonics, 22 (5).

Thomas, W. A. (2007), Balancing tectonic shortening in contrasting deformation styles through a mechanically heterogeneous stratigraphic succession, Special Paper - Geological Society of America, 433, pp. 277-290.

Torres Carbonell, P. J., E. B. Olivero, and L. V. Dimieri (2008), Structure and evolution of the Fuegian Andes foreland thrust-fold belt, Tierra del Fuego, Argentina: Paleogeographic implications, Journal of South American Earth Sciences, 25 (4), 417-439.

Turcotte, D. L. (1986), A fractal model for crustal deformation, Tectonophysics, 132, 261-269.

Twiss, R. J., and E. M. Moores (2007), Structural Geology, 736 pp., W.H. Freeman and Company, New York.

Wilson, T. J. (1991), Transition from back-arc to foreland basin development in the southernmost Andes; stratigraphic record from the Ultima Esperanza District, Chile, Geological Society of America Bulletin, 103, 98-111.

Winn, R. D., and R. H. Dott (1979), Deep-water fan-channel conglomerates of Late Cretaceous age, southern Chile, Sedimentology, 26, 203-228.

Winslow, M. A. (1981), Mechanisms for basement shortening in the Andean foreland fold belt of southern South America, Geological Society, London, Special Publications, *9*(1), 513-528.

Winslow, M. A. (1982), The structural evolution of the Magallanes Basin and neotectonics in the southernmost Andes, in Antarctic Geoscience, edited by C. Craddock, pp. 143-154, Univ. of Wis. Press, Madison.

Zahid, K. M., and D. L. Barbeau Jr (2010), Provenance of eastern Magallanes foreland basin sediments: Heavy mineral analysis reveals Paleogene tectonic unroofing of the Fuegian Andes hinterland, Sedimentary Geology, 229 (1-2), 64-74.